CO$_2$ Hydrogenation to Methanol over Heterogeneous Catalysts: Copper and Beyond

PROEFSCHRIFT

ter verkrijging van de graad van doctor aan de Technische Universiteit Eindhoven, op gezag van de rector magnificus prof.dr.ir. F.P.T. Baaijens, voor een commissie aangewezen door het College voor Promoties, in het openbaar te verdedigen op vrijdag 4 december 2020 om 16:00 uur

door

Jiadong Zhu

geboren te Zhejiang, China

Dit proefschrift is goedgekeurd door de promotoren en de samenstelling van de promotiecommissie is als volgt:

voorzitter: prof.dr. A.P.H.J. Schenning

1^e promotor: prof.dr.ir. E.J.M. Hensen

copromotor: dr. N. Kosinov

leden: prof.dr. A. Urakawa (TUD)

                   prof.dr. M. Behrens (Universität Duisburg Essen)

                   prof.dr.ir. J. van der Schaaf

                   prof.dr.ir. L. Lefferts (Universiteit Twente)

                   prof.dr.eng. F. Gallucci

Het onderzoek of ontwerp dat in dit proefschrift wordt beschreven is uitgevoerd in overeenstemming met de TU/e Gedragscode Wetenschapsbeoefening.

To my grandma

Jiadong Zhu

CO₂ Hydrogenation to Methanol over Heterogeneous Catalysts: Copper and Beyond

TABLE OF CONTENTS

CHAPTER 1

Introduction and Scope

1.1 Sustainability Transition

Ever since the coal-powered steam engine was developed during the first industrial revolution, the world has been largely shaped by fossil fuels – coal, petroleum oil and nature gas. The energy from the sun accumulated in fossil fuels for millions of years provides the foundation of progress and prosperity of a large fraction of the world population. In addition to providing energy, these fossil sources and most prominently crude oil supply the intermediate chemicals needed for the production of polymers, materials, and pharmaceuticals. Nevertheless, there is growing concern about the widespread and still growing use of fossil fuels. Fossil fuels are mixtures of hydrocarbons with varying hydrogen-to-carbon ratios. Upon their combustion to release energy, carbon is transformed into carbon dioxide (CO_2), which accumulates in the Earth's atmosphere. The increasing anthropogenic CO_2 concentration is considered as the main cause of global warming, posing a serious threat to humanity.[1] Moreover, fossil fuels are non-renewable resources and will be inevitably depleted in the long term. This will lead to a serious energy crisis and will also affect the supply of many materials that we use on a daily basis. Therefore, a transition to sustainable development is required, in which the needs of the present energy-intensive society will be met without compromising the life quality of future generations.[2]

As noted by Ahmed Zaki Yamani, former Oil Minister of Saudi Arabia "*the Stone Age did not end for lack of stone and the Oil Age will end long before the world runs out of oil.*" Nowadays, much effort is being dedicated to developing solutions to reduce our reliance on fossil fuels. For example, a significant progress has been achieved in converting renewable biomass into a range of bio-based chemicals and energy, which can in many aspects compete with traditional fossil-fuel-based refinery.[3] A significant growth in global energy production from renewable resources such as solar, wind and tidal contributes to decarbonizing the energy sector.[4,5] Nonetheless, these new advantageous technologies also bring challenges. One of the essential problems, yet to be solved, is the efficient storage of renewable energy at a large scale as there is a mismatch between the current electricity grid systems and the intermittent availability of the renewable sources.[6] It has been reported that more than 20% integration of intermittent renewable energy can cause serious disruptions to the current grid system.[7] At present, pumped hydroelectric energy storage is the main way to store energy, but it has limited capacity and is geographically constrained.[7] It becomes clear that innovation in large-scale energy storage

technologies will be a critical component to realize the sustainable energy transition.

Storing surplus renewable electricity in chemical bonds is regarded a promising approach, because it can be effective in terms of density of the stored energy, compatibility with the existing energy infrastructure and provide an interface with a sustainable chemical industry via chemical building blocks. As most of the current energy carriers and nearly all chemicals are based on carbon, the conversion of CO_2 using surplus renewable electricity to chemical compounds is attractive, the more since it would also reduce atmospheric CO_2 levels when performed at a very large scale.[8] Besides using waste CO_2 streams from point sources such as the cement industry or from the upgrading of renewables (e.g., biomass), direct capture of CO_2 from the air using advanced gas separation technologies is considered a long-term objective.[9] Regarding CO_2 conversion, the renewable electricity can be used directly to upgrade CO_2 via electrochemical reactions[10] or used to first generate H_2, which then reacts with CO_2 to yield the desired products.[11]

1.2 Methanol Economy

CO_2 can be converted to useful chemical intermediates or fuels via thermocatalytic routes such as the reverse water-gas shift reaction (rWGS), methanation, and methanol synthesis.[12–15] The rWGS can be used to upgrade CO_2 with H_2 to syngas ($CO + H_2$), which is a versatile chemical platform giving access to many chemicals. Methanation allows production of synthetic natural gas, which can be directly injected into the existing gas grid. Related to this, synthesis gas can also be converted to higher hydrocarbons by Fischer-Tropsch synthesis, which gives rise to amongst others transportation fuels. Methanol synthesis is probably the most lucrative route of CO_2 conversion. Methanol is currently a large-volume chemical intermediate, and in the context of sustainability it is also proposed to be an important renewable energy carrier and storage chemical. The concept of the methanol economy has been advocated by Nobel laureate George A. Olah since the 1990s.[16,17] An illustration of methanol economy based on CO_2 recycling is given in **Figure 1.1.** In this concept, methanol can serve as a clean burning fuel, a convenient storage material for renewable energy and a versatile raw material to produce hydrocarbons. In contrast to H_2, methanol is a liquid (b.p.= 64.7 °C) which makes the use of existing transport and storage infrastructural possible. Owing to its high octane rating, methanol can be used as an additive or substitute for gasoline in internal combustion engines. The commercially available M85 fuel for instance is a blend of 85% methanol and 15% gasoline. Furthermore, the energy chemically stored in methanol can be released as electricity using for instance direct methanol fuel cells.[18]

Besides its significant potential in energy applications, methanol plays an important role in the chemical industry. Methanol is one of the key chemical building blocks and its demand is projected to continuously grow in the future.[19] Various bulk chemicals can be produced from methanol including formaldehyde, methyl methacrylate, acetic acid and methyl chloride,

among others.[20] Notably, methanol can also be converted to ethylene/propylene and gasoline using mature methanol-to-olefin (MTO) and methanol-to-gasoline (MTG) technologies, linking the methanol economy with the petrochemical industry.[21] Another advantage of methanol economy lies in its potential contribution to global warming mitigation, because atmospheric CO_2 can be used as feedstock for methanol production.[20] In such a methanol economy where CO_2 is the carbon source, an anthropogenic carbon cycle can be realized, which is similar to the one operated by flora in nature.
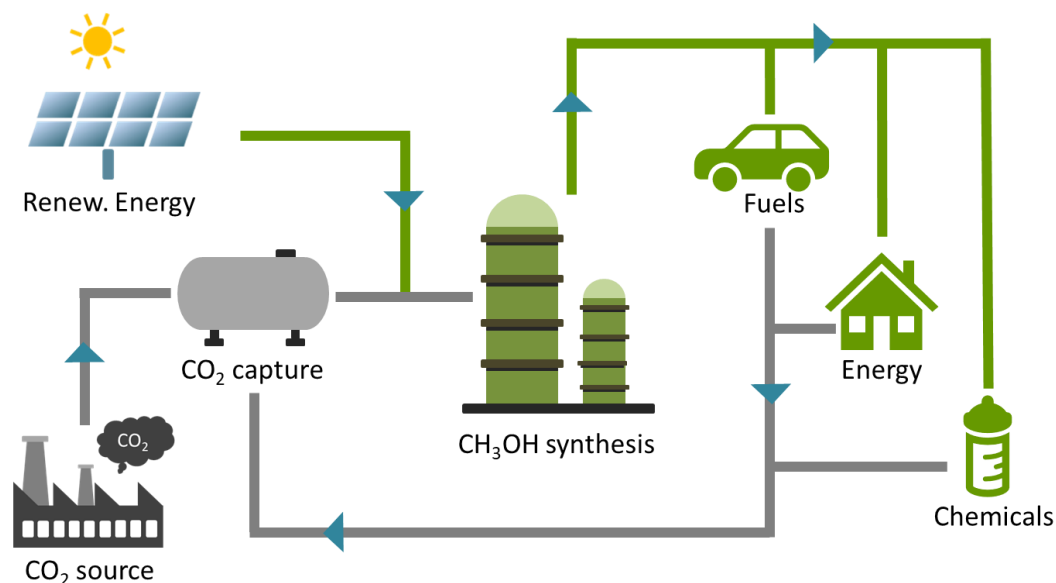
Figure 1.1. Simplified overview of CO_2-based methanol economy.

1.3 Methanol Production and Catalysis

Methanol, also known as wood alcohol, was initially produced by dry distillation of wood, yielding an extract with many impurities (wood vinegar). It was not until 1661 that pure methanol was obtained by Robert Boyle.[22] He purified the wood vinegar through reacting it with milk of lime and further distillation. The wood distillation process remained the dominant way of methanol production until the emergence of the syngas-to-methanol process in the 1920s. Benefiting from the development of high-pressure reactor technology, Alwin Mittasch and co-workers at Badische Anilin und Soda Fabrik (BASF) discovered that methanol was produced from CO and H_2 over iron oxide catalysts during their developmental works on ammonia synthesis (Haber-Bosch process).[23] The next decisive step was made by Mathias Pier and co-workers who developed a sulfur-resistant ZnO-Cr_2O_3 methanol synthesis catalyst through extensive catalyst screening in the early 1920s.[24,25] Afterwards, the first large-scale industrial methanol production process was launched by BASF at the Leuna site in 1923. The BASF process was operated at high pressure (25-35 MPa) and temperature (320-450 °C). This process dominated the industrial methanol production for more than 40 years. After the BASF high pressure methanol (HPM) process, Imperial Chemical Industries (ICI) developed a low

pressure methanol (LPM) process in the 1960s, which was operated at 5-10 MPa and a much lower temperature (200-300 °C).[26] The success of the LPM process was intimately linked to the innovations in the clean syngas production by improved steam reforming technology at the same time. The availability of syngas free of impurities (e.g., sulfur and chlorine) enabled the utilization of poison-sensitive but highly active copper-based catalysts ($Cu/ZnO/Al_2O_3$) in methanol production.[27] The first LPM plant was built and commissioned by ICI in Billingham in 1966. Since then, LPM processes using Cu-ZnO based catalysts have rapidly replaced the HPM processes, and LPM is still the state-of-the-art methanol production technology.

As demonstrated by the history of methanol production, modern chemical industry strongly relies on catalysis. It is estimated that 85-90 % of all the chemical products include catalytic processes.[28] Besides methanol production, other important large-scale catalytic chemical processes include ammonia synthesis, Fischer–Tropsch synthesis, methane steam reforming, fluid catalytic cracking (FCC), hydrodesulfurization, etc. Furthermore, catalysis also plays a critical role in environmental protection and pollution control. The most prominent example is probably the three-way catalyst (TWC), which simultaneously converts CO, unburned hydrocarbon (C_xH_y) and NO_x from the car exhaust into less harmful CO_2, N_2 and H_2O.[29] By simple definition, catalyst is a substance that accelerates chemical reaction without being consumed or altered during the reaction. A catalytic reaction is achieved by establishing a multistep catalytic cycle with favourable kinetics as compared to a non-catalytic reaction. To illustrate this, **Figure 1.2** shows the potential energy diagrams of catalytic and non-catalytic pathways for a hypothetical gas phase reaction (A + B → P). For the non-catalytic pathway, reaction proceeds in the gas phase when A and B collide with sufficient energy to overcome the high activation energy barrier. The presence of a catalyst offers an alternative reaction pathway: A and B first bond to the catalyst, where they react to form P, after which P leaves the catalyst, closing the catalytic cycle. Notably, the interactions between reactants and catalyst result in a significantly lower activation energy. The lower activation energy means that the reaction can take place with higher yield or at milder conditions. Besides increasing the reaction rate, catalyst can influence the product selectivity in complex reactions by promoting desired reactions and/or inhibiting the undesired ones. Despite the changes in reaction kinetics (*i.e.,* activity and selectivity), it should be mentioned that the overall changes in reaction Gibbs free energy are the same for catalytic and non-catalytic reactions, meaning that catalysts do not affect reaction thermodynamics.

Three main branches of catalysis exist – heterogeneous, homogeneous and bio-catalysis. This thesis is dedicated to heterogeneous catalysis, one where the catalyst and reactants are in different phases. An obvious advantage of heterogeneous catalysis is the ease of product separation from the catalysts, enabling continuous operation of chemical processes. To maximize the utilization of catalytic materials for the surface reactions, heterogeneous catalysts are typically of high specific surface area. The use of support or carrier materials is a common

strategy to disperse the active phases (*e.g.*, transition metals, metal sulfides and metal phosphides), and to provide thermal and mechanical stability.[30] Metal oxides, such as SiO_2, Al_2O_3, TiO_2 and CeO_2, are often used for that purpose. In addition to acting as a structural promoter, it has become clear that support often plays an important role in facilitating catalytic reactions (*vide infra*). Given the comprehensive research in syngas-to-methanol conversion and the analogy between methanol synthesis from syngas and CO_2, several important catalysis aspects of syngas-to-methanol conversion, with an emphasis on Cu-ZnO system, will be discussed in the next section.
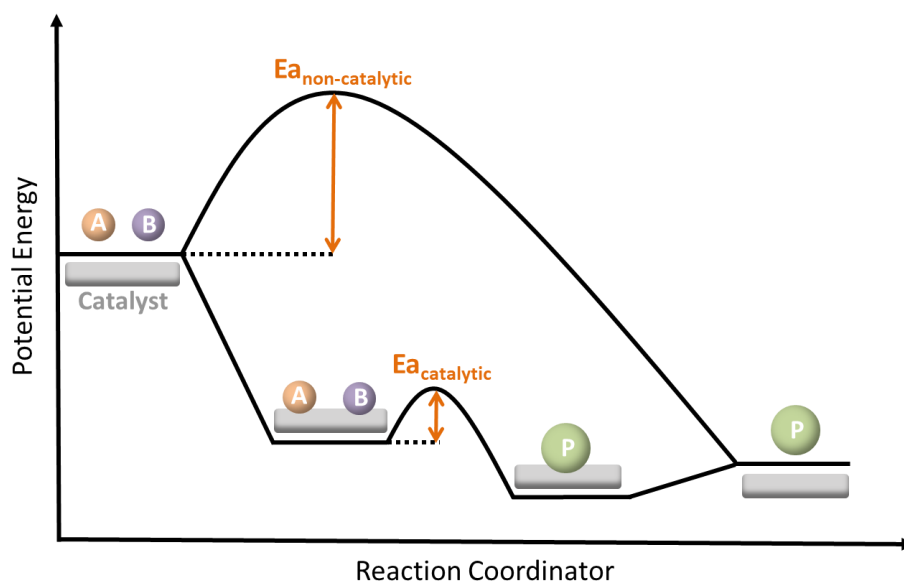
Figure 1.2. Potential energy diagrams of non-catalytic and catalytic reactions.

1.3.1 Active sites

ZnO is a major component (15 – 50 wt%) of modern Cu-based methanol synthesis catalysts.[31] Earlier research demonstrated that ZnO can strongly promote the Cu surface for methanol synthesis in comparison to other supports.[32,33] The origin of this unique Cu-Zn synergy is one of the central questions in methanol synthesis catalysis. Different and sometimes conflicting arguments have been proposed to explain the Cu-Zn synergy. Explanations include a Schottky junction effect at the Cu-ZnO interface,[34] reverse hydrogen spillover from ZnO to Cu,[35,36] active electron-deficient $Cu^{\delta+}$ sites,[37–39] and support-induced lattice strain and defects in Cu particles.[40,41] Dynamic changes of the catalyst were investigated in more detail in later studies to elucidate the Cu-Zn synergy. Using in situ XRD and XAFS, Grunwaldt et al. demonstrated that Cu particles supported on ZnO undergo reversible morphology changes in response to the changes in gas atmosphere.[42] Using low-energy ion scattering (LEIS), Jansen et al. showed that the Cu surface is decorated with ZnO_x species in $^{63}Cu/^{68}ZnO/SiO_2$ catalysts.[43] The presence of a ZnO_x overlayer on the Cu surface was also confirmed in a later quasi in situ TEM study.[44] The decoration of the Cu surface by ZnO_x species is in line with the importance of the Cu-

ZnO$_x$ interface in methanol synthesis. In contrast, Fujitani et. al ascribed the Cu-Zn synergy to the formation of a surface Cu-Zn alloy under methanol synthesis conditions.[45,46] A surface alloy model was further elaborated in two recent studies in which Cu step sites decorated with Zn atoms were suggested to be the active sites[47] and Zn migration to Cu surface was quantitively described as a function of methanol synthesis conditions and particle size of Cu and ZnO.[48]
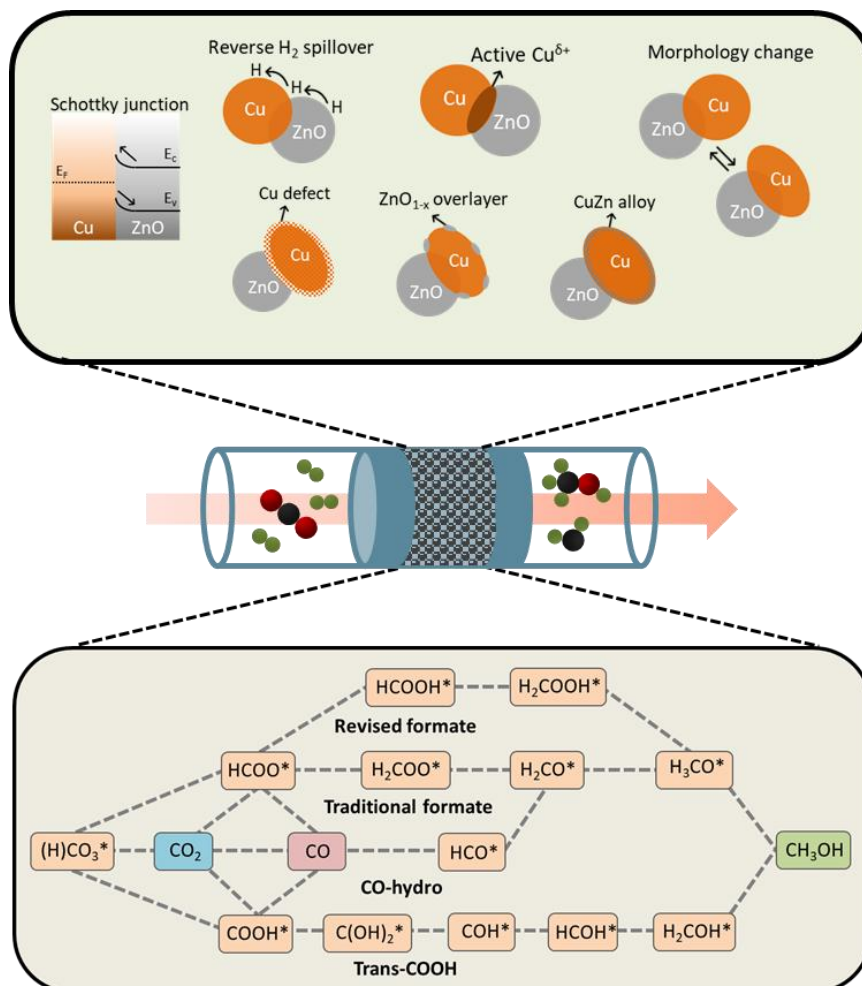
Figure 1.3. Active sites and mechanism of syngas-to-methanol reaction over Cu-ZnO catalysts.

1.3.2 Reaction mechanism

It is well known that methanol synthesis over Cu-ZnO based catalysts can be boosted by adding a small amount of CO_2 to the CO/H_2 feed.[49–51] Investigations on CO_2 promotion revealed that CO_2 is the actual source of methanol synthesis, while CO acts as a precursor to CO_2 via the water-gas shift (WGS) reaction and as an oxygen scavenger to maintain the catalyst in the reduced state.[52–55] The reaction mechanism and the involved intermediates constitute another complex and long-debated aspect of methanol synthesis catalysis. Significant advances in understanding the mechanistic details of methanol synthesis have been made during the past decade, largely driven by the development of computational catalysis and advanced characterization tools. The main proposed mechanisms are illustrated in **Figure 1.3**. Starting

from H-assisted CO_2 activation, formate species (HCOO*) or carboxyl species (COOH*) can be formed depending on where the H atoms are located. Two reaction pathways have been proposed for the hydrogenation of HCOO* to methanol, namely traditional formate and revised formate pathways. In the traditional formate pathway, the hydrogenation of HCOO* proceeds via H_2COO*, H_2CO* and CH_3O*.[56–58] The reaction follows the sequence of HCOOH*, H_2COOH*, H_2CO* and CH_3O* in the revised formate pathway.[59,60] Although formate species were often observed by various characterization techniques, their role as reaction intermediate has been challenged by other studies in which formate species were suggested to be merely reaction spectator due to their high stability.[61–64] Therefore, two alternative reaction pathways have been proposed where methanol synthesis proceeds via COOH*, *i.e.,* CO-hydro and trans-COOH pathways. In the CO-hydro pathway, COOH* is first decomposed to CO and then hydrogenated to methanol via HCO*, H_2CO* and CH_3O*.[65,66] In contrast, the step-wise hydrogenation of COOH* produces $C(OH)_2*$, COH*, HCOH* and H_2COH* in the trans-COOH pathway.[67] It should be noted that CO_2 and CO are also interconnected through the (reverse) water gas shift ((r)WGS) reactions, which proceed either via direct bond breaking/formation or specific surface intermediates.[68,69] Besides the complex reaction network, the autocatalytic behaviour initiated by reaction products (H_2O or CH_3OH) can play a critical role in the methanol synthesis from syngas.[63,70,71]

1.4 Methanol Synthesis from CO_2

Despite the similarities between methanol synthesis from CO and CO_2, critical differences exist which pose challenges for the development of efficient CO_2-to-methanol heterogeneous catalysts. As shown by equations [1] and [2], methanol synthesis from CO_2 is less exothermic compared to that from CO, pointing to a less favourable thermodynamics. Thus, the conversion limit of CO_2 hydrogenation to methanol is significantly lower than that of CO hydrogenation at similar reaction conditions as shown in **Figure 1.4**. In addition, the endothermic rWGS reaction (equation [3]) competes with methanol synthesis during CO_2 conversion, particularly at high reaction temperature. In contrast to CO hydrogenation, an equal (molar) amount of water is produced as by-product when CO_2 is hydrogenated to methanol or CO. Another important difference is related to the redox potential of these two catalytic systems – CO is a strong reductant, while CO_2 is a mild oxidant.

$$CO_2 + 3H_2 \rightleftharpoons CH_3OH + H_2O \qquad \Delta H_{298K} = \text{-49.5 kJ/mol} \qquad [1]$$

$$CO + 2H_2 \rightleftharpoons CH_3OH \qquad \Delta H_{298K} = \text{-90.6 kJ/mol} \qquad [2]$$

$$CO_2 + H_2 \rightleftharpoons CO + H_2O \qquad \Delta H_{298K} = \text{41.2 kJ/mol} \qquad [3]$$
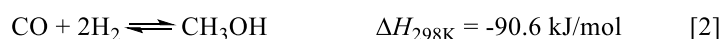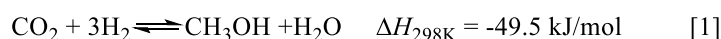
Owing to the differences between CO_2 and CO hydrogenation, several issues have to be resolved for the development of efficient CO_2-to-methanol catalysts. To increase single-pass

conversion, the catalysts should display high activity at a temperature lower than the traditional methanol synthesis temperature. Further, the undesired rWGS reaction should be inhibited to achieve a high methanol selectivity. It is well known that the presence of water can accelerate deactivation of conventional methanol synthesis catalysts via hydrothermal sintering.[72–74] Therefore, water resistance is another important aspect of CO_2-to-methanol catalysts. Significant advances have been made, especially in the past decade, for methanol synthesis from CO_2 since the initial investigations back to the 1980s. In the following section, different types of catalysts for converting CO_2 to methanol are discussed.
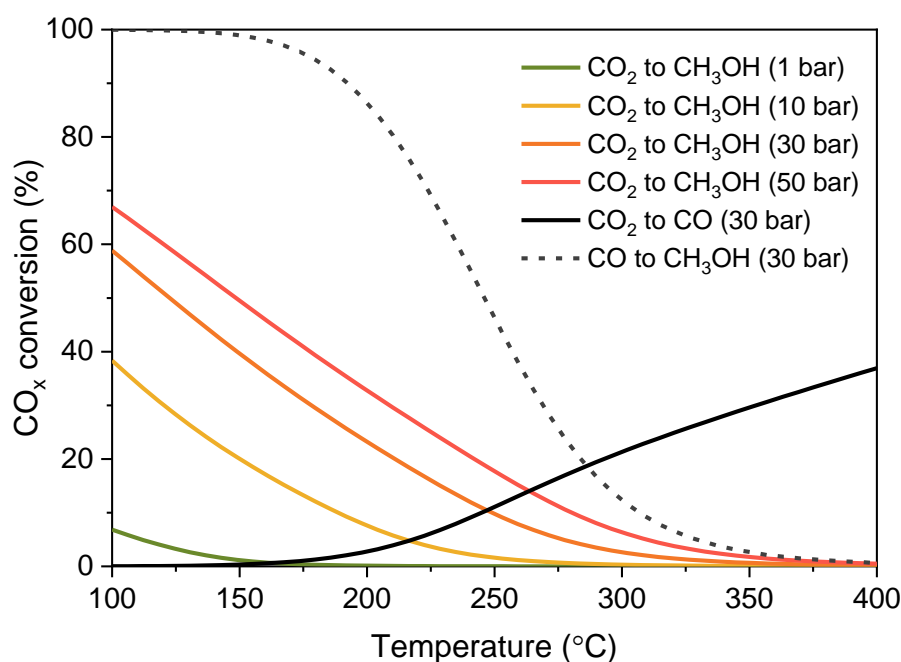
Figure 1.4. Thermodynamic calculations of CH_3OH synthesis ($CO_x/H_2 = 3$) performed with HSC 6.0.

1.4.1 Metal-based catalysts

Significant efforts have been devoted to optimizing Cu-based catalysts for methanol synthesis from CO_2 hydrogenation. Cu-ZnO based catalysts for instance have been extensively studied to understand the dynamic Cu-Zn interactions under CO_2 hydrogenation conditions.[56,75–81] A model catalyst study[77] and advanced high-pressure operando characterization[76] demonstrated that CuZn alloy is not stable during CO_2 hydrogenation and that it will decompose into metallic copper and zinc oxide. Tisseraud et al.[78–80] put forward a geometrical model based on Kirkendall effect to quantify the Cu-ZnO interactions (*i.e.*, Zn migration), and found that the activity of CO_2 hydrogenation is linearly correlated with the extent of Zn migration. Based on DFT calculations, Wu et al. proposed that the CuZn alloy can be hydroxylated by water and the formed ZnOH/Cu is the most active phase for CO_2 activation.[75] Zirconia (ZrO_2) is another widely studied support material to promote the activity of Cu for methanol synthesis from CO_2.[82–88] Bell and co-workers studied zirconia promotion on methanol synthesis over Cu/SiO_2

catalysts and proposed a bifunctional mechanism where zirconia and copper activate CO_2 and H_2, respectively.[88] In a combined experimental and theoretical study, Larmier et al. identified that formate species located at the Cu-ZrO_2 interface are the reaction intermediates.[84] To maximize the Cu-ZrO_2 interactions, Liu et al. prepared a $Cu@ZrO_2$ catalyst via in situ reconstruction of a $Cu@UiO$-66 precursor.[82] As ZnO and ZrO_2 both promote the methanol synthesis activity from CO_2, ternary $Cu/ZnO/ZrO_2$ catalysts have also been intensively investigated.[89–91] Other supports were reported to be beneficial for CO_2-to-CH_3OH conversion on Cu-based catalysts, including $La_2O_2CO_3$,[92] TiO_2,[93] Ga_2O_3,[94] CeO_2,[95,96] GaO_x-HoO_y[97] and metal-organic frameworks (MOFs).[98]

Other metals also have been explored for methanol synthesis. Au supported on zinc oxide displays a remarkable activity in CO_2 hydrogenation to methanol at milder reaction conditions as compared to $Cu/ZnO/Al_2O_3$ catalysts.[99–102] It was reported that Pd/ZnO and Pd/Ga_2O_3 catalysts outperform Cu-ZnO based catalysts in converting CO_2 to methanol.[103–106] Nørskov and co-workers discovered an active and selective Ni-Ga catalyst for CO_2-to-methanol conversion through a descriptor-based computational analysis approach.[107] Embedding Pt nanoparticles (NPs) in Zr-based UiO-67 MOFs was found to be active for CO_2 hydrogenation to methanol at low temperature and pressure, and the interface between Pt NPs and linker-deficient Zr_6O_8 nodes was proposed to be the active site.[108] By using silica as both support and ligand, Wang et al. demonstrated that $Co@Si_x$ catalysts displayed substantially higher methanol synthesis rate via CO_2 hydrogenation at high temperature (T > 300 °C) than a commercial $Cu/ZnO/Al_2O_3$ catalyst.[108] Moreover, bimetallic catalysts have been explored to achieve better catalytic performance than monometallic catalysts.[109–112] Pérez-Ramírez and co-workers found that adding Au, an electron-withdrawing metal, can significantly boost methanol synthesis activity of Cu-ZnO based catalysts.[112] Song et al. observed a strong synergy in Pd-Cu bimetallic catalysts for methanol synthesis from CO_2 hydrogenation, apparently associated with the formation of Pd-Cu alloy.[109]

1.4.2 Non-metal based catalysts

The past years have seen a resurgence in the application of metal oxide catalysts in methanol synthesis since the BASF's HPM process.[113–117] Li and co-workers reported a highly selective and stable ZnO-ZrO_2 catalyst for high-temperature (T > 300 °C) methanol synthesis from CO_2 hydrogenation.[114] Notably, significant advances have been made in converting CO_2 to methanol over In_2O_3 based materials.[116,117] Martin et al. showed that supporting In_2O_3 on ZrO_2 can increase the density of active oxygen vacancies and thus led to a significant increase in CO_2-to-methanol activity.[118] In a combined experimental and DFT study, Song and co-workers demonstrated that an appropriate amount of H_2O (0.1 mol%) can enhance methanol synthesis from CO_2 over In_2O_3/ZrO_2 catalysts. In addition to metal oxides, other materials have been

exploited for CO_2 hydrogenation to methanol, including metal carbides,[119,120] molybdenum phosphide,[121] molybdenum sulfides.[66,122]

1.5 Scope of this thesis

The objective of this thesis is to explore and understand new types of heterogeneous catalysts for CO_2 hydrogenation to methanol. For this purpose, two research directions are explored in this thesis, *i.e.*, improving Cu-based catalysts and discovering novel catalyst formulations. In the first part of this thesis, efforts are directed towards improving Cu-based catalysts for CO_2-to-methanol conversion by introducing strong metal-support interaction (SMSI). The impact of strong $Cu-CeO_2$ interactions is investigated for Cu/CeO_2 and $Cu/ZnO-CeO_2$ catalysts. The second part of this thesis focuses on two alternative catalyst systems based on In_2O_3 and MoC_x. To derive proper structure-performance relationships, catalysts with controlled metal-support interactions and surface composition are obtained by different preparation methods and evaluated for CO_2-to-methanol conversion under industrially relevant conditions. A one-step flame spray pyrolysis (FSP) approach shows great potential in preparing multi-component methanol synthesis catalysts from CO_2 hydrogenation. Furthermore, advanced (in situ) characterization and density functional theory calculations are carried out to gain mechanistic insights at the nanoscale (*e.g.*, active site, reaction intermediate and catalyst poisoning) of the investigated catalysts.

In **Chapter 2**, the role of the ceria support in CO_2 hydrogenation is studied for a set of Cu/CeO_2 catalysts with different support morphologies and compared with a reference Cu/SiO_2 catalyst. The influence of the strong $Cu-CeO_2$ interactions on Cu dispersion and CO_2 hydrogenation to CH_3OH and CO are evaluated. Mechanistic studies are performed to explain the changes in the activity of methanol synthesis and reverse water gas shift (rWGS) reactions. The investigation of Cu/CeO_2 catalyst for methanol synthesis from CO_2 is continued in **Chapter 3**, where the role of $Cu-CeO_2$ interface in methanol synthesis is scrutinized. For this purpose, the methanol activity of a Cu/CeO_2 catalyst prepared by deposition-precipitation method is studied as a function of the carbon-containing reactant, *i.e.*, CO *vs*. CO_2. In-depth (in situ) characterization is conducted to understand how the interactions between reactants (CO/CO_2) and Cu/CeO_2 catalyst influence its methanol activity. The utilization of ceria is expanded in **Chapter 4** in which a series of well-defined Cu-Zn-Ce ternary oxide catalysts are prepared by a one-step FSP method. The as-prepared catalysts are characterized in detail with respect to Cu dispersion and Cu-support interactions and evaluated for CO_2 hydrogenation. The changes of CH_3OH and CO formation rates from CO_2 hydrogenation are discussed in the context of Cu-ZnO and Cu-CeO_2 interactions.

The following two chapters are dedicated to two alternative catalyst systems for methanol synthesis from CO_2. In **Chapter 5**, catalyst screening using FSP is carry out to study metal-promoted In_2O_3 catalysts for CO_2-to-methanol conversion. In particular, Ni promotion is

extensively investigated on a series of NiO-In$_2$O$_3$ catalysts. The Ni species and oxygen vacancies in Ni-promoted In$_2$O$_3$ catalysts are characterized by various techniques to elucidate the underlying mechanism of Ni promotion. Finally, the activity of molybdenum (oxy)carbide (Mo(O)$_x$C$_y$) materials in CO$_2$ conversion is investigated in **Chapter 6**. Specifically, Mo(O)$_x$C$_y$ catalysts with different carburization degree are synthesized by varying carburization temperature and evaluated for CO$_2$ hydrogenation. Extensive quasi in situ characterization is carried out to determine the bulk and surface properties of the as-prepared catalysts. The nature of active site for CO$_2$ hydrogenation is revealed by correlating the characterization results to the catalytic reaction data.

References

1   J. Rogelj, M. Den Elzen, N. Höhne, T. Fransen, H. Fekete, H. Winkler, R. Schaeffer, F. Sha, K. Riahi and M. Meinshausen, *Nature*, 2016, **534**, 631–639.

2   B. R. Keeble and M. Mrcgp, *Med. War*, 1988, **4**, 17–25.

3   F. Cherubini, *Energy Convers. Manag.*, 2010, **51**, 1412–1421.

4   A. Varone and M. Ferrari, *Renew. Sustain. Energy Rev.*, 2015, **45**, 207–218.

5   S. Chu and A. Majumdar, *Nature*, 2012, **488**, 294–303.

6   H. Blanco, W. Nijs, J. Ruf and A. Faaij, *Appl. Energy*, 2018, **232**, 617–639.

7   T. M. Gür, *Energy Environ. Sci.*, 2018, **11**, 2696–2767.

8   I. Dimitriou, P. Garcia-Gutierrez, R. H. Elder, R. M. Cuellar-Franca, A. Azapagic and R. W. K. Allen, *Energy Environ. Sci*, 2015, **8**, 1775–1789.

9   A. Brunetti, F. Scura, G. Barbieri and E. Drioli, *J. Memb. Sci.*, 2010, **359**, 115–125.

10 R. J. Lim, M. Xie, M. A. Sk, J. M. Lee, A. Fisher, X. Wang and K. H. Lim, *Catal. Today*, 2014, **233**, 169–180.

11 G. Centi, E. A. Quadrelli and S. Perathoner, *Energy Environ. Sci.*, 2013, **6**, 1711–1731.

12 Y. A. Daza and J. N. Kuhn, *RSC Adv.*, 2016, **6**, 49675–49691.

13 M. Younas, L. Loong Kong, M. J. K. Bashir, H. Nadeem, A. Shehzad and S. Sethupathi, *Energy and Fuels*, 2016, **30**, 8815–8831.

14 H. Yang, C. Zhang, P. Gao, H. Wang, X. Li, L. Zhong, W. Wei and Y. Sun, *Catal. Sci. Technol.*, 2017, **7**, 4580–4598.

15 W. Wang, S. Wang, X. Ma and J. Gong, *Chem Soc Rev*, 2011, **40**, 3703–3727.

16 G. A. Olah, A. Goeppert and G. K. Surya Prakash, in *Beyond Oil and Gas: The Methanol Economy*, WILEY-VCH, 2009, pp. 179–184.

17 G. A. Olah, *Angew. Chem. Int. Ed.*, 2005, **44**, 2636–2639.

18 S. K. Kamarudin, F. Achmad and W. R. W. Daud, *Int. J. Hydrogen Energy*, 2009, **34**, 6902–6916.

19 J. Sehested, *J. Catal.*, 2019, **371**, 368–375.

20 A. Goeppert, M. Czaun, J.-P. Jones, G. K. Surya Prakash and G. A. Olah, *Chem.Soc.Rev.*, 2014, **43**, 7995–8048.

21 P. Tian, Y. Wei, M. Ye and Z. Liu, *ACS Catal.*, 2015, **5**, 1922–1938.

22 J. Ott, V. Gronemann, F. Pontzen, E. Fiedler, G. Grossmann, D. B. Kersebohm, G. Weiss and C. Witte, in *Ullmann's encyclopedia of industrial chemistry*, WILEY-VCH, 2012.

23 R. S. Tour, *J. Ind. Eng. Chem.*, 1920, **12**, 844–852.

24 US Patemt 1,558,559, 1925.

25 US Patent 1,569,775, 1926.

26 D. Sheldon, *Johnson Matthey Technol. Rev.*, 2017, **61**, 172–182.

27 F. Dalena, A. Senator, A. Marino, A. Gordano, M. Basile and A. Basile, in *Methanol: Science*

and Engineering, Elsevier B.V., 2018, pp. 10–12.

28 I. Chorkendorff and J. W. Niemantsverdriet, in *Concepts of Modern Catalysis and Kinetics*, WILEY-VCH, 2003, pp. 1–22.

29 S. Matsumoto, *Catal. Today*, 2004, **90**, 183–190.

30 P. Munnik, P. E. De Jongh and K. P. De Jong, *Chem. Rev.*, 2015, **115**, 6687–6718.

31 G. Bozzano and F. Manenti, *Prog. Energy Combust. Sci.*, 2016, **56**, 71–105.

32 R. Burch and R. J. Chappell, *Appl. Catal.*, 1988, **45**, 131–150.

33 G. J. J. Bartley and R. Burch, *Appl. Catal.*, 1988, **43**, 141–153.

34 J. C. Frost, *Nature*, 1988, **334**, 577–580.

35 R. Burch, S. E. Golunski and M. S. Spencer, *Catal. Letters*, 1990, **5**, 55–60.

36 R. Burch, S. E. Golunski and M. S. Spencer, *J. Chem. Soc. Faraday Trans.*, 1990, **86**, 2683–2691.

37 Y. Kanai, T. Watanabe, T. Fujitani, T. Uchijima and J. Nakamura, *Catal. Letters*, 1996, **38**, 157–163.

38 J. Nakamura, T. Uchijima, Y. Kanai and T. Fujitani, *Catal. Today*, 1996, **28**, 223–230.

39 R. G. Herman, K. Klier, G. W. Simmons, B. P. Finn, J. B. Bulko and T. P. Kobylinski, *J. Catal.*, 1978, **23**, 595–615.

40 I. Kasatkin, P. Kurr, B. Kniep, A. Trunschke and R. Schlögl, *Angew. Chem. Int. Ed.*, 2007, **46**, 7324–7327.

41 M. M. Günter, T. Ressler, B. Bems, C. Büscher, T. Genger, O. Hinrichsen, M. Muhler and R. Schlögl, *Catal. Letters*, 2001, **71**, 37–44.

42 J. D. Grunwaldt, A. M. Molenbroek, N. Y. Topsøe, H. Topsøe and B. S. Clausen, *J. Catal.*, 2000, **194**, 452–460.

43 W. P. A. Jansen, J. Beckers, J. C. V. D. Heuvel, A. W. D. V.D. Gon, A. Bliek and H. H. Brongersma, *J. Catal.*, 2002, **210**, 229–236.

44 P. L. Hansen, J. B. Wagner, S. Helveg, J. R. Rostrup-Nielsen, B. S. Clausen and H. Topsøe, *Science.*, 2002, **295**, 2053–2055.

45 T. Fujitani and J. Nakamura, *Catal. Letters*, 1998, **56**, 119–124.

46 T. Fujitani and J. Nakamura, *Appl. Catal. A Gen.*, 2000, **191**, 111–129.

47 M. Behrens, F. Studt, I. Kasatkin, S. Kühl, M. Hävecker, F. Abild-pedersen, S. Zander, F. Girgsdies, P. Kurr, B. Kniep, M. Tovar, R. W. Fischer, J. K. Nørskov and R. Schlögl, *Science.*, 2012, **336**, 893–898.

48 S. Kuld, *Science.*, 2016, **352**, 969–974.

49 K. Klier, V. Chatikavanij, R. G. Herman and G. W. Simmons, *J. Catal.*, 1982, **74**, 343–360.

50 G. Liu, D. Willcox, M. Garland and H. H. Kung, *J. Catal.*, 1984, **90**, 139–146.

51 O. Martin and J. Pérez-Ramírez, *Catal. Sci. Technol.*, 2013, **3**, 3343–3352.

52 G. C. Chinchen, P. J. Denny, D. G. Parker, M. S. Spencer and D. A. Whan, *Appl. Catal.*, 1987, **30**, 333–338.

53   K. C. Waugh, *Catal. Today*, 1992, **15**, 51–75.

54   A. Y. Rozovskii and G. I. Lin, *Top. Catal.*, 2003, **22**, 137–150.

55   D. Xu, P. Wu and B. Yang, *Catal. Sci. Technol.*, 2020, **10**, 3346–3352.

56   Y. Yang, J. Evans, J. A. Rodriguez, M. G. White and P. Liu, *Phys Chem Chem Phys*, 2010, **12**, 9909–9917.

57   T. Kakumoto, *Energy Convers. Manag.*, 1995, **36**, 661–664.

58   Y. Kim, T. S. B. Trung, S. Yang, S. Kim and H. Lee, *ACS Catal.*, 2016, **6**, 1037–1044.

59   F. Studt, M. Behrens, E. L. Kunkes, N. Thomas, S. Zander, A. Tarasov, J. Schumann, E. Frei, J. B. Varley, F. Abild-Pedersen, J. K. Nørskov and R. Schlögl, *ChemCatChem*, 2015, **7**, 1105–1111.

60   L. C. Grabow and M. Mavrikakis, *ACS Catal.*, 2011, **1**, 365–384.

61   N. D. Nielsen, A. D. Jensen and J. M. Christensen, *Catal. Letters*, 2020, **150**, 2447–1456.

62   Y. Yang, D. Mei, C. H. F. Peden, C. T. Campbell and C. A. Mims, *ACS Catal.*, 2015, **5**, 7328–7337.

63   Y. Yang, C. A. Mims, D. H. Mei, C. H. F. Peden and C. T. Campbell, *J. Catal.*, 2013, **298**, 10–17.

64   Q. Sun, C. W. Liu, W. Pan, Q. M. Zhu and J. F. Deng, *Appl. Catal. A Gen.*, 1998, **171**, 301–308.

65   Y. Yang, M. G. White and P. Liu, *J. Phys. Chem. C*, 2012, **116**, 248–256.

66   P. Liu, Y. Choi, Y. Yang and M. G. White, *J Phys Chem A*, 2010, **2**, 3888–3895.

67   Y. F. Zhao, Y. Yang, C. Mims, C. H. F. Peden, J. Li and D. Mei, *J. Catal.*, 2011, **281**, 199–211.

68   A. A. Gokhale, J. A. Dumesic and M. Mavrikakis, *J. Am. Chem. Soc.*, 2008, **130**, 1402–1414.

69   G. C. Wang and J. Nakamura, *J. Phys. Chem. Lett.*, 2010, **1**, 3053–3057.

70   J. Thrane, S. Kuld, N. D. Nielsen, A. D. Jensen, J. Sehested and J. M. Christensen, *Angew. Chem. Int. Ed.*, 2020, **59**, 18189-18193.

71   M. Sahibzada, I. S. Metcalfe and D. Chadwick, *J. Catal.*, 1998, **174**, 111–118.

72   M. S. Jingang Wu Masami Takeuchi Taiki Watanabe, *Appl. Catal. A Gen.*, 2001, **218**, 235–240.

73   B. Liang, J. Ma, X. Su, C. Yang, H. Duan, H. Zhou, S. Deng, L. Li and Y. Huang, *Ind. Eng. Chem. Res.*, 2019, **58**, 9030–9037.

74   A. Prašnikar, A. Pavlišič, F. Ruiz-Zepeda, J. Kovač and B. Likozar, *Ind. Eng. Chem. Res.*, 2019, **58**, 13021–13029.

75   X. K. Wu, G. J. Xia, Z. Huang, D. K. Rai, H. Zhao, J. Zhang, J. Yun and Y. G. Wang, *Appl. Surf. Sci.*, 2020, **525**, 146481–146489.

76   M. Zabilskiy, V. L. Sushkevich, D. Palagin, J. A. Van Bokhoven, M. A. Newton and F. Krumeich, *Nat. Commun.*, 2020, **11**, 2409–2416.

77   S. Kattel, P. J. Ramírez, J. G. Chen, J. A. Rodriguez and P. Liu, *Science.*, 2017, **355**, 1296–1299.

78   C. Tisseraud, C. Comminges, S. Pronier, Y. Pouilloux and A. Le Valant, *J. Catal.*, 2016, **343**, 106–114.

79   C. Tisseraud, C. Comminges, T. Belin, H. Ahouari, A. Soualah, Y. Pouilloux and A. Le Valant,

J. Catal., 2015, **330**, 533–544.

80 A. Le Valant, C. Comminges, C. Tisseraud, C. Canaff, L. Pinard and Y. Pouilloux, *J. Catal.*, 2015, **324**, 41–49.

81 J. Schumann, T. Lunkenbein, A. Tarasov, N. Thomas, R. Schlögl and M. Behrens, *ChemCatChem*, 2014, **6**, 2889–2897.

82 T. Liu, X. Hong and G. Liu, *ACS Catal.*, 2020, **10**, 93–102.

83 S. Tada, S. Kayamori, T. Honma, H. Kamei, A. Nariyuki, K. Kon, T. Toyao, K. I. Shimizu and S. Satokawa, *ACS Catal.*, 2018, **8**, 7809–7819.

84 K. Larmier, W.-C. Liao, S. Tada, E. Lam, R. Verel, A. Bansode, A. Urakawa, A. Comas-Vives and C. Copéret, *Angew. Chem. Int. Ed.*, 2017, **56**, 2318–2323.

85 S. Kattel, B. Yan, Y. Yang, J. G. Chen and P. Liu, *J. Am. Chem. Soc.*, 2016, **138**, 12440–12450.

86 I. Ro, Y. Liu, M. R. Ball, D. H. K. Jackson, J. P. Chada, C. Sener, T. F. Kuech, R. J. Madon, G. W. Huber and J. A. Dumesic, *ACS Catal.*, 2016, **6**, 7040–7050.

87 K. Samson, M. Sliwa, R. P. Socha, K. Góra-Marek, D. Mucha, D. Rutkowska-Zbik, J. F. Paul, M. Ruggiero-Mikoajczyk, R. Grabowski and J. Soczyński, *ACS Catal.*, 2014, **4**, 3730–3741.

88 I. a Fisher, H. C. Woo and a T. Bell, *Catal. Letters*, 1997, **44**, 11–17.

89 Y. Wang, S. Kattel, W. Gao, K. Li, P. Liu, J. G. Chen and H. Wang, *Nat. Commun.*, 2019, **10**, 1166–1175.

90 X. Guo, D. Mao, G. Lu, S. Wang and G. Wu, *J. Catal.*, 2010, **271**, 178–185.

91 F. Arena, G. Italiano, K. Barbera, S. Bordiga, G. Bonura, L. Spadaro and F. Frusteri, *Appl. Catal. A Gen.*, 2008, **350**, 16–23.

92 K. Chen, X. Duan, H. Fang, X. Liang and Y. Yuan, *Catal. Sci. Technol.*, 2018, **8**, 1062–1069.

93 G. Qi, X. Zheng, J. Fei and Z. Hou, *Catal. Letters*, 2001, **72**, 191–196.

94 E. Lam, G. Noh, K. W. Chan, K. Larmier, D. Lebedev, K. Searles, P. Wolf, O. V. Safonova and C. Copéret, *Chem. Sci.*, 2020, **11**, 7593–7598.

95 J. A. R. Jesús Graciani, Kumudu Mudiyanselage, Fang Xu, Ashleigh E. Baber, Jaime Evans, Sanjaya D. Senanayake, Darío J. Stacchiola, Ping Liu, Jan Hrbek, Javier Fernández Sanz, *Science.*, 2014, **345**, 546–550.

96 J. B. Branco, A. C. Ferreira, A. P. Gonçalves, C. O. Soares and T. Almeida Gasche, *J. Catal.*, 2016, **341**, 24–32.

97 B. Zohour, I. Yilgor, M. A. Gulgun, O. Birer, U. Unal, C. Leidholm and S. Senkan, *ChemCatChem*, 2016, **8**, 1464–1469.

98 H. Kobayashi, J. M. Taylor, Y. Mitsuka, N. Ogiwara, T. Yamamoto, T. Toriyama, S. Matsumura and H. Kitagawa, *Chem. Sci.*, 2019, **10**, 3289–3294.

99 A. Vourros, I. Garagounis, V. Kyriakou, S. A. C. Carabineiro, F. J. Maldonado-Hódar, G. E. Marnellos and M. Konsolakis, *J. CO2 Util.*, 2017, **19**, 247–256.

100 Y. Hartadi, D. Widmann and R. J. Behm, *J. Catal.*, 2016, **333**, 238–250.

101 J. Strunk, K. Kähler, X. Xia, M. Comotti, F. Schüth, T. Reinecke and M. Muhler, *Appl. Catal. A Gen.*, 2009, **359**, 121–128.

102 H. Sakurai and M. Haruta, *Catal. Today*, 1996, **29**, 361–365.

103   E. M. Fiordaliso, I. Sharafutdinov, H. W. P. Carvalho, J. D. Grunwaldt, T. W. Hansen, I. Chorkendorff, J. B. Wagner and C. D. Damsgaard, *ACS Catal.*, 2015, **5**, 5827–5836.

104   T. Fujitani, M. Saito, Y. Kanai, T. Watanabe, J. Nakamura and T. Uchijima, *Appl. Catal.*, 1995, **125**, 0–3.

105   N. Iwasa, H. Suzuki, M. Terashita, M. Arai and N. Takezawa, *Catal. Letters*, 2004, **96**, 75–78.

106   H. Bahruji, M. Bowker, G. Hutchings, N. Dimitratos, P. Wells, E. Gibson, W. Jones, C. Brookes, D. Morgan and G. Lalev, *J. Catal.*, 2016, **343**, 133–146.

107   F. Studt, I. Sharafutdinov, F. Abild-Pedersen, C. F. Elkjær, J. S. Hummelshoj, S. Dahl, I. Chorkendorff and J. K. Norskov, *Nat. Chem.*, 2014, **6**, 320–324.

108   E. S. Gutterød, A. Lazzarini, T. Fjermestad, G. Kaur, M. Manzoli, S. Bordiga, S. Svelle, K. P. Lillerud, E. Skúlason, S. Øien-ØDegaard, A. Nova and U. Olsbye, *J. Am. Chem. Soc.*, 2020, **142**, 999–1009.

109   X. Jiang, X. Nie, X. Wang, H. Wang, N. Koizumi, Y. Chen, X. Guo and C. Song, *J. Catal.*, 2019, **369**, 21–32.

110   B. Hu, Y. Yin, G. Liu, S. Chen, X. Hong, S. Chi, E. Tsang and S. C. E. Tsang, *J. Catal.*, 2018, **359**, 17–26.

111   X. Jiang, N. Koizumi, X. Guo and C. Song, *Appl. Catal. B Environ.*, 2015, **170**–**171**, 173–185.

112   O. Martin, C. Mondelli, D. Curulla-Ferré, C. Drouilly, R. Hauert and J. Pérez-Ramírez, *ACS Catal.*, 2015, **5**, 5607–5616.

113   C.-S. Li, G. Melaet, W. T. Ralston, K. An, C. Brooks, Y. Ye, Y.-S. S. Liu, J. Zhu, J. Guo, S. Alayoglu and G. A. Somorjai, *Nat Commun*, 2015, **6**, 6538.

114   J. Wang, G. Li, Z. Li, C. Tang, Z. Feng, H. An, H. Liu, T. Liu and C. Li, *Sci. Adv.*, 2017, **3**, 1–10.

115   J. Wang, C. Tang, G. Li, Z. Han, Z. Li, H. Liu, F. Cheng and C. Li, *ACS Catal.*, 2019, **9**, 10253–10259.

116   J. Ye, C. Liu, D. Mei and Q. Ge, *ACS Catal.*, 2013, **3**, 1296–1306.

117   K. Sun, Z. Fan, J. Ye, J. Yan, Q. Ge, Y. Li, W. He, W. Yang and C. Liu, *J. CO2 Util.*, 2015, **12**, 1–6.

118   O. Martin, A. J. Martin, C. Mondelli, S. Mitchell, T. F. Segawa, R. Hauert, C. Drouilly, D. Curulla-Ferre and J. Perez-Ramirez, *Angew. Chem. Int. Ed.*, 2016, **55**, 6261–6265.

119   W. Geng, H. Han, F. Liu, X. Liu, L. Xiao and W. Wu, *J. CO2 Util.*, 2017, **21**, 64–71.

120   S. Posada-Perez, F. Vineses, J. A. Rodriguez and F. Illas, *Top. Catal.*, 2015, **58**, 159–173.

121   M. S. Duyar, C. Tsai, J. L. Snider, J. A. Singh, A. Gallo, J. S. Yoo, A. J. Medford, F. Abild-Pedersen, F. Studt, J. Kibsgaard, S. F. Bent, J. K. Nørskov and T. F. Jaramillo, *Angew. Chem. Int. Ed.*, 2018, **57**, 15045–15050.

122   C. Liu and P. Liu, *ACS Catal.*, 2015, **5**, 1004–1012.

CHAPTER 2

On the Role of Metal-Support Interactions in CO$_2$ Hydrogenation to Methanol over Cu/CeO$_2$

ABSTRACT

Understanding how metal-support interactions influence the CO$_2$ hydrogenation performance is essential for the development of efficient CO$_2$-to-methanol catalysts. Herein, we systematically investigated the role of Cu-CeO$_2$ interactions in CO$_2$ hydrogenation over a series of Cu/CeO$_2$ catalysts with different support properties. A combined CO$_2$-N$_2$O titration approach was developed enabling simultaneous quantification of the exposed metallic copper sites and ceria oxygen vacancies in the reduced Cu/CeO$_2$ catalysts. Together with other characterization techniques (XRD, TPR, and STEM-EDX), we demonstrate that copper dispersion is significantly facilitated by the Cu-CeO$_2$ interactions. The CO$_2$ hydrogenation results show that the Cu/CeO$_2$ catalysts displayed higher methanol selectivity compared to the reference Cu/SiO$_2$ catalyst. Structure-sensitivity analysis based on turnover frequencies (TOFs) reveals that the improved methanol selectivity is not related to the promotion of intrinsic methanol synthesis activity but rather results from the effective supressing of reverse water gas shift (rWGS) activity. Mechanistic studies (DFT simulation and in situ IR) suggest that the inhibition of rWGS activity in the Cu/CeO$_2$ catalysts is associated with the stabilization of formate species on copper.

1. Introduction

The release of large amounts of carbon dioxide (CO_2) into the atmosphere represents one of the major threats to humanity because it can lead to serious climate change. Considering CO_2 as a feedstock instead of waste is seen as a possible route to mitigate the adverse effects of rising atmospheric CO_2 concentration. A promising route is the catalytic hydrogenation of CO_2 to methanol ($CO_2 + 3H_2 \rightarrow CH_3OH + H_2O$), using green hydrogen generated from renewable energy sources.[1] Methanol is an attractive target of CO_2 conversion, because it can replace fossil resources in Olah's methanol economy concept.[2] Besides being a clean-burning fuel itself, methanol can also be converted into other fuels such as dimethyl ether, gasoline, and diesel as well as into useful chemicals such as olefins, formaldehyde and acetic acid using known chemical processes.[3] Methanol is also preferred over hydrogen (H_2) as a carrier and storage medium of intermittent renewable energy due to its higher volume energy density, operational safety and compatibility with the current infrastructure.[4]

Methanol is commercially produced from synthesis gas over $Cu/ZnO/Al_2O_3$ catalyst at elevated pressure (50 – 100 bar) and temperature (200 – 300 °C).[5] This process benefits from co-feeding a small amount of CO_2 to the methanol synthesis reactor.[6] It has been proposed that CO_2 instead of CO is the real carbon source for methanol synthesis.[7] For direct CO_2-to-methanol conversion, copper-based catalysts are also the most investigated catalytic system due to their low cost and good performance.[3,8]. Importantly, it has been known that the competing reverse water-gas shift (rWGS) reaction ($CO_2 + H_2 \rightarrow CO + H_2O$) is the dominant pathway on pure copper surface and copper-support interactions play a key role in promoting methanol synthesis from CO_2.[9–11] This has led to a significant body of research focusing on the optimization of copper-support interaction for CO_2 hydrogenation to methanol. Besides ZnO,[12,13] other promoters such as ZrO_2,[14,15] In_2O_3,[16] La_2O_3,[17] Mo_2C[18], and $La_2O_2CO_3$[19] have been investigated. Notably, the support promoting effect can be classified into two categories, namely structural promotion and electronic promotion. Structural promotion refers to the stabilization of smaller copper particles (*i.e.*, higher copper dispersion) by strong copper-promoter interaction, which increases the quantity of available active sites. Copper-support interaction can also lead to new active sites with higher intrinsic activity (electronic promotion). Furthermore, for structure-sensitive reactions such as methanol synthesis,[20] the catalytic surface will contain different active sites, whose proportion will depend on the particle size. Therefore, it is important to disentangle the structural and electronic promotions in order to gain a better understanding how copper-support interaction influences methanol synthesis from CO_2 hydrogenation.

Ceria (CeO_2), a reducible metal oxide, interacts strongly with copper, leading to excellent performance of Cu/CeO_2 in many important reactions such as CO oxidation,[21] soot oxidation,[22] NO reduction,[23] N_2O decomposition[24], and the WGS reaction.[25] Recently, the $Cu-CeO_2$

interface has also been proposed to be an novel active site for methanol synthesis from CO$_2$ based on an inverse CeO$_2$/Cu(111) model catalyst.[26] Following that, the Cu/CeO$_2$ was investigated in more detailed in several studies using conventional catalyst preparation methods. Ouyang et al. showed that copper supported on ceria nanorods was more active than on ceria nanocubes and nanospheres due to the stronger copper-support interaction in ceria nanorods.[27] Using in situ DRIFTS, Wang et al. associated the enhanced methanol selectivity of Cu/CeO$_2$ than pure copper surface with surface carbonate intermediates, which were resulted from interaction between CO$_2$ and ceria oxygen vacancies.[28] Sripada et al. found that Cu/CeO$_2$ prepared by deposition-precipitation resulted in a higher copper dispersion and higher methanol productivity than co-precipitation method.[29] Despite these important advances, the exact role of Cu-CeO$_2$ interaction (structural promotion and/or electronic promotion) with respect to CO$_2$ hydrogenation to methanol remains largely unresolved.

In the present study, we prepared six Cu/CeO$_2$ catalysts with different support morphologies and one reference Cu/SiO$_2$ catalyst to investigate the effect of Cu-CeO$_2$ interaction on CO$_2$ hydrogenation. The catalysts were characterized in detail using XRD, TPR, STEM-EDX and chemisorption. A combined CO$_2$-N$_2$O chemisorption method was developed to simultaneously quantify the exposed metallic copper sites and ceria oxygen vacancies. The Cu/CeO$_2$ and Cu/SiO$_2$ catalysts were evaluated in CO$_2$ hydrogenation at 250°C and 30 bar. An improved methanol selectivity was found for the Cu/CeO$_2$ catalysts in comparison to the Cu/SiO$_2$ catalyst. Structure-sensitivity analysis reveals that the improved methanol selectivity is mainly due to the inhibition of rWGS activity. The mechanism of rWGS inhibition in Cu/CeO$_2$ was further investigated using in situ IR spectroscopy combined with density functional theory simulation.

2. Experimental section

2.1 Catalyst preparation

2.1.1 Cu/CeO$_2$

Three ceria supports with different morphologies (i.e., cube, rod, and sphere) were prepared by a hydrothermal method adapted from literature.[30] For ceria rods synthesis, the following procedure was used. Ce(NO$_3$)$_3$·6H$_2$O (99.99%, Sigma Aldrich) was dissolved in 5 mL deionized water to obtain a concentration of 1.0 M. The resulting solution was then added to 35 mL of 17.1 M NaOH ($\geq$ 98%, Sigma Aldrich) solution, followed by stirring at room temperature for 30 min. The obtained white slurry was diluted to 100 mL with deionized water in a 125 mL Teflon liner, which was then placed in a stainless-steel autoclave. The final Ce(NO$_3$)$_3$ and NaOH concentrations before the hydrothermal synthesis were 0.05 M and 6 M, respectively. Hydrothermal synthesis was performed at 100 °C for 24 h. The resulting solid was retrieved and washed by centrifugation-decantation cycles, 5 times with deionized water and 3 times with ethanol, followed by drying at 110 °C overnight. Finally, the product was

calcined at 500 °C for 4 h in static air at a rate of 5 °C/min to yield the ceria support. Similar procedures were used for the ceria cubes and spheres synthesis with certain modifications: a higher hydrothermal synthesis temperature of 180 °C for ceria cubes synthesis and a lower final NaOH concentration of 0.08 M for ceria spheres synthesis.

Another ceria support with high specific surface area was prepared by flame spray pyrolysis (FSP) method using a Tethis NPS10 setup.[31] The cerium precursor solution was prepared by dissolving cerium acetylacetonate (99.9%, Sigma Aldrich) in glacial acetic acid (99.7%, Sigma Aldrich) at 80 °C to a concentration of 0.1 M. The cerium precursor solution was then injected into the nozzle of the Tethis setup at a flow rate of 5 mL/min, and the flame was fed with a 1.5 L/min methane and 3.0 L/min oxygen flow with an additional 5.0 L/min oxygen dispersion flow around it. The resulting solid was collected gently from quartz filter using a plastic spatula. This sample is denoted as FSP.

To deposit copper (5 wt%) onto the ceria supports (commercial ceria powder (< 25 nm, Sigma Aldrich, denoted as CM), cubes, rods, spheres and FSP), a wet impregnation method was used. Typically, 0.83 mmol $Cu(NO_3)_2 \cdot 3H_2O$ (99%, Sigma Aldrich) was dissolved in 20 mL deionized water, followed by addition of 1.0 g of ceria support. The obtained dispersion was stirred at room temperature for 30 min, and the water was then gradually removed by heating at 80 °C until a homogeneous slurry was obtained. Next, the slurry was dried at 110 °C overnight and calcined at 500 °C for 2 h in static air at a rate of 5 °C/min. The obtained catalysts are denoted as Cu/CeO_2-X (X = CM, Cube, Sphere, Rod and FSP).

Another Cu/CeO_2 catalyst was prepared by a co-precipitation method. For this purpose, 4.80 g of $Ce(NO_3)_3 \cdot 6H_2O$ (99.99%, Sigma Aldrich) and 0.38 g of $Cu(NO_3)_2 \cdot 3H_2O$ (99%, Sigma Aldrich) were dissolved in 200 mL deionized water, and Na_2CO_3 (99.5%, Sigma Aldrich) was dissolved in deionized water to a concentration of 0.2 M as precipitation agent. The precipitation process was initiated by dropwise addition of the precipitation agent to the precursor solution at 70 °C until pH=10 was reached, followed by 1 h aging at the same temperature. Next, the solid was retrieved by filtration, washed with copious amounts of deionized water, and dried at 110 °C overnight. The dried catalyst precursor was crushed and calcined at 500 °C for 2 h in static air at a rate of 5 °C/min. The resulting catalyst is denoted as Cu/CeO_2-CP.

2.1.2 Cu/SiO₂

A Cu/SiO_2 catalyst (5 wt% Cu) was prepared by incipient wetness impregnation. Specifically, an appropriate amount of $Cu(NO_3)_2 \cdot 3H_2O$ (99%, Sigma Aldrich) was dissolved in a volume of deionized water equal to the pore volume of silica support (Davisil Grade 62, 75-250 μm, S_{BET} = 283 $m^2/_{gcat}$). The precursor solution was then dropwise added to the support with vigorous stirring, followed by drying at 40 °C overnight. The dried catalyst precursor was calcined at

350 °C at a rate of 3 °C/min for 3 h in a 20 vol% O$_2$ in He flow (200 mL/min). The obtained catalyst is denoted as Cu/SiO$_2$.

2.2 Catalyst characterization

Inductively coupled plasma optical emission spectroscopy (ICP-OES). The copper loading of the fresh catalysts was determined by ICP-OES (Spectro CIROS CCD spectrometer). Prior to measurements, the catalysts were dissolved in 5 mL of concentrated sulfuric acid under heating at 150 °C for about 1 h.

N$_2$ physisorption. The textual properties of the fresh catalysts were analyzed by N$_2$ physisorption at -196 °C with a Miromeritics TriStar II 3020 instrument. Typically, about 100 mg of sample was transferred into a glass sample tube and pretreated at 120 °C overnight under nitrogen flow. The Brunauer-Emmett-Teller (BET) method was used to calculate the catalyst specific surface area.

X-ray diffraction (XRD). The crystal structure of the fresh catalysts was studied with a Bruker D2 Phaser diffractometer using Cu Kα radiation with a wavelength of 1.54 Å. The XRD patterns were recorded between 20-85˚ with a step size of 0.1˚ at 1.0 s/step scan rate.

Transmission electron microscopy (TEM). The morphology of the reduced catalysts (250 °C, 1 h, 10 vol% H$_2$ in He) was studied by TEM using FEI Tecnai 20 (type Sphera) instrument operating at an acceleration voltage of 200 kV. Regarding sample preparation, the reduced catalysts after passivation were dispersed in ethanol by ultrasonication and deposited on a holey Cu grid. The elemental distribution over the reduced catalysts (250 °C, 1 h, 10 vol% H$_2$ in He) was measured by scanning TEM combined with energy dispersive X-ray analysis (STEM-EDX) on a FEI cubed Cs-corrected Titan instrument operating at an acceleration voltage of 300 kV. The reduced catalysts after passivation were dispersed in ethanol by ultrasonication and deposited on a holey Au grid.

Temperature programmed reduction (H$_2$-TPR). The reducibility of the fresh catalysts was studied by H$_2$-TPR using a Micromeritics AutoChem II setup. Typically, 50 mg of sample was loaded into a quartz U-tube between two quartz wool layers. Prior to the measurement, the sample was pretreated at 200 °C for 1 h in a He flow (50 mL/min) to remove adsorbed water. The TPR profile was recorded by heating the sample from 40 °C to 700 °C at a rate of 10 °C/min in a 4 vol% H$_2$ in He flow (50 mL/min). The hydrogen consumption was recorded by a TCD and calibrated against a Cu/SiO$_2$ reference sample. The molar ratio of hydrogen consumption to copper loading (H$_2$/Cu) was further calculated based on the elemental analysis results.

N$_2$O titration. The exposed metallic copper sites in the reduced catalysts were measured by N$_2$O titration at 50 °C,[32] using a plug-flow setup equipped with an online mass spectrometer (Balzers TPG 251). To separate N$_2$O consumption from metallic copper sites and ceria oxygen

vacancies, two N_2O pulsing experiments were performed. In the first one, an appropriate amount (ca. 30 mg) of catalyst was loaded into a stainless-steel reactor and pretreated in a 10 vol% H_2 in He (50 mL/min) flow at 250°C for 1 h at a rate of 5°C/min, followed by cooling to 50 °C in a He flow (50 ml/min). Next, 1 ml of a 2 vol% N_2O in He gas mixture was periodically injected to the sample using a 1 mL sample loop until no N_2O consumption was observed. This N_2O consumption amount is denoted as $n_{N2O,\ 1}$. For the second N_2O experiment, the same pretreatment procedure was used. After cooling to 50 °C in a He flow (50 ml/min), pulses of pure CO_2 (5 ml) were injected to the sample to cover the ceria oxygen vacancies. After CO_2 pulsing, the same N_2O pulsing experiment was carried out to titrate the remaining metallic copper sites. This N_2O consumption amount is denoted as $n_{N2O,\ 2}$. The N_2O consumption by ceria oxygen vacancies was derived from the difference between these two N_2O titration experiments. The density of exposed metallic copper sites ($N_{Cu(0)}$) and ceria oxygen vacancies (N_{Ov}) were calculated by the following equations assuming a stoichiometry of $N_2O/Cu = 0.5$ and $N_2O/O_v = 1$:

$$N_{Cu(0)} = \frac{n_{N2O,\ 2}}{m_{cat}} \quad [1]$$

$$N_{Ov} = \frac{n_{N2O,\ 1} - n_{N2O,\ 2}}{m_{cat}} \quad [2]$$

The copper specific surface area ($S_{Cu(0)}$), copper dispersion (D_{Cu}), effective copper diameter ($d_{Cu,\ eff}$) and Cu-CeO$_2$ interface length ($L_{int.}$) were further estimated by the following equations assuming hemispherical particle shape [33,34]:

$$S_{Cu(0)} = \frac{N_{Cu(0)}N_A}{SD_{Cu}} \quad [3]$$

$$D_{Cu} = \frac{N_{Cu(0)}M_{Cu}}{W_{Cu}} \quad [4]$$

$$d_{Cu,\ eff} = \frac{6M_{Cu}}{D_{Cu}\rho\sigma N_A} \quad [5]$$

$$L_{int} = \frac{S_{Cu(0)}}{d_{Cu,\ eff}} \quad [6]$$

where SD_{Cu} is the copper surface density (1.47×10^{19} atoms/m^2), N_A the Avogadro's number (6.022×10^{23} mol^{-1}), M_{Cu} the atomic weight of copper (63.546 g/mol), ρ the copper metal density (8.94 g/cm^3), and δ the area occupied by a surface copper atom (6.85 Å^2 per atom).

Infrared spectroscopy (IR). In situ IR spectra during CO_2 hydrogenation were measured on a Nicolet FT-IR spectrometer equipped with a cryogenic MCT detector. Self-supporting wafer

of catalyst (ca. 15 mg) was pressed and loaded into an infrared cell equipped with CaF_2 windows. The catalyst wafer was pretreated at 250 °C (rate 5°C/min) and 1 bar for 1 h in a 10 vol% H_2 in He (50 mL/min) flow, followed by exposure to a CO_2/H_2 gas mixture (CO_2:H_2=1:3, 50 mL/min) for 30 min. A background spectrum (64 scans with a resolution of 4 cm^{-1}) was taken after the pretreatment. Spectra (64 scans with a resolution of 4 cm^{-1}) during reaction were recorded continuously after exposing to the CO_2/H_2 gas mixture.

2.3 Catalytic activity measurements

CO₂ hydrogenation. The catalytic performance of the as-prepared catalysts in CO_2 hydrogenation was evaluated in a down-flow stainless-steel reactor (ID = 4 mm) at 250 °C and 30 bar. Typically, about 50 mg catalyst (125-250 μm), diluted with 200 mg SiC, was loaded into the reactor and pretreated at 250 °C (rate = 5 °C/min) and 1 bar for 1 h in a 10 vol% H_2 in He flow (50 mL/min). Afterwards, the catalyst was exposed to a reaction mixture flow (CO_2:H_2:N_2 = 5:15:5 mL/min) and the pressure in the reactor was increased to 30 bar by a back-pressure regulator. The effluent gas mixture was analysed by an online gas chromatograph (Interscience, CompactGC) equipped with Rtx-1 (FID), Rt-QBond and Molsieve 5A (TCD), and Rt-QBond (TCD) columns. The measurements were taken after ca. 2 h time-on-stream. CO_2 conversion, product selectivity and product formation rate were calculated using the following equations:

$$X(CO_2) = \frac{F(CO)_{out} + F(CH_3OH)_{out} + F(CH_4)_{out}}{F(CO_2)_{out} + F(CO)_{out} + F(CH_3OH)_{out} + F(CH_4)_{out}} \quad [7]$$

$$S(product) = \frac{F(product)_{out}}{F(CO)_{out} + F(CH_3OH)_{out} + F(CH_4)_{out}} \quad [8]$$

$$r(product) = \frac{F(product)_{out}}{V_m \times m_{cat}} \quad [9]$$

where F stands for the volumetric flow rate calculated based on nitrogen internal standard using calibrated response factors and V_m is the molar volume of ideal gas at standard temperature and pressure. The methane selectivity in all the measurements was very low (< 1 %). The turnover frequency (TOF) is defined as the product formation rate normalized by the amount of exposed metallic copper sites determined by N_2O chemisorption. For the Cu/SiO₂ catalyst, a reduction temperature of 300 °C was used and the reaction flow rate was doubled to 50 mL/min to achieve a similar conversion level as in the Cu/CeO₂ case.

CO hydrogenation. The CO hydrogenation activity of the as-prepared catalysts was evaluated in the same catalytic setup as used for CO_2 hydrogenation. The pretreatment and reaction conditions were kept the same as those in CO_2 hydrogenation except CO_2 being replaced by CO. Effluent analysis was done after ca. 2 h time-on-stream. CO conversion, product selectivity

and product formation rate were calculated using the following equations:

$$X(CO) = \frac{F(CO_2)_{out} + F(CH_3OH)_{out} + F(CH_4)_{out}}{F(CO)_{out} + F(CO_2)_{out} + F(CH_3OH)_{out} + F(CH_4)_{out}} \quad [10]$$

$$S(product) = \frac{F(product)_{out}}{F(CO_2)_{out} + F(CH_3OH)_{out} + F(CH_4)_{out}} \quad [11]$$

$$r(product) = \frac{F(product)_{out}}{V_m \times m_{cat}} \quad [12]$$

where F stands for the volumetric flow rate calculated based on nitrogen internal standard using calibrated response factors and V_m is the molar volume of ideal gas at standard temperature and pressure. The methanol selectivity in all the measurements was very high (> 97 %).

2.4 Density functional theory calculations

Spin-polarized calculations were carried out within the density functional theory (DFT) framework as implemented in the Vienna *ab initio* simulation package (VASP)[35]. The ion-electron interactions were represented by the projector-augmented wave (PAW) method[36] and the electron exchange-correlation by the generalized gradient approximation (GGA) with the Perdew-Burke-Ernzerhof (PBE) exchange-correlation functional[37]. The Kohn-Sham valence states were expanded in a plane-wave basis set with a cut-off energy of 400 eV. The Ce(5s, 5p, 6s, 4f, 5d), O(2s, 2p), Au(4d, 5s) and C(2s, 2p) electrons were treated as valence states. The DFT+U approach was used, in which U is a Hubbard-like term describing the on-site Coulombic interactions[38]. This approach improves the description of localized states in ceria, where standard LDA and GGA functionals fail. A value of $U = 4.5$ eV was adopted for Ce, which was calculated self-consistently by Fabris et al.[39] using the linear response approach of Cococcioni and de Gironcoli[40], and is within the 3.0-6.0 eV range that results in the localization in Ce 4f orbitals of the electrons left upon oxygen removal from ceria[41]. A Cu$_{14}$/CeO$_2$(111) model, consisting of a Cu$_{14}$ cluster placed on a periodic ceria slab with a (4×4) surface unit cell exposing the (111) surface, was used to model the metal-support interface. For Brillouin zone integration, a 1×1×1 Monkhorst-Pack mesh was used. The bulk equilibrium lattice constant (5.49 Å) previously calculated at the PBE+U level ($U = 4.5$ eV) was used[42]. The CeO$_2$(111) slab model consists of three Ce-O-Ce layers and a vacuum gap of 15 Å. The atoms in the bottom layer were frozen to their bulk positions and only the top two Ce-O-Ce layers were relaxed. The climbing image nudged-elastic band (CI-NEB) algorithm[43,44] was used to identify the transition states for the elementary reaction steps of methanol synthesis and rWGS reactions of CO$_2$ hydrogenation.

3. Results and discussion

3.1 Catalyst characterization

The basic physicochemical properties of the fresh catalysts are summarized in **Table 2.1**. ICP elemental analysis showed that the actual copper loadings in all the samples were close to the targeted value of 5 wt% . The fresh Cu/CeO$_2$ catalysts cover a wide range of catalyst specific surface areas (26-139 m^2/g$_{cat}$), among which the Cu/CeO$_2$-CP has the largest value. The Cu/SiO$_2$ has a surface area of 264 m^2/g$_{cat}$, which relates to the lower density of silica support compared to ceria supports. Bright-field TEM images (**Figure A.1**) of the reduced catalysts confirm the different ceria support morphologies: the average length and width of rod support were 61 $\pm$ 26 nm and 8 $\pm$ 1 nm; the average size of cube, sphere and FSP supports were 19 $\pm$ 7 nm, 12 $\pm$ 3 nm and 4 $\pm$ 1 nm, respectively.

Table 2.1. Physicochemical properties of the Cu/CeO$_2$ and Cu/SiO$_2$ catalysts.

Catalyst	Cu loading (wt%)	S$_{BET}$ (m^2/g$_{cat}$)	D$_{cu}$ (%)[a]	N$_{Cu(0)}$ (μmol/g$_{cat}$)[a]	S$_{Cu(0)}$ (m^2/g$_{cat}$)[a]	N$_{Ov}$ (μmol/g$_{cat}$)[a]	H$_2$/Cu ratio[b]
Cu/CeO$_2$-CM	4.6	30	14.4	106	4.4	56	1.2
Cu/CeO$_2$-Cube	4.8	26	6.9	52	2.1	49	1.1
Cu/CeO$_2$-Sphere	4.4	47	30.2	208	8.5	72	1.4
Cu/CeO$_2$-Rod	4.6	79	38.7	287	11.8	159	1.6
Cu/CeO$_2$-FSP	4.9	90	28.9	223	9.1	164	1.5
Cu/CeO$_2$-CP	4.6	139	36.1	259	10.6	237	1.6
Cu/SiO$_2$	5.1	264	9.4	74	3.0	0	1.0

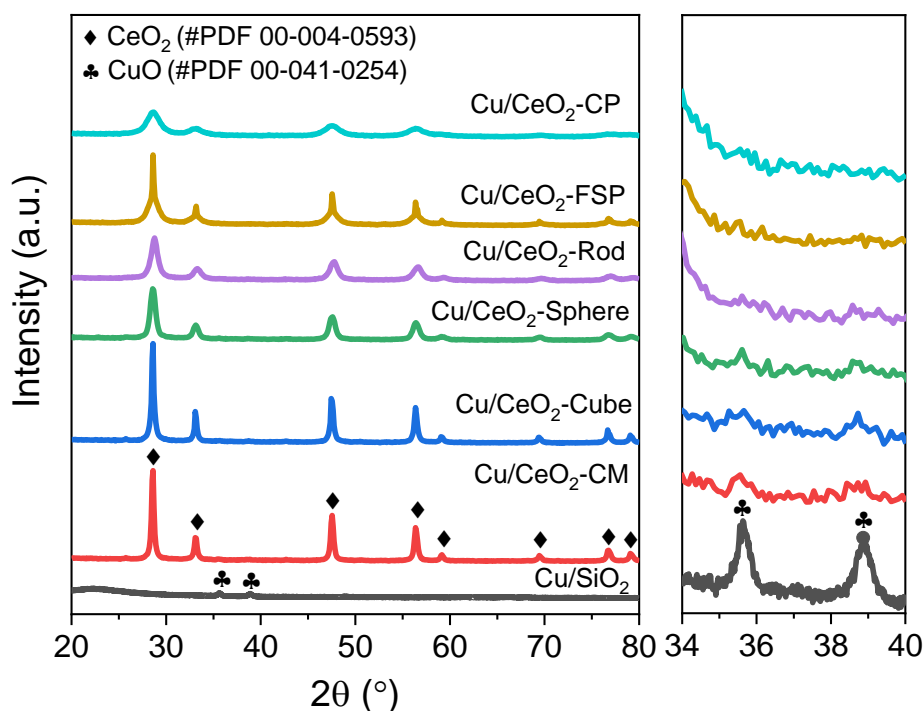[a] Derived from CO$_2$-N$_2$O titration [b] Derived from H$_2$-TPR.

Figure 2.1. XRD patterns of (a) Cu/CeO$_2$ and Cu/SiO$_2$ with (b) a zoom-in of CuO region.

We used H_2-TPR to probe the influence of copper-ceria interaction on the reducibility of Cu/CeO_2 catalysts. **Figure 2.2** shows that the reduction temperature of Cu/CeO_2 catalysts is significantly lower than that of Cu/SiO_2 catalyst. The observation of different reduction features (α, β, and γ peaks) points to the heterogeneous nature of the copper species in the Cu/CeO_2 samples. Based on previous studies,[25,45] we assign the α peak to dispersed copper species that strongly interact with ceria support (e.g., CuO_x clusters), the β peak to a $Cu-CeO_2$ solid solution, and the γ peak to copper oxide that is weakly interacting with ceria (e.g., CuO particles). It should be noted that the ceria supports were also reduced during copper reduction, as can be derived from the higher than unity values of the H_2/Cu molar ratios for all the Cu/CeO_2 catalysts (**Table 2.1**).

The above results demonstrate that the strong $Cu-CeO_2$ interactions in the fresh Cu/CeO_2 catalysts results in different types of copper species (CuO_x clusters, $Cu-CeO_2$ solid solution and CuO particles). We then characterized the reduced Cu/CeO_2 catalysts with respect to exposed metallic copper sites, an important parameter for CO_2 hydrogenation.[33] Accurate quantification of metallic copper sites in Cu/CeO_2 using N_2O, a well-established chemisorption probe for metallic copper, is challenging due to the simultaneous reaction of N_2O with ceria oxygen vacancies.[46] As it has been reported that CO_2 can block oxygen vacancies in ceria-supported metal catalysts,[47] we developed a combined CO_2-N_2O chemisorption approach during which CO_2 titration was carried out to block ceria oxygen vacancies prior to N_2O titration. By adopting such an approach, we can more accurately determine the exposed metallic copper sites and, at the same time, the amount of ceria oxygen vacancies in the reduced catalysts.
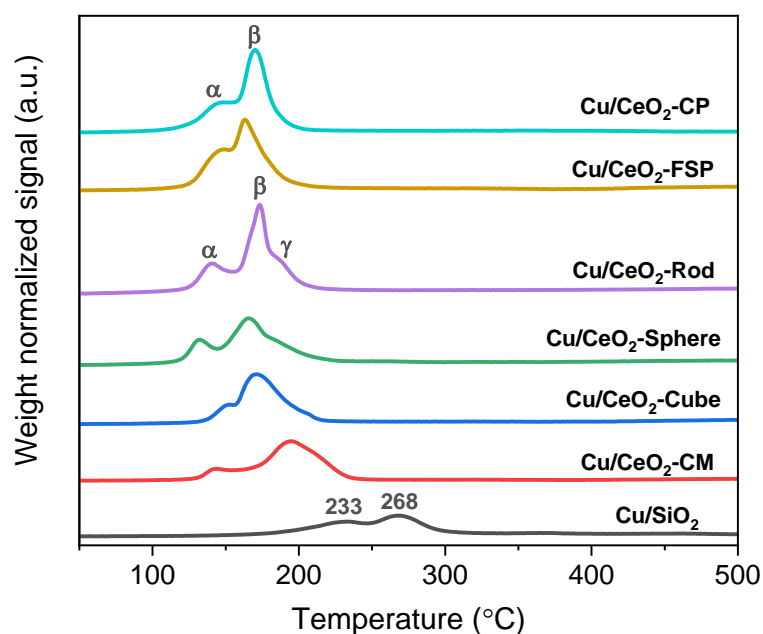

Figure 2.2. H_2-TPR profiles of the Cu/CeO_2 and Cu/SiO_2 catalysts.

To validate this CO$_2$-N$_2$O chemisorption approach, a reference experiment with Cu/SiO$_2$ catalyst showed that the difference in N$_2$O consumption between measurements with and without CO$_2$ titration prior to N$_2$O exposure is negligible. This finding indicates that CO$_2$ does not adsorb strongly on nor oxidizes the metallic copper surface. In contrast, N$_2$O consumption decreased significantly after CO$_2$ pulsing for the Cu/CeO$_2$ catalysts, in line with the notion that CO$_2$ interacts strongly with reduced ceria surface.[47] **Figure 2.3a** shows that the density of ceria oxygen vacancies (O$_v$) is proportional to the specific surface area of the Cu/CeO$_2$ catalysts. We further estimate that the surface-area-normalized oxygen vacancy density is ~1.0 O$_v$/nm^2. It should be mentioned that ceria oxygen vacancy formation is also affected by the exposed crystal plane,[48] although the current data do not allow drawing firm conclusions in this respect.
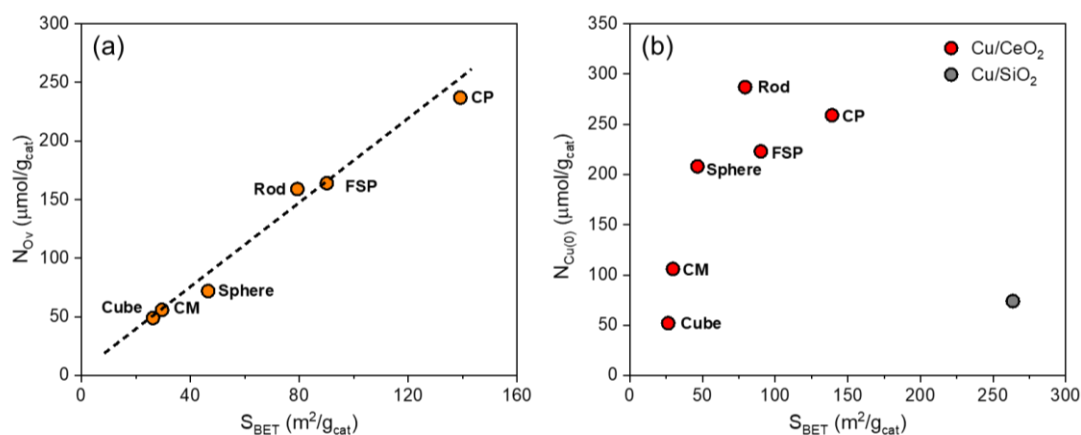

Figure 2.3. Correlation between the density of (a) ceria oxygen vacancy and (b) metallic copper site and specific surface area of the Cu/CeO$_2$ and Cu/SiO$_2$ catalysts.
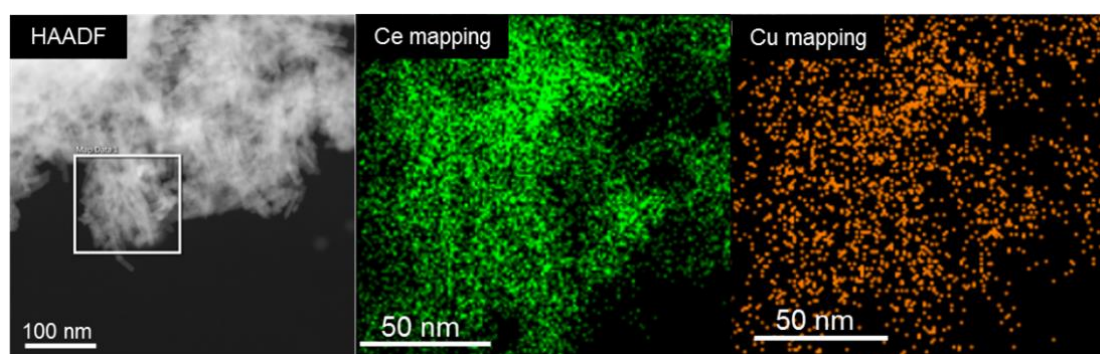
Figure 2.4. HAADF-STEM images with corresponding EDX mappings of the reduced Cu/CeO$_2$-Rod (250 °C, 1 h, in 50 mL/min 10% H$_2$/He).

Figure 2.3b shows the relation between the density of metallic copper sites and the catalyst specific surface area. Similar to the case of fresh catalysts, the ceria supports promote copper dispersion in the reduced catalysts compared to the silica support. Within the set of Cu/CeO$_2$ catalysts, a higher catalyst specific surface area generally leads to a higher density of metallic copper sites. Nonetheless, we observe that the Cu/CeO$_2$-Rod sample displayed the highest

metallic copper site density, although its specific surface area was not the highest. The superiority of the rod support in dispersing copper can be related to the large amount of surface defects, where the Cu-CeO_2 interaction can be maximized.[49–51] The copper dispersion (D_{Cu}) and copper specific surface area ($S_{Cu(0)}$) were further calculated based on the copper loading and the metallic copper site density (**Table 2.1**). A higher metallic copper sites density correlates directly with a higher copper dispersion, because the copper loading in all the catalysts is nearly the same. The copper specific surface area of the Cu/CeO_2 catalysts ranges from 2.1 m^2/g_{cat} to 10.6 m^2/g_{cat}, which is about 8-18 % of the total catalyst specific surface area. The effective copper diameter ($d_{Cu, eff}$) was calculated from the copper dispersion data, ranging from about 3 nm to 15 nm based on hemispherical assumption. It should be mentioned that the latter assumption may introduce a systematic error given the strong Cu-CeO_2 interaction.[25]

Besides N_2O chemisorption, STEM-EDX results show that the highly dispersed copper species were homogeneously dispersed over the ceria rod support (**Figure 2.4**), being in line with the high copper dispersion (38.7 %) derived from N_2O chemisorption. In summary, through a combination of XRD, H_2-TPR, N_2O chemisorption, and STEM-EDX we have demonstrated that, due to strong Cu-CeO_2 interaction, ceria significantly promotes copper dispersion compared to silica. The highest copper dispersion is observed for the Cu/CeO_2-Rod catalyst.

3.2 CO_2 hydrogenation performance

The Cu/CeO_2 and Cu/SiO_2 catalysts were evaluated in CO_2 hydrogenation reaction at 250 °C and 30 bar (**Figure 2.5** and **Table A.1**). Compared to the Cu/SiO_2, all the Cu/CeO_2 catalysts, except for the Cu/CeO_2-cube, showed a more than two times higher methanol selectivity. The lower methanol selectivity of the Cu/CeO_2-Cube is probably related to the comparatively weak Cu-CeO_2 interaction as revealed by the characterization results. Moreover, we observed that higher copper dispersion did not lead to a higher methanol formation rate for the Cu/CeO_2 catalysts. Further analysis revealed that the CO_2-to-methanol activity did not correlated with the Cu-CeO_2 perimeter interface length for the Cu/CeO_2 catalysts (**Figure A.3a**). These important observations strongly indicate that the Cu-CeO_2 interface does not significantly contribute to the CO_2-to-methanol conversion. We thus conclude that methanol synthesis predominantly occurs on the metallic copper surface in the Cu/CeO_2 catalysts. In contrast to methanol production, significant activity differences existed in terms of CO production: the Cu/SiO_2 catalyst was about two times more active than the Cu/CeO_2 catalysts in the rWGS reaction.

To understand better the catalytic data, CH_3OH and CO turnover frequencies (TOFs) were plotted against the effective copper particle size for all the Cu/CeO_2 and Cu/SiO_2 catalysts. **Figure 2.6a** shows that the TOF(CH_3OH) increases with particle size up to about 7.5 nm and then levels off, which is in keeping with the trend observed by Karelovic et al. for Cu/SiO_2 catalysts with a controlled copper particle size.[52] Such structure-sensitivity trend of

TOF(CH$_3$OH) indicates that CO$_2$-to-methanol conversion predominantly occurs on the metallic copper surface in the Cu/CeO$_2$ catalysts. In contrast, there were significant differences in the TOF(CO) between the Cu/CeO$_2$ and Cu/SiO$_2$ catalysts (**Figure 2.6b**). Specifically, the TOF(CO) of the Cu/SiO$_2$ catalyst was significantly higher than the TOF(CO) of the Cu/CeO$_2$ catalysts. Combining the characterization and catalytic results, we conclude that (i) the Cu-CeO$_2$ interaction leads to promotion in copper dispersion (i.e., structural promotion) but not to promotion in intrinsic methanol activity (i.e., electronic promotion) and (ii) the higher methanol selectivity in Cu/CeO$_2$ compared to Cu/SiO$_2$ is mainly a consequence of effective inhibition of the rWGS activity.
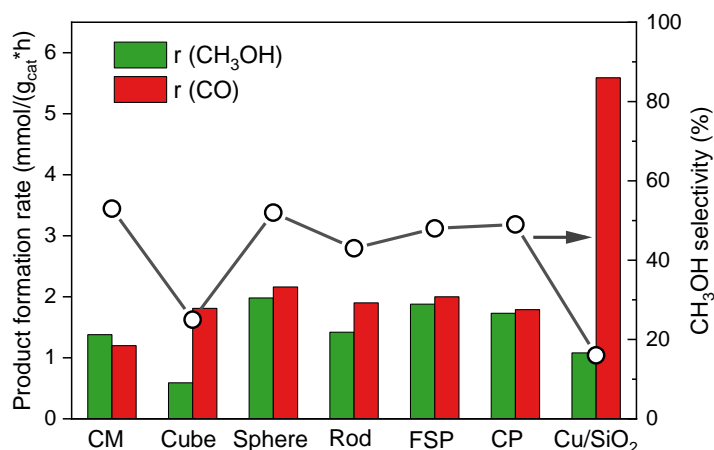
Figure 2.5. CO$_2$ hydrogenation performance of as-prepared Cu/CeO$_2$ and Cu/SiO$_2$ catalysts
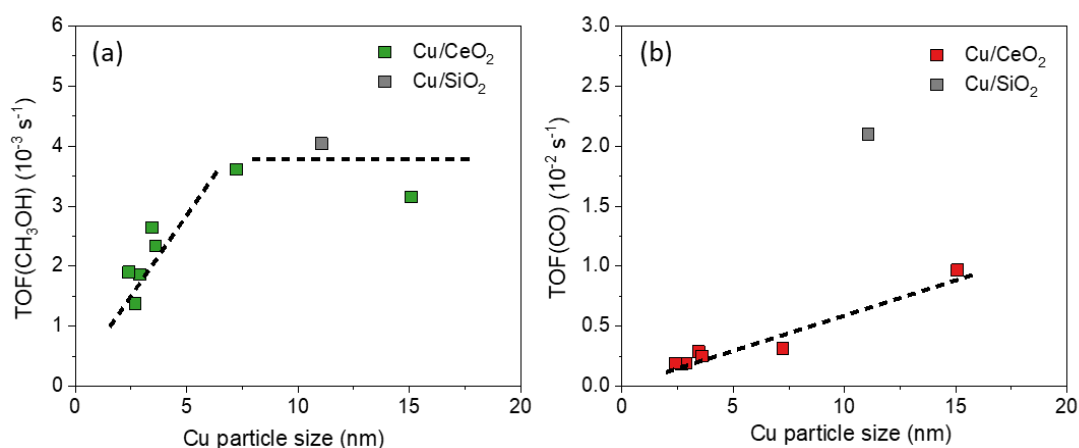
Figure 2.6. Structure-sensitivity trends for (a) TOF(CH$_3$OH) and (b) TOF(CO).

3.3 rWGS inhibition mechanism

To rationalise the above catalytic results, we used DFT calculations to investigate how Cu-CeO$_2$ interaction affects CO$_2$ hydrogenation. We used Cu$_{14}$/CeO$_2$ and Cu(111) models to represent, respectively, Cu/CeO$_2$ and Cu/SiO$_2$. Three important initial steps of CO$_2$ hydrogenation were investigated: (i) CO$_2$ → CO + O (direct CO$_2$ dissociation), (ii) CO$_2$ + H

$\rightarrow$ COOH (carboxyl formation) and (iii) $CO_2 + H \rightarrow$ HCOO (formate formation). It is generally accepted that direct CO_2 dissociation and carboxyl formation are important elementary steps for rWGS activity.[10,53,54] **Figure 2.7** shows potential energy diagrams for these reactions on $Cu(111)$ and Cu_{14}/CeO_2. The corresponding structures of intermediate and transition states can be found in **Figures A.4-5**. On the $Cu(111)$, the activation barriers for direct CO_2 dissociation and carboxyl formation are 1.48 eV and 1.61 eV, respectively. The corresponding values on Cu_{14}/CeO_2 are 0.82 eV and 0.84 eV. Thus, the kinetic barriers for CO_2 activation cannot explain the inhibition of the rWGS reaction for highly dispersed Cu in Cu/CeO_2.
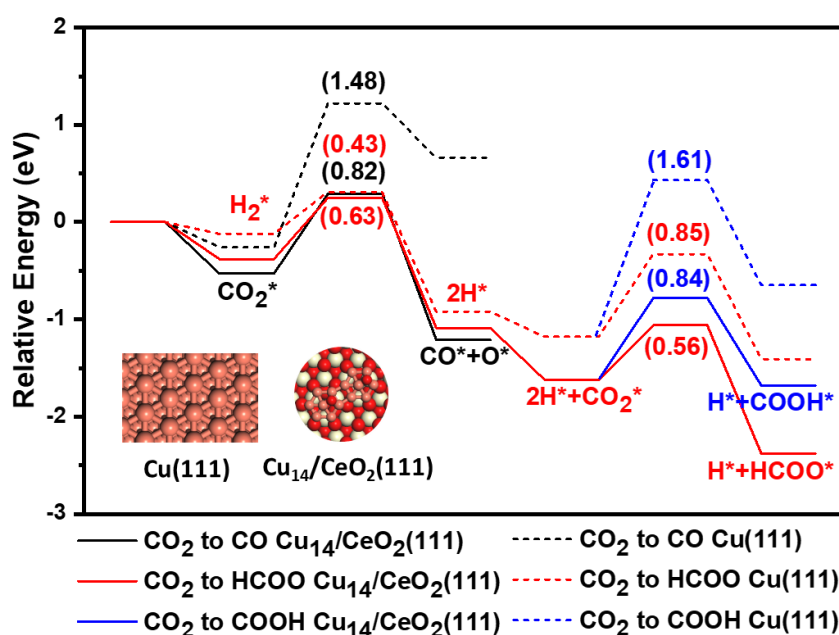

Figure 2.7. Potential energy diagrams of CO_2 hydrogenation on $Cu_{14}/CeO_2(111)$ and $Cu(111)$.

Next, the influence of formate formation was considered as a possible mechanism for inhibition of the rWGS reaction. **Figure 2.7** shows that formate formation on the Cu_{14}/CeO_2 proceeds with a significant lower activation barrier (0.56 eV) than direct CO_2 dissociation and carboxyl formation. This means that formate is the preferred product from the first CO_2 hydrogenation step on Cu_{14}/CeO_2. Moreover, as follows from the potential energy diagrams, formate formation is easier and formate is much more stable on Cu_{14}/CeO_2 than on $Cu(111)$. These results suggest that formate is a major surface species during CO_2 hydrogenation and its coverage on Cu_{14}/CeO_2 is significantly higher than on $Cu(111)$. We thus infer that rWGS inhibition is due to the blocking of copper surface sites by highly stable surface formate species, which is also suggested by other studies on methanol synthesis.[55–58]

These computational results were verified by in situ IR spectroscopy (**Figure 2.8**). The IR band at around 2850 cm^{-1} can be assigned to v(C-H) of formate species on copper.[52,59] We observe that the formate IR signal in Cu/CeO_2-Rod is much more intense than in Cu/SiO_2. Thus, the

formate coverage in Cu/SiO$_2$ is much lower than in Cu/CeO$_2$-Rod, which is in line with the higher formate stability on Cu$_{14}$/CeO$_2$(111) as shown by the calculation results. Combining these DFT modelling and IR results, the inhibition of rWGS reaction in Cu/CeO$_2$ can be rationalized as follows. The strong Cu-CeO$_2$ interaction leads to stabilization of formate species on copper, which blocks copper surface sites and inhibits the reaction routes associated with rWGS activity, which involve direct CO$_2$ dissociation and carboxyl intermediate formation.
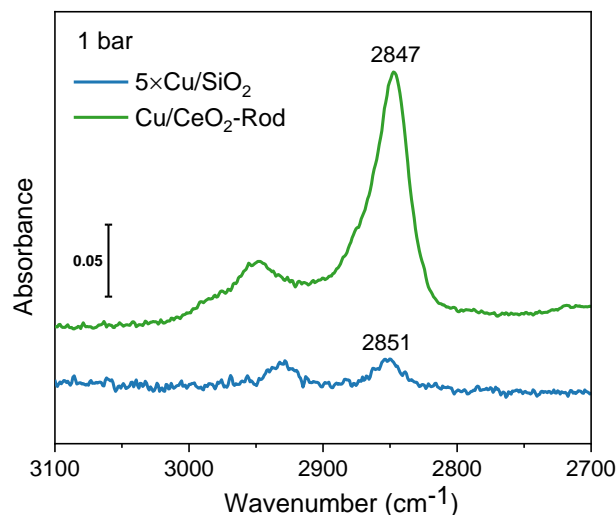

Figure 2.8. IR bands of adsorbed formate species during CO$_2$ hydrogenation over the Cu/SiO$_2$ and Cu/CeO$_2$-Rod. Reaction conditions: 250 °C, 1 bar and H$_2$/CO$_2$ = 3.

3.4 Role of Cu-CeO$_2$ interface

In the work of Graciani et al., it was proposed that the Cu-CeO$_2$ interface is the active site for CO$_2$ hydrogenation to methanol via CO intermediate.[26] In the present study, we found that all the Cu/CeO$_2$ catalysts (except for Cu/CeO$_2$-Cube) showed comparable methanol formation rates regardless the copper dispersion (i.e., Cu-CeO$_2$ interface site density). This observation contradicts the notion that Cu-CeO$_2$ interface sites are responsible for the hydrogenation of CO$_2$ to methanol. To understand this difference, we carried out CO hydrogenation experiments. **Figure 2.9b** shows that the Cu/CeO$_2$ catalysts were much more active in the hydrogenation of CO to methanol than Cu/SiO$_2$, which is in line with an earlier report.[60] We also found that the CO-to-methanol activity strongly correlates with the Cu-CeO$_2$ perimeter length of the Cu/CeO$_2$ catalysts (**Figure A.3b**). Moreover, we observed that methanol activity of Cu/CeO$_2$ was highly affected by CO$_2$. **Figure 2.9b** shows that CO-to-methanol activity of the most active Cu/CeO$_2$-Rod catalyst decreased substantially if the catalyst was treated with CO$_2$ flow (160 °C, 1 bar, 1 h) after reduction, and the lowest methanol activity was obtained in CO$_2$ hydrogenation. Combining these catalytic results, we found that (i) Cu-CeO$_2$ interface is active for CO hydrogenation to methanol and (ii) CO$_2$ may act as a poison for the interfacial sites under methanol synthesis conditions. A follow-up study was carried out in **Chapter 3** to investigate the role of CO$_2$ in more detail.
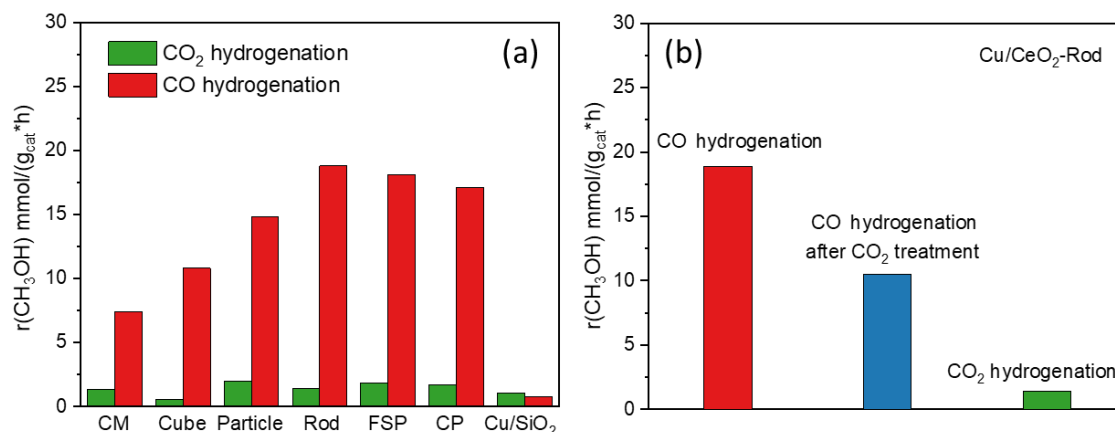
Figure 2.9. (a) Methanol activity of CO and CO_2 hydrogenation of the Cu/CeO_2 and Cu/SiO_2 catalysts. (b) Methanol activity of CO hydrogenation (red and blue bars) and CO_2 hydrogenation (green bar) of the Cu/CeO_2-Rod catalyst.

4. Conclusions

We prepared a series of Cu/CeO_2 catalysts with different support properties to study the role of metal-support interactions in CH_3OH synthesis via CO_2 hydrogenation for Cu/CeO_2 catalysts. Characterization results show that copper dispersion is significantly facilitated by strong Cu-CeO_2 interaction in both fresh and reduced catalysts. Catalytic results show that Cu/CeO_2 catalysts display a higher CH_3OH selectivity compared to Cu/SiO_2 catalyst. Further structure-sensitivity analysis reveals that the improved CH_3OH selectivity is not due to promotion of intrinsic CH_3OH activity but to the inhibition of reverse water gas shift (rWGS) activity. Mechanistic studies (DFT simulation and in situ IR) indicate that the rWGS inhibition in Cu/CeO_2 is due to site-blocking by stabilized formate species on copper surface. Overall, these findings demonstrate that, for CO_2-to-methanol conversion, the strong Cu-CeO_2 interactions in Cu/CeO_2 lead to significant structural promotion but not to electronic promotion.

References

1   G. Centi, E. A. Quadrelli and S. Perathoner, *Energy Environ. Sci.*, 2013, **6**, 1711–1731.

2   G. A. Olah, *Angew. Chem. Int. Ed.*, 2005, **44**, 2636–2639.

3   A. Goeppert, M. Czaun, J.-P. Jones, G. K. Surya Prakash and G. A. Olah, *Chem.Soc.Rev.*, 2014, **43**, 7995–8048.

4   S. Gumber and A. V. P. Gurumoorthy, in *Methanol: Science and Engineering*, Elsevier B.V., 2018, pp. 661–674.

5   Malte Behrens, Felix Studt, Igor Kasatkin, Stefanie Kühl, Michael Hävecker, Frank Abild-Pedersen, Stefan Zander, Frank Girgsdies, Patrick Kurr, Benjamin-Louis Kniep, Michael Tovar, Richard W. Fischer, Jens K. Nørskov and Robert Schlög, Science., 2012, **336**, 893–897.

6   O. Martin and J. Pérez-Ramírez, *Catal. Sci. Technol.*, 2013, **3**, 3343–3352.

7   G. C. Chinchen, P. J. Denny, D. G. Parker, M. S. Spencer and D. A. Whan, *Appl. Catal.*, 1987, **30**, 333–338.

8   M. D. Porosoff, B. Yan and J. G. Chen, *Energy Environ. Sci.*, 2016, **9**, 62–73.

9   J. A. Rodriguez, P. Liu, D. J. Stacchiola, S. D. Senanayake, M. G. White and J. G. Chen, *ACS Catal.*, 2015, **5**, 6696–6706.

10   S. Kattel, P. Liu and J. G. Chen, *J. Am. Chem. Soc.*, 2017, **139**, 9739–9754.

11   S. Zander, E. L. Kunkes, M. E. Schuster, J. Schumann, G. Weinberg, D. Teschner, N. Jacobsen, R. Schlögl and M. Behrens, *Angew. Chem. Int. Ed.*, 2013, **52**, 6536–6540.

12   F. Liao, Y. Huang, J. Ge, W. Zheng, K. Tedsree, P. Collier, X. Hong and S. C. Tsang, *Angew. Chem. Int. Ed.*, 2011, **50**, 2162–2165.

13   S. Kattel, P. J. Ramírez, J. G. Chen, J. A. Rodriguez and P. Liu, *Science.*, 2017, **355**, 1296–1299.

14   I. a Fisher, H. C. Woo and a T. Bell, *Catal. Letters*, 1997, **44**, 11–17.

15   K. Larmier, W.-C. Liao, S. Tada, E. Lam, R. Verel, A. Bansode, A. Urakawa, A. Comas-Vives and C. Copéret, *Angew. Chem. Int. Ed.*, 2017, **56**, 2318–2323.

16   Z. Shi, Q. Tan, C. Tian, Y. Pan, X. Sun, J. Zhang and D. Wu, *J. Catal.*, 2019, **379**, 78–89.

17   K. Chen, H. Fang, S. Wu, X. Liu, J. Zheng, S. Zhou, X. Duan, Y. Zhuang, S. Chi Edman Tsang and Y. Yuan, *Appl. Catal. B Environ.*, 2019, **251**, 119–129.

18   W. Xu, P. J. Ramírez, D. Stacchiola, J. L. Brito and J. A. Rodriguez, *Catal. Letters*, 2015, **145**, 1365–1373.

19   K. Chen, X. Duan, H. Fang, X. Liang and Y. Yuan, *Catal. Sci. Technol.*, 2018, **8**, 1062–1069.

20   R. Van Den Berg, G. Prieto, G. Korpershoek, L. I. van der Wal, A. J. van Bunningen, S. Lægsgaard-Jørgensen, P. E. De Jongh and K. P. De Jong, *Nat. Commun.*, 2016, **7**, 13057–13063.

21   W.-W. Wang, W.-Z. Yu, P.-P. Du, H. Xu, Z. Jin, R. Si, C. Ma, S. Shi, C.-J. Jia and C.-H. Yan, *ACS Catal.*, 2017, **7**, 1313–1329.

22   K. N. Rao, P. Venkataswamy and B. M. Reddy, *Ind. Eng. Chem. Res.*, 2011, **50**, 11960–11969.

23   L. Liu, Z. Yao, Y. Deng, F. Gao, B. Liu and L. Dong, *ChemCatChem*, 2011, **3**, 978–989.

24   M. Zabilskiy, P. Djinović, B. Erjavec, G. Dražić and A. Pintar, *Appl. Catal. B Environ.*, 2015, **163**, 113–122.
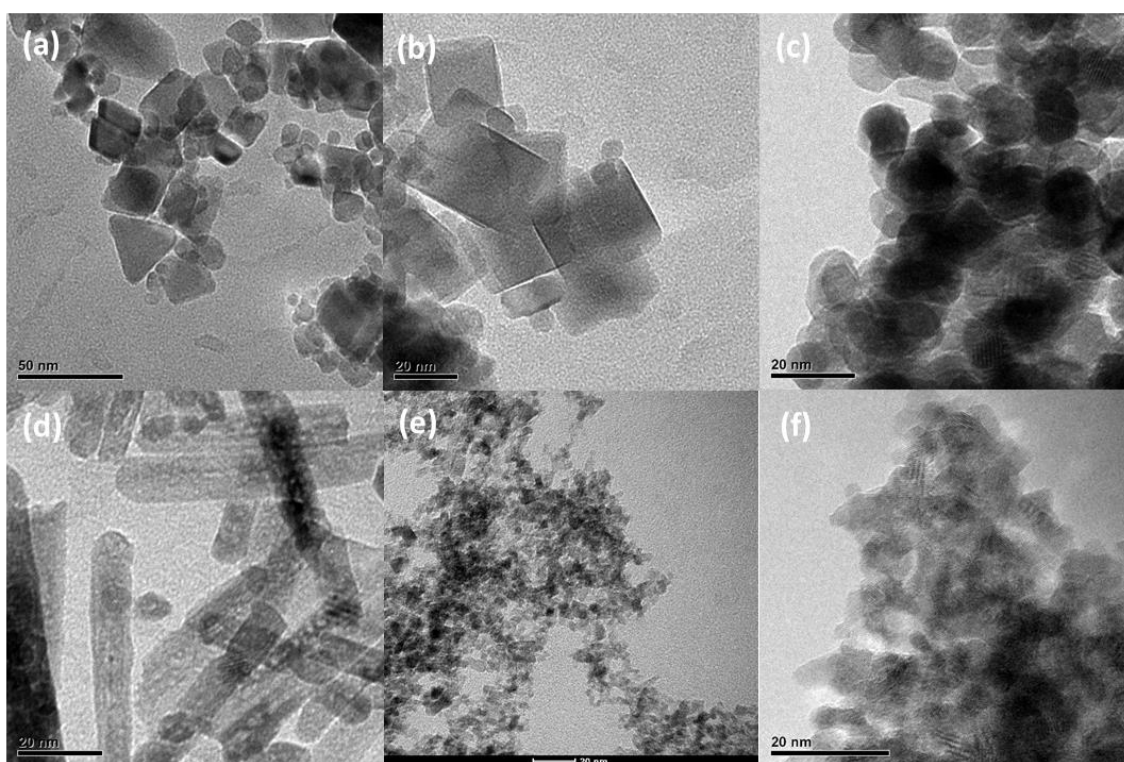
25   A. Chen, X. Yu, Y. Zhou, S. Miao, Y. Li, S. Kuld, J. Sehested, J. Liu, T. Aoki, S. Hong, M. F. Camellone, S. Fabris, J. Ning, C. Jin, C. Yang, A. Nefedov, C. Wöll, Y. Wang and W. Shen, *Nat. Catal.*, 2019, **2**, 334–341.

26   J. A. R. Jesús Graciani, Kumudu Mudiyanselage, Fang Xu, Ashleigh E. Baber, Jaime Evans, Sanjaya D. Senanayake, Darío J. Stacchiola, Ping Liu, Jan Hrbek, Javier Fernández Sanz, *Science.*, 2014, **345**, 546–550.

27   B. Ouyang, W. Tan and B. Liu, *Catal. Commun.*, 2017, **95**, 36–39.

28   W. Wang, Z. Qu, L. Song and Q. Fu, *J. Energy Chem.*, 2020, **40**, 22–30.

29   P. Sripada, J. Kimpton, A. Barlow, T. Williams, S. Kandasamy and S. Bhattacharya, *J. Catal.*, 2020, **381**, 415–426.

30   H. X. Mai, L. D. Sun, Y. W. Zhang, R. Si, W. Feng, H. P. Zhang, H. C. Liu and C. H. Yan, *J. Phys. Chem. B*, 2005, **109**, 24380–24385.

31   W. Y. Teoh, R. Amal, L. Mädler and L. Madler, *Nanoscale*, 2010, **2**, 1324–1347.

32   J. R. Jensen, T. Johannessen and H. Livbjerg, *Appl. Catal. A Gen.*, 2004, **266**, 117–122.

33   S. Natesakhawat, J. W. Lekse, J. P. Baltrus, P. R. Ohodnicki, B. H. Howard, X. Deng and C. Matranga, *ACS Catal.*, 2012, **2**, 1667–1676.

34   A. Karelovic and P. Ruiz, *Catal. Sci. Technol.*, 2015, **5**, 869–881.

35   G. Kresse and J. Hafner, *Phys. Rev. B*, 1994, **49**, 14251–14269.

36   P. E. Blöchl, *Phys. Rev. B*, 1994, **50**, 17953–17979.

37   J. P. Perdew, K. Burke and M. Ernzerhof, *Phys. Rev. Lett.*, 1996, **77**, 3865–3868.

38   S. Dudarev and G. Botton, *Phys. Rev. B - Condens. Matter Mater. Phys.*, 1998, **57**, 1505–1509.

39   S. Fabris, S. De Gironcoli, S. Baroni, G. Vicario and G. Balducci, *Phys. Rev. B - Condens. Matter Mater. Phys.*, 2005, **72**, 1–2.

40   M. Cococcioni and S. De Gironcoli, *Phys. Rev. B - Condens. Matter Mater. Phys.*, 2005, **71**, 1–16.

41   C. W. M. Castleton, J. Kullgren and K. Hermansson, *J. Chem. Phys.*, 2007, **127**, 244704.

42   J. L. F. Da Silva, M. V. Ganduglia-Pirovano, J. Sauer, V. Bayer and G. Kresse, *Phys. Rev. B - Condens. Matter Mater. Phys.*, 2007, **75**, 19–24.

43   G. Henkelman and H. Jónsson, *J. Chem. Phys.*, 2000, **113**, 9978–9985.

44   D. Sheppard, R. Terrell and G. Henkelman, *J. Chem. Phys.*, 2008, **128**, 134106.

45   W. W. Wang, P. P. Du, S. H. Zou, H. Y. He, R. X. Wang, Z. Jin, S. Shi, Y. Y. Huang, R. Si, Q. S. Song, C. J. Jia and C. H. Yan, *ACS Catal.*, 2015, **5**, 2088–2099.

46   N. A. Koryabkina, A. A. Phatak, W. F. Ruettinger, R. J. Farrauto and F. H. Ribeiro, *J. Catal.*, 2003, **217**, 233–239.

47   T. Takeguchi, S. Manabe, R. Kikuchi, K. Eguchi, T. Kanazawa, S. Matsumoto and W. Ueda, *Appl. Catal. A Gen.*, 2005, **293**, 91–96.

48   M. Nolan, J. E. Fearon and G. W. Watson, *Solid State Ionics*, 2006, **177**, 3069–3074.

49   S. Agarwal, L. Lefferts, B. L. Mojet, D. A. J. J. Michel Ligthart, E. J. M. Hensen, D. R. G. Mitchell, W. J. Erasmus, B. G. Anderson, E. J. Olivier, J. H. Neethling and A. K. Datye,

ChemSusChem, 2013, **6**, 1898–1906.

50   G. Spezzati, Y. Su, J. P. Hofmann, A. D. Benavidez, A. T. DeLaRiva, J. McCabe, A. K. Datye and E. J. M. Hensen, *ACS Catal.*, 2017, **7**, 6887–6891.

51   J. C. González, J. C. Hernández, M. López-Haro, E. Del Río, J. J. Delgado, A. B. Hungría, S. Trasobares, S. Bernal, P. A. Midgley and J. J. Calvino, *Angew. Chem. Int. Ed.*, 2009, **48**, 5313–5315.

52   A. Karelovic, G. Galdames, J. C. Medina, C. Yévenes and Y. Barra, *J. Catal.*, 2019, **369**, 415–426.

53   L. Dietz, S. Piccinin and M. Maestri, *J. Phys. Chem. C*, 2015, **119**, 4959–4966.

54   Y. Li, S. H. Chan and Q. Sun, *Nanoscale*, 2015, **7**, 8663–8683.

55   P. Wu and B. Yang, *ACS Catal.*, 2017, **7**, 7187–7195.

56   W. Janse Van Rensburg, M. A. Petersen, M. S. Datt, J. A. Van Den Berg and P. Van Helden, *Catal. Letters*, 2015, **145**, 559–568.

57   F. Studt, M. Behrens, E. L. Kunkes, N. Thomas, S. Zander, A. Tarasov, J. Schumann, E. Frei, J. B. Varley, F. Abild-Pedersen, J. K. Nørskov and R. Schlögl, *ChemCatChem*, 2015, **7**, 1105–1111.

58   Y. F. Zhao, Y. Yang, C. Mims, C. H. F. Peden, J. Li and D. Mei, *J. Catal.*, 2011, **281**, 199–211.

59   S. ichiro Fujita, M. Usui, E. Ohara and N. Takezawa, *Catal. Letters*, 1992, **13**, 349–358.

60   W.-J. Shen, Y. Ichihashi and Y. Matsumura, *Appl. Catal. A Gen.*, 2005, **282**, 221–226.

Appendix A

Table A.1. CO_2 hydrogenation performance of as-prepared Cu/CeO_2 and Cu/SiO_2 catalysts

Catalyst	X(CO_2) (%)	S(CH_3OH) (%)	r(CH_3OH) (mmol/g_{cat})	r(CO) (mmol/g_{cat})	TOF(CH_3OH) ($10^{-3}s^{-1}$)	TOF(CO) ($10^{-3}s^{-1}$)
Cu/CeO_2-CM	1.0	53	1.4	1.2	3.6	3.1
Cu/CeO_2-Cube	0.9	25	0.6	1.8	3.2	9.7
Cu/CeO_2-Sphere	1.5	52	2.0	2.2	2.6	2.9
Cu/CeO_2-Rod	1.2	43	1.4	1.9	1.4	1.8
Cu/CeO_2-FSP	1.4	48	1.9	2.0	2.3	2.5
Cu/CeO_2-CP	1.3	49	1.7	1.8	1.9	1.9
Cu/SiO_2	1.1	16	1.1	5.6	4.0	21.0

Figure A.1. TEM images of reduced Cu/CeO_2 catalysts (250 °C, 1 h, in 50 mL/min 10% H_2/He). (a) Cu/CeO_2-CM, (b) Cu/CeO_2-Cube, (c) Cu/CeO_2-Sphere, (d) Cu/CeO_2-Rod, (e) Cu/CeO_2-FSP and (f) Cu/CeO_2-CP

Figure A.2. H_2-TPR profiles of the different CeO_2 supports.
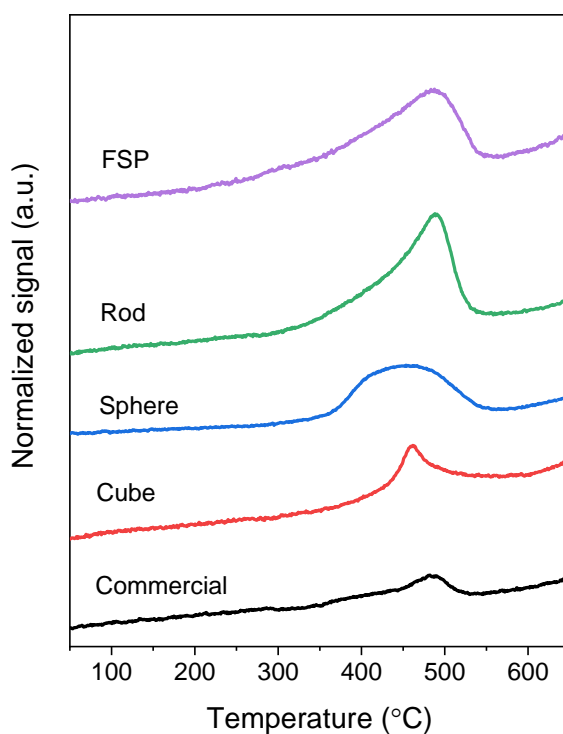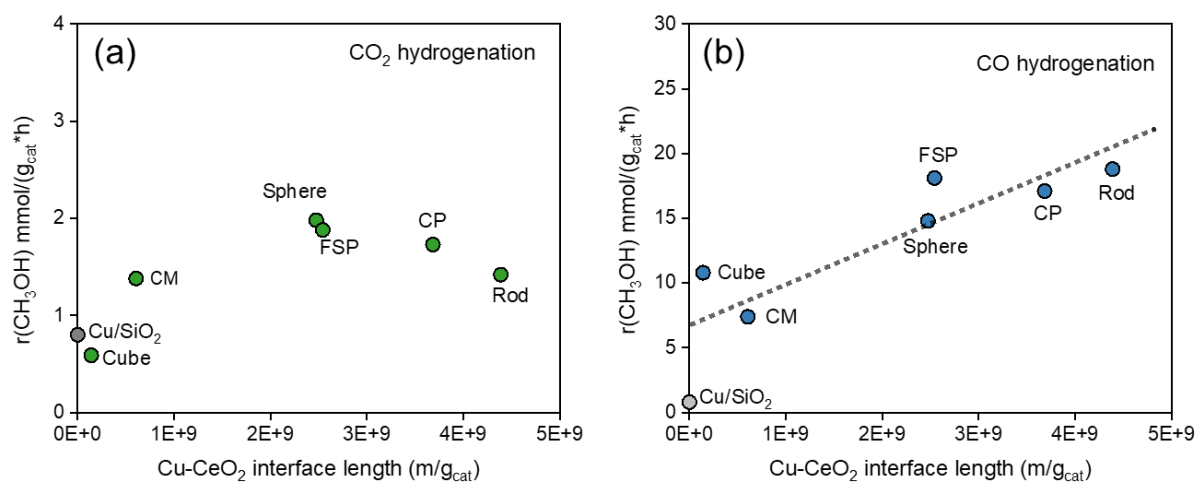

Figure A.3. Correlation between methanol activity and estimated interface length in the Cu/CeO_2 catalysts derived from CO_2 and CO hydrogenation.
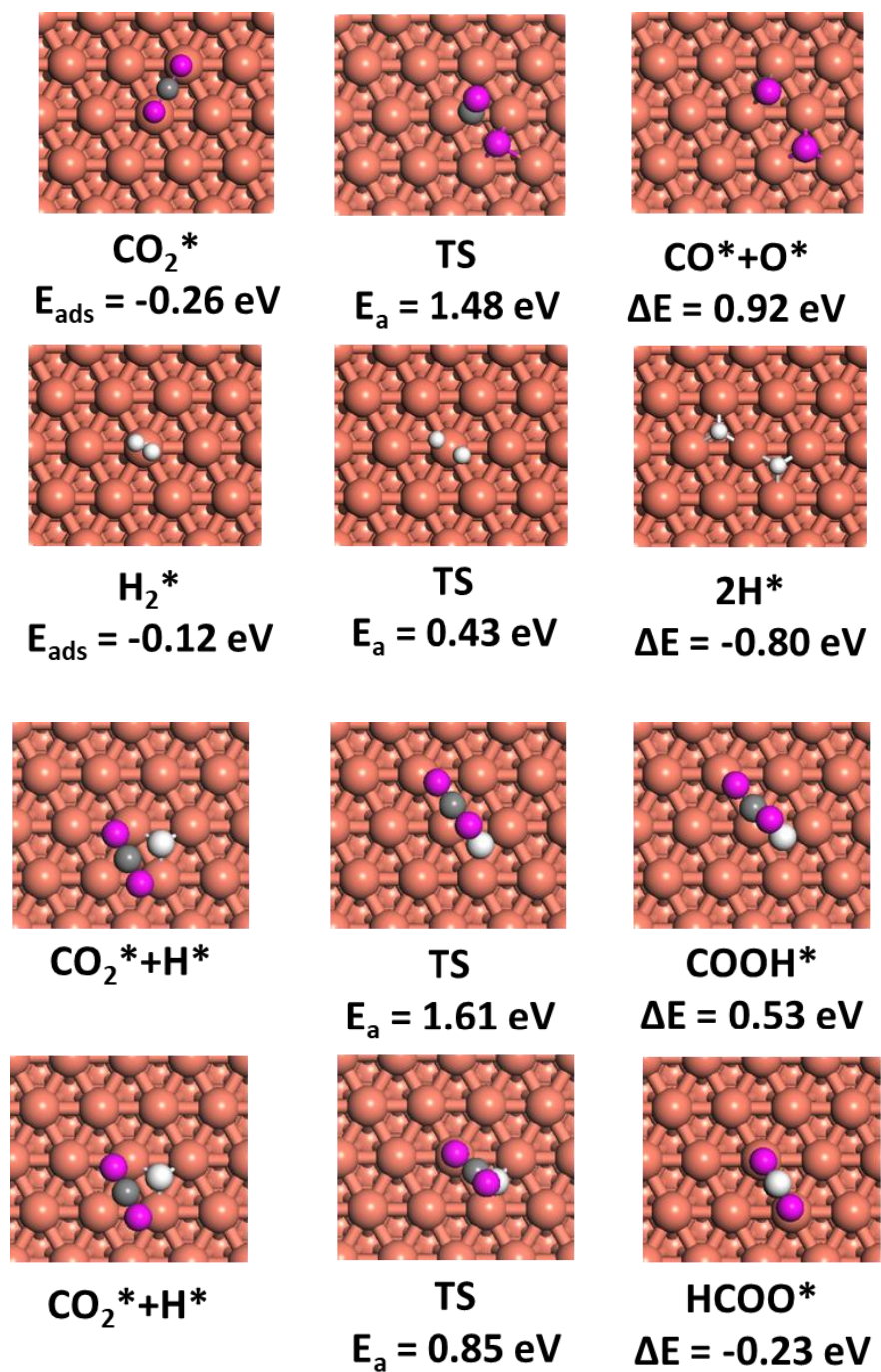
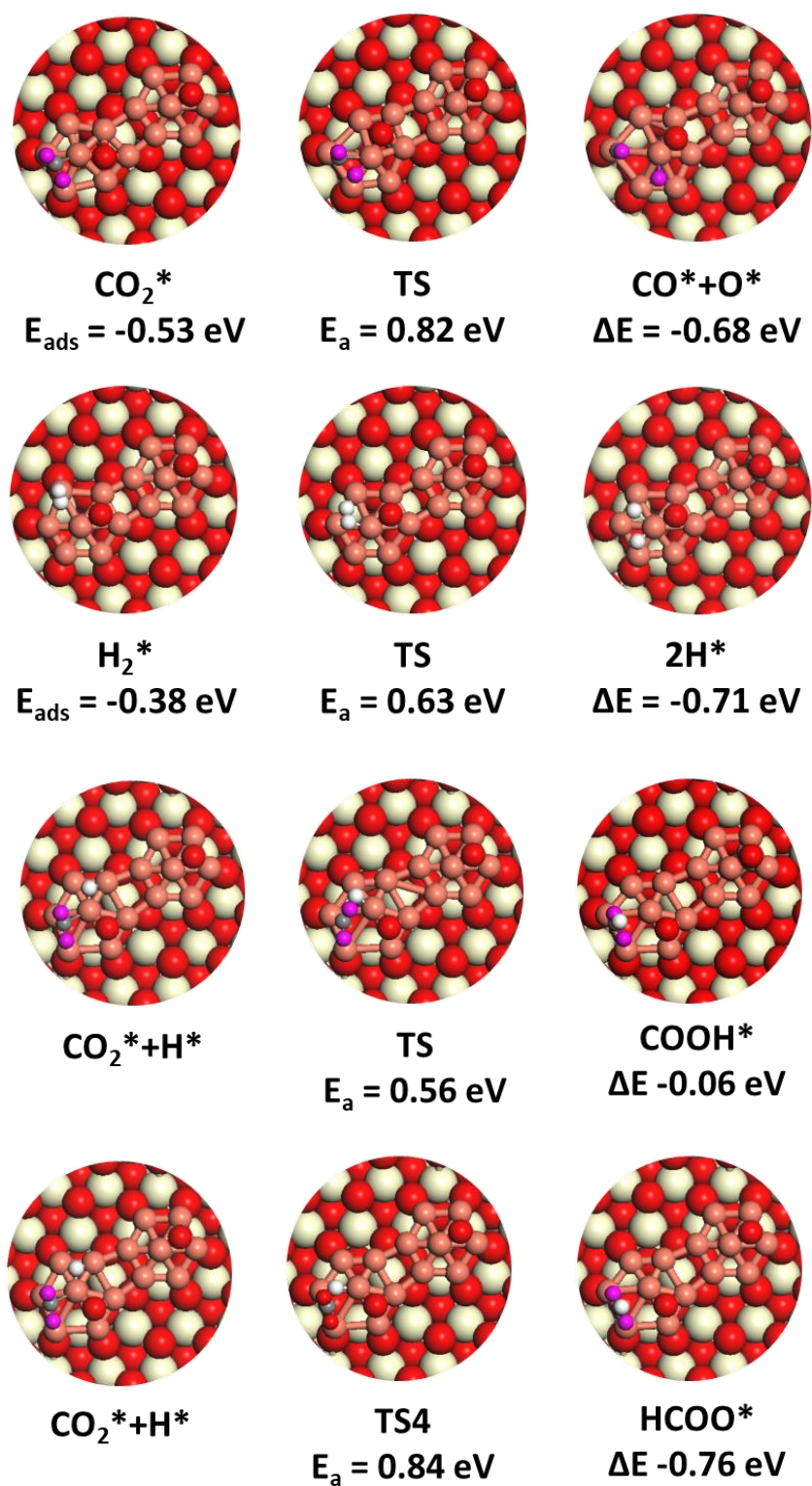**Figure A.4**. Reaction intermediates and transition states of CO_2 hydrogenation on Cu(111).

Figure A.5. Reaction intermediates and transition states of CO_2 hydrogenation on $Cu_{14}/CeO_2(111)$.

CHAPTER 3

On the Role of CO$_2$ in CO Hydrogenation to Methanol over Cu/CeO$_2$

ABSTRACT

Methanol synthesis from synthesis gas remains one of the most important chemical processes. The conventional Cu/ZnO/Al$_2$O$_3$ catalysts benefit from the presence of CO$_2$ in the synthesis gas feed. Herein, we investigated the effect of CO$_2$ co-feeding during methanol synthesis from CO over Cu/CeO$_2$, which exhibits a high copper dispersion and promising CO-to-methanol activity due to strong Cu-CeO$_2$ interactions (**Chapter 2**). A Cu/CeO$_2$ catalyst was prepared by deposition-precipitation and characterized using XRD, STEM-EDX, H$_2$-TPR and N$_2$O titration. The Cu/CeO$_2$ catalyst consists of highly dispersed copper species strongly interacting with ceria support. Steady-state and transient activity measurements demonstrate that the methanol synthesis rate of a CO/H$_2$ feed is strongly decreased when CO$_2$ is added. Extensive (quasi) in situ characterization (TPH, XPS, SSITKA and IR spectroscopy) were used to understand the CO$_2$ poisoning effect. The results emphasize the role of Cu-CeO$_2$ interface in the hydrogenation of CO to methanol via a formyl intermediate. Co-feeding small amounts of CO$_2$ to CO/H$_2$ blocks these interface sites due to formation of carbonate-like species. Methanol formation proceeds then mainly via direct CO$_2$ hydrogenation for which metallic Cu surface provides the active sites.

1. Introduction

Methanol is one of the most important intermediates of the chemical industry with a global annual production close to 100 million tons in 2019 and its demand is projected to grow at an annual rate of about 6%.[1,2] Methanol is mainly used for the production of other chemicals such as formaldehyde, dimethyl ether, acetic acid, methyl chloride, and olefins, but is also increasingly considered as a clean-burning fuel to replace liquid transportation fuels derived from oil feedstock.[3] Methanol economy concept was envisioned, where methanol produced from anthropogenic carbon dioxide (CO_2) using hydrogen derived from renewable energy sources plays a central role in the storage, transport and supply of energy and chemicals.[4]

Methanol is currently produced at industrial scale by converting CO_2-containing synthesis gas ($CO/CO_2/H_2$) over $Cu/ZnO/Al_2O_3$ catalysts at elevated temperature (200-300 °C) and pressure (50-100 bar).[5] Although $Cu/ZnO/Al_2O_3$ is highly optimized for methanol production from synthesis gas, this catalyst displays insufficient activity in converting pure CO_2 with H_2 to methanol due to competing rWGS reaction[6] ($CO_2 + H_2 \rightarrow CO + H_2O$) and water-induced deactivation.[7–9] Thus, for realizing future scenarios in which methanol plays a central role novel catalyst formulations for efficient CO_2-to-methanol conversion are necessary. Cu/CeO_2 is a promising candidate for that purpose owing to the beneficial role of Cu-CeO_2 interactions. Methanol synthesis from syngas using Cu/CeO_2 was reported more than three decades ago by Nix et al.[10] A $CuCe_2$ intermetallic precursor activated in CO/H_2 was found to be an active catalyst and the methanol activity did not correlate with the copper surface area. The active sites of this catalyst was therefore postulated to be linked to the intimate interaction of copper with cerium oxide.[10,11] After these initial studies, Matsumura and co-workers found that Cu/CeO_2 catalysts prepared by co-precipitation method showed better low-temperature methanol synthesis activity (< 200°C) from CO/H_2 in comparison to Cu/ZnO-based catalysts.[12,13]

Cu/CeO_2 was recently also reported to be highly active in the hydrogenation of CO_2 to methanol.[14] Graciani et al. used a combined experimental and theoretical study of an inverse $CeO_x/Cu(111)$ catalyst to propose that the copper-ceria interface can provide a highly favorable methanol synthesis pathway via CO intermediate.[14] Several reports appeared later dedicated to investigate Cu/CeO_2 for CO_2 conversion using more conventional catalyst preparation methods.[15–19] Despite these studies, the role of the copper-ceria interface in CO_2-to-methanol conversion under industrially relevant conditions still remains unclear. In Chapter 2 it was found that the Cu-CeO_2 interactions facilitate the copper dispersion but does not promote the intrinsic methanol activity as compared to a reference Cu/SiO_2 catalyst. A further comparison between CO and CO_2 hydrogenation suggested that the methanol formation rate over Cu/CeO_2 strongly depends on the carbon source, *viz.* CO and CO_2, which is a well-known phenomenon in the methanol synthesis field.[20–24] In industrial practice, methanol synthesis over

$Cu/ZnO/Al_2O_3$ is promoted by co-feeding a small amount of CO_2 to the CO/H_2 reaction mixture.[21,24] Behm and co-workers showed that the oxygen vacancy concentration in Au/ZnO was modulated by the carbon sources which in turn determines its methanol activity.[25,26] For Cu/CeO_2, the presence of CO_2 was found to be detrimental for CO-to-methanol conversion over a catalyst derived from a $CuCe_2$ intermetallic compound.[10] Recently, Van der Water et al. showed that Cu/CeO_2 was self-poisoned by in situ generated CO_2 during an induction period of CO hydrogenation reaction. The authors speculated that the CO_2 poisoning is due to surface carbonate and formate species, which hinder the adsorption of reactants to the Cu^+/CeO_{2-x} active sites.[27]

In this contribution, we compared the performance of a Cu/CeO_2 catalyst in the hydrogenation of CO, CO_2 and mixtures thereof. The Cu/CeO_2 catalyst was prepared by deposition-precipitation and extensively characterized by XRD, STEM-EDX, H_2-TPR, and N_2O chemisorption. Steady-state and transient co-feeding catalytic activity measurements were carried out to investigate the influence of the carbon source composition on methanol production. Quasi in situ analysis involving temperature-programmed hydrogenation and XPS were used to characterize the used catalysts. Steady-state isotopic transient kinetic analysis (SSITKA) and in situ IR spectroscopy provided mechanistic insights into the role of CO_2 on methanol synthesis.

2. Experimental section

2.1 Catalyst preparation

A 5 wt% Cu/CeO_2 catalyst was prepared using commercial ceria powder (< 25 nm, Sigma Aldrich) by a deposition-precipitation method. For this purpose, 6.3 mmol $Cu(NO_3)_2 \cdot 3H_2O$ (99%, Sigma Aldrich) was dissolved in 400 mL deionized water, followed by addition of 8.0 g ceria support. After sonicating for 10 min, 0.1 M Na_2CO_3 (99.5 %, Sigma Aldrich) solution was added dropwise to the ceria support dispersion to initiate the DP process until a pH of 10 was reached. The resulting dispersion was aged at room temperature for 3 h. The solid was retrieved by filtration and washed with copious amounts of deionized water until pH=7 of the filtrate was reached, and then dried at 60 °C overnight. The dried material was calcined at 400 °C (rate = 5 °C/min) for 3 h in static air to yield the fresh catalyst, which is denoted as Cu/CeO_2-DP.

2.2 Catalyst characterization

Inductively coupled plasma optical emission spectroscopy (ICP-OES). The copper loading of the fresh catalyst was determined by ICP-OES (Spectro CIROS CCD spectrometer). Prior to analysis, the catalyst was dissolved in 5 mL concentrated sulfuric acid under heating at 150 °C for about 1 h.

N$_2$ physisorption. Textual properties were determined by recording N$_2$ physisorption isotherms at -196 °C on a Micromeritics TriStar II 3020 instrument. For this purpose, about 100 mg of sample was transferred into a glass sample tube and pretreated at 120 °C overnight night under nitrogen flow. The Brunauer-Emmett-Teller (BET) method was used to calculate the specific surface area.

X-ray diffraction (XRD). The crystal structure of the fresh catalyst was studied with a Bruker D2 Phaser diffractometer using Cu Kα radiation with a wavelength of 1.54 Å. The XRD patterns were recorded between 20-85˚ with a step size of 0.02˚ at a 0.5 s/step scan rate.

Temperature programmed reduction (H$_2$-TPR). H$_2$-TPR measurements were carried out in a Micromeritics AutoChem II setup. About 50 mg of sample was loaded into a quartz U-tube between two quartz wool layers. Prior to measurements, the sample was pretreated in a He flow (50 ml/min) at 200 °C for 1 h to remove adsorbed water. The TPR profile was recorded by heating the sample from 40 °C to 700 °C at a rate of 10 °C/min in a 4 vol% H$_2$ in He flow (50 ml/min). Hydrogen consumption was determined by a thermal conductivity detector. The hydrogen signal was calibrated using a Cu/SiO$_2$ reference sample.

STEM-EDX. The elemental distribution over the reduced catalyst (250 °C, 1 h, 10 vol% H$_2$ in He) was measured by STEM-EDX on a FEI cubed Cs-corrected Titan instrument operating at 300 kV. The reduced samples after passivation were dispersed in ethanol by ultrasonication and then deposited on a holey Au grid.

N$_2$O titration. The exposed metallic copper sites and ceria oxygen vacancies in the reduced catalyst were determined by a combined CO$_2$-N$_2$O titration approach using a plug flow setup equipped with an online mass spectrometer (Balzers TPG 251). The detailed procedures were described in Chapter 2. In brief, the experiments consisted of two N$_2$O pulse titrations at 50 °C after catalyst reduction, the first one with CO$_2$ pulsing before the N$_2$O pulsing and the second one without. CO$_2$ pulsing was applied to block ceria oxygen vacancies in the reduced catalyst so that the metallic copper sites can be measured more accurately.

Temperature programmed hydrogenation (TPH). The catalyst surface modification after methanol synthesis was studied by TPH using the same setup as used for N$_2$O chemisorption. Typically, about 15 mg of used catalyst was loaded into a stainless-steel reactor and sealed by two valves in a glovebox before being transferred to the setup. After flushing with He flow, TPH was performed by ramping the sample to 500 °C at a rate of 10 °C/min in a 10 vol% H$_2$ in He flow (50 mL/min).

X-ray photoelectron spectroscopy (XPS). (i) The interaction between CO$_2$ and reduced Cu/CeO$_2$ catalyst was investigated by in situ XPS using a Kratos AXIS Ultra 600 spectrometer with a monochromatic Al Kα X-ray source (1486.68 eV). A high-temperature cell (Kratos, WX-530) was used to treat the catalyst, which was supported on a stainless-steel stub, allowing

in vacuo sample transfer to the measurement chamber. The sample was reduced in a 50 vol% H$_2$ in Ar flow (50 mL/min) at atmospheric pressure at 300 °C for 3 h Afterwards, the sample was cooled and subsequently transferred to the measurement chamber. Survey scan was recorded at pass energy of 160 eV with step size 0.5 eV, while the region scans were recorded at pass energy of 80 eV with step size 0.1 eV. After measurement, the sample was transferred back to the reaction cell. The CO$_2$ treatment was performed in a 10 vol% CO$_2$ in Ar flow (50 mL/min) at atmospheric pressure at 50 °C for 0.5 h. The same measurement procedure was applied after the CO$_2$ treatment. (ii) The surface of the used catalysts was analyzed using a K-Alpha X-ray Photoelectron Spectrometer (Thermo Scientific) with a monochromatic small-spot X-ray source and an 180˚ double focusing hemispherical analyzer. For sample preparation, the used catalysts were placed on a double-sided carbon tape in a glovebox and then transferred to the spectrometer via an air-tight transfer holder. Spectra were collected using an aluminum anode (Al Kα = 1486.68 eV) operating at 72 W and a spot size of 400 μm. Survey scans were measured at a constant pass energy of 200 eV and region scans at 50 eV. All spectra were analyzed with CasaXPS software and energy calibration was done against C 1s of adventitious carbon with a binding energy at 284.6 eV.

Steady-state isotopic transient kinetic analysis (SSITKA). SSITKA measurements were carried out to study transient behavior upon switches of feed gases. The setup used for these measurements has been described in detail elsewhere.[28] Typically, 500 mg of catalyst diluted with SiC was loaded into a stainless-steel reactor. The sample was pretreated in a 10 vol% H$_2$ in Ar flow (50 mL/min) by heating to 250 °C at a rate of 5°C/min followed by an isothermal dwell of 1 h. The SSITKA measurements were performed in four steps: (i) the reactor was switched to the first reaction mixture (^{12}CO/H$_2$/Ar = 12/36/2 mL/min) whilst gradually increasing the pressure from atmospheric to 2.5 bar, (ii) the reactor was switched to the second reaction mixture (^{12}CO/^{13}CO$_2$/H$_2$/Ne = 10/2/36/2 mL/min), (iii) the reactor was switched to third reaction mixture (^{12}CO/^{12}CO$_2$/H$_2$/Ar = 10/2/36/2 mL/min) and (iv) the reactor was switched to fourth reaction mixture (^{13}CO/^{12}CO$_2$/H$_2$/Ne = 10/2/36/2 mL/min). The signals of ^{12}CO (m/z = 28), ^{13}CO (m/z = 29), ^{12}CO$_2$ (m/z = 44), ^{13}CO$_2$ (m/z = 45), ^{12}CH$_3$OH (m/z = 31), and ^{13}CH$_3$OH (m/z = 33) were recorded by an online mass spectrometry (EES, GeneSys).

Infrared spectroscopy (IR). In situ IR spectra during CO hydrogenation and CO$_2$ cofeeding were measured on a Nicolet FT-IR spectrometer equipped with a cryogenic MCT detector. Self-supporting wafer of catalyst (ca. 15 mg) was prepared and loaded into an infrared cell equipped with CaF$_2$ windows. The wafer was pretreated at 250 °C and 1 bar for 1 h in a 10 vol% H$_2$ in He flow (50 mL/min), followed by exposure to a CO/H$_2$ mixture flow (CO:H$_2$=1:3, 50 mL/min) for 1 h. Afterwards, 1 mL/min of CO$_2$ was added to the flow for another 1 h. A background spectrum (64 scans with a resolution of 4 cm^{-1}) was taken after catalyst pretreatment. Spectra (64 scans with a resolution of 4 cm^{-1}) during the reaction were recorded continuously after exposing the catalyst to the reaction mixture.

2.3 Catalytic activity measurements

CO+CO₂ hydrogenation. The effect of carbon source composition ($CO_2/(CO+CO_2)$) = 0, 0.25, 0.5, 0.75 and 1) on methanol activity of Cu/CeO₂-DP was investigated in a down-flow stainless-steel reactor (internal diameter of 4 mm) at 250 °C and 30 bar. Typically, 100 mg of catalyst (sieve fraction 125-250 μm) was loaded into the reactor and pretreated at 250°C (heating rate 5°C/min) and 1 bar for 1 h in a 10 vol% H_2 in He flow (50 mL/min). Afterwards, the catalyst was exposed to a reaction mixture flow ($CO+CO_2/H_2/N_2$ = 10/30/10 mL/min) and the pressure in the reactor was increased to 30 bar using a back-pressure regulator. The effluent gas mixture was analyzed by an online gas chromatograph (Interscience, CompactGC) equipped with Rtx-1 (FID), Rt-QBond and Molsieve 5A (TCD), and Rt-QBond (TCD) columns. The measurements were taken after ca. 2 h time-on-stream. The methanol formation rate was calculated using the following equation:

$$r(CH_3OH) = \frac{F(CH_3OH)_{out}}{V_m \times m_{cat}} \quad [1]$$

where F stands for the volumetric flow rate calculated based on the nitrogen internal standard using calibrated response factors, and V_m is the molar volume of ideal gas at standard temperature and pressure.

CO₂ co-feeding. The effect of CO_2 on CO-to-methanol activity of Cu/CeO₂-DP was evaluated in the same catalytic setup. For this purpose, about 100 mg of catalyst (sieve fraction 125-250 μm) was loaded into the reactor and pretreated at 250°C (heating rate 5°C/min) and 1 bar for 1 h in a 10 vol% H_2 in He flow (50 mL/min). The pretreated catalyst was then exposed to a reaction mixture flow ($CO/H_2/N_2$ = 10/30/10 mL/min) and the pressure in the reactor was increased to 30 bar using a back-pressure regulator. After reaching steady-state of CO hydrogenation, 1 mL/min of CO_2 was co-fed to the above reaction flow. Catalyst regeneration experiments were also carried out after the CO_2 co-feeding. The regeneration was done at either 250°C, 350°C, or 400°C (heating rate 5°C/min) and 1 bar for 1 h in a 10 % H_2 in He flow (50 mL/min). After each regeneration, the catalyst was tested again for CO hydrogenation. A reference CO_2 co-feeding experiment was performed at 250 °C and 30 bar, during which 1 mL/min of CO_2 was co-fed to a gas flow without CO (H_2/N_2 = 30:20 mL/min). Moreover, the same CO_2 co-feeding to CO hydrogenation were carried out at lower pressures (atmospheric pressure and 3 bar) to examine the pressure effect on the CO_2 co-feeding behavior. The used catalysts after reaction at 30 bar were analyzed via a quasi in situ approach in which the reactor was depressurized at 250 °C, cooled to room temperature in a nitrogen flow, sealed by two valves, transferred to a glovebox for sample storage, and transferred to the respective TPH and XPS setups.

3. Results and discussion

3.1 Characterization

The basic physiochemical properties of the Cu/CeO_2-DP catalyst are listed in **Table B.1**. The actual copper loading of 4.6 wt% is close to the targeted value of 5 wt%. The XRD pattern of the fresh catalyst (**Figure 3.1a**) shows that all the peaks belong to the fluorite structure of CeO_2. No peak assignable to Cu-containing phases were observed, indicating that copper species in the fresh catalyst are either very small crystallites or in an amorphous phase. The reducibility of the copper
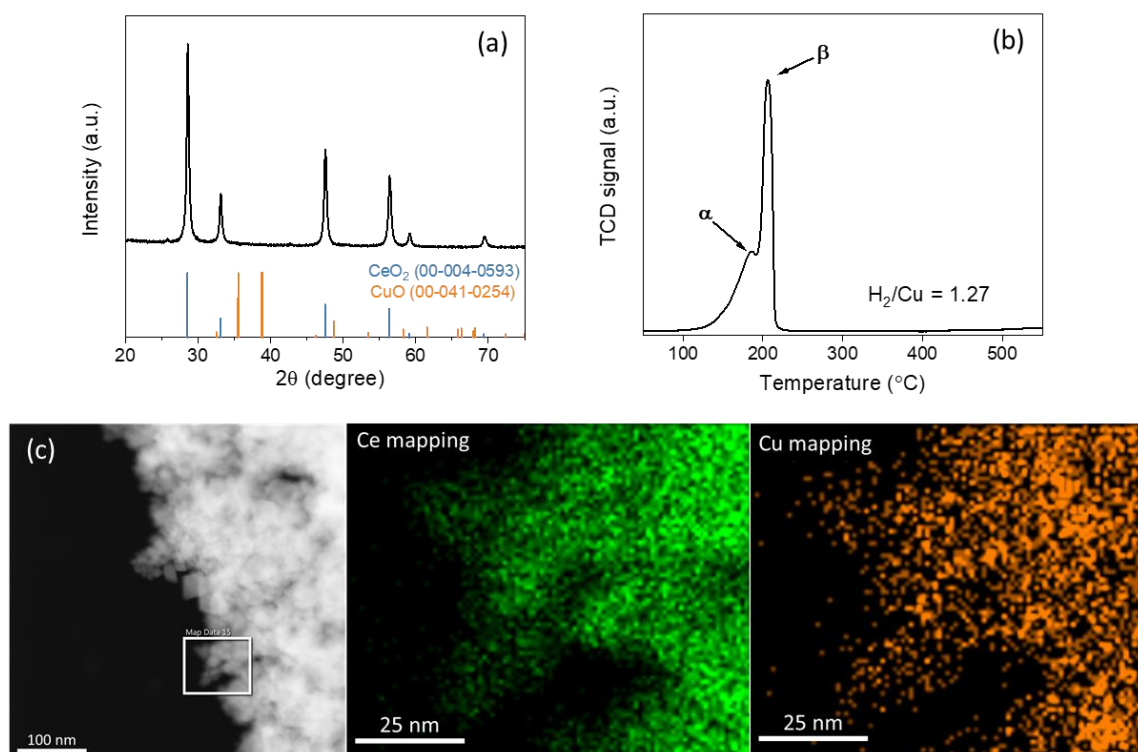

Figure 3.1. (a) XRD pattern and (b) H_2-TPR profile of the fresh Cu/CeO_2-DP catalyst. (c) HAADF-STEM images with corresponding EDX mappings of the reduced Cu/CeO_2-DP catalyst (250 °C, 1 h, in 50 mL/min 10% H_2/He).

species in the catalyst was studied by H_2-TPR (**Figure 3.1b**). The TPR profile consists of two main features (α and β peaks), which can be attributed to CuO_x clusters strongly interacting with ceria and Cu-CeO_2 solid solution.[29,30] It should be noted that the ceria support was also partially reduced during the reduction of copper species, manifested by a higher than unity value of the H_2/Cu molar ratio.

The reduced catalyst was analyzed by N_2O chemisorption to determine the amount of metallic copper sites and ceria oxygen vacancies (**Table B.1**). The specific metallic copper surface area is 12.9 m^2/g_{cat}, which represents about 30% of the total catalyst surface (44.7 m^2/g_{cat})

determined by N_2 physisorption. The N_2O chemisorption results indicate a very high copper dispersion of 43.3 % for the reduced Cu/CeO_2-DP. The reduced catalyst was also investigated by HAADF-STEM and the elemental distribution mapping results (**Figure 3.1c**) confirmed the high copper dispersion determined by N_2O chemisorption. To summarize, in agreement with the results in Chapter 2, both the fresh and reduced Cu/CeO_2-DP materials contain highly dispersed copper species strongly interacting with the ceria support.

3.2 Catalytic activity measurements

We first investigated the effect of carbon source composition on the methanol formation rate over Cu/CeO_2-DP at 30 bar (**Figure 3.2a**, blue curve). The highest methanol rate was achieved using only CO as the carbon source. When 25 mol% CO in the carbon source was replaced by CO_2, the methanol formation rate decreased about 70 % and remained constant upon further increase of the CO_2 fraction in the feed. We then carried out a transient CO_2 co-feeding experiment at the same conditions (**Figure 3.2b**). The reaction was started in a CO/H_2 mixture, resulting in a methanol formation rate that slowly declined from ~12 mmol/($g_{cat} \times$h) to ~11 mmol/($g_{cat} \times$h) in 3.5 h. After that, 2 vol% CO_2 was added to the reactor, which led to a substantial decrease of the methanol formation rate, while CO_2 appeared slightly later in the reactor effluent. The addition of 2 vol% CO_2 represents a $CO/(CO+CO_2)$ ratio of 0.1. Due to the gas phase hold up of the system at 30 bar, the methanol formation rate was seen to decrease with increasing CO_2 effluent concentration. The transient CO_2-cofeeding data is also shown in **Figure 3.2a** (red curve) and emphasizes that the methanol activity was strongly poisoned by a small amount of CO_2 and remains nearly unchanged above a $CO_2/(CO+CO_2)$ ratio of 0.1. This behavior of Cu/CeO_2 contrasts that of conventional $Cu/ZnO/Al_2O_3$, emphasizing different methanol formation pathways and interactions between CO_2 and the active sites for these catalysts.[21,27]
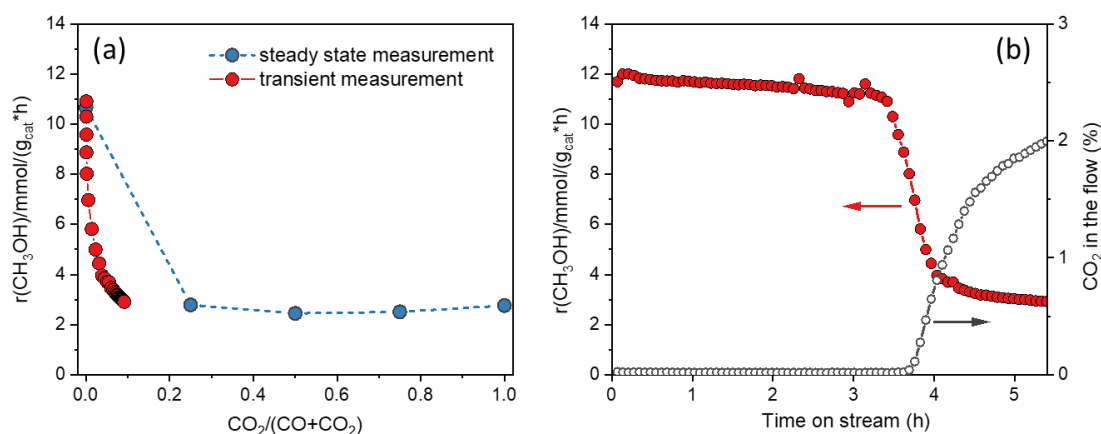

Figure 3.2. (a) Methanol activity as a function of carbon feedstock composition. (b) Time-on-stream methanol activity and CO_2 concertation profiles during CO_2 co-feeding to $CO/H_2/N_2$ stream. Reactions conditions: 250 °C, 30 bar, 100 mg of Cu/CeO_2-DP catalyst and total flow of 50 mL/min.

To understand the CO_2 co-feeding behavior several reference experiments were performed. **Figure 3.3a** shows that addition of CO_2 to a feed of N_2 and H_2 led to an increase of the methanol formation rate to ~2.5 mmol/($g_{cat}×h$), which is close to the methanol formation rate in $CO/CO_2/H_2$ at $CO_2/(CO+CO_2)$ ratios above 0.1 (**Figure 3.2a**). The CO_2 co-feeding experiments to $CO/H_2/N_2$ and H_2/N_2 mixtures are compared in **Figure 3.3b** and point to similar steady-state methanol formation rates. These findings suggest that CO_2 is the dominant carbon source for methanol synthesis when CO and CO_2 are simultaneously fed to the reactor. We also performed the same CO_2-cofeeding to CO/H_2 mixture at 1 bar and 3 bar. As shown in **Figure B.1**, the decrease of steady-state methanol formation rate after CO_2 co-feeding was similar regardless of the pressure, although a transient increase in methanol concentration appeared immediately after co-feeding CO_2, likely related to the replacement of original surface intermediates (e.g. methoxyl) by CO_2.
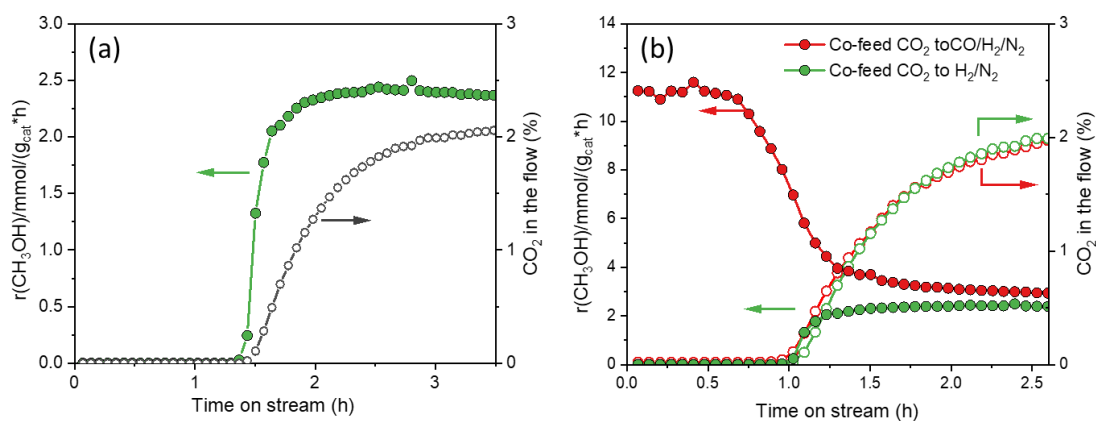
Figure 3.3. (a) Time-on-stream methanol activity and CO_2 concentration profiles during CO_2 co-feeding to the H_2/N_2 stream. (b) Time-on-stream profile comparison between CO_2 co-feeding to $CO/H_2/N_2$ and H_2/N_2 streams. Reaction conditions: 250 °C, 30 bar, 100 mg of Cu/CeO_2 catalyst and total flow of 50 mL/min.
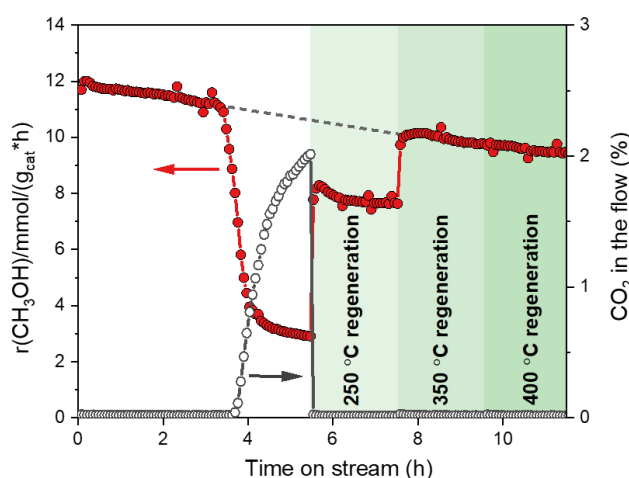

Figure 3.4. Time-on-stream methanol activity and CO_2 concentration profiles during CO_2 cofeeding at 30 bar and following catalyst regeneration experiments.

49

Catalyst regeneration by hydrogenation was also studied after CO_2-cofeeding at 30 bar. For this purpose, the catalyst was regenerated at increasing hydrogenation temperature (250 °C, 350 °C and 400 °C) followed by an activity evaluation for CO hydrogenation after each regeneration. **Figure 3.4** shows that (i) significant part of methanol activity was recovered after regeneration at 250 °C compared to the activity before CO_2-cofeeding, (ii) the methanol activity was fully recovered after regeneration at 350 °C with respect to the slow catalyst deactivation in CO hydrogenation (dash line) and (iii) no further improvement in methanol activity was observed after regeneration at 400 °C.

3.3 SSITKA

We performed isotopic CO_2 co-feeding experiments in a SSITKA setup to determine the carbon source for methanol synthesis. The experiment consisted of three steps during which the carbon source was changed sequentially: $^{12}CO \rightarrow {}^{12}CO + {}^{13}CO_2 \rightarrow {}^{12}CO + {}^{12}CO_2 \rightarrow {}^{13}CO + {}^{12}CO_2$. The isotopic distribution in CO, CO_2 and CH_3OH after the first and third switches (^{12}CO + $^{13}CO_2$ and ^{13}CO + $^{12}CO_2$) were estimated from the corresponding MS signal (**Figure B.5-6**). Notably, the presence of both labelled and non-labelled species in CO or CO_2 after reaction is due to partial oxygen isotopic scrambling under the reaction conditions.[31] **Figure 3.5** shows that the carbon isotope distributions in CH_3OH correlated strongly to the distribution in CO_2 but not to the distribution in CO. Thus, we can conclude that in the presence of CO_2 methanol synthesis from CO is inhibited and CO_2 becomes the dominant carbon source.

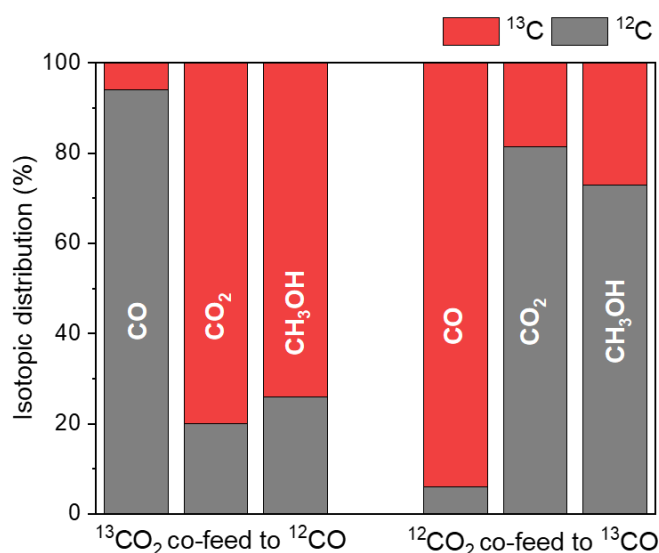**Figure 3.5.** Isotopic distribution in carbon sources (CO and CO_2) and methanol during isotopic CO_2-cofeeding. Conditions: 250 °C, 2.5 bar and $CO_2/(CO+CO_2)=1/6$.

3.4 In situ IR spectroscopy

We employed in situ IR spectroscopy to gain insights into how co-feeding CO_2 affects CO hydrogenation to methanol. IR spectra during CO hydrogenation without and with CO_2 are

shown in **Figure B.7** and indicate the presence of different surface species. The influence of CO_2 co-feeding on the time-resolved evolution of these surface species becomes clear from the difference spectra after co-feeding CO_2 to CO hydrogenation (**Figure 3.6**). In the C-O vibrational region (**Figure 3.6a**), three broad bands (1533 cm^{-1}, 1475 cm^{-1} and 1403 cm^{-1}) developed when CO_2 was added to the feed, pointing to the formation of carbonate-like species.[32–34] The presence of these species was also indicated by quasi in situ analysis (TPH and XPS) of the used catalysts (Figs. S2 and S3). As the catalytic data demonstrates that CO hydrogenation to methanol is inhibited by CO_2, we speculate that these carbonate-like species block the active sites for CO-to-methanol conversion on Cu/CeO$_2$. A similar blocking effect of carbonate-like species has been repeatedly mentioned in the literature.[27,35,36]
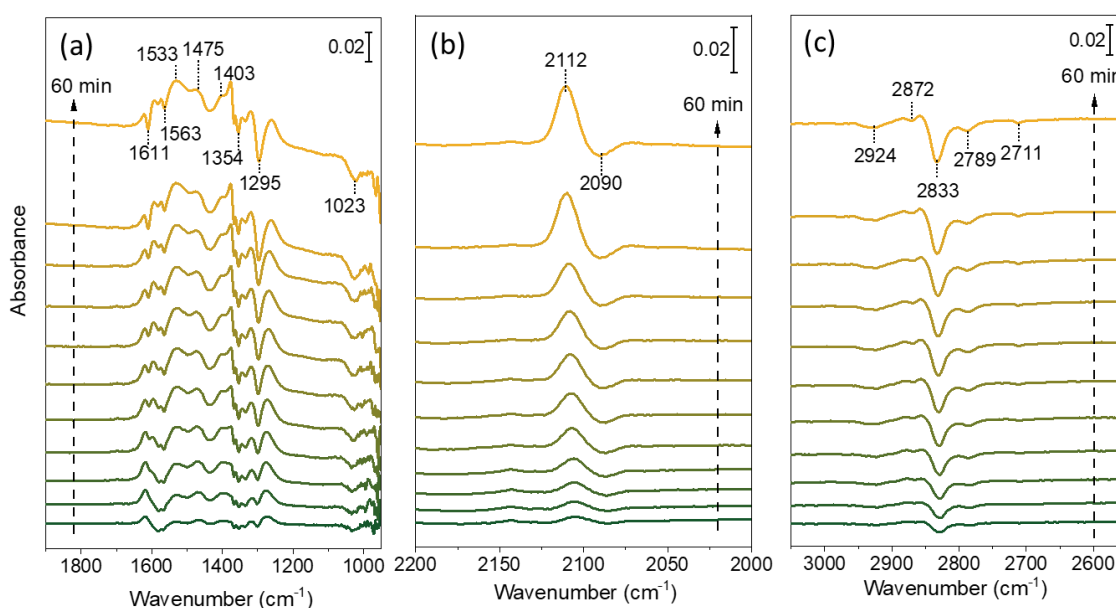

Figure 3.6. IR difference spectra after CO_2 co-feeding to CO/H$_2$ in the regions of (a) 1850-950 cm^{-1} (C-O vibration), (b) 2200-2000 cm^{-1} (carbonyl vibration) and (c) 3050-2550 cm^{-1} (C-H vibration).

Further, two negative features appeared at 2872 cm^{-1} and 2789 cm^{-1}, which can be related to ν(C-H) modes of methoxyl species.[33,37,38] In line with this, a negative feature associated with ν(C-O) of methoxyl species appeared at 1023 cm^{-1}.[33,37,38] Besides the decrease in methoxyl species, we observed the decrease in formyl species as indicated by the negative peak at 2711 cm^{-1} in **Figure 3.6c**.[19,32] A positive peak emerged at 2112 cm^{-1} in the carbonyl region (**Figure 3.6b**), which is due to CO adsorbed on Cu$^+$ at the Cu-CeO$_2$ interface.[34,39] It should be mentioned that the negative peak at 2090 cm^{-1} assignable to CO adsorbed on Cu^0 is most likely caused by the decrease of CO partial pressure in IR cell after CO_2 co-feeding.[34,39] To summarize, after co-feeding CO_2 to CO/H$_2$, we observed that (i) the concentration of methoxyl and formyl species decreased likely because of competitive adsorption of CO_2 to form carbonate-like species and (ii) the concentration of CO species adsorbed on interfacial Cu$^+$ increased. Given that hydrogenation of CO to methanol is inhibited by CO_2, the decrease in methoxyl and formyl

species and the increase in CO adsorbed on interfacial Cu^+ indicates that methanol synthesis from CO over Cu/CeO_2 follows a direct hydrogenation mechanism via formyl intermediate ($CO^* \rightarrow CHO^* \rightarrow CH_3O^*$). This mechanism of CO-to-methanol conversion over Cu/CeO_2 has been proposed in literature.[14,27,40] After adding CO_2 to the feed, we also observed the disappearance of monodentate formate (ν_{as}(O-C-O): 1611 cm^{-1}, ν_s(O-C-O): 1295 cm^{-1}, ν(C-H): 2833 cm^{-1} and δ(C-H)+ν_{as}(O-C-O): 2924 cm^{-1}) and bidentate formate (ν_{as}(O-C-O): 1563 cm^{-1}, ν_s(O-C-O): 1354 cm^{-1}, ν(C-H): 2833 cm^{-1} and δ(C-H)+ν_{as}(O-C-O): 2924 cm^{-1}) species in the IR spectra.[19,33,41–44] These species are formed due to the reaction of CO with hydroxyl groups of the ceria support,[41,43] as manifested by the two negative bands at 3652 cm^{-1} and 3548 cm^{-1} in the O-H vibrational region during CO hydrogenation (**Figure B.7a**). Thus, these formate species are most likely spectators during the reaction.[27,45]

3.5 Discussion

Scheme 3.1 summarizes the main mechanistic findings of our work. There are two pathways for CH_3OH synthesis over Cu/CeO_2: a direct CO_2 hydrogenation pathway and a pathway involving a CO intermediate. The direct CO_2 hydrogenation pathway occurs on copper and follows the known structure sensitivity requirements of CH_3OH synthesis, therefore requiring larger Cu particles (>5 nm) for optimum performance.[46] The CO pathway involves the Cu-CeO_2 interface, where CO can be directly hydrogenated to methanol via a formyl intermediate. Our results show that CH_3OH synthesis over Cu/CeO_2 proceeds much faster via the CO pathway than the direct CO_2 pathway under industrially relevant conditions. We also observed that co-feeding a small amount of CO_2 poisons the Cu-CeO_2 interfacial sites for CO hydrogenation. Methanol synthesis then proceeds predominantly via CO_2 hydrogenation on the metallic copper surface. Mechanistic studies indicate that the CO pathway is inhibited by carbonate-like species formed by CO_2 adsorption at the Cu-CeO_2 interface. Similar poisoning
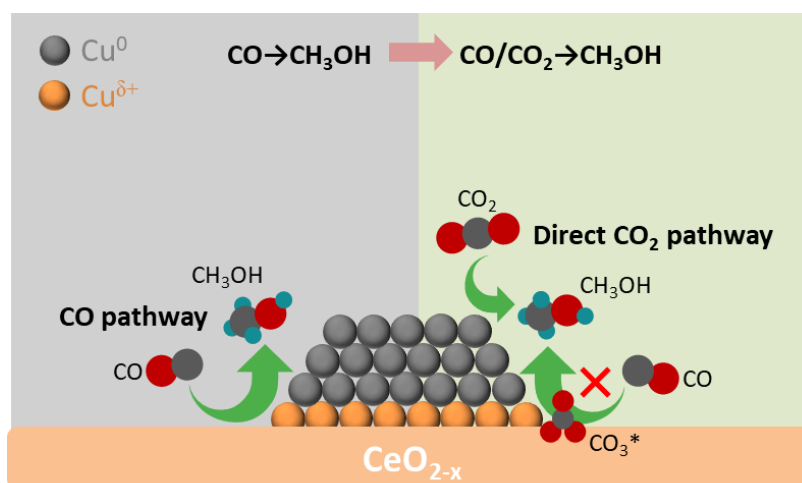
Scheme 3.1. Proposed mechanism of methanol synthesis from CO/CO_2 over Cu/CeO_2.

effect by carbonate-like species has been reported earlier.[34,7] Furthermore, methanol synthesis from CO$_2$ is not influenced by the CO$_2$ content of the feed mixture under the investigated conditions (Figure 5a), i.e., the reaction order of methanol synthesis with respect to CO$_2$ is zero. This observation demonstrates that CO$_2$ interacts strongly with the copper surface in Cu/CeO$_2$, which is also demonstrated by the theoretical calculations reported in **Chapter 2**. We also observed that the reverse water-gas shift (rWGS) reaction is inhibited due to strong Cu-CeO$_2$ interactions, resulting in a higher CH$_3$OH selectivity of Cu/CeO$_2$ catalysts than that of a reference Cu/SiO$_2$ catalyst. Our results indicate that the inhibition of rWGS could be related to a high coverage of formate species on the copper surface, which block the active sites required for the rWGS reaction.

4. Conclusions

We investigated how the carbon feedstock (CO or CO$_2$) influences methanol synthesis over Cu/CeO$_2$ in the presence of H$_2$. Adding CO$_2$ to synthesis gas (CO/H$_2$) over Cu/CeO$_2$ catalyst can not lead to promotion but to poisoning in methanol activity in contrast to traditional Cu/ZnO/Al$_2$O$_3$ catalyst. The CO$_2$ poisoning was investigated in more detail by transient CO$_2$ co-feeding experiments and (quasi) in situ characterization. Compared to direct methanol synthesis from CO$_2$ on metallic Cu sites in **Chapter 2**, CO-to-methanol conversion proceeds faster at Cu-CeO$_2$ interface via CO hydrogenation through a formyl intermediate. CO$_2$ poisons these interface sites active for CO conversion by forming carbonate-like surface species. In general, the current study highlights the importance of studying the dynamic interactions between copper-based methanol synthesis catalysts and carbon feedstock (CO/CO$_2$) under reaction conditions.

References

1   CH_3OH production and demand, https://www.methanol.org/methanol-price-supply-demand.

2   J. Sehested, *J. Catal.*, 2019, **371**, 368–375.

3   A. Goeppert, M. Czaun, J.-P. Jones, G. K. Surya Prakash and G. A. Olah, *Chem.Soc.Rev.*, 2014, **43**, 7995–8048.

4   G. A. Olah, *Angew. Chem. Int. Ed.*, 2005, **44**, 2636–2639.

5   Malte Behrens, Felix Studt, Igor Kasatkin, Stefanie Kühl, Michael Hävecker, Frank Abild-Pedersen, Stefan Zander, Frank Girgsdies, Patrick Kurr, Benjamin-Louis Kniep, Michael Tovar, Richard W. Fischer, Jens K. Nørskov and Robert Schlög, *Science.*, 2012, **336**, 893–897.

6   M. Behrens, *Angew. Chem. Int. Ed.*, 2016, **55**, 14906–14908.

7   B. Liang, J. Ma, X. Su, C. Yang, H. Duan, H. Zhou, S. Deng, L. Li and Y. Huang, *Ind. Eng. Chem. Res.*, 2019, **58**, 9030–9037.

8   M. S. Jingang Wu Masami Takeuchi Taiki Watanabe, *Appl. Catal. A Gen.*, 2001, **218**, 235–240.

9   A. Prašnikar, A. Pavlišič, F. Ruiz-Zepeda, J. Kovač and B. Likozar, *Ind. Eng. Chem. Res.*, 2019, **58**, 13021–13029.

10   R. M. Nix, T. Rayment, R. M. Lambert, J. R. Jennings and G. Owen, *J. Catal.*, 1987, **106**, 216–234.

11   M. E. Fakley, J. R. Jennings and M. S. Spencer, *J. Catal.*, 1989, **118**, 483–486.

12   W. J. Shen, Y. Ichihashi and Y. Matsumura, *Catal. Letters*, 2002, **83**, 33–35.

13   W.-J. Shen, Y. Ichihashi and Y. Matsumura, *Appl. Catal. A Gen.*, 2005, **282**, 221–226.

14   J. A. R. Jesús Graciani, Kumudu Mudiyanselage, Fang Xu, Ashleigh E. Baber, Jaime Evans, Sanjaya D. Senanayake, Darío J. Stacchiola, Ping Liu, Jan Hrbek, Javier Fernández Sanz, *Science.*, 2014, **345**, 546–550.

15   B. Ouyang, W. Tan and B. Liu, *Catal. Commun.*, 2017, **95**, 36–39.

16   K. Chang, T. Wang and J. G. Chen, *Appl. Catal. B Environ.*, 2017, **206**, 704–711.

17   W. Wang, Z. Qu, L. Song and Q. Fu, *J. Energy Chem.*, 2020, **40**, 22–30.

18   S. Li, L. Guo and T. Ishihara, *Catal. Today*, 2020, **339**, 352–361.

19   P. Sripada, J. Kimpton, A. Barlow, T. Williams, S. Kandasamy and S. Bhattacharya, *J. Catal.*, 2020, **381**, 415–426.

20   O. Martin, C. Mondelli, A. Cervellino, D. Ferri, D. Curulla-Ferré and J. Pérez-Ramírez, *Angew. Chem. Int. Ed.*, 2016, **55**, 11031–11036.

21   O. Martin and J. Pérez-Ramírez, *Catal. Sci. Technol.*, 2013, **3**, 3343–3352.

22   J. S. Lee, K. H. Lee, S. Y. Lee and Y. G. Kim, *J. Catal.*, 1993, **144**, 414–424.

23   G. C. Chinchen, P. J. Denny, D. G. Parker, M. S. Spencer and D. A. Whan, *Appl. Catal.*, 1987, **30**, 333–338.

24   K. Klier, V. Chatikavanij, R. G. Herman and G. W. Simmons, *J. Catal.*, 1982, **74**, 343–360.

25   K. Wiese, A. M. Abdel-Mageed, A. Klyushin and R. J. Behm, *Catal. Today*, 2018, **336**, 193–202.

26   A. M. Abdel-Mageed, A. Klyushin, A. Knop-Gericke, R. Schlögl and R. J. Behm, *J. Phys. Chem. Lett.*, 2019, **10**, 3645–3653.

27   L. G. A. van de Water, S. K. Wilkinson, R. A. P. Smith and M. J. Watson, *J. Catal.*, 2018, **364**,

57–68.

28   W. Chen, R. Pestman, B. Zijlstra, I. A. W. Filot and E. J. M. Hensen, *ACS Catal.*, 2017, **7**, 8050–8060.

29   W. W. Wang, P. P. Du, S. H. Zou, H. Y. He, R. X. Wang, Z. Jin, S. Shi, Y. Y. Huang, R. Si, Q. S. Song, C. J. Jia and C. H. Yan, *ACS Catal.*, 2015, **5**, 2088–2099.

30   W.-W. Wang, W.-Z. Yu, P.-P. Du, H. Xu, Z. Jin, R. Si, C. Ma, S. Shi, C.-J. Jia and C.-H. Yan, *ACS Catal.*, 2017, **7**, 1313–1329.

31   Y. Madier, C. Descorme, A. M. Le Govic and D. Duprez, *J. Phys. Chem. B*, 1999, **103**, 10999–11006.

32   C. Li, Y. Sakata, T. Arai, K. Domen, K. Maruya and T. Onishi, *J. Chem. Soc., Faraday Trans.*, 1989, **85**, 929–943.

33   C. Binet, M. Daturi and J.-C. Lavalley, *Catal. Today*, 1999, **50**, 207–225.

34   P. Bera, A. Lo, A. Horne and A. Martı, *J. Phys. Chem. C*, 2009, **113**, 10689–10695.

35   A. Rezvani, A. M. Abdel-mageed, T. Ishida, M. Parlinska-wojtan and R. J. Behm, *ACS Catal.*, 2020, **10**, 3580–3594.

36   J. Saavedra, C. Powell, B. Panthi, C. J. Pursell and B. D. Chandler, *J. Catal.*, 2013, **307**, 37–47.

37   A. Badri, C. Binet and J. C. Lavalley, *J. Chem. Soc. - Faraday Trans.*, 1997, **93**, 1159–1168.

38   C. Yang, F. Bebensee, A. Nefedov, C. Wöll, T. Kropp, L. Komissarov, C. Penschke, R. Moerer, J. Paier and J. Sauer, *J. Catal.*, 2016, **336**, 116–125.

39   A. Chen, X. Yu, Y. Zhou, S. Miao, Y. Li, S. Kuld, J. Sehested, J. Liu, T. Aoki, S. Hong, M. F. Camellone, S. Fabris, J. Ning, C. Jin, C. Yang, A. Nefedov, C. Wöll, Y. Wang and W. Shen, *Nat. Catal.*, 2019, **2**, 334–341.

40   Z. J. Zuo, P. De Han, Z. Li, J. S. Hu and W. Huang, *Appl. Surf. Sci.*, 2012, **261**, 640–646.

41   C. Li, Y. Sakata, T. Arai, K. Domen, K. I. Maruya and T. Onishi, *J. Chem. Soc. Faraday Trans. 1 Phys. Chem. Condens. Phases*, 1989, **85**, 1451–1461.

42   C. Li, K. Domen, K. ichi Maruya and T. Onishi, *J. Catal.*, 1990, **125**, 445–455.

43   P. G. Lustemberg, M. V. Bosco, A. Bonivardi, H. F. Busnengo and M. V. Ganduglia-Pirovano, *J. Phys. Chem. C*, 2015, **119**, 21452–21464.

44   M. S. Duyar, C. Tsai, J. L. Snider, J. A. Singh, A. Gallo, J. S. Yoo, A. J. Medford, F. Abild-Pedersen, F. Studt, J. Kibsgaard, S. F. Bent, J. K. Nørskov and T. F. Jaramillo, *Angew. Chem. Int. Ed.*, 2018, **57**, 15045–15050.

45   A. Goguet, F. C. Meunier, D. Tibiletti, J. P. Breen and R. Burch, *J. Phys. Chem. B*, 2004, **108**, 20240–20246.

46   A. Karelovic, G. Galdames, J. C. Medina, C. Yévenes and Y. Barra, *J. Catal.*, 2019, **369**, 415–426.

Appendix B

Catalyst characterization

Figure B.1a shows that a large decrease in Ce^{3+} contribution (from 27% to 11%) was observed after treating the reduced Cu/CeO_2-DP with CO_2. This observation demonstrates that the surface ceria oxygen vacancies can be readily healed upon CO_2 interacting with reduced CeO_2 surface. We consider that the remaining Ce_{3+} signal comes from the subsurface layers and the corresponding species therefore cannot be oxidized by CO_2. The interaction between CO_2 and Cu surface was studied by comparing the Cu 2p and Cu LMM Auger spectra. The peak position and width remained unchanged and no satellite peak was observed in the Cu 2p spectra after the CO2 treatment **(Figure B.1b)**, pointing to the absence of Cu^{2+}. Furthermore, Cu^0 (918.6 eV) and Cu^+ (916.3 eV) contributions were observed in the Cu Auger spectra as shown in **Figure B.1c**.[1] Analysis of the Auger spectra suggests that metallic Cu remained the dominant contribution after the CO_2 treatment (from 79% to 74%), indicative that Cu surface is barely influenced by CO_2. Thus, we conclude that CO_2 treatment can selectively oxidize the CeO_{2-x} surface, while not significantly affecting the metallic Cu surface.
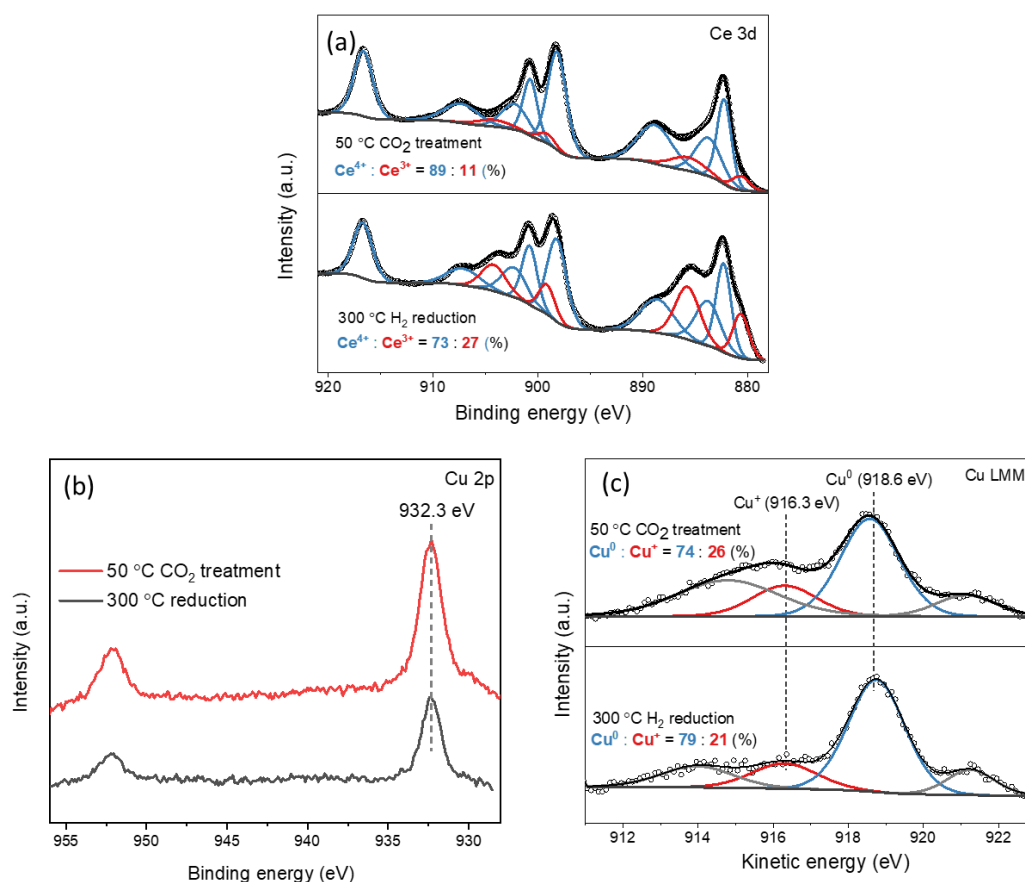

Figure B.1. In situ XP spectra of the reduced and CO_2-treated Cu/CeO_2-DP catalysts

Table B.1. Basic physicochemical properties of the Cu/CeO_2-DP catalyst.

Copper loading (wt%)	4.6
S_{BET} (m^2/g_{cat})	44.7
$D_{cu(0)}$ (%)	43.3
$N_{Cu(0)}$ ($\mu mol/g_{cat}$)	313
$S_{Cu(0)}$ (m^2/g_{cat})	12.9
N_{Ov} ($\mu mol/g_{cat}$)	44

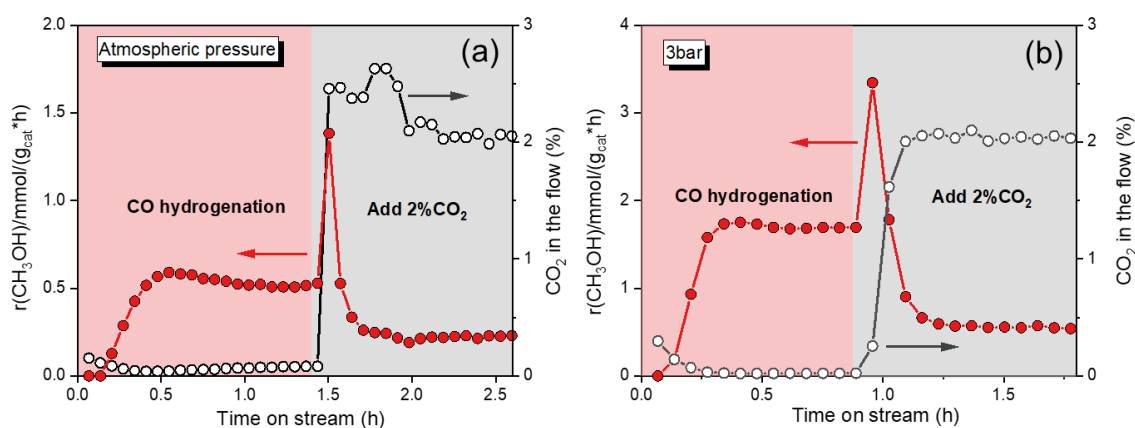## CO_2-cofeeding activity measurements

Figure B.2. Time-on-stream methanol activity and CO_2 concentration profiles during CO_2 cofeeding to $CO/H_2/N_2$ stream at (a) atmospheric pressure and (b) 3 bar. Reaction conditions: 250 °C, 100 mg of Cu/CeO_2 catalyst and total flow of 50 mL/min

Used catalysts analysis

We used TPH and XPS to analyze the catalyst surface after reaction via a quasi in situ approach using a glovebox, *i.e.,* no air exposure between catalytic reaction and sample analysis. Three samples after catalytic reaction at 30 bar (CO hydrogenation, CO_2 cofeeding and CO_2 hydrogenation) together with a reduced sample were selected for these studies. The TPH results (**Figure B.3b-c**) showed that there were significantly more CO (*m/z = 28*) and CO_2 (*m/z = 44*) produced from the catalyst after CO_2 hydrogenation compared to other catalysts. This observation suggests that strongly bonded oxygen-containing surface species (e.g., carbonates) can be formed due to the interaction between CO_2 and catalyst surface under the reaction conditions.

The existence of such surface species was further confirmed by XPS measurements. Compared to other catalysts, the catalyst after CO_2 hydrogenation showed much stronger signal of oxygen- containing surface species in the C 1s spectrum and a stronger contribution of carbonates in O 1s spectrum (**Figure B.4a-b**). Furthermore, the surface Cu and Ce oxidation

states of the used catalysts were studied by XPS (**Figure B.4c-d**). Surprisingly, we found that
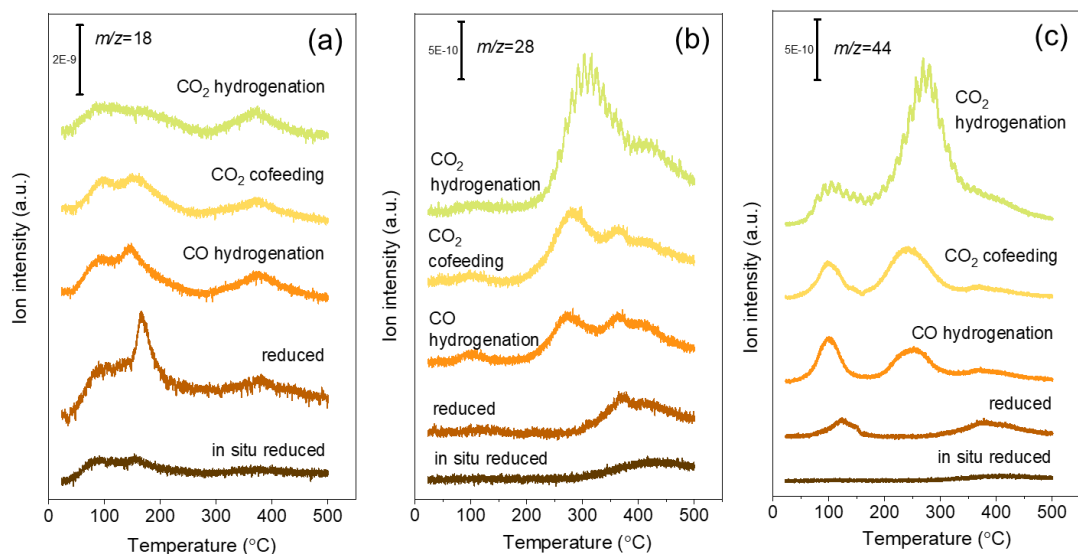

Figure B.3. Quasi in situ TPH profiles of the used Cu/CeO_2-DP catalysts.
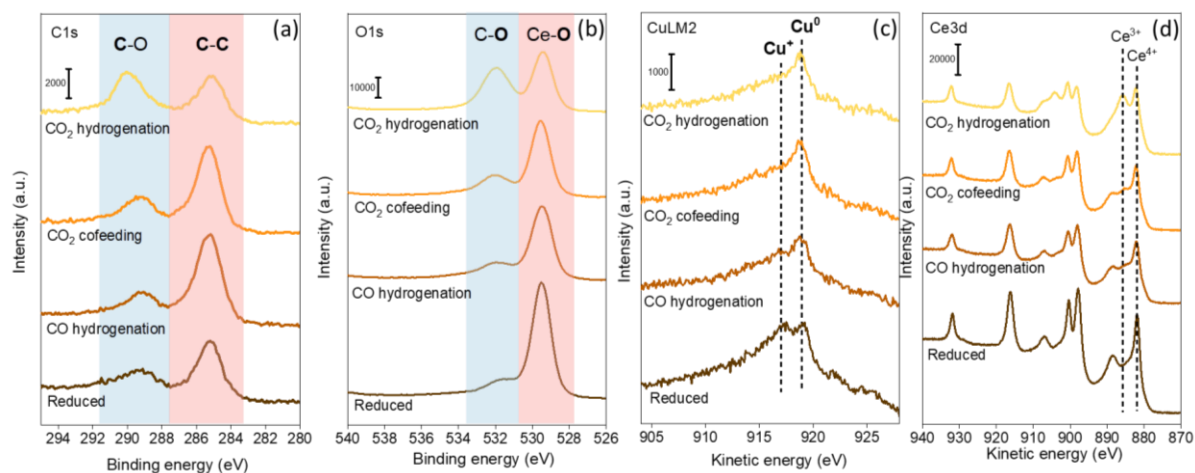
Figure B.4. Quasi in situ XP spectra of the used Cu/CeO_2-DP catalysts.

the reduced catalyst was significantly oxidized while the catalyst after CO_2 hydrogenation was kept highly reduced. The oxidation of the reduced catalyst suggests that quasi in situ approach cannot completely prevent the oxidation of highly oxophilic Cu/CeO_2 catalyst: significant oxidation of Cu/CeO_2 catalyst occurred during the sample storage and/or sample transfer. The oxidation of the reduced catalyst was further confirmed by the H_2O signal (*m/z = 18*) during the TPH (**Figure B.3a**) – much higher amount of water was produced from the reduced catalyst compared to the in situ reduced sample at the setup. Following that, we suggest that the highly reduced state of the catalyst after CO_2 hydrogenation is associated with the presence of large amounts of strongly bonded surface species (e.g., carbonates), covering the catalyst surface and preventing it from oxidation. Specifically, these surface species act as a protection layer for Cu/CeO_2 preventing its oxidation by external oxygen. In summary, the characterization of

used catalysts demonstrates that strongly bonded surface species (e.g., carbonates) are easily produced from CO_2 under the reaction conditions and in situ characterization techniques are necessary to study the Cu/CeO_2 system to prevent external catalyst oxidation.

SSITKA measurements

Blank switches at room temperature (**Figure B.5**) show that $^{12}CH_3OH$ signal ($m/z = 31$) was influenced by isotopic switch but $^{13}CH_3OH$ signal ($m/z = 33$) not. Thus, $^{13}CH_3OH$ signal ($m/z = 33$) was selected for quantitative analysis.
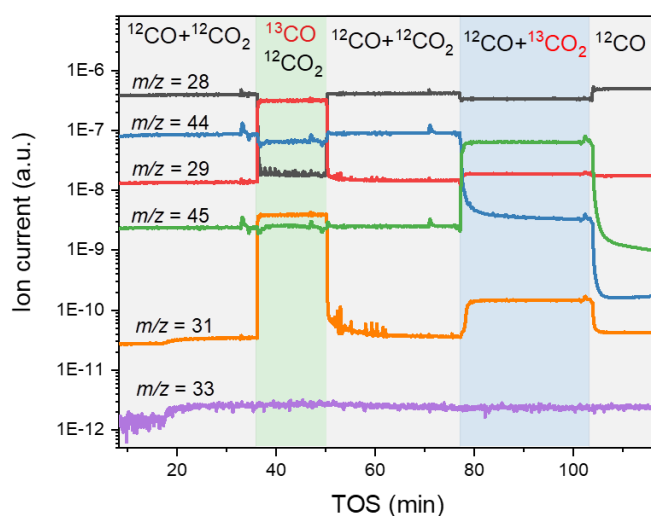

Figure B.5. Time-on-stream behavior of carbon source (CO/CO_2) MS signals during SSITKA switches at room temperature.
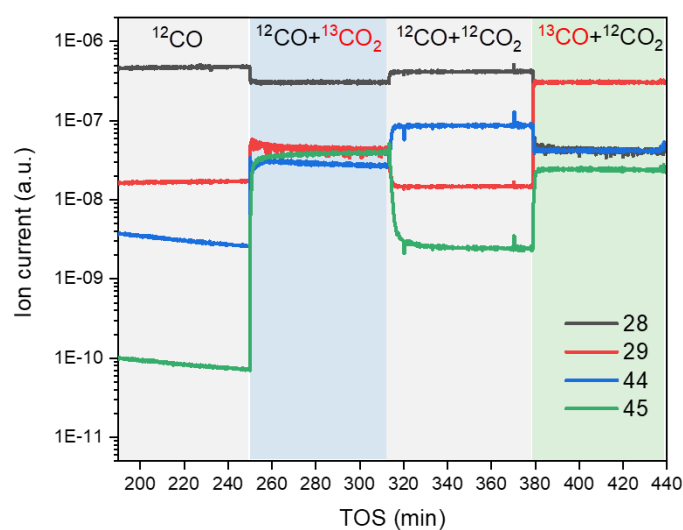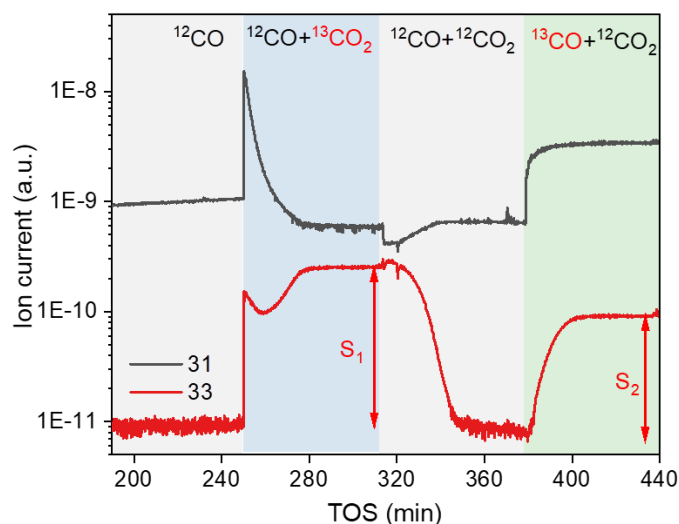

Figure B.6. Time-on-stream behavior of carbon source (CO/CO_2) MS signals during SSITKA switches at 250 °C.

Table B.2. Carbon source isotopic composition estimated from MS signal.

^{12}C and ^{13}C in CO or CO_2	$^{12}CO + ^{13}CO_2$ flow		$^{13}CO + ^{12}CO_2$ flow	
	Outlet	Average	Outlet	Average
$^{12}CO/(^{12}CO+^{13}CO)$	88	94	12	6
$^{13}CO/(^{12}CO+^{13}CO)$	12	6	88	94
$^{12}CO_2/(^{12}CO_2+^{13}CO_2)$	40	20	64	82
$^{13}CO_2/(^{12}CO_2+^{13}CO_2)$	60	80	36	18

Figure B.7. Time-on-stream behavior of methanol MS signals during SSITKA switches at 250 °C.

The MS signals of CO and CO_2 during the SSITKA measurements are shown in **Figure B.6**. The ^{13}C and ^{12}C fractions in CO or CO_2 after the first and third switches were estimated based on the MS data (**Table B.2**). We observed that there were considerable amounts of ^{13}CO and $^{12}CO_2$ detected after reaction during the $^{12}CO + ^{13}CO_2$ flowing. Similarly, ^{12}CO and $^{13}CO_2$ were detected after switching to the $^{13}CO + ^{12}CO_2$ flowing. These observations suggest that some oxygen isotope scrambling took place under the reaction conditions.[2] Moreover, the significant difference between the ^{13}C/^{12}C ratio in CO and in CO_2 of these two cases indicates that the isotope scrambling is still far away from equilibrium. As there is no isotope scrambling before the reaction, we calculated the average ^{13}C and ^{12}C fractions in CO or CO_2 based on the outlet values (**Table B.2**).

Table B.2 shows that, after the first switch ($^{12}CO \rightarrow ^{12}CO + ^{13}CO_2$) and third switch ($^{12}CO + ^{12}CO_2 \rightarrow ^{13}CO + ^{12}CO_2$), the ^{13}C/^{12}C signal ratios of CO (12/88 vs 88/12) and of CO_2 (60/40 vs. 36/64) were almost reciprocal. Added to that, the methanol formation rate was monitored by simultaneous CG analysis and it was similar during the whole SSITKA measurement. Based on these observations, we can deduce that the ^{13}C/^{12}C signal ratio of methanol should also be almost reciprocal after these two switches. After knowing that, the ^{13}C fraction in methanol can be calculated only using the $^{13}CH_3OH$ signal (S_1 and S_2) in **Figure B.7**. The corresponding

formulas of ^{13}C fraction in methanol after the first and third switches are $S_1/(S_1+S_2)$ and $S_2/(S_1+S_2)$, respectively.
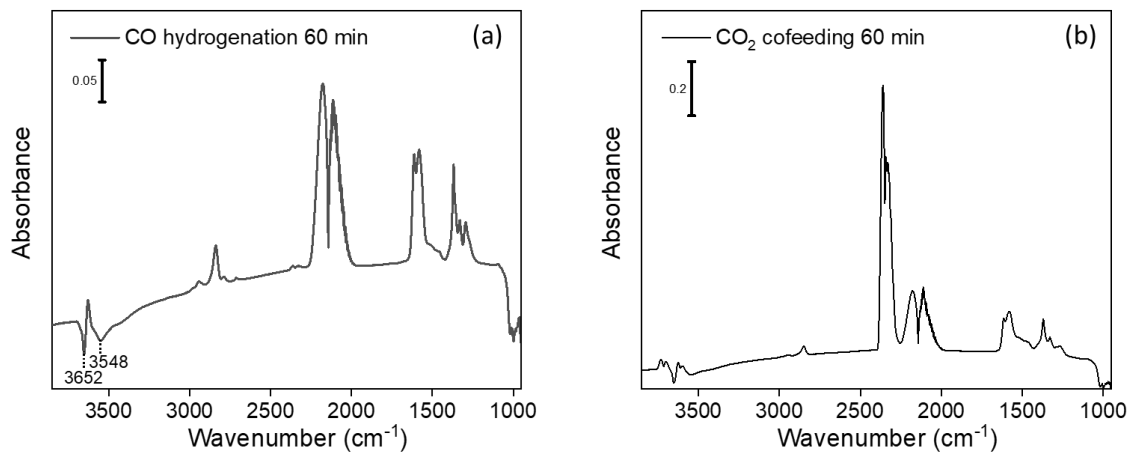
In situ IR data

Figure B.8. In situ steady-state IR spectra during CO hydrogenation and CO_2 cofeeding experiments.

References

1   J. P. Espinós, J. Morales, A. Barranco, A. Caballero, J. P. Holgado and A. R. González-Elipe, *J. Phys. Chem. B*, 2002, **106**, 6921–6929.

2   Y. Madier, C. Descorme, A. M. Le Govic and D. Duprez, *J. Phys. Chem. B*, 1999, **103**, 10999–11006.

CHAPTER 4

Flame Synthesis of Cu/ZnO-CeO$_2$ Catalysts: CeO$_2$ Promotes Methanol Selectivity of Cu/ZnO in CO$_2$ Hydrogenation

ABSTRACT

The hydrogenation of CO$_2$ to CH$_3$OH is an important reaction for future renewable energy scenarios. We investigated Cu/ZnO, Cu/CeO$_2$ and Cu/ZnO-CeO$_2$ catalysts obtained in a single preparation step through flame spray pyrolysis (FSP). For the ternary oxide catalysts, the Cu and CeO$_2$ contents were varied independently. Extensive characterization shows that CeO$_2$ promotes Cu dispersion in comparison to ZnO owing to strong Cu-CeO$_2$ interactions. Regarding CH$_3$OH synthesis from CO$_2$ hydrogenation, Cu/ZnO-CeO$_2$ catalysts displayed a substantially higher CH$_3$OH selectivity as compared to Cu/ZnO and a commercial methanol synthesis catalyst. Structure-sensitivity analysis based on turnover frequencies indicate that the improved CH$_3$OH selectivity is a consequence of synergistic interactions between Cu, CeO$_2$ and ZnO: Cu-ZnO interactions promote CH$_3$OH synthesis, while Cu-CeO$_2$ interactions inhibit the reverse water-gas shift (rWGS) reaction.

1. Introduction

Methanol is currently an important commodity in the chemical industry and it is expected to play a central role as a platform chemical for the production of energy carriers and chemicals in the transition towards a sustainable economy.[1] Modern industrial methanol production is based on the conversion of synthesis gas using $Cu/ZnO/Al_2O_3$ catalysts operated at elevated temperature (200 – 300 °C) and pressure (50 – 100 bar).[2] Catalytic conversion of CO_2 to methanol ($CO_2 + 3H_2 \rightarrow CH_3OH + H_2O$) using green hydrogen generated from sustainable energy sources has recently attracted significant attention.[3,4] This approach allows the reuse of the greenhouse gas CO_2 for the production of fuels and chemicals using methanol as a platform.[4,5] Although $Cu/ZnO/Al_2O_3$ catalysts are active for CO_2 hydrogenation to CH_3OH , there are several problems with respect to its practical implementation for this purpose. A major drawback lies in the high reverse water-gas shift (rWGS, $CO_2 + H_2 \rightarrow CO + H_2O$) activity of $Cu/ZnO/Al_2O_3$ catalysts. The WGS reaction ($CO + H_2O \rightarrow CO_2 + H_2$) is important for methanol synthesis from synthesis gas, because the main reaction pathway involves direct hydrogenation of CO_2 over these catalysts.[6–8] However, a high rWGS activity of the catalyst is undesirable for CO_2 hydrogenation to CH_3OH, because it produces a larger amount of CO as by-product, decreasing CH_3OH selectivity and H_2 utilization efficiency.[8] The formation of water by-product during hydrogenation of CO_2 in comparison to hydrogenation of CO poses a challenge to catalyst stability, because water accelerates the deactivation of the $Cu/ZnO/Al_2O_3$ catalyst.[9–12]

A strategy to improve Cu-ZnO-based catalysts for CO_2-to-CH_3OH conversion is the replacement of Al_2O_3 by other supports. ZrO_2 for instance has been widely investigated in this respect.[13–16] CeO_2 has also been studied although to a lesser extent. CeO_2 is more basic and less hydrophilic than Al_2O_3, which can be beneficial for CH_3OH productivity and catalyst stability, respectively.[17,18] CeO_2 interacts strongly with Cu, which may improve the dispersion and resistance against sintering of Cu particles.[19] While Cu/CeO_2 is known for its high activity in CO-to-CH_3OH conversion,[20,21] a recent study showed that it is also promising for CO_2-to-CH_3OH conversion.[22] The influence of CeO_2 addition to Cu-ZnO-based catalysts has been investigated.[17,23–27]. Bonura et al. used a reverse co-precipitation method under ultrasonic conditions to prepare promoted Cu-based catalysts and found that CeO_2 was a better promoter for CH_3OH formation during CO_2 hydrogenation than ZrO_2.[23] Gao et al. prepared a series of promoted Cu-Zn-Al catalysts from hydrotalcite-like precursors[24] and showed that the copper surface area and the fraction of strongly basic sites increased after ceria addition, resulting in a higher CO_2 conversion and CH_3OH selectivity compared to the unpromoted catalyst. Despite these interesting results, structure-performance relations for Cu-ZnO-CeO_2 catalysts in CO_2 hydrogenation to CH_3OH remain largely unaddressed.

Regarding catalyst preparation, most academic studies have used conventional impregnation methods to load copper on a support.[28,29] However, this method is limited by the relatively low Cu loading that can be achieved.[30] Co-precipitation is another often used method to obtain methanol synthesis catalysts and it is the commercial method to prepare Cu/ZnO/Al$_2$O$_3$ catalysts.[31–33] There are however some disadvantages associated with co-precipitation.[34] First, co-precipitation is time-consuming in comparison to impregnation and cannot be operated in a continuous process. A washing step is required to remove the precipitation agent, which involves the use of a large amount of solvent. An alternative method to prepare catalysts in a single step is flame spray pyrolysis (FSP), which offers advantages in terms of flexibility, speed and scalability.[35–40] In an earlier report, Jensen et al. demonstrated that Cu/ZnO/Al$_2$O$_3$ catalysts with a relatively high specific surface area (> 100 m^2/g$_{cat}$) can be obtained by a flame combustion method.[40] Copéret and co-workers recently prepared Cu/ZrO$_2$ catalysts such that only the Cu particle size was varied via a two-nozzle spray pyrolysis approach.[36] They found that catalysts with a smaller Cu particle size had a higher CH$_3$OH activity and selectivity. Tada et al. demonstrated that efficient CO$_2$-to- CH$_3$OH Cu/ZrO$_2$ catalysts with high Cu loading (up to 80 wt%) can be conveniently synthesized by flame spray pyrolysis.[35]

In this study, we prepared two series of Cu-Zn-Ce oxide oxide catalysts with varying support composition and Cu loading by a one-step flame spray pyrolysis (FSP) method. This method allows for homogeneous mixing of different components at the nanoscale,[41,42] which is advantageous for elucidating the role of Cu-ZnO and Cu-CeO$_2$ interactions in CO$_2$ hydrogenation. The as-prepared Cu-Zn-Ce oxide catalysts were characterized by ICP, N$_2$ physisorption, TEM, STEM-EDX, XRD, TPR and N$_2$O chemisorption, demonstrating that well-defined catalysts with controlled Cu dispersion and Cu-support interactions were obtained via FSP method. The Cu-Zn-Ce oxide catalysts were evaluated for their CO$_2$ hydrogenation performance under conditions of 250 °C and 30 bar. The catalytic results showed that (i) combing ZnO and CeO$_2$ led to a higher CH$_3$OH selectivity as compared to Cu/ZnO and Cu/CeO$_2$ catalysts and (ii) the Cu-Zn-Ce oxide catalyst with highest Cu loading (~ 40 wt%) outperformed a commercial methanol synthesis catalyst with respect to CH$_3$OH selectivity. Based on the characterization and catalytic results, the improved CH$_3$OH selectivity of Cu-Zn-Ce oxide ternary oxide catalysts is discussed in the context of synergistic interactions between the Cu, ZnO and CeO$_2$ components.

2. Experimental section

2.1 Catalyst preparation

Ternary Cu-Zn-Ce oxide oxide catalysts were prepared by the flame spray pyrolysis (FSP) method using a Tethis NPS10 apparatus. The catalyst precursor solution was prepared by dissolving appropriate amounts of Cu(NO$_3$)$_2$·3H$_2$O (99%, Sigma Aldrich), Zn(NO$_3$)$_2$·6H$_2$O

(99%, Sigma Aldrich) and $Ce(NO_3)_3 \cdot 6H_2O$ (99%, Sigma Aldrich) in a 1:1 (vol%) solvent mixture of ethanol (HPLC, Sigma Aldrich) and 2-ethylhexanoic acid (99%, Sigma Aldrich) at room temperature. The total metal concentration was 0.15 M. The precursor solution was then injected into the nozzle of the Tethis setup at a flow rate of 5 mL/min. The flame was fed with a 1.5 L/min methane flow and a 3.0 L/min oxygen flow with an additional 5.0 L/min oxygen dispersion flow around it. The resulting catalyst powder was collected from the quartz filter placed after the combustion zone. The as-prepared Cu-Zn-Ce oxide catalysts are denoted as $Cu(x)/CeO_2$, $Cu(x)/ZnO$ or $Cu(x)/ZnO-CeO_2(y)$ where x and y respectively stands for Cu loading (wt %) and Zn atomic ratio in support (Zn/(Zn+Ce)). Additionally, a commercial methanol synthesis catalyst (MSC) was obtained from Alfa Aesar (#45776).

2.2 Catalyst characterization

Inductively coupled plasma optical emission spectroscopy (ICP-OES). The metal composition of the as-prepared catalysts was determined by ICP-OES analysis (Spectro CIROS CCD Spectrometer). The catalysts were completely dissolved in 5 mL concentrated sulfuric acid (H_2SO_4) under heating at 150 °C for about 1 h.

N_2 physisorption. Textural properties were determined by determining N_2 physisorption isotherms at -196 °C on a Micromeritics TriStar II 3020 instrument. For this purpose, about 100 mg of sample was placed into a glass sample tube and pretreated at 120 °C overnight under a nitrogen flow. The Brunauer-Emmett-Teller (BET) method was used to calculate the specific surface area.

X-ray diffraction (XRD). The crystal structure of the fresh catalysts was determined with a Bruker D2 Phaser diffractometer using Cu Kα radiation with a wavelength of 1.54 Å. XRD patterns were recorded between 20-85˚ with a step size of 0.05˚ at 1.0 s/step scan rate.

Transmission electron microscopy (TEM). The morphology of the as-prepared catalysts was studied by TEM using a FEI Tecnai 20 (type Sphera) instrument operating at an acceleration voltage of 200 kV. For this purpose, appropriate amounts of sample were dispersed in ethanol by ultrasonication and then deposited on a holey Cu grid. The elemental distribution for reduced catalysts was determined by scanning TEM combined with energy dispersive X-ray analysis (STEM-EDX) on a FEI cubed Cs-corrected Titan instrument operating at an acceleration voltage of 300 kV. The samples were first reduced in a flow of 10 vol% H_2 in He at 250 °C for 1 h, followed by passivation in 2 vol% O_2 in He at room temperature. These samples were dispersed in ethanol by ultrasonication and then deposited on a holey Au grid.

Temperature programmed reduction (H_2-TPR). H_2-TPR measurements were done using a Micromeritics AutoChem II instrument. Typically, about 50 mg of sample was held between two quartz wool layers in a quartz U-tube. The sample was pretreated at 200 °C for 1 h in a He flow of 50 mL/min prior to TPR measurement. The TPR profile was recorded by heating the

sample from 40 °C to 700 °C at a rate of 10 °C/min in a 4 vol% H_2 in He flow (total flow 50 mL/min). The hydrogen consumption was recorded by a TCD and the signal was calibrated against a Cu/SiO_2 reference sample. The molar consumed hydrogen to Cu ratio ($R_{H2/Cu}$) was determined in this way.

N_2O titration. The exposed metallic Cu surface and ceria oxygen vacancies in the reduced catalysts were determined by a CO_2-N_2O pulsing titration using a plug flow setup equipped with an online mass spectrometer (Balzers TPG 251). The detailed procedures and calculation were described in **Chapter 2**. In brief, the experiment consisted of two sequential N_2O pulse titrations carried out at 50 °C and the sample was reduced at 250 °C before each N_2O titration measurement. CO_2 was pulsed prior to the first N_2O titration and the second one did not involve CO_2 pulsing. As CO_2 pulsing blocks ceria oxygen vacancies in the reduced ceria support,[43] the difference between the two N_2O titration measurements provides an estimate of the metallic Cu surface.

2.3 Catalytic activity measurements

CO_2 hydrogenation. The performance of the Cu-Zn-Ce oxide catalysts in CO_2 hydrogenation was evaluated at 250 °C and 30 bar using a down-flow stainless-steel reactor with an internal diameter of 4 mm. An amount of 50 mg catalyst pressed, crushed and sieved to a 125-250 μm fraction and diluted with 200 mg SiC was loaded into the reactor. Prior to reaction, the catalyst was reduced in a 10 vol% H_2 in He flow of 50 ml/min whilst heating to 250 °C at a rate of 5 °C/min followed by a dwell of 1 h. The reaction was started by switching the pretreatment feed to the reaction feed, which was a mixture of CO_2:H_2:N_2 at a volumetric ratio of 1:3:1. The total flow rate was 50 mL/min flow and the reaction pressure was 30 bar. The effluent gas was analyzed by an online gas chromatograph (Interscience, CompactGC) equipped with Rtx-1 (FID), Rt-QBond and Molsieve 5A (TCD), and Rt-QBond (TCD) analysis sections. Online measurements were typically taken for ca. 3 h until steady-state was reached, and CO_2 conversion, product selectivity and product formation rate at the end of measurements were calculated as follows:

$$X(CO_2) = \frac{F(CO)_{out} + F(CH_3OH)_{out} + F(CH_4)_{out}}{F(CO_2)_{out} + F(CO)_{out} + F(CH_3OH)_{out} + F(CH_4)_{out}} \quad [1]$$

$$S(product) = \frac{F(product)_{out}}{F(CO)_{out} + F(CH_3OH)_{out} + F(CH_4)_{out}} \quad [2]$$

$$r(product) = \frac{F(product)_{out}}{V_m \times m_{cat}} \quad [3]$$

where F stands for the volumetric flow rate calculated based on the nitrogen internal standard using calibrated response factors and V_m for the molar volume of ideal gas at standard

temperature and pressure. The CH_4 selectivity in all the measurements was very low (< 1%). The turnover frequency (TOF) is computed as the product formation rate normalized by the amount of surface metallic Cu sites determined by N_2O chemisorption. For the commercial methanol synthesis catalyst, a reduction temperature of 300 °C instead of 250 °C was used. The amount of this catalyst was about 25 mg in order to achieve similar conversion levels as for the Cu-Zn-Ce oxide catalysts.

CO hydrogenation. The CO hydrogenation activity of the Cu-Zn-Ce oxide catalysts was evaluated in the same catalytic setup as used for CO_2 hydrogenation. The pretreatment and reaction conditions were kept the same as done for CO_2 hydrogenation. CO_2 in the reaction feed mixture being replaced by the same amount of CO. Online measurements were taken for ca. 3 h, and CO_2 conversion, product selectivity and product formation rate at the end of measurements were calculated as follows:

$$X(CO) = \frac{F(CO_2)_{out} + F(CH_3OH)_{out} + F(CH_4)_{out}}{F(CO)_{out} + F(CO_2)_{out} + F(CH_3OH)_{out} + F(CH_4)_{out}} \quad [4]$$

$$S(product) = \frac{F(product)_{out}}{F(CO_2)_{out} + F(CH_3OH)_{out} + F(CH_4)_{out}} \quad [5]$$

$$r(product) = \frac{F(product)_{out}}{V_m \times m_{cat}} \quad [6]$$

where F stands for the volumetric flow rate calculated based on the nitrogen internal standard using calibrated response factors and V_m for the molar volume of ideal gas at standard temperature and pressure. The CH_3OH selectivity in all the measurements was very high (> 97%).

3. Results and discussion

3.1 Characterization

The physicochemical properties of the catalysts prepared by FSP and the commercial methanol synthesis reference catalyst are listed in **Table 4.1**. The Cu loading and support composition of all the Cu-Zn-Ce oxide catalysts are close to the targeted values. The FSP-derived samples possess high specific surface areas ranging from 82 m^2/g_{cat} to 130 m^2/g_{cat}. The Cu/CeO_2 and Cu/ZnO samples exhibit respectively the largest and smallest surface areas. The surface area of these samples slightly decreases with increasing Cu content. The morphology of the as-prepared Cu-Zn-Ce oxide catalysts with varying support composition was examined by TEM. **Figure 4.1** shows that (i) all the samples consist of homogeneously distributed nanoparticles and (ii) the Cu/CeO_2 sample has a polyhedral-like morphology, while the Zn-containing samples are comprised of rounder particles. The Cu/ZnO particles were substantially larger

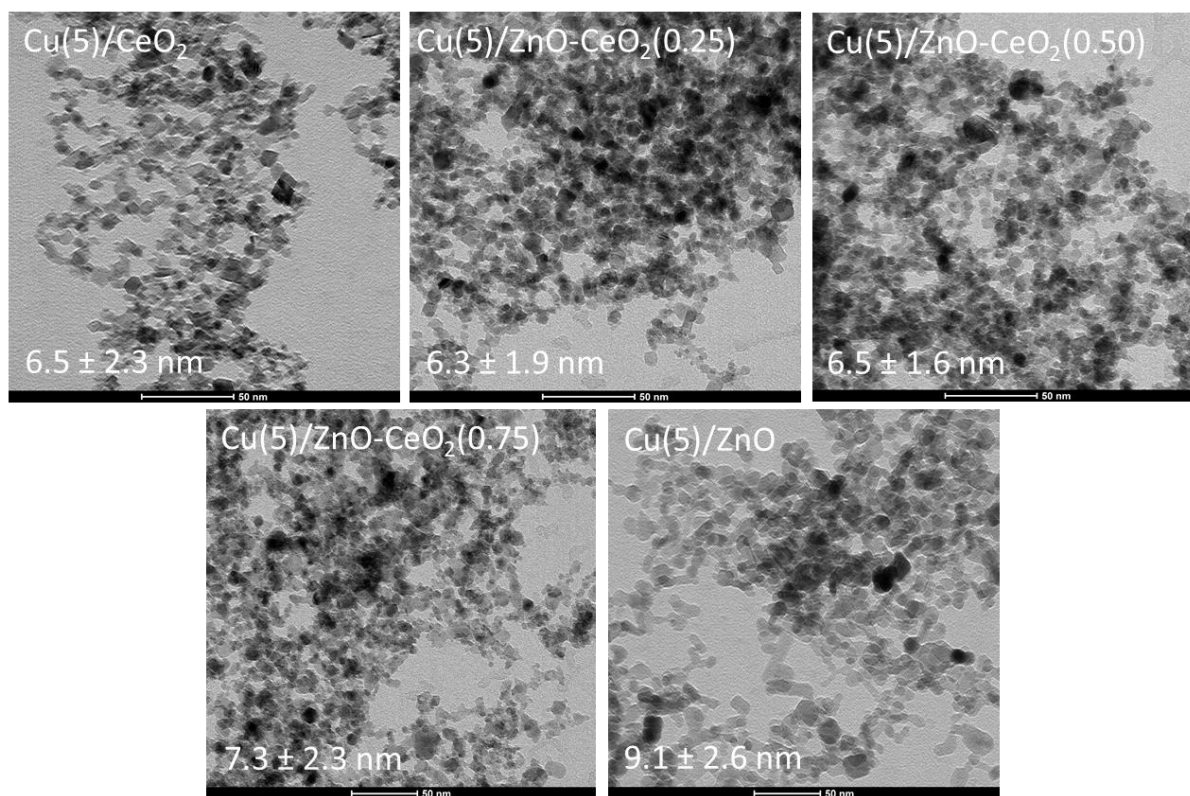than the Ce-containing samples, in line with surface area measurements.

Figure 4.1. TEM images of as-prepared Cu-Zn-Ce oxide catalysts by FSP.

The as-prepared Cu-Zn-Ce oxide catalysts were investigated by XRD (**Figure 4.2a**). The Cu/CeO_2 and Cu/ZnO end members of the Cu-Zn-Ce oxide series exhibited XRD patterns consistent with the fluorite and wurtzite structures of CeO_2 and ZnO, respectively. The broadening of the diffraction peaks points to the nanocrystalline nature of the support material (CeO_2 or ZnO). All the Ce-containing samples display clear diffraction peaks due to CeO_2, and no systematic shift in CeO_2 diffraction peaks was observed with respect to ZnO content (**Figure C.2**). Only for samples with a high Zn content, i.e. $Zn/(Zn+Ce) \geq 0.50$, clear ZnO diffraction peaks are observed. No diffraction peaks assignable to metallic or oxidic Cu phases are present in the XRD patterns in **Figure 4.2a**, indicative of the high Cu dispersion. The Cu-Zn-Ce oxide catalysts with varying Cu loading were also examnied by XRD (**Figure 4.2b**). The results show that (i) the fluorite CeO_2 diffraction peaks dominate in the diffraction patterns of all samples and (ii) two diffraction peaks assigned to CuO phase can be observed in the sample with the highest Cu loading (~40 wt%). These findings point to an improved Cu dipersion due to the presence of CeO_2.
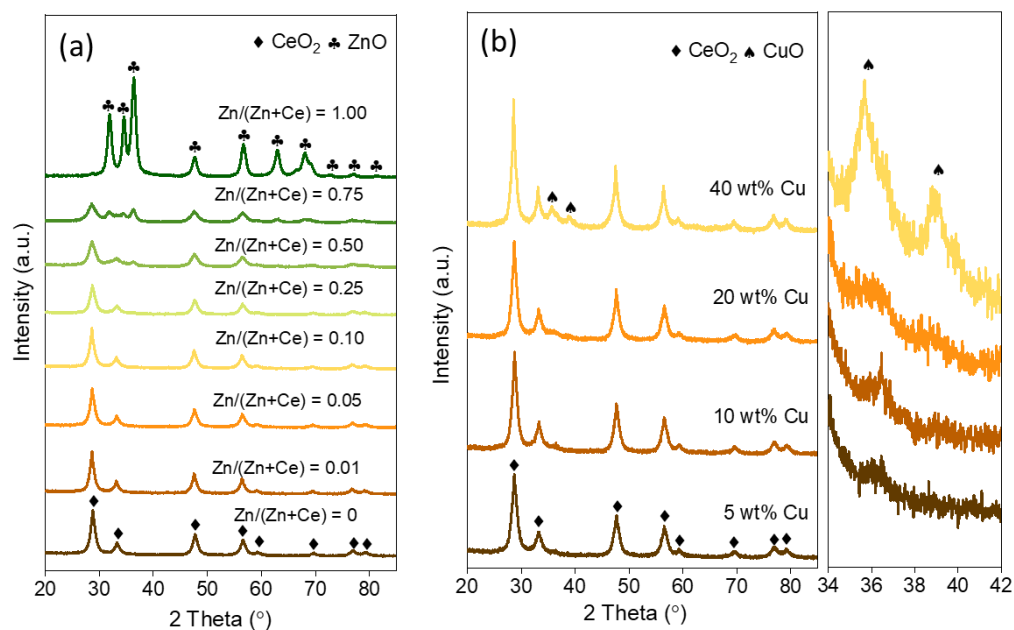
Figure 4.2. XRD patterns of the (a) Cu(5)/ZnO-CeO$_2$(y) and (b) Cu(x)/ZnO-CeO$_2$(0.25) catalysts with a zoom-in of CuO region.
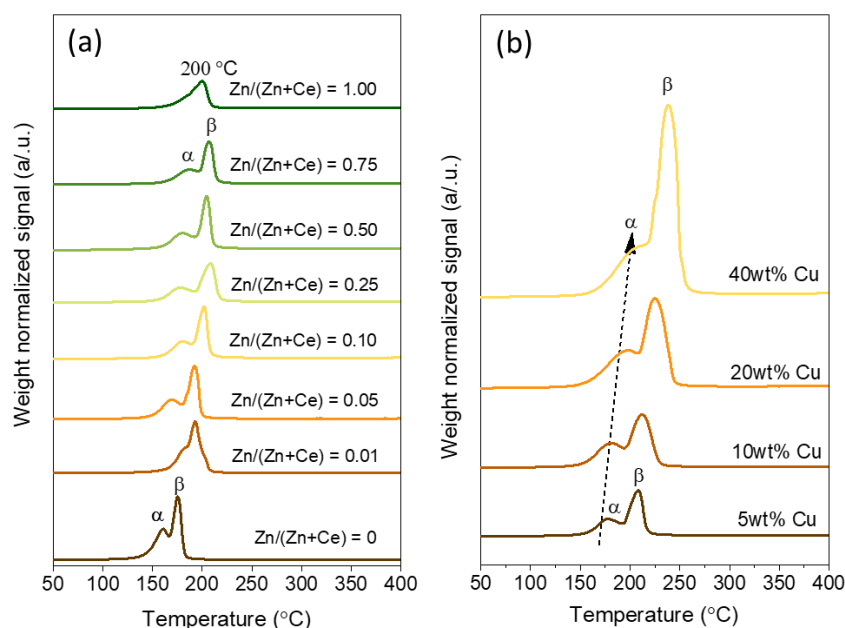
Figure 4.3. TPR profiles of the (a) Cu(5)/ZnO-CeO$_2$(y) and (b) Cu(x)/ZnO-CeO$_2$(0.25) catalysts.

H$_2$-TPR was carried out to probe the Cu-support interactions in the Cu-Zn-Ce oxide catalysts with varying support composition. **Figure 4.3a** shows that the Ce-containing samples exhibit two distinct reduction peaks (α and β) in the H$_2$-TPR profiles, which can be assigned respectively to dispersed Cu species strongly interacting with ceria support and a Cu-CeO$_2$ solid solution.[44,45] Thus, Cu preferably interacts with CeO$_2$ in the FSP-prepared samples. Notably, the ceria support in these samples was partially reduced together with Cu as evidenced

Table 4.1. Physicochemical properties of the Cu(x)/ZnO-CeO$_2$(y) catalysts.

Catalyst	Cu loading (wt%)	Zn/(Zn+Ce) atomic ratio	Zn/Cu atomic ratio	S_{BET} (m^2/g$_{cat}$)	D_{cu} (%)[a]	$S_{Cu(0)}$ (m^2/g$_{cat}$)[a]	$N_{Cu(0)}$ (µmol/g$_{cat}$)[a]	N_{Ov} (µmol/g$_{cat}$)[a]	H_2/Cu molar ratio[b]
Cu(5)/CeO$_2$	4.8	0	0	130	62.4	19.4	472	174	1.7
Cu(5)/ZnO-CeO$_2$(0.01)	4.5	0.01	0.08	116	64.6	18.8	458	143	1.6
Cu(5)/ZnO-CeO$_2$(0.05)	4.7	0.05	0.37	128	61.1	18.5	452	206	1.6
Cu(5)/ZnO-CeO$_2$(0.10)	4.8	0.10	0.74	115	55.6	17.2	420	208	1.4
Cu(5)/ZnO-CeO$_2$(0.25)	4.7	0.26	2.17	104	52.5	15.9	388	203	1.6
Cu(5)/ZnO-CeO$_2$ (0.50)	4.7	0.51	4.97	112	46.8	14.2	347	132	1.5
Cu(5)/ZnO-CeO$_2$(0.75)	4.8	0.76	9.29	110	30.2	9.4	228	111	1.2
Cu(5)/ZnO	5.0	1.00	15.11	82	10.0	3.2	79	7	0.9
Cu(10)/ZnO-CeO$_2$(0.25)	9.5	0.25	0.93	99	27.1	16.7	406	120	1.2
Cu(20)/ZnO-CeO$_2$(0.25)	18.6	0.24	0.40	95	16.4	19.6	479	137	1.1
Cu(40)/ZnO-CeO$_2$(0.25)	35.6	0.24	0.16	87	9.4	21.7	528	224	1.0
Commercial MSC	45.6	1.00	0.37	89	6.5	19.0	464	67	1.0

[a] Derived from N$_2$O titration. [b] Derived from H$_2$-TPR.

by the higher than unity values of the H_2/Cu molar ratios (**Table 4.1**). Moreover, we found that the α and β reduction peaks shifted to higher temperatures after adding even a small amount of ZnO, which is likely related either to the modification of CeO_2 support or to the decoration of Cu particles by Zn species. The TPR profile of Cu(5)/ZnO shows an asymmetric reduction peak at 200 °C with a small low-temperature shoulder. This reduction feature can be attributed to dispersed Cu species interacting with ZnO.[46] Furthermore, Cu-Zn-Ce oxide catalysts with varying Cu loading were investigated. **Figure 4.3b** shows that the two reduction peaks due to Cu-CeO_2 interactions shifted to higher temperature with Cu content. The shift in reduction temperature can be explained by the fact that the Cu species are larger at higher Cu content (*vide infra*).
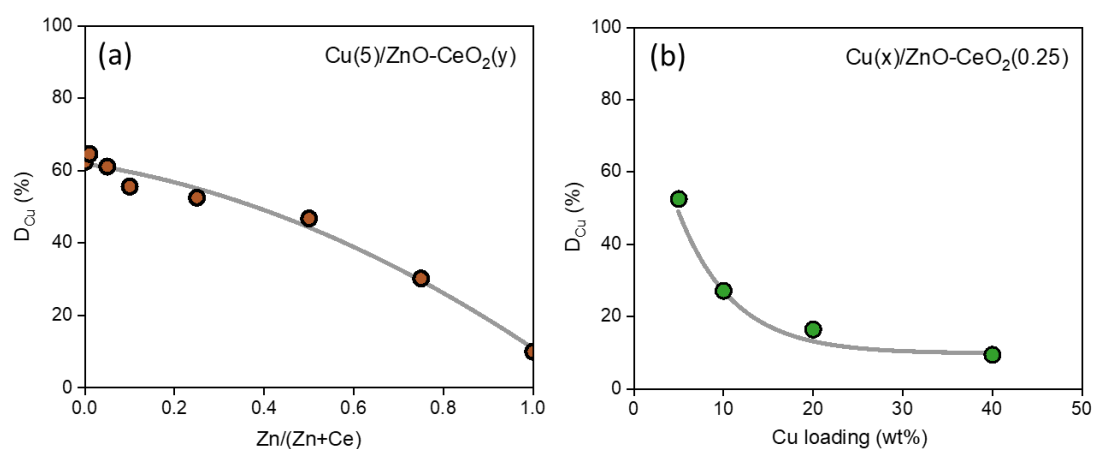

Figure 4.4. Copper dispersion of the Cu-Zn-Ce oxide catalysts determined from N_2O titration as a function of (a) support composition and (b) copper loading.

We used N_2O chemisorption to quantify the metallic Cu surface of the reduced catalysts, which is a key descriptor for methanol synthesis in Cu-based catalysts.[47,48] The densities of metallic Cu sites are listed in **Table 4.1** and the calculated Cu dispersion as a function of Zn and Cu content is plotted in **Figure 4.4**. For the catalysts with varying support composition, Cu dispersion decreases from ~60 % for the pure CeO_2 end member to ~10% for the ZnO one. The very high Cu dispersion for Cu(5)/CeO_2 is the result of the stronger Cu-CeO_2 than Cu-ZnO interactions, resulting in part from the intimate mixing during FSP preparation.[19,49] Addition of small amounts of Zn led only to minor changes in Cu dispersion, while samples containing predominantly Zn display a much lower Cu dispersion (**Figure 4.4a**). This observation is in line with the H_2-TPR results, showing the stronger interaction of Cu with CeO_2. For the Cu(x)/ZnO-CeO(25) samples, **Figure 4.4b** shows that the Cu dispersion decreases strongly with Cu content. The Cu-Zn-Ce oxide catalyst with the highest Cu content of ~40 wt% has a Cu dispersion of 8.4 %.

STEM-EDX was used to study the distribution of the three metal components in the reduced catalysts (**Figure 4.5**). Although the data do not warrant a statistical analysis of the distribution

of the Zn and Ce in the support, inspection of the STEM-EDX maps indicates segregation of these two components at the nanometer scale (circles in **Figure 4.5b**). Cu is homogeneously and finely dispersed in the reduced Cu(5)/CeO$_2$ and Cu(5)/ZnO-CeO$_2$(0.25) catalysts. In contrast, larger Cu particles can be distinguished in reduced Cu(5)/ZnO. Clearly, the Cu dispersion in Cu(5)/CeO$_2$ is much higher than in Cu(5)/ZnO. Thus, we can conclude that flame spray pyrolysis is a powerful technique to prepare well-dispersed Cu particles on support materials consisting of (mixed) oxides of Ce and Zn. The resulting materials display similar morphological and textural properties in a broad support composition range. A similar high Cu dispersion is achieved in Cu-Zn-Ce oxide catalysts with a relatively low Zn content (Zn/(Ce+Zn) $\leq$ 0.05), while Cu is present in a more agglomerated form in Zn-rich support compositions.
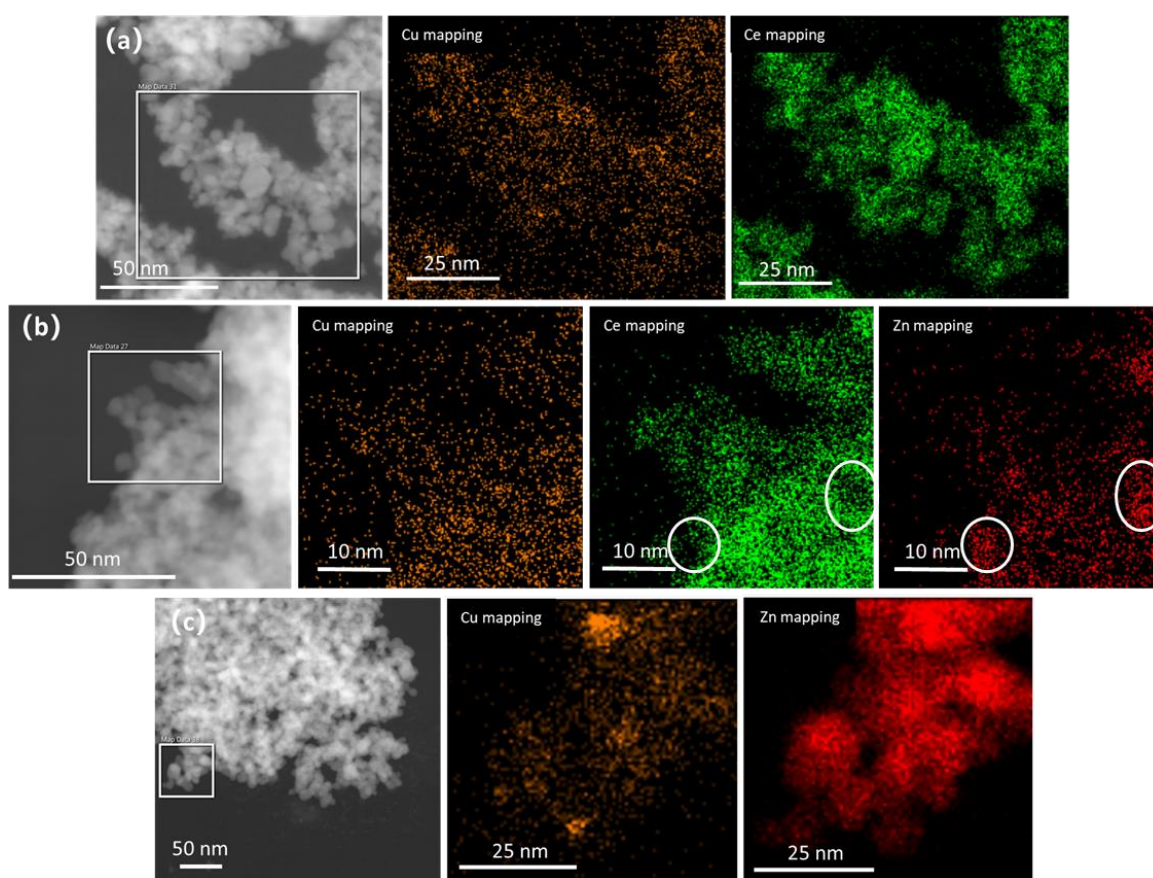
Figure 4.5. STEM images with corresponding elemental mappings of reduced (a) Cu(5)/CeO$_2$, (b) Cu(5)/ZnO-CeO$_2$(0.25) and (c) Cu(5)/ZnO catalysts. Reduction: 250 C, 1 h and 10 vol% H$_2$ in He.

3.2 Catalytic activity measurements

We studied the influence of Cu-CeO$_2$ and Cu-ZnO interactions on the catalytic performance in CO$_2$ hydrogenation. **Figure 4.6a** shows the CO$_2$ conversion and CH$_3$OH selectivity of the catalysts as a function of the Zn content. Clearly, there is a synergistic effect between Zn and Ce with respect to the CH$_3$OH selectivity. The CO$_2$ conversion is lowest for the Cu(5)/CeO$_2$

sample and increases with Zn content until Zn/(Ce+Zn) = 0.05. The activity of the Cu(5)/ZnO-CeO$_2$ catalysts is nearly constant for higher Zn content, while the Cu(5)/ZnO catalyst is slightly more active than the ternary Cu-Zn-Ce oxide oxide catalysts. **Figure 4.6b** shows the CH$_3$OH and CO formation rates as a function of the Zn content. The CH$_3$OH formation rate increases more than twice upon adding a small amount of ZnO (Zn/(Ce+Zn) ≤ 0.05) and remains nearly the same at higher Zn content. This observation suggests that maximum Zn promotion for CH$_3$OH synthesis is achieved for Cu(5)/ZnO-CeO$_2$(y) with y ≥ 0.05. In contrast, the CO formation rate is similar for all the Ce-containing catalysts, while the CO formation rate of the Cu/ZnO catalyst is nearly two times higher.

As the Cu dispersion is nearly similar for the catalysts with a low Zn content (Zn/(Ce+Zn) ≤ 0.05), the higher CH$_3$OH formation rate can be linked to synergistic Cu-Zn interactions.[50] As it has been suggested that CO can be an intermediate in CH$_3$OH synthesis from CO$_2$,[51] we evaluated the activity of the samples in CO hydrogenation under similar reaction conditions. **Figure 4.6c** shows that the CH$_3$OH formation rate from CO sharply decreases after adding a small amount of ZnO, i.e. Zn/(Ce+Zn) ≤ 0.05. The opposite trends of CH$_3$OH formation rate from CO$_2$ and CO as a function of ZnO content suggest that CO$_2$ hydrogenation to methanol over the Cu-Zn-Ce oxide catalysts does not proceed via CO. This is in line with the more common notion that CH$_3$OH is mainly formed by hydrogenation of CO$_2$.[6,7]

Figure 4.6. (a) CO$_2$ conversion and CH$_3$OH selectivity, and (b) CH$_3$OH and CO formation rates as a function of support composition. (c) Comparison between CH$_3$OH formation rate from CO$_2$ and CO hydrogenation over Cu(5)/ZnO-CeO$_2$(y) catalysts. Conditions: 250 °C, 30 bar and H$_2$/CO$_2$ = 3.

The influence of Cu loading on CO$_2$ hydrogenation was investigated for a series of Cu/ZnO-CeO$_2$(25) catalysts (**Figure 4.7**). The CO$_2$ conversion increases almost linearly with Cu loading, although the CH$_3$OH selectivity slightly decreased. The catalyst with the highest Cu loading (~40 wt%) has a CH$_3$OH formation rate of ~22 mmol/g$_{cat}$×h. We compared the most active Cu-Zn-Ce oxide catalyst, i.e. Cu(40)/ZnO-CeO$_2$(25), to a commercial methanol synthesis catalyst. **Figure 4.7c** shows that the Cu-Zn-Ce oxide catalyst displays a higher initial CH$_3$OH selectivity than the reference catalyst at similar conversion level (~ 7%). With increasing time on stream, the CH$_3$OH selectivity of the Cu-Zn-Ce oxide catalyst slowly increased at the expense of the CO$_2$ conversion. A similar trade-off between CH$_3$OH selectivity and CO$_2$ conversion was

reported for Cu-based catalysts and attributed to either H_2O inhibition or secondary CH_3OH decomposition.[52,53] After 15 h, the CH_3OH selectivity of the Cu-Zn-Ce oxide catalyst was ~10% higher than that of the reference catalyst.
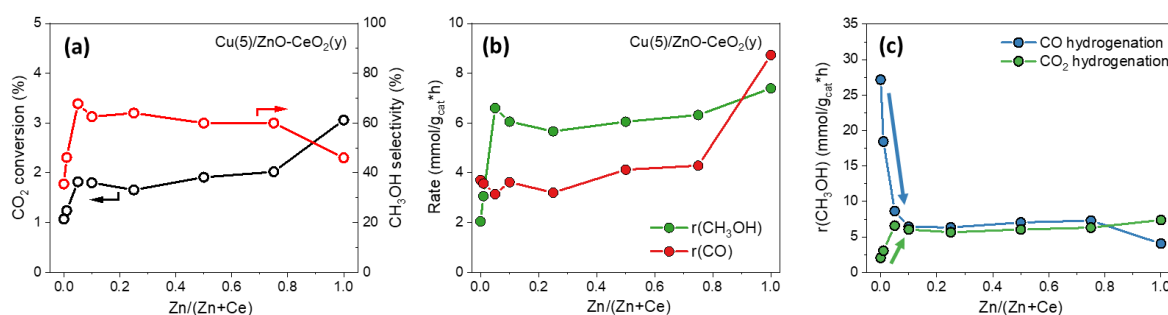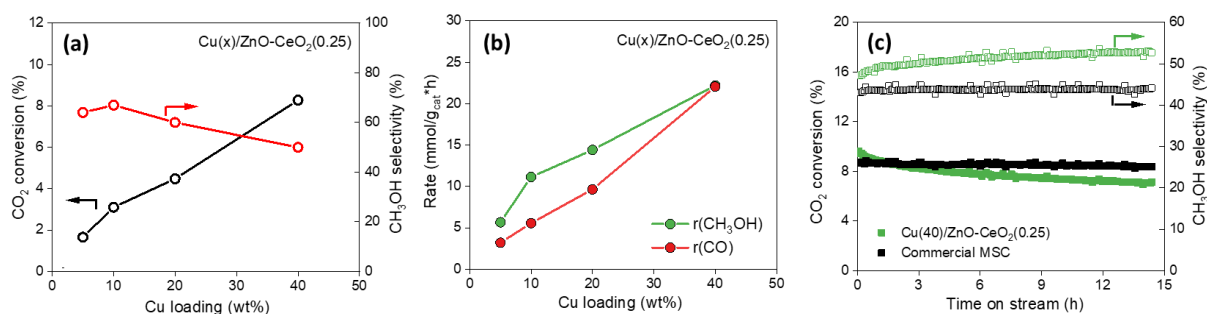

Figure 4.7. (a) CO_2 conversion and CH_3OH selectivity, and (b) CH_3OH and CO formation rates as a function of Cu loading. (c) Time-on-stream behavior comparison between Cu(40)/ZnO-CeO$_2$(0.25) and a commercial methanol synthesis catalyst. Conditions: 250 °C, 30 bar and $H_2/CO_2 = 3$.

We plotted the intrinsic CH_3OH and CO formation rates (*i.e.*, turnover frequencies) against the Cu particle size estimated from N_2O chemisorption. A reference Cu(5)/SiO$_2$ catalyst from Chapter 2 was also included. We analyzed the ternary Cu-Zn-Ce oxide interactions by considering separately (i) the effect of ZnO addition to Cu and (ii) the effect of CeO_2 addition on Cu-ZnO. The comparison of Cu(5)/ZnO and Cu(5)/SiO$_2$ with similar Cu particle sizes shows that ZnO substantially improves the intrinsic CH_3OH formation rate. This observation is in line with the catalytic results of Cu-Zn-Ce oxide catalysts with low Zn content (Zn/(Ce+Zn) ≤ 0.05) in **Figure 4.6**, which is also highlighted with circle in **Figure 4.8a**. Such ZnO promotion for Cu-based catalysts can be attributed to the decoration of the Cu particles by ZnO, forming new active sites for CO_2 hydrogenation to methanol.[50,54,55] Next, we analyzed the effect of CeO_2 addition on Cu-ZnO. This is not straightforward, because the addition of CeO_2 has a strong influence on the Cu particle size. Further, CH_3OH synthesis on Cu nanoparticles is a structure-sensitive reaction with the CH_3OH formation rate increasing with particle size until a size of about 8-10 nm as reported by Berg et al.[47] and Karelovic et al.[48] Thus, we extrapolated the TOF(CH_3OH) of our Cu(5)/ZnO-CeO$_2$(y) catalysts already with maximum Zn promotion (y ≥ 0.05) to that Cu particle size region. The extrapolated TOF(CH_3OH) in that region is close to the TOF(CH_3OH) of Cu(5)/ZnO, which suggests that Cu-CeO$_2$ interactions do not promote the intrinsic CH_3OH formation rate over Cu-ZnO catalysts. It should be mentioned that the deviation of Cu(x)/ZnO-CeO$_2$(0.25) catalysts (x = 20 and 40) can be explained by sub-optimal Zn promotion as indicated by their low Zn/Cu ratios (**Table 4.1**). The competing rWGS reaction was also examined (**Figure 4.8b**). The higher TOF(CO) of Cu(5)/ZnO as compared to Cu(5)/SiO$_2$) indicates that Cu-ZnO interactions provide additional active sites for rWGS reaction, i.e. the Cu-ZnO interface.[56,57] Next, the effect of CeO_2 addition on rWGS reaction was examined. **Figure 4.8b** shows that all the Ce-containing catalysts

display a significantly lower TOF(CO) than Cu(5)/SiO$_2$, indicating that Cu-CeO$_2$ interactions inhibit the intrinsic rWGS activity on Cu surface. Moreover, the TOF(CO) decreases with Cu particle size within the set of Ce-containing catalysts. This structure-sensitivity trend suggests that the Cu-CeO$_2$ interface is not active for rWGS reaction in contrast to the Cu-ZnO interface.
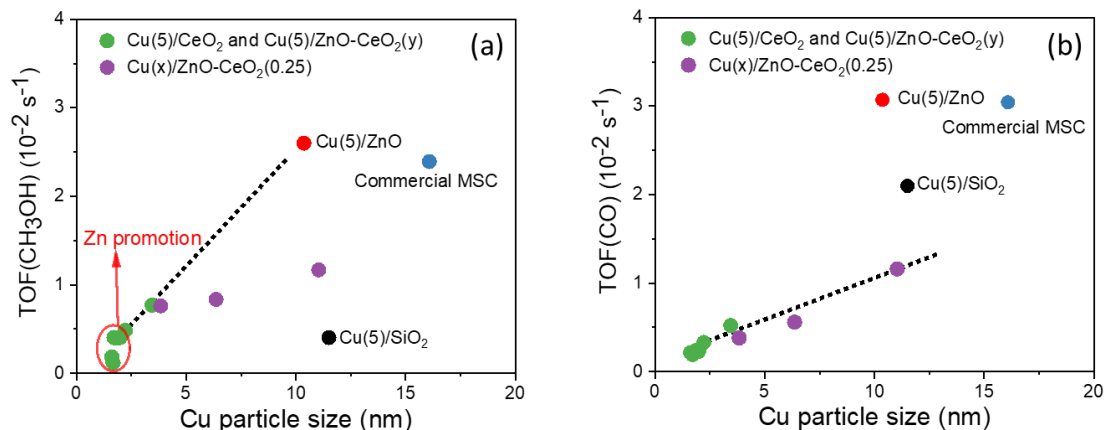
Figure 4.8. Structure-sensitivity plots of (a) TOF(CH$_3$OH) and (b) TOF(CO) as a function of Cu particle size. The data of Cu(5)/SiO$_2$ is from Chapter 2. Conditions: 250 °C, 30 bar and H$_2$/CO$_2$ = 3.
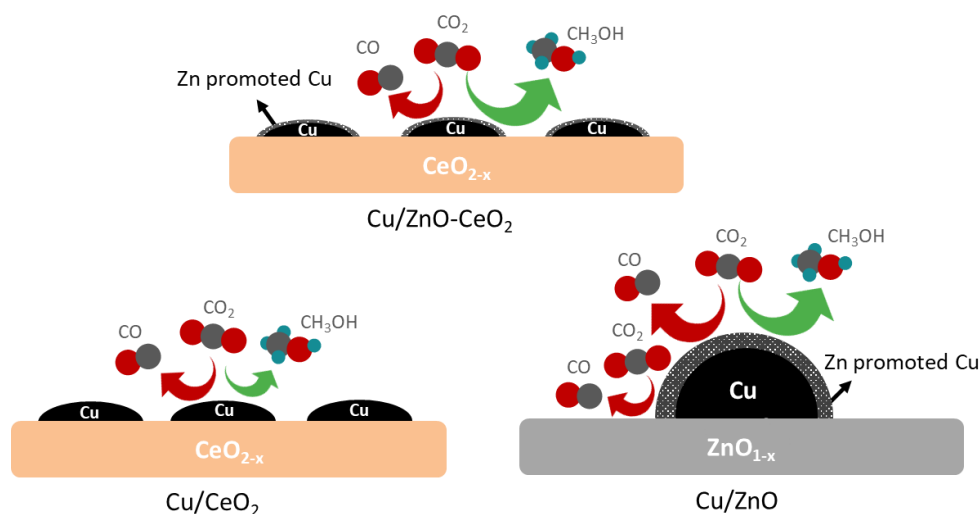
Scheme 4.1. Proposed models of FSP-prepared Cu/CeO$_2$, Cu/ZnO-CeO$_2$ and Cu/ZnO catalysts.

Three models are proposed to represent the FSP-synthesized catalysts in this work based on the characterization and catalytic data, showing how the support influences the rate of CO and CH$_3$OH formation (**Scheme 4.1**). Highly dispersed Cu nanoparticles are formed in Cu/CeO$_2$ and Cu/ZnO-CeO$_2$ catalysts due to the strong Cu-CeO$_2$ interactions. In contrast, large Cu particles are present in Cu/ZnO catalyst because of the weaker interactions between Cu and ZnO. The higher CH$_3$OH selectivity of ternary Cu-Zn-Ce oxide oxide catalysts for CO$_2$ hydrogenation in comparison with Cu-Zn and Cu-Ce oxide catalysts is associated with the synergistic interactions between Cu, ZnO and CeO$_2$: the role of ZnO is to promote the Cu surface for CH$_3$OH synthesis from CO$_2$, while CeO$_2$ inhibits the rWGS activity on the Cu

surface and the Cu-ZnO interface.

4. Conclusions

Well-defined ternary Cu-Zn-Ce oxide methanol synthesis catalysts were synthesized by a one-step FSP approach. The support composition and Cu loading were systematically varied in the Cu-Zn-Ce oxide catalysts to investigate how Cu-ZnO and Cu-CeO$_2$ interactions affect CO_2 hydrogenation to CH$_3$OH. Catalyst characterization indicates that Cu interacts more strongly with CeO$_2$ than ZnO, leading to an improved Cu dispersion in the Ce-containing catalysts. CO_2 hydrogenation data show that (i) the Cu-Zn-Ce oxide catalysts display a significantly higher CH$_3$OH selectivity in comparison to the respective binary oxide catalysts and (ii) the Cu-Zn-Ce oxide catalyst with the highest Cu loading (~40 wt%) outperformed a commercial methanol synthesis catalyst by ~10% in terms of CH$_3$OH selectivity. The turnover frequencies of the Cu-Zn-Ce oxide catalysts are lower because of smaller Cu particle sizes in these samples. Structure-sensitivity analysis reveals that the improved CH$_3$OH selectivity of Cu-Zn-Ce oxide catalysts can be explained by (i) the promotion of CO_2-to-CH$_3$OH activity by ZnO and (ii) the inhibition of rWGS activity by CeO$_2$.

References

1   J. Sehested, *J. Catal.*, 2019, **371**, 368–375.

2   Malte Behrens, Felix Studt, Igor Kasatkin, Stefanie Kühl, Michael Hävecker, Frank Abild-Pedersen, Stefan Zander, Frank Girgsdies, Patrick Kurr, Benjamin-Louis Kniep, Michael Tovar, Richard W. Fischer, Jens K. Nørskov and Robert Schlög, Science., 2012, **336**, 893–897.

3   J. Zhong, X. Yang, Z. Wu, B. Liang, Y. Huang and T. Zhang, *Chem. Soc. Rev.*, 2020, **49**, 1385–1413.

4   A. Goeppert, M. Czaun, J.-P. Jones, G. K. Surya Prakash and G. A. Olah, *Chem.Soc.Rev.*, 2014, **43**, 7995–8048.

5   G. A. Olah, *Angew. Chem. Int. Ed.*, 2005, **44**, 2636–2639.

6   G. C. Chinchen, P. J. Denny, D. G. Parker, M. S. Spencer and D. A. Whan, *Appl. Catal.*, 1987, **30**, 333–338.

7   D. Xu, P. Wu and B. Yang, *Catal. Sci. Technol.*, 2020, **10**, 3346–3352.

8   M. Behrens, *Angew. Chem. Int. Ed.*, 2016, **55**, 14906–14908.

9   A. Prašnikar, A. Pavlišič, F. Ruiz-Zepeda, J. Kovač and B. Likozar, *Ind. Eng. Chem. Res.*, 2019, **58**, 13021–13029.

10   B. Liang, J. Ma, X. Su, C. Yang, H. Duan, H. Zhou, S. Deng, L. Li and Y. Huang, *Ind. Eng. Chem. Res.*, 2019, **58**, 9030–9037.

11   T. Lunkenbein, F. Girgsdies, T. Kandemir, N. Thomas, M. Behrens, R. Schlögl and E. Frei, *Angew. Chem. Int. Ed.*, 2016, **55**, 12708–12712.

12   M. S. Jingang Wu Masami Takeuchi Taiki Watanabe, *Appl. Catal. A Gen.*, 2001, **218**, 235–240.

13   Y. Wang, S. Kattel, W. Gao, K. Li, P. Liu, J. G. Chen and H. Wang, *Nat. Commun.*, 2019, **10**, 1166–1175.

14   F. Arena, G. Italiano, K. Barbera, S. Bordiga, G. Bonura, L. Spadaro and F. Frusteri, *Appl. Catal. A Gen.*, 2008, **350**, 16–23.

15   F. Arena, K. Barbera, G. Italiano, G. Bonura, L. Spadaro and F. Frusteri, *J. Catal.*, 2007, **249**, 185–194.

16   X. Guo, D. Mao, G. Lu, S. Wang and G. Wu, *J. Catal.*, 2010, **271**, 178–185.

17   X. Hu, W. Qin, Q. Guan and W. Li, *ChemCatChem*, 2018, **10**, 4438–4449.

18   B. Zhao, Y. X. Pan and C. J. Liu, *Catal. Today*, 2012, **194**, 60–64.

19   M. Konsolakis, *Appl. Catal. B Environ.*, 2016, **198**, 49–66.

20   L. G. A. van de Water, S. K. Wilkinson, R. A. P. Smith and M. J. Watson, *J. Catal.*, 2018, **364**, 57–68.

21   W.-J. Shen, Y. Ichihashi and Y. Matsumura, *Appl. Catal. A Gen.*, 2005, **282**, 221–226.

22   J. A. R. Jesús Graciani, Kumudu Mudiyanselage, Fang Xu, Ashleigh E. Baber, Jaime Evans, Sanjaya D. Senanayake, Darío J. Stacchiola, Ping Liu, Jan Hrbek, Javier Fernández Sanz, *Science.*, 2014, **345**, 546–550.

23   G. Bonura, F. Arena, G. Mezzatesta, C. Cannilla, L. Spadaro and F. Frusteri, *Catal. Today*, 2011, **171**, 251–256.

24   P. Gao, F. Li, N. Zhao, F. Xiao, W. Wei, L. Zhong and Y. Sun, *Appl. Catal. A Gen.*, 2013, **468**, 442–452.

25   F. Arena, G. Mezzatesta, G. Zafarana, G. Trunfio, F. Frusteri and L. Spadaro, *Catal. Today*, 2013, **210**, 39–46.

26   F. Arena, G. Mezzatesta, G. Zafarana, G. Trunfio, F. Frusteri and L. Spadaro, *J. Catal.*, 2013, **300**, 141–151.

27   K. Chang, T. Wang and J. G. Chen, *Ind. Eng. Chem. Res.*, 2019, **58**, 7922–7928.

28   J. Schumann, M. Eichelbaum, T. Lunkenbein, N. Thomas, M. C. Álvarez Galván, R. Schlögl and M. Behrens, *ACS Catal.*, 2015, **5**, 3260–3270.

29   H. Lei, R. Nie, G. Wu and Z. Hou, *Fuel*, 2015, **154**, 161–166.

30   C. Perego and P. Villa, *Catal. Today*, 1997, **34**, 281–305.

31   J. Wu, S. Luo, J. Toyir, M. Saito, M. Takeuchi and T. Watanabe, *Catal. Today*, 1998, **45**, 215–220.

32   C. Baltes, S. Vukojevic and F. Schuth, *J. Catal.*, 2008, **258**, 334–344.

33   M. Behrens, *J. Catal.*, 2009, **267**, 24–29.

34   J. A. Schwarz, C. Contescu and A. Contescu, *Chem. Rev.*, 1995, **95**, 477–510.

35   S. Tada, K. Fujiwara, T. Yamamura, M. Nishijima, S. Uchida and R. Kikuchi, *Chem. Eng. J.*, 2020, **381**, 122750–122760.

36   S. Tada, K. Larmier, R. Büchel and C. Copéret, *Catal. Sci. Technol.*, 2018, **8**, 2056–2060.

37   R. Ahmad, M. Hellinger, M. Buchholz, H. Sezen, L. Gharnati, C. Wöll, J. Sauer, M. Döring, J. D. Grunwaldt and U. Arnold, *Catal. Commun.*, 2014, **43**, 52–56.

38   K. Wegner, B. Schimmoeller and B. Thie-, *Kona*, 2011, **29**, 251–265.

39   F. Huber, H. Meland, M. Rønning, H. Venvik and A. Holmen, *Top. Catal.*, 2007, **45**, 101–104.

40   J. R. Jensen, T. Johannessen, S. Wedel and H. Livbjerg, *J. Catal.*, 2003, **218**, 67–77.

41   R. Koirala, S. E. Pratsinis and A. Baiker, *Chem. Soc. Rev.*, 2016, **45**, 3053–3068.

42   W. Y. Teoh, R. Amal, L. Mädler and L. Madler, *Nanoscale*, 2010, **2**, 1324–1347.

43   T. Takeguchi, S. Manabe, R. Kikuchi, K. Eguchi, T. Kanazawa, S. Matsumoto and W. Ueda, *Appl. Catal. A Gen.*, 2005, **293**, 91–96.

44   W. W. Wang, P. P. Du, S. H. Zou, H. Y. He, R. X. Wang, Z. Jin, S. Shi, Y. Y. Huang, R. Si, Q. S. Song, C. J. Jia and C. H. Yan, *ACS Catal.*, 2015, **5**, 2088–2099.

45   W.-W. Wang, W.-Z. Yu, P.-P. Du, H. Xu, Z. Jin, R. Si, C. Ma, S. Shi, C.-J. Jia and C.-H. Yan, *ACS Catal.*, 2017, **7**, 1313–1329.

46   S. Natesakhawat, J. W. Lekse, J. P. Baltrus, P. R. Ohodnicki, B. H. Howard, X. Deng and C. Matranga, *ACS Catal.*, 2012, **2**, 1667–1676.

47   R. Van Den Berg, G. Prieto, G. Korpershoek, L. I. van der Wal, A. J. van Bunningen, S. Lægsgaard-Jørgensen, P. E. De Jongh and K. P. De Jong, *Nat. Commun.*, 2016, **7**, 13057–13063.

48   A. Karelovic, G. Galdames, J. C. Medina, C. Yévenes and Y. Barra, *J. Catal.*, 2019, **369**, 415–426.

49   R. Kydd, W. Y. Teoh, K. Wong, Y. Wang, J. Scott, Q. H. Zeng, A. B. Yu, J. Zou and R. Amal,

Adv. Funct. Mater., 2009, **19**, 369–377.

50   S. Kuld, M. Thorhauge, H. Falsig, C. F. Elkjær, S. Helveg, I. Chorkendorff and J. Sehested, *Science.*, 2016, **352**, 969–974.

51   S. Kattel, B. Yan, Y. Yang, J. G. Chen and P. Liu, *J. Am. Chem. Soc.*, 2016, **138**, 12440–12450.

52   K. Larmier, W.-C. Liao, S. Tada, E. Lam, R. Verel, A. Bansode, A. Urakawa, A. Comas-Vives and C. Copéret, *Angew. Chem. Int. Ed.*, 2017, **56**, 2318–2323.

53   S. Tada, F. Watanabe, K. Kiyota, N. Shimoda, R. Hayashi, M. Takahashi, A. Nariyuki, A. Igarashi and S. Satokawa, *J. Catal.*, 2017, **351**, 107–118.

54   S. Kattel, P. J. Ramírez, J. G. Chen, J. A. Rodriguez and P. Liu, *Science.*, 2017, **355**, 1296–1299.

55   M. Behrens, F. Studt, I. Kasatkin, S. Kühl, M. Hävecker, F. Abild-pedersen, S. Zander, F. Girgsdies, P. Kurr, B. Kniep, M. Tovar, R. W. Fischer, J. K. Nørskov and R. Schlögl, *Science.*, 2012, **336**, 893–898.

56   Y. Yang, J. Evans, J. A. Rodriguez, M. G. White and P. Liu, *Phys. Chem. Chem. Phys.*, 2010, **12**, 9909–9917.

57   C. Álvarez Galván, J. Schumann, M. Behrens, J. L. G. Fierro, R. Schlögl and E. Frei, *Appl. Catal. B Environ.*, 2016, **195**, 104–111.
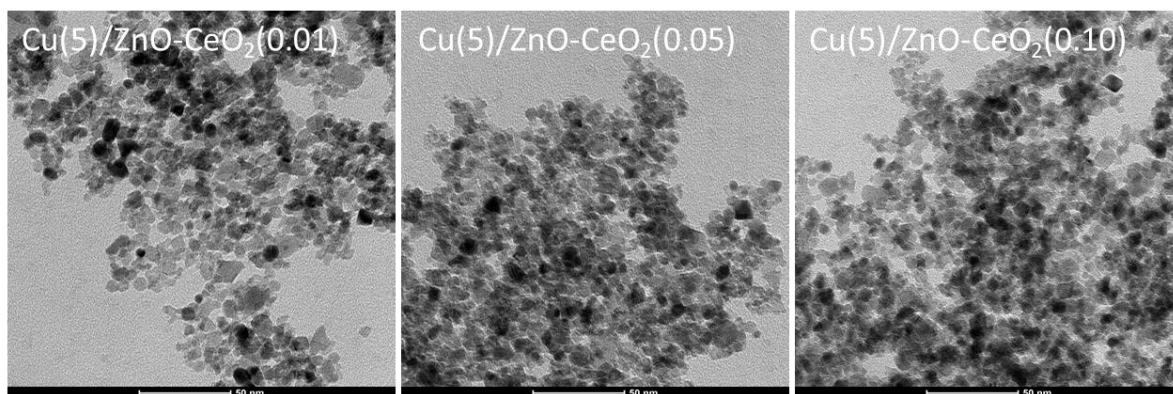
Appendix C

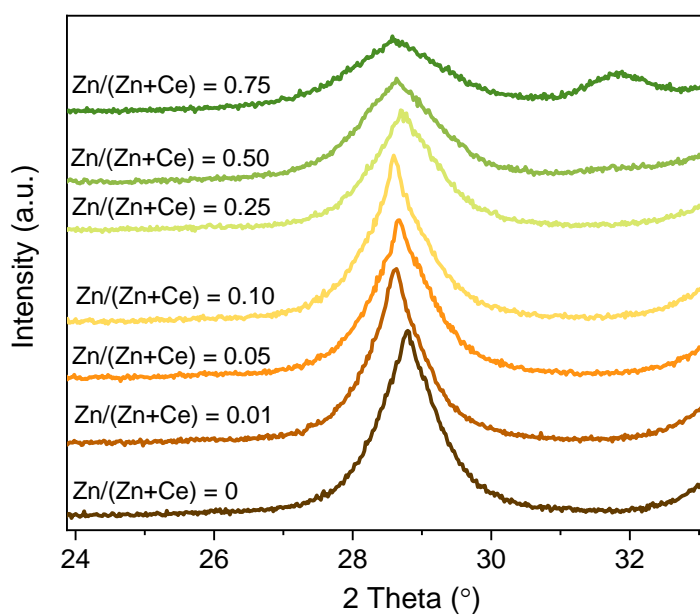**Figure C.1.** Additional TEM images of as-prepared Cu-Zn-Ce oxide catalysts by FSP

.

Figure C.2. A zoom-in of the main CeO_2 diffraction peaks of Cu(5)/ZnO-CeO_2(y) catalysts.
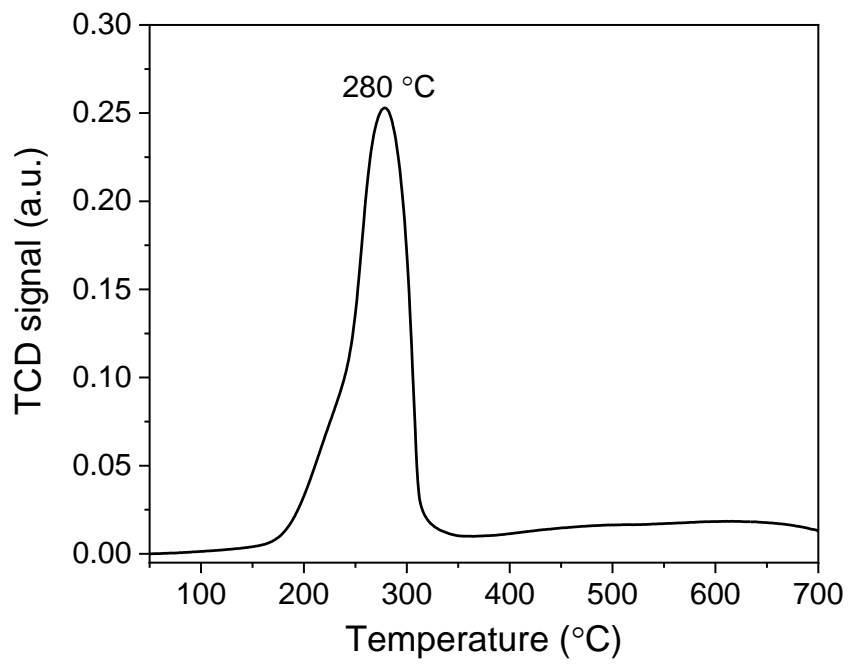
Figure C.3. H_2-TPR profile of the commercial methanol synthesis catalyst.

CHAPTER 5

Ni-In Synergy in CO$_2$ Hydrogenation to Methanol

ABSTRACT

Indium oxide (In$_2$O$_3$) is a promising catalyst for selective methanol synthesis from CO$_2$ but displays insufficient activity at relatively low reaction temperature. By screening a range of transition metal (Co, Ni, Cu, Pd) promoters using flame spray pyrolysis (FSP), we found that Ni is the most suitable promoter among the first-row transition metals with similar performance to Pd-In$_2$O$_3$. The NiO-In$_2$O$_3$ system was further optimized by preparing catalysts in a wide compositional range using the FSP approach. The resulting oxides including In$_2$O$_3$ and NiO end members have similar high specific surface areas. At high NiO content the samples can be described as In$_2$O$_3$ supported on NiO, while at low NiO content ($\leq$ 6 wt%) the samples can be characterized as very small NiO species dispersed on In$_2$O$_3$. In CO$_2$ hydrogenation, these catalysts produce CH$_3$OH and CO as main products with CH$_4$ being only observed at high NiO content. Optimum CH$_3$OH rate (~0.25 g$_{MeOH}$/(g$_{cat}$×h), 250 °C and 30 bar) is obtained for a NiO content of 6 wt%. Detailed characterization evidences the strong interactions between Ni cations and In$_2$O$_3$, and at least part of the Ni substitutes as Ni^{3+} for In^{3+} in In$_2$O$_3$. In line with this, H$_2$-TPR indicates reduction features for surface oxygen vacancy (O$_v$) formation associated with In and Ni lattice cations. The presence of Ni in In$_2$O$_3$ lattice leads to a higher O$_v$ density, which is likely due to distortion of In$_2$O$_3$ lattice. Characterization of the used catalysts by XPS and XAS shows that most of the oxidic Ni species are reduced to small metallic Ni particles. Besides a contribution from the increased O$_v$ density, it is concluded that, in analogy with other metal-promoted In$_2$O$_3$ catalysts, the reduced Ni species facilitate H$_2$ dissociation for the hydrogenation of CO$_2$ adsorbed on O$_v$ in the In$_2$O$_3$ surface.

1. Introduction

The large amounts of CO_2 released into the atmosphere, mainly by the combustion of fossil fuels, constitutes a significant threat to human well-being, because it can lead to severe climate changes including global warming, sea level rise and ocean acidification.[1–3] A promising solution is to capture CO_2 from combustion processes or directly from air for reuse in fuels and chemicals, followed by reduction to products with a higher energy content. This can for instance be achieved by catalytic hydrogenation of CO_2 with H_2 generated from renewable energy sources such as solar and wind.[4–7] This carbon capture and use (CCU) approach has the advantage over carbon capture and storage (CCS) that carbon is used in a circular manner, eventually leading to the replacement of fossil fuels by renewable resources for covering the energy demand. Besides sustainable energy carriers, hydrogenation of CO_2 can also be used to obtain important intermediates for the chemical industry. Methanol is particularly attractive in the overall context of sustainability, because it can be directly used as a fuel or precursor to other fuels such as dimethyl ether and conventional hydrocarbon fuels and a wide range of chemicals.[8–10]

The current commercial methanol process developed by Imperial Chemical Industries (ICI) in the 1960s employs $Cu/ZnO/Al_2O_3$ catalysts.[11,12] Such catalysts, which are optimized for the conversion of synthesis gas (a mixture of mainly CO/H_2), is not suitable for converting CO_2 with H_2 to methanol. The high activity of Cu-ZnO based catalysts in the reverse water-gas shift (rWGS) reaction decreases the CH_3OH selectivity and H_2 efficiency.[13] Moreover, the catalyst deactivation is accelerated by the large amounts of water by-product formed during CO_2 hydrogenation.[14–16] Many efforts have been made to optimize Cu-based catalysts for CO_2 hydrogenation to methanol.[5,17] An important corollary of these studies is that tuning copper-support interactions by using supports other than alumina can mitigate some of these drawbacks. For example, zirconia (ZrO_2) has been widely investigated as an alternative support, displaying promising performance in comparison to Cu-ZnO based catalysts.[18–21]

Exploring completely new catalytic formulations is another approach to develop catalysts for practical hydrogenation of CO_2 to methanol. Several promising materials have been reported, such as mixed oxides ($ZnO-ZrO_2$ and MnO_x/Co_3O_4)[22,23], molybdenum carbides[24,25], molybdenum phosphides[26] and intermetallic compounds ($GaPd_2$ and Ni_5Ga_3)[27,28]. In recent years, oxygen-defective In_2O_3 has been proposed as an alternative catalyst for efficient CO_2 hydrogenation to CH_3OH.[29–33] The role of O vacancies in the surface of In_2O_3 has been emphasized for CO_2 adsorption and hydrogenation.[29,30] Furthermore, zirconia (ZrO_2) was extensively studied as a support for In_2O_3 because of the beneficial interactions between these two components.[34–39] Pérez-Ramirez' group reported that nanosizing In_2O_3 by supporting it on ZrO_2 can substantially enhance methanol synthesis from CO_2.[39] Addition of Pd instead of ZrO_2 was also found to significantly promote In_2O_3 for CO_2 hydrogenation to methanol.[40–44] Low-

nuclearity Pd clusters stabilized by Pd doped into the In$_2$O$_3$ surface can enhance H$_2$ activation, leading to a higher methanol productivity.[43]

Given its price, it would be advantageous to replace Pd by a more Earth-abundant metal. Earlier investigations have shown that the activity of In$_2$O$_3$ can be promoted by Co and Cu.[45–47] The replacement of Pd by Ni, a typical catalyst for CO$_2$ methanation, has also been studied. Richard and Fan, for instance, found that NiInAl/SiO$_2$ catalysts derived from phyllosilicate precursors can catalyze CO$_2$ hydrogenation to methanol at ambient pressure, although with low selectivity (< 4%).[48] In another study, Snider et al. suggested that the higher activity of bimetallic Ni-In catalysts for methanol synthesis from CO$_2$ in comparison to In$_2$O$_3$ is related to the synergistic interactions between a Ni-In alloy and In$_2$O$_3$.[42] Using wet chemical reduction with sodium borohydride, Jia et al. observed a similar promoting effect of Ni on In$_2$O$_3$ for CO$_2$ hydrogenation to methanol. Different from Snider et al., the authors proposed that Ni promotion is due to highly dispersed Ni species in strong interaction with In$_2$O$_3$.[49]

In this study, a series of NiO-In$_2$O$_3$ catalysts were studied to understand Ni promotion on In$_2$O$_3$ for CH$_3$OH synthesis from CO$_2$. For this purpose, a one-step flame spray pyrolysis (FSP) method[51] was used to synthesize well-defined NiO-In$_2$O$_3$ catalysts with controlled Ni-In interactions. Catalytic activity measurements at 250 °C and 30 bar point to a significant synergy between Ni and In$_2$O$_3$: small amounts of Ni leads to increased methanol formation rates, while higher Ni content leads to formation of methane. Various techniques including N$_2$ physisorption, TEM, XRD, H$_2$-TPR, XPS and XAS were employed to characterize the as-prepared and used NiO-In$_2$O$_3$ catalysts to understand the observed synergy.

2. Experimental section

2.1 Catalyst preparation

A series of metal (M = Co, Cu, Ni and Pd and loading = 5 wt%) promoted In$_2$O$_3$ catalysts were prepared by a one-step flame spray pyrolysis (FSP) method using a Tethis NPS10 setup. Typically, a precursor solution was prepared by dissolving appropriate amounts of In(NO$_3$)$_3$•xH$_2$O (99%, Alfa Aesar) and metal precursor (Co(NO$_3$)$_2$•6H$_2$O (98%, Sigma Aldrich), Cu(NO$_3$)$_2$•3H$_2$O (99.5%, Sigma Aldrich), Ni(NO$_3$)$_2$•6H$_2$O (98.5%, Sigma Aldrich) and Pd(OCOCH$_3$)$_2$ (98%, Sigma Aldrich)) in a 1:1 (vol%) solvent mixture of ethanol (HPLC, Sigma Aldrich) and 2-ethylhexanoic acid (99%, Sigma Aldrich) at room temperature to a total metal concentration of 0.15 M. The synthesis started by injecting the precursor solution into the nozzle of the flame synthesis setup at a flow rate of 5 mL/min. The flame was fed with a 1.5 L/min methane and 3.0 L/min oxygen flow with an additional 5.0 L/min oxygen dispersion flow around it. The synthesized solid was collected from the quartz filter placed downstream of the flame region. The as-prepared catalysts are denoted as M-In$_2$O$_3$. Another series of catalysts were prepared using the same procedure to further study Ni promotion. The as-

prepared catalysts are denoted as In_2O_3, $NiO(x)$-In_2O_3 and NiO, where x stands for NiO content (wt%).

2.2 Catalyst characterization

N_2 physisorption. The textural properties of the as-prepared catalysts were studied by N_2 physisorption at -196 °C at a Micrometrics TriStar II 3020 instrument. For the measurement, approximate 100 mg of sample was transferred into a glass sample tube and then pretreated at 120 °C overnight under N_2 flow. The Brunauer-Emmett-Teller (BET) method was used to estimate specific surface area of the catalysts.

X-ray diffraction (XRD). The crystal structure of the as-prepared catalysts was analyzed using a Bruker D2 Phaser diffractometer with Cu Kα radiation (1.5406 Å). The XRD patterns were recorded between 15-80˚ with a step size of 0.05˚ at 1.0 s/step scan rate.

Transmission electron microscopy (TEM). The morphology of the as-prepared catalysts was studied by TEM using a FEI Tecnai (type Sphera) instrument operating at an acceleration voltage of 200 kV. For this purpose, appropriate amounts of sample were dispersed in ethanol under ultrasonic exposure and then deposited on a holey Cu grid.

Temperature programmed reduction (H_2-TPR). The reducibility of the as-prepared catalysts was analyzed by H_2-TPR using a Micromeritics AutoChem II setup. Typically, about 50 mg of sample was loaded into a quartz U-tube between two quartz wool layers. The sample was pretreated at 200 °C for 1 h in a 5 vol% O_2 in He flow (50 mL/min) before the measurement. The TPR profile was recorded by heating the sample from 40 °C to 700 °C at a rate of 10 °C/min in a 4 vol% H_2 in He flow (50 mL/min). The H_2 consumption was recorded by a TCD and calibrated against a reference Cu/SiO_2 sample.

X-ray photoelectron spectroscopy (XPS). The surface chemical properties of the as-prepared and used catalysts after CO_2 hydrogenation were studied using a K-Alpha XPS instrument (Thermo Scientific) with a monochromatic small-spot X-ray source and an 180˚ double focusing hemispherical analyzer. For the analysis of used catalysts, a quasi in situ approach was adopted. Specifically, the samples were placed on a double-sided carbon tape in a glovebox and then transferred to the spectrometer via an air-tight transfer holder. The sample preparation of the as-prepared catalysts was carried out at ambient conditions. Spectra were collected using an aluminum anode (Al Kα = 1486.68 eV) operating at 72 W and a spot size of 400 μm. Survey scans were measured at a constant pass energy of 200 eV and region scans at 50 eV. The spectra were analyzed using the CasaXPS software (version 3.2.23) and energy calibration was performed again the C 1s peak of adventitious carbon set at a binding energy of 284.6 eV.

X-ray absorption spectroscopy (XAS). Extended X-ray absorption fine structure (EXAFS) measurements at Ni K-edge and In K-edge were done at beamline B18 of the Diamond Light

Source (Didcot, UK). EXAFS measurements of fresh and used catalysts were performed in fluorescence mode with a 36-element Ge detector. The NiO reference was measured in transmission mode. Ni and In foils were measured simultaneously with each catalyst sample in transmission mode for energy calibration. Si(111) and Si(311) monochromators were used at the Ni and In K-edges, respectively. EXAFS data reduction including energy calibration, background subtraction, normalization and EXAFS fitting analysis was carried out using the Demeter package (Athena/Artemis software)[52]. Scattering paths were calculated by using FEFF6 code based on crystal structures of NiO, Ni metal and In$_2$O$_3$. A Ni-In single scattering path was also included for the EXAFS fitting. In a typical fitting procedure, the energy shift (E$_0$), distance change (ΔR), coordination number (CN), and Debye-Waller factor (σ^2) were fitted, whereas the amplitude reduction factors (S$_0^2$) were determined from the EXAFS fitting of NiO reference and the sample of as-prepared In$_2$O$_3$ sample. The amplitude reduction factors were fixed when fitting other parameters. The plotted Fourier transformed EXAFS results weighted by k^3 have not been phase corrected.

2.3 Catalytic activity measurements

The catalytic performance of the NiO-In$_2$O$_3$ catalysts in CO$_2$ hydrogenation was evaluated at 250 °C and 30 bar using a down-flow stainless-steel reactor (ID = 4 mm). Typically, about 50 mg of sieved catalyst (125-250 μm), diluted with 200 mg SiC, was loaded into the reactor and then pretreated at 250 °C (rate = 5 °C/min) and 1 bar for 1 h in a N$_2$ flow (10 mL/min). After finishing the pretreatment, the catalyst was exposed to a reaction mixture flow (CO$_2$:H$_2$:N$_2$ = 10:30:10 mL/min) and the pressure in the reactor was increased to 30 bar. The effluent gas mixture was continuously analyzed by an online gas chromatography (Interscience, CompactGC) equipped with Rtx-1 (FID), Rt-QBond and Molsieve 5A (TCD), and Rt-QBond (TCD) columns. Measurements were typically taken for ca. 12 h when steady-state was reached. CO$_2$ conversion (X), product selectivity (S) and product formation rate (r) were calculated using the following equations:

$$X(CO_2) = \frac{F(CO)_{out} + F(CH_3OH)_{out} + F(CH_4)_{out}}{F(CO_2)_{out} + F(CO)_{out} + F(CH_3OH)_{out} + F(CH_4)_{out}} \quad [1]$$

$$S(product) = \frac{F(product)_{out}}{F(CO)_{out} + F(CH_3OH)_{out} + F(CH_4)_{out}} \quad [2]$$

$$r(product) = \frac{F(product)_{out}}{V_m \times m_{cat}} \quad [3]$$

where F stands for the volumetric flow rate calculated based on N$_2$ internal standard using calibrated response factors and V_m the molar volume of ideal gas at standard temperature and pressure. For post-reaction analysis of XPS and XAS, the used catalysts after catalytic tests

were transferred avoiding air exposure: the reactor was depressurized at 250 °C, cooled to room temperature in N_2 flow, sealed with two three-way valves and transferred into a glovebox for storage and further processing.

3. Results and discussion

3.1 Screening of metal promotion

Using a one-step FSP approach, we prepared several In_2O_3-based catalysts promoted by typical base hydrogenation metals (Co, Ni, and Cu) together with Pd-promoted and unpromoted In_2O_3 catalysts. The loading of the promoter metal was 5 wt% in all cases. XRD measurements (**Figure D.1**) show that all the diffraction peaks belong to In_2O_3 phase (#PDF 00-006-0416). The average crystallite size of the samples estimated by use of the Scherrer equation was ~9 nm, irrespective of the doping metal. No diffraction peak related to the promoter in the form of metal or metal oxide was observed (**Figure D.1**), suggesting that all the promoter metals are highly dispersed. The $M-In_2O_3$ and In_2O_3 catalysts were evaluated for CO_2 hydrogenation to CH_3OH under industrially relevant conditions. The complete results are listed in **Table D.1**. A comparison of CH_3OH rates at 250 °C is presented in **Figure 5.1**. The $Co-In_2O_3$ and $Cu-In_2O_3$ catalysts displayed lower CH_3OH rates than In_2O_3, while Ni and Pd promotion gave rise to similar reaction rates. Note however, the the CH_3OH selectivity of the $Pd-In_2O_3$ catalyst was higher than that of the $Ni-In_2O_3$ catalyst. As Pd is a relatively expensive precious group metal and has already been extensively investigated to promote In_2O_3 for CH_3OH synthesis from CO_2,[40–43] we focused in this work on the development of practical In_2O_3-based catalysts for CO_2-to-methanol conversion using Ni as promoter.

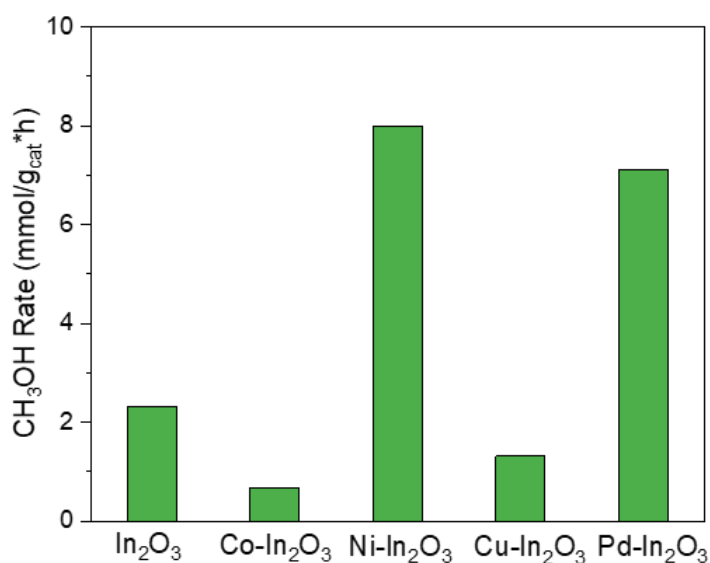**Figure 5.1.** Screening of metal promotion(M = 5 wt%) for In_2O_3 in CO_2 hydrogenation to methanol.

3.2 Basic characterization NiO-In$_2$O$_3$ catalysts

The textural properties of the as-prepared NiO-In$_2$O$_3$ catalysts were characterized with N$_2$ physisorption. The surface areas are given in **Table 5.1**. The specific surface area of In$_2$O$_3$ is 123 m^2/g. The binary NiO-In$_2$O$_3$ samples have a slightly lower surface area in the range 98-114 m^2/g. The NiO reference has a surface area of 137 m^2/g. The morphology and average particle size of the as-prepared catalysts were studied by transmission electron microscopy as shown in **Figure 5.2**. All the catalysts prepared by FSP displayed a similar morphology consisting of homogeneously distributed globular nanoparticles. The average particle size of the samples is in the 6.5-7.5 nm range, irrespective of the chemical composition.

Table 5.1. Specific surface areas and In$_2$O$_3$ lattice constants of as-prepared NiO-In$_2$O$_3$ catalysts.

Catalyst	S$_{BET}$ (m^2/g)	Lattice constant a (Å)
In$_2$O$_3$	123	10.118
NiO(1)-In$_2$O$_3$	110	10.112
NiO(6)-In$_2$O$_3$	98	10.110
NiO(25)-In$_2$O$_3$	104	-
NiO(50)-In$_2$O$_3$	110	-
NiO(75)-In$_2$O$_3$	114	-
NiO	137	-
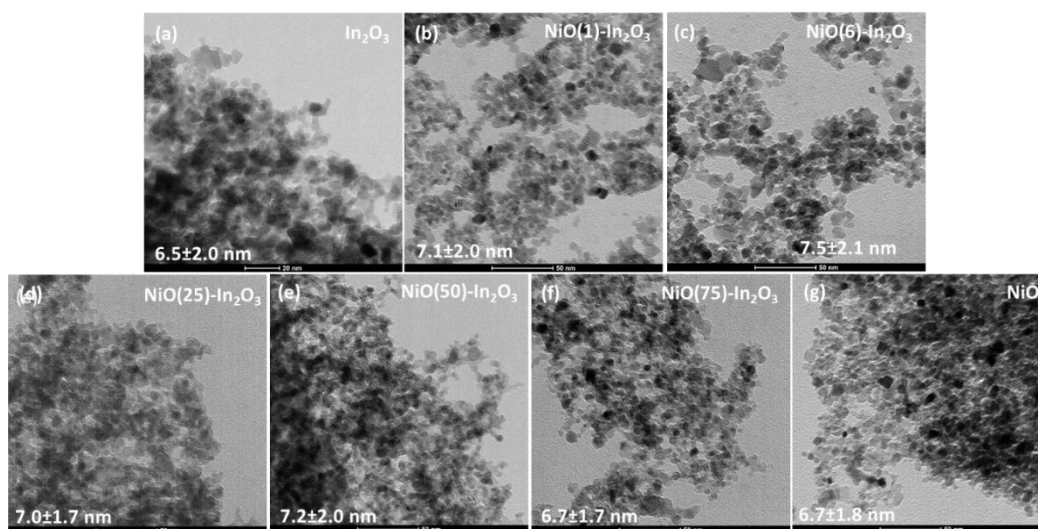
Figure 5.2. TEM images of as-prepared NiO-In$_2$O$_3$ catalysts with varying NiO content.

XRD patterns of the as-prepared NiO-In$_2$O$_3$ catalysts are given in **Figure 5.3**. We observe that the samples with a NiO content up to 6 wt% have the crystal structure of In$_2$O$_3$ (#PDF 00-006-0416). In addition, the In$_2$O$_3$ lattice constant decreases with increasing NiO loading (**Table 5.1**), implying the substitution of smaller Ni atoms in In$_2$O$_3$ phase. It should be noted that the changes in the lattice constant are very small. The samples with a NiO content of 50 wt% or higher mainly consist of the NiO phase (#PDF 00-047-1049). The sample with an intermediate NiO

content of 25 wt% displays new diffraction peaks, which could be linked to a spinel phase (e.g., $NiIn_2O_4$).[53–55] In line with the N_2 physisorpion and TEM results, the XRD patterns of the NiO-In_2O_3 catalysts show significant broadening of the diffractions peaks which points to the nanocrystalline nature of catalyst particles.

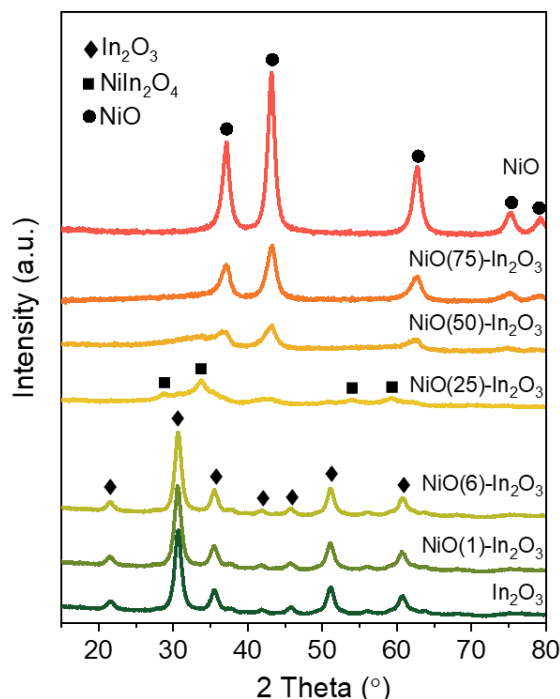**Figure 5.3.** XRD patterns of as-prepared NiO-In_2O_3 catalysts with varying NiO content.

3.3 Catalytic performance

The CO_2 hydrogenation performance of the NiO-In_2O_3 catalysts was determined at 250 °C and 30 bar. **Figure 5.4a** shows that addition of a small amount of NiO (1 wt% or 6 wt%) led to a substantial increase of CO_2 conversion, while the product distribution remains almost the same with CH_3OH and CO as the main reaction products. This indicates that the active sites for CO_2 activation in the NiO-In_2O_3 catalysts are not affected by Ni addition. The following trends are observed when the NiO content was further increased: (i) CO_2 conversion decreased as compared to NiO(*6*)-In_2O_3 and (ii) the CO and CH_4 selectivity increased at the expense of CH_3OH selectivity. Based on these observations and the XRD results, it is clear that In_2O_3 phase plays a pivotal role in the selective CH_3OH synthesis from CO_2 as in line with recent reports.[29,30,32] **Figure 5.4b** shows that CH_3OH rate first increased and then decreased with respect to NiO content, pointing to Ni-In synergy in CH_3OH synthesis from CO_2. At the optimum NiO content (6 wt%), the CH_3OH rate is nearly 4 times higher than that of In_2O_3. The formation of CH_4 at high NiO content points to the formation of metallic Ni particles, which are known to catalyze CO_2 methanation.[56] **Figure 5.4c** and **5.4d** show that CO_2 conversion and CH_3OH rates for In_2O_3, NiO(*1*)-In_2O_3 and NiO(*6*)-In_2O_3 were stable during the performance test of ~12 h.
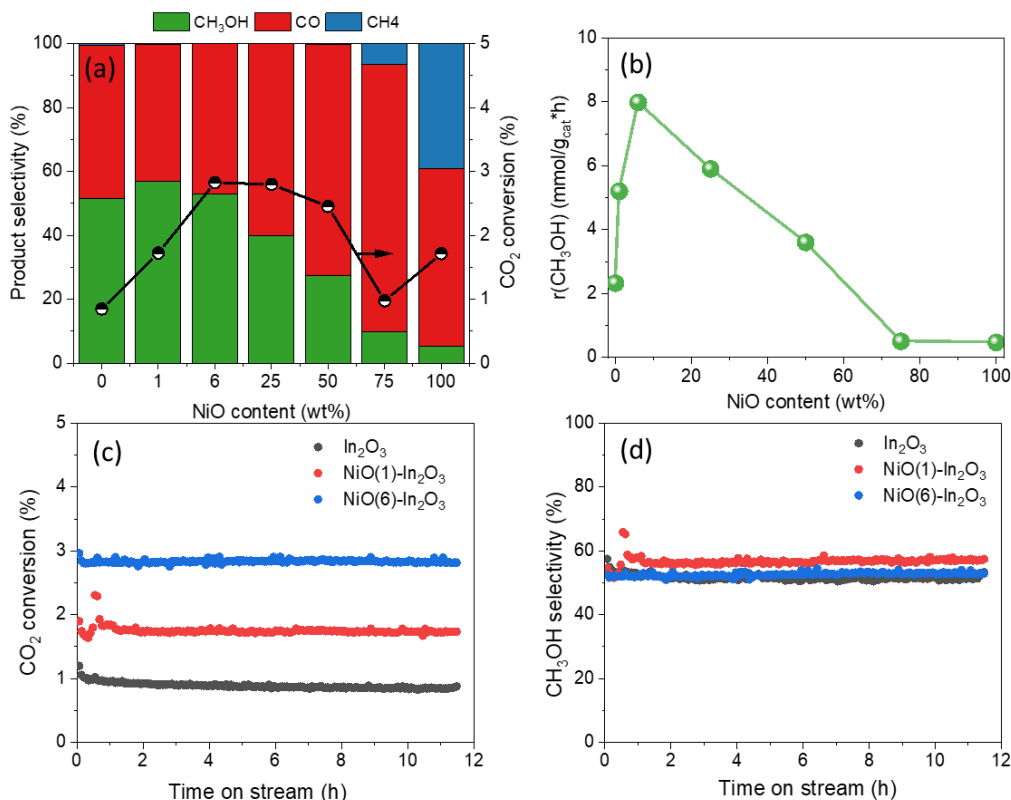
Figure 5.4. (a) CO$_2$ conversion and product distribution and (b) CH$_3$OH formation rate versus NiO content. Time-on-stream (TOS) behavior of (c) CO$_2$ conversion and (d) CH$_3$OH selectivity over In$_2$O$_3$, NiO(1)-In$_2$O$_3$ and NiO(6)-In$_2$O$_3$ catalysts.

3.4 Characterization Ni-In synergy

Figure **5.5a** and **5.5b** show Ni 2p$_{3/2}$ and In 3d$_{5/2}$ XP spectra of the as-prepared NiO-In$_2$O$_3$ catalysts. Interpretation of the 2p core level of transition metal oxides with unfilled d-orbitals is complex because of the main line multiplet contributions as well as satellite peaks.[57] The NiO spectrum is similar to that of polycrystalline NiO with complex multiplet splitting of the main lines at binding energies (BE) of 853.0 eV and 854.9 eV and a main shake-up feature at 860.1 eV. The Ni 2p$_{3/2}$ XP spectra for the NiO-In$_2$O$_3$ catalysts are different. The XP spectra of NiO(75)-In$_2$O$_3$ and Ni(50)-In$_2$O$_3$ contain similar lines as NiO, although the contribution around 854.9 eV is less intense. The presence of bulk NiO in these samples is consistent with the XRD results. Reducing the NiO content leads to a strong decrease of the intensity of the peak at 853.0 eV. The main peaks at about 855.1 eV of NiO(1)-In$_2$O$_3$ and NiO(6)-In$_2$O$_3$ samples can have different origins. In principle, this feature can be due to Ni^{3+}.[58,59] Similar XP spectra with a main contribution at 855.5 eV (N.B. BE of C 1s set at 285.0 eV) were also reported for Ni/TiO$_2$ and Ni/CeO$_2$ samples and explained by the presence of very small NiO patches stabilized by strong metal-support interactions.[59] The XP spectra of the In 3d region of the NiO(1)-In$_2$O$_3$ and NiO(6)-In$_2$O$_3$ samples show a significant shift of the In 3d$_{5/2}$ core line to lower BE in comparison to the spectrum for In$_2$O$_3$. This shift can be associated with Ni substitution in the

In$_2$O$_3$ lattice because the Ni-O bond is stronger than the In-O bond.[60] This shift is absent in the other samples, suggesting an electronic structure similar to undoped In$_2$O$_3$ for NiO(x)-In$_2$O$_3$ catalysts ($x \geq 25$).
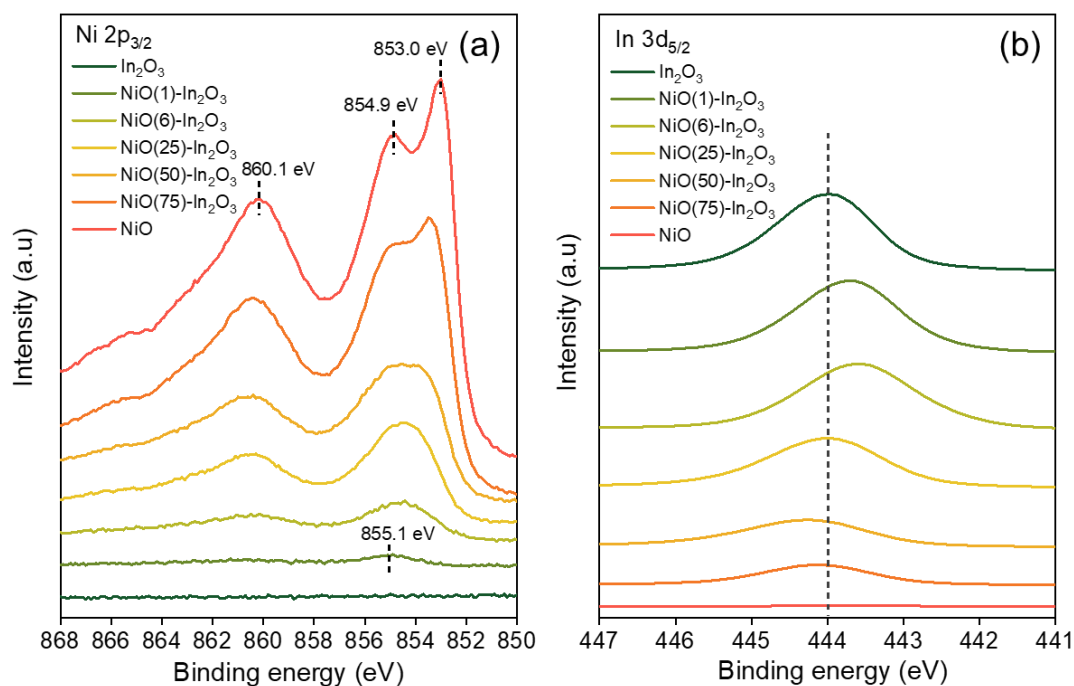

Figure 5.5 Ni 2p$_{3/2}$ and In 3d$_{5/2}$ XP spectra of as-prepared NiO-In$_2$O$_3$ catalysts.

Normalized XANES spectra at the Ni K-edge are presented in **Figure 5.6**. The half-edge energies for NiO(1)-In$_2$O$_3$ and NiO(6)-In$_2$O$_3$ are located at 8344.2 eV and 8343.9 eV. These values are substantially higher than the half-edge energy of 8342.5 eV observed for NiO. Therefore, it appears likely that Ni is in the 3+ state in these NiO(x)-In$_2$O$_3$ (x $\leq$ 6) samples. EXAFS analysis was used to investigate the Ni-In interactions in these samples. **Figure 5.7** displays the Fourier transforms of the k^3-weighted EXAFS data of the Ni-promoted and unpromoted In$_2$O$_3$ samples and the fit results for the Ni EXAFS are collected in **Table 5.2**. It was found that NiO(1)-In$_2$O$_3$ and NiO(6)-In$_2$O$_3$ samples contain a Ni-In shell due to Ni-O-In contributions as shown in **Figure 5.7a**.[61] This Ni-In (oxidic) shell has CN of 6.30 and 5.25 for the samples with 1 and 6 wt% NiO, respectively. Each Ni atom is surrounded by 6 O atoms, as expected. The lower CN of the Ni-In (oxidic) shell for NiO(6)-In$_2$O$_3$ goes together with the presence of a Ni-Ni (oxidic) shell due to Ni-O-Ni contributions in NiO. The corresponding CN is 7.5. The coordination environment of In in In$_2$O$_3$ does not change profoundly for the as-prepared NiO-In$_2$O$_3$ catalysts (**Figure 5.7b**), which is to be expected in view of the high In$_2$O$_3$ content. The fit results of In EXAFS are collected in **Table D.2** also confirm that the bulk of In$_2$O$_3$ did not change significantly among the as-prepared and used catalysts.
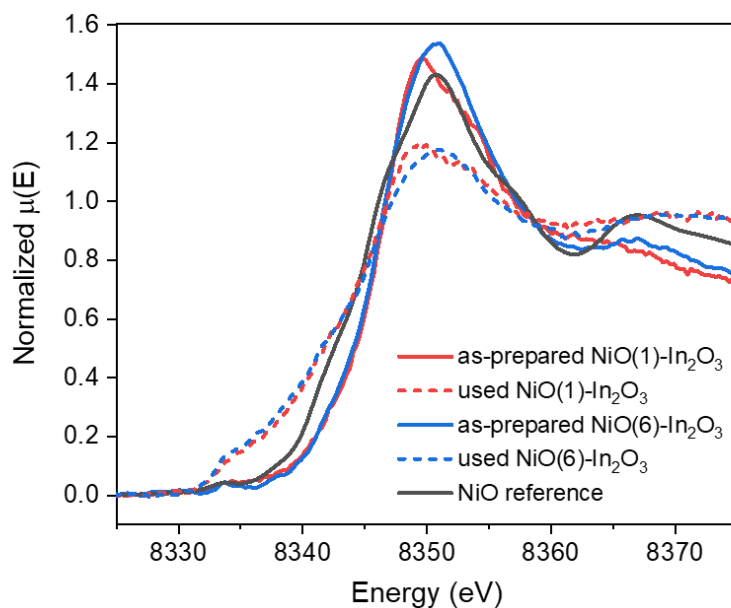
Figure 5.6. Normalized XANES spectra at Ni K-edge of as-prepared and used NiO(x)-In$_2$O$_3$ (x = 1 and 6) catalysts with NiO reference.
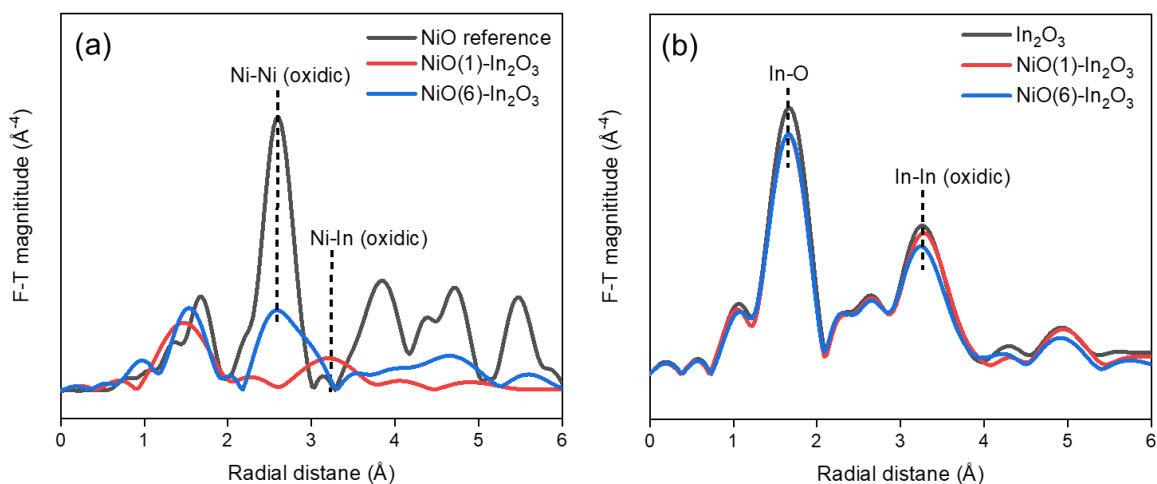
Figure 5.7. (a) Ni and (b) In K-edge k^3-weighted R-space plots of as-prepared In$_2$O$_3$, NiO(1)-In$_2$O$_3$ and NiO(6)-In$_2$O$_3$ catalysts.

Based on the preceding XPS and XAS results, we conclude that NiO(1)-In$_2$O$_3$ contains highly dispersed and possibly isolated Ni cations, which are mostly substituting for In in the In$_2$O$_3$ lattice. The NiO(6)-In$_2$O$_3$ sample additionally contains very small Ni-oxide patches stabilized by the In$_2$O$_3$ support. Increasing NiO content of the NiO-In$_2$O$_3$ results in the formation of larger NiO particles as evident from the increasing contribution of the XP component with a BE of 853.0 eV. Combined with the XRD results, we can state that the samples with a NiO content up to 6 wt% contain a small amount of Ni substituted in In$_2$O$_3$ and very small Ni-oxide patches dispersed on In$_2$O$_3$, and that Ni in the highly dispersed Ni-oxide phases is likely present as Ni^{3+}.

Table 5.2: Fit parameters of k^3-weighted EXAFS spectra at Ni K-edge.

	Path	r(Å) [±]	CN[±]	δ^2 (Å^2) [±]	r^2
As-prepared NiO(1)-In$_2$O$_3$	Ni-O	2.04 [0.02]	6.02 [1.20]	0.007 [0.004]	0.054
	Ni-In (oxidic)	3.34 [0.05]	6.30 [2.20]	0.016 [0.008]	
Used NiO(1)-In$_2$O$_3$	Ni-O	1.97 [0.06]	1.74 [set]	0.001 [0.003]	0.017
	Ni-Ni (metallic)	2.37 [0.06]	7.38 [4.04]	0.032 [0.010]	
	Ni-In (oxidic)	3.33 [0.05]	2.31 [set]	0.007 [0.005]	
As-prepared NiO(6)-In$_2$O$_3$	Ni-O	2.09 [0.03]	6.25 [1.92]	0.007 [0.006]	0.030
	Ni-Ni (oxidic)	3.01 [0.03]	7.46 [5.21]	0.008 [0.007]	
	Ni-In (oxidic)	3.33 [0.28]	5.25 [set]	0.032 [0.037]	
Used NiO(6)-In$_2$O$_3$	n.a.*	n.a.	n.a.	n.a.	n.a.

* no proper fit was obtained.

H$_2$-TPR was used to investigate how Ni addition affects oxygen vacancy (O$_v$) formation in In$_2$O$_3$ (**Figure 5.8a**). The TPR profile of In$_2$O$_3$ is characterized by a feature around 200 °C due to the formation of surface oxygen vacancies (O$_v$) in In$_2$O$_3$[39]. Bulk reduction starts above 400 °C. For NiO(*1*)-In$_2$O$_3$ and NiO(*6*)-In$_2$O$_3$ samples, we observed that the low-temperature reduction peak due to O$_v$ formation is broadened (two features resolved for NiO(1)-In$_2$O$_3$). This can be explained by the introduction of Ni in the In$_2$O$_3$ lattice, resulting in more heterogeneous reduction behavior of the surface. Note that the Ni-O bond dissociation energy of 396 kJ/mol is higher than that of In-O (346 kJ/mol).[60] Quantification of the reduction peaks indicates that the O$_v$ densities are respectively 54 and 52 μmol/g$_{cat}$ for NiO(*1*)-In$_2$O$_3$ and NiO(*6*)-In$_2$O$_3$, which are slightly higher than the value of 42 μmol/g$_{cat}$ for In$_2$O$_3$. The corresponding specific surface area normalized O$_v$ densities are 0.34, 0.49 and 0.53 μmol/m^2 for In$_2$O$_3$, NiO(1)-In$_2$O$_3$ and NiO(6)-In$_2$O$_3$, respectively. Thus, although one excepts less O$_v$ upon Ni substitution due to the stronger Ni-O than In-O bond, it may be that the substitution of a smaller cation distorts the In$_2$O$_3$ lattice and weakens the In-O bonds.

The TPR profile of NiO(*1*)-In$_2$O$_3$ also contains a new reduction feature at ~300 °C. We attribute this feature to the reduction of Ni cations substituted in the In$_2$O$_3$ lattice. The H$_2$/Ni ratio corresponding to this feature amounts to 0.7, indicating that likely only a part of Ni can be reduced. This may be due to a part of Ni cations residing in the bulk of In$_2$O$_3$. The TPR profile of NiO(*6*)-In$_2$O$_3$ contains more reduction features than NiO(*1*)-In$_2$O$_3$, which is indicative of the more heterogeneous speciation of Ni in this sample. It should be also mentioned that spillover hydrogen from metallic Ni can facilitate the reduction of In$_2$O$_3$ at lower temperature, further complicating the interpretation of this profile. Furthermore, O 1s XP spectra (**Figure 5.8b**) of the used catalysts were analyzed to estimate the surface O$_v$ density after CO$_2$ hydrogenation reaction. The peaks at binding energy of 529.3 eV and 531.2 eV are assigned to lattice O in In$_2$O$_3$ (O$_{lattice}$) and O close to oxygen vacancies (O$_{vacancy}$), respectively.[40] Peak deconvolution indicates that In$_2$O$_3$, NiO(*1*)-In$_2$O$_3$ and NiO(*6*)-In$_2$O$_3$ contain comparable density of surface O$_v$, although the addition of Ni leads to a slight increase of O$_v$ density.
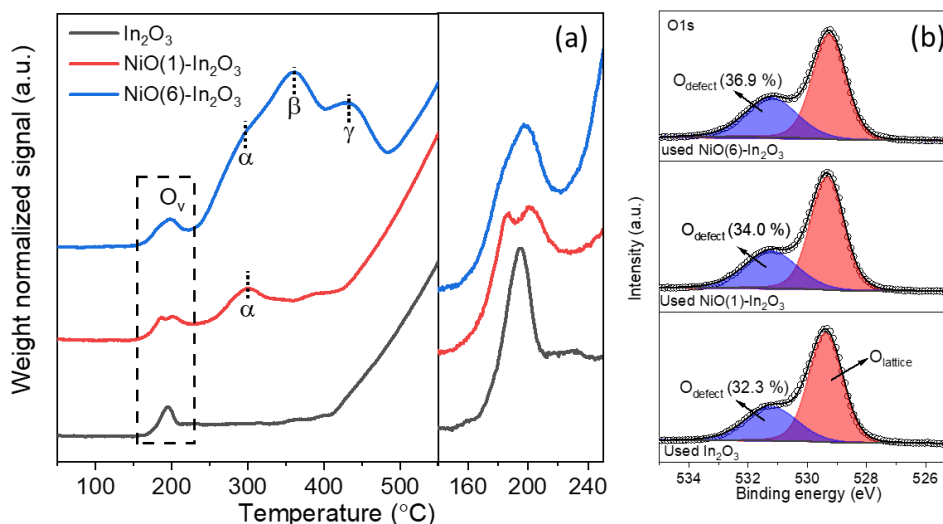
Figure 5.8. (a) H₂-TPR profiles of as-prepared In₂O₃, NiO(*1*)-In₂O₃ and NiO(*6*)-In₂O₃ catalysts. (b) O 1s XP spectra of used In₂O₃, NiO(*1*)-In₂O₃ and NiO(*6*)-In₂O₃ catalysts.

We next compare the Ni 2p$_{3/2}$ XP spectra (**Figure 5.9a**) and EXAFS data at the Ni K-edge (**Figure 5.9b**) of as-prepared and used NiO(*1*)-In₂O₃ and NiO(*6*)-In₂O₃ catalysts. Ni reduction is evidenced by the strong decrease of the Ni component at 855.1 eV and the appearance of a Ni^0 component at 851.9 eV in the XP spectra. Although Ni reduction is extensive, some Ni cations remain in both used samples and its absolute amount appears to be higher for NiO(*6*)-In₂O₃. The Ni reduction also follows from the clear change of the XANES spectrum, i.e., the edge half energy of the XANES spectra shifts from ~8344.0 eV to ~8341.5 eV (**Figure 5.6**). The Ni EXAFS data (**Figure 5.8b, Table 5.2**) show that the Ni-O, Ni-O-Ni and Ni-O-In contributions strongly decrease after exposure to the reducing reaction conditions. It was not possible to obtain a proper fit for the used NiO(*6*)-In₂O₃ sample. The strong decrease in the Ni-O and Ni-In (oxidic) shells with final CN of 1.7 and 2.3 together with the appearance of a Ni-Ni (metallic) shell with CN ~ 7 demonstrate that a substantial fraction of Ni cations were reduced into small Ni particles.

It is by now accepted that oxygen vacancies in In₂O₃ serve as the active sites for CH₃OH synthesis from CO₂ hydrogenation.[29,30,32] In the present study, the H₂-TPR and O 1s XPS spectra indicate that introduction of Ni in the In₂O₃ lattice by FSP results in a larger amount of O$_v$ in comparison to a pure In₂O₃ sample. The higher O$_v$ density due to Ni addition can contribute to a higher CH₃OH rate. Nevertheless, the increase in the CH₃OH rate is much larger (In₂O₃:NiO(1)-In₂O₃:NiO(6)-In₂O₃ ≈ 1:2:4) than that in the estimated O$_v$ density normalized by surface area (In₂O₃:NiO(1)-In₂O₃:NiO(6)-In₂O₃ ≈ 1:1.4:1.6). Another important aspect of CH₃OH synthesis on In₂O₃ is H₂ activation. It has been demonstrated that heterolytic H₂ dissociation on unpromoted In₂O₃ catalysts requires overcoming a high activation barrier of 0.95 eV (~91 kJ/mol).[32] This is also in line with the strong dependence of the CH₃OH rate on
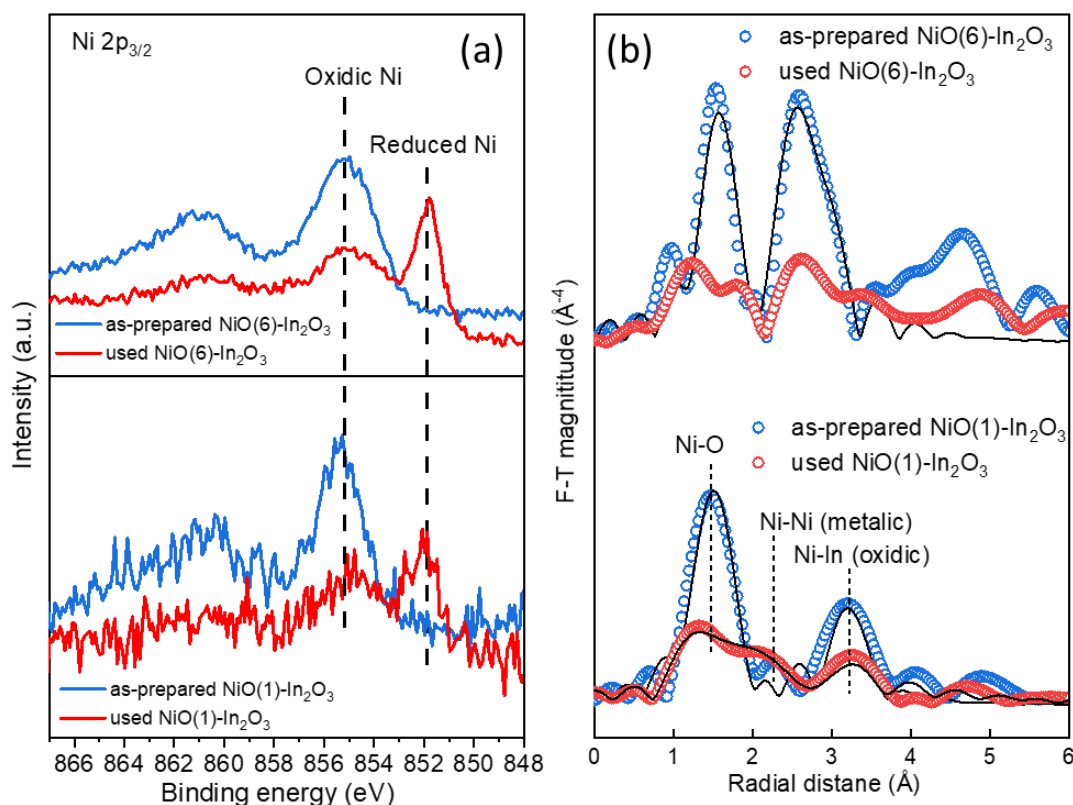
Figure 5.9. (a) Ni $2p_{3/2}$ XP spectra and (b) Ni K-edge k^3-weighted R-space plots of as-prepared and used NiO(x)-In$_2$O$_3$ ($x \leq 6$) catalysts.

the H$_2$ partial pressure.[32,43,62] Our characterization of the used NiO-In$_2$O$_3$ catalysts demonstrate that the highly dispersed Ni phase in the as-prepared NiO-In$_2$O$_3$ catalysts, present as Ni substituted in the In$_2$O$_3$ lattice and dispersed NiO on In$_2$O$_3$, can be reduced to form metallic Ni particles during CO$_2$ hydrogenation. These Ni particles will facilitate H$_2$ activation and, therefore, increase the rate of hydrogenation of CO$_2$ adsorbed on O$_v$. Such a metal promotion mechanism has been discussed for other In$_2$O$_3$-based catalysts.[42,43,49,63] A detailed study of Perez-Ramirez' group[43] emphasized the role of very finely dispersed Pd clusters in H$_2$ activation and the role of H atoms in hydrogenating of the O$_v$-adsorbed CO$_2$. The CH$_3$OH rate of our best-performing NiO-In$_2$O$_3$ catalyst (~0.25 g$_{CH3OH}$/(g$_{cat}$×h), 250 °C and 30 bar) is nearly similar with the CH$_3$OH rate of Pd-In$_2$O$_3$ catalysts (~0.6-1.0 g$_{CH3OH}$/(g$_{cat}$×h), 280 °C and 50 bar). Thus, we conclude that Ni can be considered a potential replacement for Pd in developing practical In$_2$O$_3$-based catalysts for CO$_2$ hydrogenation to methanol.

4. Conclusions

Aiming at improving In$_2$O$_3$ catalyst for CO$_2$ hydrogenation to CH$_3$OH, a bimetallic Ni-In system was identified by catalyst screening using one-step FSP approach in current study, displaying comparable performance to Pd-In$_2$O$_3$ and much higher performance than Co- and Cu-In$_2$O$_3$. N$_2$-physisorption and TEM results demonstrate the NiO-In$_2$O$_3$ catalysts prepared by

FSP have similar particle sizes (ca. 7 nm) and morphology. Catalytic activity measurements point to a strong Ni-In synergy in CO$_2$ hydrogenation to CH$_3$OH with an optimal NiO content of 6 wt%. Characterization of the catalysts with low NiO content ($\leq$ 6 wt%) show that a small amount of Ni is substituted in In$_2$O$_3$ lattice, the remainder being present as highly dispersed Ni-oxide, while Ni is present as bulk NiO particles at high NiO content ($\geq$ 50 wt%). H$_2$-TPR measurements show an increased O$_v$ density for the catalysts with a low NiO content ($\leq$ 6 wt%), suggesting that Ni substitution distorts the In$_2$O$_3$ lattice. XPS and XAS measurements demonstrate that the use of as-prepared NiO-In$_2$O$_3$ catalysts in CO$_2$ hydrogenation led to Ni reduction and formation of small Ni particles. Besides the increased O$_v$ density, it is concluded that mainly the formation of metallic Ni species enhancing H$_2$ dissociation can explain the Ni-In synergy in CO$_2$ hydrogenation to methanol for the NiO-In$_2$O$_3$ catalysts.

References

1   M. He, Y. Sun and B. Han, *Angew. Chem. Int. Ed.*, 2013, **52**, 9620–9633.

2   G. Centi, E. A. Quadrelli and S. Perathoner, *Energy Environ. Sci.*, 2013, **6**, 1711–1731.

3   J. Rogelj, M. Den Elzen, N. Höhne, T. Fransen, H. Fekete, H. Winkler, R. Schaeffer, F. Sha, K. Riahi and M. Meinshausen, *Nature*, 2016, **534**, 631–639.

4   X. Jiang, X. Nie, X. Guo, C. Song and J. G. Chen, *Chem. Rev.*, 2020, **120**, 7984–8034.

5   J. Zhong, X. Yang, Z. Wu, B. Liang, Y. Huang and T. Zhang, *Chem. Soc. Rev.*, 2020, **49**, 1385–1413.

6   H. Yang, C. Zhang, P. Gao, H. Wang, X. Li, L. Zhong, W. Wei and Y. Sun, *Catal. Sci. Technol.*, 2017, **7**, 4580–4598.

7   A. Álvarez, A. Bansode, A. Urakawa, A. V. Bavykina, T. A. Wezendonk, M. Makkee, J. Gascon and F. Kapteijn, *Chem. Rev.*, 2017, **117**, 9804–9838.

8   S. Gumber and A. V. P. Gurumoorthy, in *Methanol: Science and Engineering*, Elsevier B.V., 2018, pp. 661–674.

9   G. A. Olah, *Angew. Chem. Int. Ed.*, 2005, **44**, 2636–2639.

10   A. Goeppert, M. Czaun, J.-P. Jones, G. K. Surya Prakash and G. A. Olah, *Chem.Soc.Rev.*, 2014, **43**, 7995–8048.

11   Malte Behrens, Felix Studt, Igor Kasatkin, Stefanie Kühl, Michael Hävecker, Frank Abild-Pedersen, Stefan Zander, Frank Girgsdies, Patrick Kurr, Benjamin-Louis Kniep, Michael Tovar, Richard W. Fischer, Jens K. Nørskov and Robert Schlög, Science., 2012, **336**, 893–897.

12   J. Sehested, *J. Catal.*, 2019, **371**, 368–375.

13   M. Behrens, *Angew. Chem. Int. Ed.*, 2016, **55**, 14906–14908.

14   B. Liang, J. Ma, X. Su, C. Yang, H. Duan, H. Zhou, S. Deng, L. Li and Y. Huang, *Ind. Eng. Chem. Res.*, 2019, **58**, 9030–9037.

15   A. Prašnikar, A. Pavlišič, F. Ruiz-Zepeda, J. Kovač and B. Likozar, *Ind. Eng. Chem. Res.*, 2019, **58**, 13021–13029.

16   M. S. Jingang Wu Masami Takeuchi Taiki Watanabe, *Appl. Catal. A Gen.*, 2001, **218**, 235–240.

17   B. Yang, L. Li, Z. Jia, X. Liu, C. Zhang and L. Guo, *Chinese Chem. Lett.*, in press, DOI:10.1016/j.cclet.2020.05.031.

18   K. Li and J. G. Chen, *ACS Catal.*, 2019, **9**, 7840–7861.

19   Y. H. Wang, W. G. Gao, H. Wang, Y. E. Zheng, W. Na and K. Z. Li, *RSC Adv.*, 2017, **7**, 8709–8717.

20   K. Larmier, W.-C. Liao, S. Tada, E. Lam, R. Verel, A. Bansode, A. Urakawa, A. Comas-Vives and C. Copéret, *Angew. Chem. Int. Ed.*, 2017, **56**, 2318–2323.

21   I. Ro, Y. Liu, M. R. Ball, D. H. K. Jackson, J. P. Chada, C. Sener, T. F. Kuech, R. J. Madon, G. W. Huber and J. A. Dumesic, *ACS Catal.*, 2016, **6**, 7040–7050.

22   J. Wang, G. Li, Z. Li, C. Tang, Z. Feng, H. An, H. Liu, T. Liu and C. Li, *Sci. Adv.*, 2017, **3**, 1–10.

23   C.-S. Li, G. Melaet, W. T. Ralston, K. An, C. Brooks, Y. Ye, Y.-S. S. Liu, J. Zhu, J. Guo, S.

Alayoglu and G. A. Somorjai, *Nat Commun*, 2015, **6**, 6538.

24 S. Posada-Perez, F. Vines, P. J. Ramirez, A. B. Vidal, J. A. Rodriguez and F. Illas, *Phys Chem Chem Phys*, 2014, **16**, 14912–14921.

25 F. Christian Kunkel Vines, Francesc Illas, *Energy Environ. Sci*, 2016, **1**, 141–144.

26 M. S. Duyar, C. Tsai, J. L. Snider, J. A. Singh, A. Gallo, J. S. Yoo, A. J. Medford, F. Abild-Pedersen, F. Studt, J. Kibsgaard, S. F. Bent, J. K. Nørskov and T. F. Jaramillo, *Angew. Chem. Int. Ed.*, 2018, **57**, 15045–15050.

27 I. Sharafutdinov, C. F. Elkjær, H. W. Pereira de Carvalho, D. Gardini, G. L. Chiarello, C. D. Damsgaard, J. B. Wagner, J. Grunwaldt, S. Dahl, I. Chorkendorff, C. Fink, H. Wallace, P. De Carvalho, D. Gardini, G. Luca, C. Danvad, J. Birkedal, J. Grunwaldt, S. Dahl and I. Chorkendorff, *J. Catal.*, 2014, **320**, 77–88.

28 E. M. Fiordaliso, I. Sharafutdinov, H. W. P. Carvalho, J. D. Grunwaldt, T. W. Hansen, I. Chorkendorff, J. B. Wagner and C. D. Damsgaard, *ACS Catal.*, 2015, **5**, 5827–5836.

29 J. Ye, C. Liu and Q. Ge, *J. Phys. Chem. C*, 2012, **116**, 7817–7825.

30 J. Ye, C. Liu, D. Mei and Q. Ge, *ACS Catal.*, 2013, **3**, 1296–1306.

31 K. Sun, Z. Fan, J. Ye, J. Yan, Q. Ge, Y. Li, W. He, W. Yang and C. Liu, *J. CO2 Util.*, 2015, **12**, 1–6.

32 M. S. Frei, M. Capdevila-Cortada, R. García-Muelas, C. Mondelli, N. López, J. A. Stewart, D. Curulla Ferré and J. Pérez-Ramírez, *J. Catal.*, 2018, **361**, 313–321.

33 S. Dang, B. Qin, Y. Yang, H. Wang, J. Cai, Y. Han, S. Li, P. Gao and Y. Sun, *Sci. Adv.*, 2020, **6**, 1–11.

34 M. S. Frei, C. Mondelli, A. Cesarini, F. Krumeich, R. Hauert, J. A. Stewart, D. C. Ferre and J. Pe, *ACS Catal.*, 2020, **10**, 1133–1145.

35 Y. Zhan, Y. Wang, D. Gu, C. Chen, L. Jiang and K. Takehira, *J. Catal.*, 2020, **383**, 283–296.

36 T. Chen, C. Cao, T. Chen, X. Ding, H. Huang, L. Shen, X. Cao, M. Zhu, J. Xu, J. Gao and Y.-F. Han, *ACS Catal.*, 2019, **9**, 8785–8797.

37 C.-Y. Chou and R. F. Lobo, *Appl. Catal. A Gen.*, 2019, **583**, 117144.

38 M. Dou, M. Zhang, Y. Chen and Y. Yu, *Surf. Sci.*, 2018, **672–673**, 7–12.

39 O. Martin, A. J. Martin, C. Mondelli, S. Mitchell, T. F. Segawa, R. Hauert, C. Drouilly, D. Curulla-Ferre and J. Perez-Ramirez, *Angew. Chem. Int. Ed.*, 2016, **55**, 6261–6265.

40 Z. Hong, Y. Cao, J. Deng and K. Fan, *Appl. Catal. B, Environ.*, 2017, **82**, 2–9.

41 A. García-Trenco, A. Regoutz, E. R. White, D. J. Payne, M. S. P. Shaffer and C. K. Williams, *Appl. Catal. B Environ.*, 2018, **220**, 9–18.

42 J. L. Snider, V. Streibel, M. A. Hubert, T. S. Choksi, E. Valle, D. C. Upham, J. Schumann, M. S. Duyar, A. Gallo, F. Abild-Pedersen and T. F. Jaramillo, *ACS Catal.*, 2019, **9**, 3399–3412.

43 M. S. Frei, C. Mondelli, R. García-Muelas, K. S. Kley, B. Puértolas, N. López, O. V. Safonova, J. A. Stewart, D. Curulla Ferré and J. Pérez-Ramírez, *Nat. Commun.*, 2019, **10**, 1–11.

44 J. Ye, C. J. Liu, D. Mei and Q. Ge, *J. Catal.*, 2014, **317**, 44–53.

45 A. Bavykina, I. Yarulina, A. J. Al Abdulghani, L. E. Gevers, M. N. Hedhili, X.-H. Miao, A. Ramirez, A. Pustovarenko, A. Dikhtiarenko, A. Cadiau, A. Aguilar Tapia, J. L. Hazemann, S. M. Kozlov, S. Ould-Chikh, L. Cavallo and J. Gascon, *ACS Catal.*, 2019, **9**, 6910–6918.

46   A. Pustovarenko, A. Dikhtiarenko, A. Bavykina, L. E. Gevers, A. Ramirez, S. Telalovic, A. Aguilar, J. L. Hazemann, S. Ould-chikh and J. Gascon, *ACS Catal.*, 2020, **10**, 5064–5076.

47   Z. Shi, Q. Tan, C. Tian, Y. Pan, X. Sun, J. Zhang and D. Wu, *J. Catal.*, 2019, **379**, 78–89.

48   A. R. Richard and M. Fan, *ACS Catal.*, 2017, **7**, 5679–5692.

49   X. Jia, K. Sun, J. Wang, C. Shen and C. Liu, *J. Energy Chem.*, 2020, **50**, 409–415.

50   W. Y. Teoh, R. Amal, L. Mädler and L. Madler, *Nanoscale*, 2010, **2**, 1324–1347.

51   R. Koirala, S. E. Pratsinis and A. Baiker, *Chem. Soc. Rev.*, 2016, **45**, 3053–3068.

52   B. Ravel and M. Newville, *J. Synchrotron Radiat.*, 2005, **12**, 537–541.

53   N. S. Hondow, Y. H. Chou, K. Sader, R. E. Douthwaite and R. Brydson, *ChemCatChem*, 2011, **3**, 990–998.

54   L. Chen, T. Horiuchi and T. Mori, *Appl. Catal. A Gen.*, 2001, **209**, 97–105.

55   J. Tasaki, T. Izushi, T. Ito, *Adv. Ceram.*, 1985, **15**, 169–174.

56   C. Vogt, E. Groeneveld, G. Kamsma, M. Nachtegaal, L. Lu, C. J. Kiely, P. H. Berben, F. Meirer and B. M. Weckhuysen, *Nat. Catal.*, 2018, **1**, 127–134.

57   A. P. Grosvenor, M. C. Biesinger, R. S. C. Smart and N. S. McIntyre, *Surf. Sci.*, 2006, **600**, 1771–1779.

58   A. N. Mansour, *Surf. Sci. Spectra*, 1994, **3**, 279–286.

59   A. Davidson, J. F. Tempere, M. Che, H. Roulet and G. Dufour, *J. Phys. Chem.*, 1996, **100**, 4919–4929.

60   Y. Li, W. Xu, W. Liu, S. Han, P. Cao, M. Fang, D. Zhu and Y. Lu, *ACS Appl. Electron. Mater.*, 2019, **1**, 1842–1851.

61   Y. An, S. Wang, D. Feng, Z. Wu and J. Liu, *Appl. Surf. Sci.*, 2013, **276**, 535–538.

62   M. S. Frei, C. Mondelli and J. Pérez-Ramírez, *Chimia (Aarau).*, 2020, **74**, 257–262.

63   Z. Han, C. Tang, J. Wang, L. Li and C. Li, *J. Catal.*, in press, DOI:10.1016/j.jcat.2020.06.018.

Appendix D
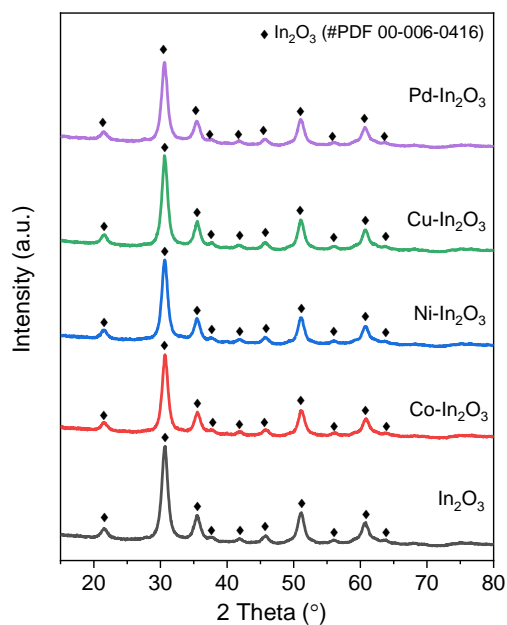
Figure D.1. XRD patterns of as-prepared In$_2$O$_3$ and M-In$_2$O$_3$ catalysts.
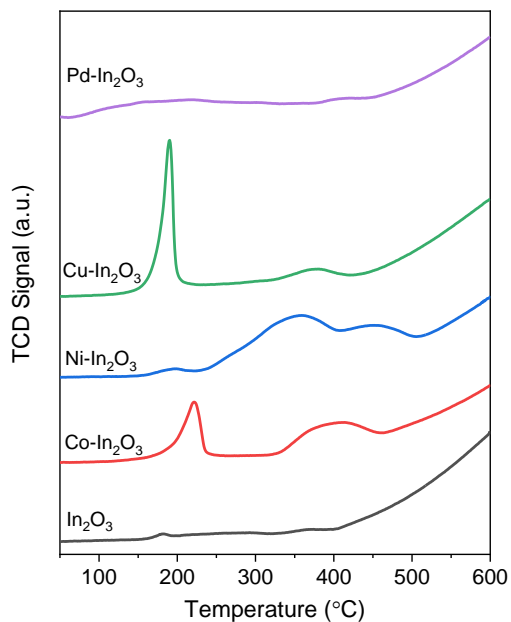

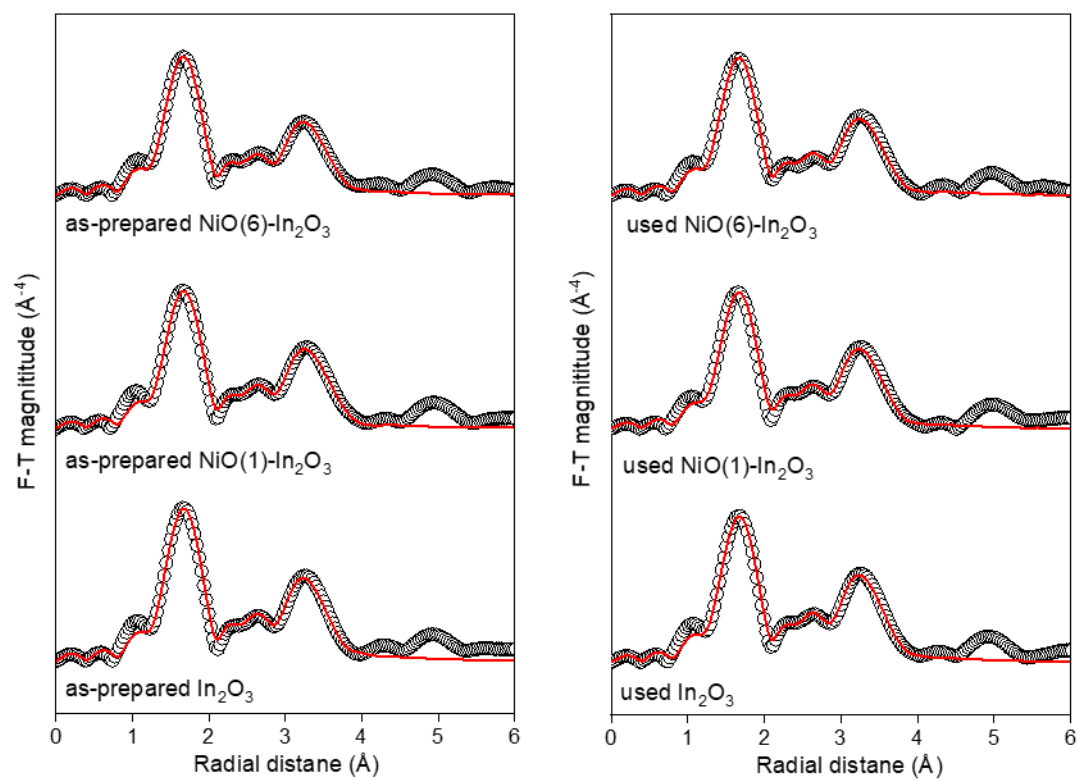**Figure D.2**. H$_2$-TPR profiles of as-prepared In$_2$O$_3$ and M-In$_2$O$_3$ catalysts.

Figure D.3. In K-edge k^3-weighted R-space plots of as-prepared and used $NiO(x)$-In_2O_3 ($x \leq 6$).

Table D.1. CO$_2$ hydrogenation performance of as-prepared In$_2$O$_3$ and M-In$_2$O$_3$ catalysts.

	X(CO$_2$) (%)	S(CH$_3$OH) (%)	r(CH$_3$OH) (mmol/g$_{cat}\times$h)	r(CO) (mmol/g$_{cat}\times$h)
In$_2$O$_3$	0.8	52	2.33	2.16
Co-In$_2$O$_3$	0.6	23	0.68	2.29
Ni-In$_2$O$_3$	2.8	53	7.98	7.06
Cu-In$_2$O$_3$	0.5	47	1.32	1.47
Pd-In$_2$O$_3$	1.9	72	7.10	2.80

Reaction conditions: 50 mg catalyst, 250 °C, 30 bar and CO$_2$:H$_2$:N$_2$ = 10:30:10 mL/min.

Table D.2. Fit parameters of k^3-weighted EXAFS spectra at the Ni K-edge.

	Path	r(Å) [±]	CN[±]	δ^2 (Å^2) [±]	r^2
As-prepared In$_2$O$_3$	In-O$_1$	2.11 [0.01]	2 [set]	0.002 [0.001]	
	In-O$_2$	2.18 [0.01]	4 [set]	0.002 [0.001]	0.009
	In-In$_1$ (oxidic)	3.38 [0.01]	6 [set]	0.005 [0.001]	
	In-In$_2$ (oxidic)	3.87 [0.03]	6 [set]	0.010 [0.004]	
Used In$_2$O$_3$	In-O$_1$	2.10 [0.01]	2 [set]	0.002 [0.001]	
	In-O$_2$	2.18 [0.01]	4 [set]	0.002 [0.001]	0.009
	In-In$_1$ (oxidic)	3.38 [0.01]	6 [set]	0.004 [0.001]	
	In-In$_2$ (oxidic)	3.87 [0.02]	6 [set]	0.008 [0.003]	
As-prepared NiO(1)-In$_2$O$_3$	In-O$_1$	2.10 [0.01]	2 [set]	0.002 [0.001]	
	In-O$_2$	2.18 [0.01]	4 [set]	0.002 [0.001]	0.010
	In-In$_1$ (oxidic)	3.38 [0.01]	6 [set]	0.005 [0.001]	
	In-In$_2$ (oxidic)	3.86 [0.02]	6 [set]	0.009 [0.003]	
Used NiO(1)-In$_2$O$_3$	In-O$_1$	2.10 [0.01]	2 [set]	0.002 [0.001]	
	In-O$_2$	2.18 [0.01]	4 [set]	0.002 [0.001]	0.010
	In-In$_1$ (oxidic)	3.37 [0.01]	6 [set]	0.005 [0.001]	
	In-In$_2$ (oxidic)	3.86 [0.03]	6 [set]	0.009 [0.004]	
As-prepared NiO(6)-In$_2$O$_3$	In-O$_1$	2.10 [0.01]	2 [set]	0.002 [0.001]	
	In-O$_2$	2.18 [0.01]	4 [set]	0.002 [0.001]	0.008
	In-In$_1$ (oxidic)	3.38 [0.01]	6 [set]	0.005 [0.001]	
	In-In$_2$ (oxidic)	3.86 [0.03]	6 [set]	0.010 [0.004]	
Used NiO(6)-In$_2$O$_3$	In-O$_1$	2.10 [0.01]	2 [set]	0.002 [0.001]	
	In-O$_2$	2.18 [0.01]	4 [set]	0.002 [0.001]	0.007
	In-In$_1$ (oxidic)	3.38 [0.01]	6 [set]	0.005 [0.001]	
	In-In$_2$ (oxidic)	3.86 [0.02]	6 [set]	0.010 [0.003]	

CHAPTER 6

Tuning the Hydrogenation Performance of Molybdenum (Oxy)carbide Catalysts by Controlling the Carburization Degree

ABSTRACT

Molybdenum (oxy)carbide catalysts supported on activated carbon were prepared by a carbothermal hydrogen reduction method without passivation step. Four carburization temperatures (500 °C, 600 °C, 700 °C and 800 °C) were selected to control the catalyst carburization degree based on studies of catalyst precursor carburization process by TGA-MS and in situ XANES. Quasi in situ XRD, XAS and XPS reveals that two types of material were produced - molybdenum oxycarbide (500 °C and 600 °C) and molybdenum carbide (700 °C and 800 °C). The oxycarbide catalysts are rich in Mo-oxide and Mo-oxycarbide species (MoO_2 and MoO_xC_y) and the carbide catalysts rich in Mo-carbide species (α-MoC_{1-x} and β-Mo_2C) with a certain remaining oxygen atoms. The carbidic and oxophilic Mo sites in the catalysts were respectively probed by CO and N_2O chemisorption. The structure-performance relationships of these catalysts in CO_2 hydrogenation and anisole hydrodeoxygenation (HDO) were studied. For CO_2 hydrogenation, the carbide catalysts were much active than the oxycarbide catalysts and CO was the main product in all the catalysts. In contrast, the oxycarbide and carbide catalysts displayed comparable activity towards anisole conversion and the main products shifted from a mixture of phenol and benzene to only benzene upon increasing the carburization temperature from 600 °C to 700 °C. These catalytic results demonstrate that the catalytic performance of molybdenum (oxy)carbide material can be effectively tuned by varying the carburization degree, and that such tuning effect depends on the nature of reactant molecules: the carbidic Mo sites in Mo-carbide species are associated with CO_2 and anisole-to-benzene conversions, and the oxophilic Mo sites in Mo-oxycarbide species are related to anisole-to-phenol conversion.

1. Introduction

Transition metal carbides and molybdenum carbide in particular are efficient and earth-abundant heterogeneous catalysts.[1–3] Molybdenum carbide displays promising catalytic performance in reactions such as alkane hydrogenolysis[4], hydrodenitrogenation of organonitrogen compounds[5], dry reforming of methane[6], the water-gas shift (WGS) reaction[7] and CO hydrogenation[8]. In recent years, the application of molybdenum carbide catalysts has also been extended to catalytic reactions relevant for the transition to a sustainable chemical industry, including CO_2 hydrogenation[9–14] and biomass valorization.[15–19]

Notwithstanding its wide catalytic applications, the nature of active site(s) and structure-performance relationship of molybdenum carbide catalysts remain rather unclear. Compared to metallic catalysts, the surface of molybdenum carbide is more complex due to the incorporation of carbon atoms. For example, it has been demonstrated that the chemical and catalytic properties of molybdenum carbides are governed by the carbon-to-metal ratio of the catalyst particles.[20] Moreover, the carbidic surface is typically prone to dynamic changes under the reaction conditions. It has, for instance, been demonstrated that oxygen atoms can be incorporated into the carbidic phase during the conversion of oxygen-containing molecules, but different opinions exist regarding the influence of incorporated oxygen on the catalytic performance.[21–26] Using density functional theory, Liu et al. showed that C-terminated Mo_2C covered with oxygen is more active than Mo_2C itself for the WGS reaction due to an optimal bonding of reaction intermediates[25]. On the other hand, Choi and co-workers demonstrated that the presence of oxygen in molybdenum carbide is detrimental to benzene hydrogenation activity.[22] Kumar et al. reported that increasing the oxygen content in molybdenum carbide catalysts shifts the selectivity in anisole hydrodeoxygenation (HDO) from benzene to phenol.[26] The authors postulated that oxygen treatment results in MoO_x/MoO_xC_y clusters with proper surface ensembles required for the aromatic C-O bond cleavage.

Another challenge in establishing accurate structure-performance relationship for molybdenum carbide catalysts is related to the synthesis procedure. Dispersed molybdenum carbide is a highly pyrophoric material and passivation in diluted oxygen is therefore commonly used after the preparation.[27,28] Nevertheless, it has been observed that oxidation still slowly proceeds at ambient conditions even after passivation.[29] Prior to evaluating its catalytic performance, the passivated samples are usually activated in hydrogen atmosphere at elevated temperature, which leads to the partial removal of O atoms but likely C atoms as well, further complicating the comparison and analysis of catalysts.[29,30] A (quasi) in situ approach without passivation-activation procedure is therefore of great advantage to understand the metal carbide catalysts.[31]

In this study, we prepared a series of molybdenum (oxy)carbide catalysts by a carbothermal hydrogen reduction method using activated carbon support as the carbon source.[32] These catalysts were tested for CO_2 hydrogenation and anisole hydrodeoxygenation (HDO) to study

the influence of catalyst carburization degree on these two reactions. For this purpose, we first studied the catalyst precursor carburization process by TPR-MS and in situ XANES. Based on the obtained insights, four different temperatures (500 °C, 600 °C, 700 °C and 800 °C) were selected to tune the carburization degree of the resulting catalysts. The as-prepared catalysts were directly transferred to a glovebox without passivation, characterized in detail and tested in the catalytic reactions without air exposure We established that the combination of CO chemisorption (sensitive to carbidic Mo sites) and N$_2$O chemisorption (sensitive to all oxophilic Mo sites) is a powerful approach to probe the surface of (oxy)carbide catalysts. The catalytic results demonstrated that the CO$_2$ conversion is govern by carbidic Mo sites, while hydrodeoxygenation of anisole is associated with both carbidic and oxophilic Mo sites.

2. Experimental section

2.1 Catalyst preparation

Activated carbon (NORIT RX-3 Extra, S$_{BET}$ = 1219 m^2/g) was used as-received, crushed and sieved to a 125-250 μm fraction before depositing the molybdenum precursor. The Mo/C catalyst precursor was prepared by wet impregnation using an aqueous solution of (NH$_4$)$_6$Mo$_7$O$_{24}$·4H$_2$O (AHM, Merck, ⩾99%). The starting Mo:C element weight ratio was 1:5. In a typical synthesis, 1.47 g of AHM was firstly dissolved in 40 mL of demineralized water followed by adding 4.0 g of the carbon support. The resulting dispersion was sonicated for 15 min and stirred at room temperature for 1 h. Next, the water was removed by rotatory evaporation and the obtained solid was further dried at 110 °C overnight. The carburization of Mo/C precursor was performed at a home-built catalyst preparation setup, enabling direct sample transfer to a glovebox. For each sample, 1.0 g of the dried Mo/C precursor was loaded into a quartz reactor and then carburized at selected temperatures (500 °C, 600 °C, 700 °C and 800 °C) for 6 h at a rate of 3 °C/min in a 10 vol% H$_2$ in Ar flow (50 mL/min). After carburization, the catalysts were cooled to room temperature in a flow of Ar (45 mL/min) and directly transferred to a glovebox, where the samples were prepared for further characterization and catalytic testing. The obtained catalysts are denoted as Mo/C(T), where T stands for the carburization temperature.

Another series of catalysts (passivated and non-passivated) was also prepared at a different preparation setup in order to examine the effect of passivation-activation procedure. Similar conditions were used to carburize the Mo/C precursor. After the carburization the obtained samples were passivated in a 2.5 vol% O$_2$ in He flow (200 ml/min) at room temperature for 3 h. The resulting passivated catalysts were further stored under ambient conditions. The non-passivated catalysts were transferred and stored in a glovebox without exposing to air.

2.2 Catalyst characterization

Inductively coupled plasma optical emission spectroscopy (ICP-OES). The Mo loading in Mo/C precursor was determined by ICP-OES (Spectro CIROS CCD spectrometer). Prior to analysis, the sample was heated in 5 mL of concentrated nitric acid at 150 °C for 1 h, and the residual activated carbon support was removed by filtration.

Thermogravimetric analysis (TGA). The weight loss of Mo/C precursor during carburization process was monitored by TGA using Mettler Toledo TGA/DSC 1 instrument. About 15 mg of sample was placed in an uncovered crucible. The sample was heated to 900 °C at a rate of 5 °C/min in a flow of 60 mL/min He and 6 mL/min H_2. The gas effluent was analysed by an online mass spectrometer (Pfeiffer ThermoStar GSD 320 T). The weight loss of as-prepared and used catalysts (after anisole HDO) was also analysed using the same instrument. For this purpose, about 15 mg of catalyst was placed in an uncovered crucible, and then heated to 800 °C at a rate of 5 °C/min in a flow of 40 mL/min He and 20 mL/min O_2.

X-ray diffraction (XRD). The crystal structure of as-prepared catalysts was studied with a Bruker D2 Phaser diffractometer using Cu Kα radiation with a step size of 0.02° at 1.0 s/step in the 2θ range of 20 – 80°. The samples were grinded, loaded to a sample holder and sealed by Kapton tape in the glovebox before being transferred to the diffractometer.

X-ray photoelectron spectroscopy (XPS). The surface composition of as-prepared catalysts was analysed using a K-Alpha XPS instrument (Thermo Scientific) with a monochromatic small-spot X-ray source and an 180˚ double focusing hemispherical analyser. The samples were placed on a double-sided carbon tape in the glovebox, and then transferred to the spectrometer using an air-tight transfer holder. Spectra were collected using an aluminium anode (Al Kα = 1486.68 eV) operating at 72 W and a spot size of 400 μm. Survey scans were measured at a constant pass energy of 200 eV and region scans at 50 eV. All spectra were analysed with CasaXPS software and energy calibration was done against activated carbon C 1s binding energy fixed at 284.6 eV.

CO chemisorption. The carbidic Mo sites in the catalysts were probed by exposure the catalysts to small pulses of CO at 50 °C using a home-built plug-flow pulsing setup equipped with an online mass spectrometer (Balzers TPG 251). An appropriate amount (ca. 30 mg) of catalyst was loaded into a stainless-steel reactor and sealed by two valves in the glovebox before being transferred to the setup. After heating to 50 °C in a He flow (50 mL/min), CO pulses were injected into the He flow by a six-way valve with a sample loop of 10 μl until no CO consumption by the catalyst was observed by the mass spectrometry.

N₂O chemisorption. The oxophilic Mo sites in the catalysts were titrated by N_2O pulsing using the same setup as for CO chemisorption. N_2O reacts with surface oxophilic Mo sites, leading to N_2 formation (see below) in a similar way as metallic Cu sites titrated by N_2O.[33] The same sample preparation and pretreatment were adopted for N_2O titration as for CO chemisorption.

After reaching 50 °C in a He flow (50 mL/min), 1 mL of 2 vol% N$_2$O in He was periodically pulsed into the He flow until no N$_2$O consumption was observed by online mass spectrometry.

X-ray absorption spectroscopy (XAS). The oxidation state and local structure of molybdenum phases were investigated using XAS. Extended X-ray Adsorption Fine Structure (EXAFS) and X-ray Absorption Near Edge Structure (XANES) spectra were collected at the Mo K-edge in a transmission mode on beamline BM26 (DUBBLE) at the European Synchrotron Radiation Facility (Grenoble, France). The X-ray energy was selected using a Si(111) monochromator and calibrated with molybdenum foil. Ex-situ samples were prepared by pressing grinded catalysts, diluted by boron nitride, into stainless-steel sample holders in the glovebox, and sealed with Kapton tape. In situ XANES measurements during Mo/C carburization and anisole HDO reaction were carried out using a high-temperature plug-flow setup as described elsewhere.[34] The Mo/C precursor was carburized in situ at 700 °C for 30 min at a rate of 10 °C/min in a H$_2$ flow (30 mL/min), and then cooled to 300 °C before starting the anisole HDO reaction. The reaction conditions were the same as these used for the catalytic measurements (see below). A separate in situ XANES experiment was performed to trace the Mo/C catalyst precursor carburization process during which the temperature was increased to 750°C at a rate of 5 °C/min in a flow of hydrogen. The EXAFS and XANES spectra were background-subtracted and analysed with Athena, which is an interface of the IFRFFIT software package.[35]

2.3 Catalytic activity measurements

CO$_2$ hydrogenation. The catalytic performance in CO$_2$ hydrogenation was evaluated in a down-flow stainless-steel reactor (ID = 4 mm) at 250 °C and 30 bar. Typically, 50 mg of catalyst was loaded in the reactor, sealed with two valves in the glovebox and transferred to the catalytic setup. After flushing the reactor with nitrogen, the reactor was pressurized with the reaction gas mixture (20 vol% CO$_2$, 60 vol% H$_2$ and 20 vol% N$_2$) at a total flow of 25 NmL/min. The reactor was then heated to the reaction temperature at a rate of 5 °C/min. The effluent gas mixture was analysed by an online gas chromatograph (Interscience, CompactGC) equipped with Rtx-1 (FID), Rt-QBond and Molsieve 5A (TCD), and Rt-QBond (TCD) columns. The CO$_2$ conversion and product selectivity were calculated after ca. 3 h time-on-stream using the following equations:

$$X(CO_2) = \frac{F(CO)_{out} + F(CH_3OH)_{out} + F(CH_4)_{out} + 2 \times F(C_2H_6)_{out} + 3 \times F(C_3H_8)_{out}}{F(CO_2)_{out} + F(CO)_{out} + F(CH_3OH)_{out} + F(CH_4)_{out} + 2 \times F(C_2H_6)_{out} + 3 \times F(C_3H_8)_{out}} \quad [1]$$

$$S(product) = \frac{F(product)_{out}}{F(CO)_{out} + F(CH_3OH)_{out} + F(CH_4)_{out} + F(C_2H_6)_{out} + F(C_3H_8)_{out}} \quad [2]$$

where F stands for the volumetric flow rate calculated based on the internal standard (N$_2$) using

calibrated response factors. For the study of passivation-activation effect, the passivated catalysts were activated in a 10 vol% H_2 in He flow (50 ml/min) at 550 °C for 1 h before the catalytic measurements.

Anisole hydrodeoxygenation (HDO). The catalytic performance in anisole HDO was evaluated in a down-flow quartz reactor (ID = 4 mm) at 300 °C and atmospheric pressure. For this purpose, about 50 mg catalyst was loaded in the reactor and sealed in the glovebox and transferred to the catalytic setup. After flushing with hydrogen, the reactor was switched to a hydrogen flow (30 NmL/min) saturated with anisole vapour and heated to the reaction temperature at a rate of 5 °C/min. The anisole vapour (0.3 kPa) was supplied by flowing hydrogen through a thermostated saturator at 19 °C. The effluent gas mixture was analysed by an online chromatograph (Trace GC 1300, Thermo, equipped with an FID detector coupled with Rxi-5Sil MS column). The anisole conversion, product selectivity and product formation rate were calculated after 18 h time-on-stream using the following equations:

$$X(anisole) = 1 - \frac{F(anisole)_{out}}{F(anisole)_{in}} \quad [3]$$

$$S(aromatic) = \frac{F(aromatic)_{out}}{\sum F(aromatic)_{out}} \quad [4]$$

$$r(product) = \frac{F(product)_{out}}{V_m \times m_{cat}} \quad [5]$$

where F stands for the volumetric flow rate calculated using calibrated response factors and V_m is the molar volume of ideal gas at normal temperature and pressure.

3. Results and discussion

3.1 Mo/C precursor carburization

It is well known that interconversions between molybdenum oxides, oxycarbides and carbides are complicated and influenced by various parameters such as the carbon source, gas atmosphere, pretreatment, metal loading, etc.[36–39] To select appropriate temperatures to obtain molybdenum (oxy)carbide catalysts, the carburization of Mo/C precursor with Mo loading of 14.9 wt% in a diluted hydrogen flow was first studied by TGA-MS (**Figure 6.1a-b**). The weight loss below 300 °C (the first weight loss region) is due to both the desorption of physisorbed water from the support and the gradual decomposition of AHM precursor to MoO_3, likely in a highly dispersed form.[40] After the complete decomposition of AHM, a weight loss peak at 490 °C appeared together with water ($m/z = 18$) formation probed by MS, which can be related to the reduction of MoO_3 to MoO_2.[40] Added to that, we observed the oxygen atoms were also slowly removed as water before the bulk reduction in the second weight loss region. This

observation can be tentatively explained by the formation of metastable MoO$_x$C$_y$ from MoO$_3$, when the formed MoO$_3$ surface vacancies are filled by carbon atoms.[41] The presence of MoO$_x$C$_y$ in addition to MoO$_2$ is consistent with the total weight loss during the second weight loss region, showing that the average oxygen atom loss per molybdenum atom is higher than unity. In the third weight loss region, oxygen atoms were continuously removed as water until the second weight loss peak appeared (ca. 740 °C). In addition to water, CO (m/z = 28) and a small amount of CH$_4$ (m/z = 15) were observed starting from 700 °C, pointing to the involvement of the carbon support in the molybdenum carburization process. Nevertheless, it should be noted that the molybdenum carburization was not complete even at 850 °C as indicated by the ongoing CO (m/z = 28) production.
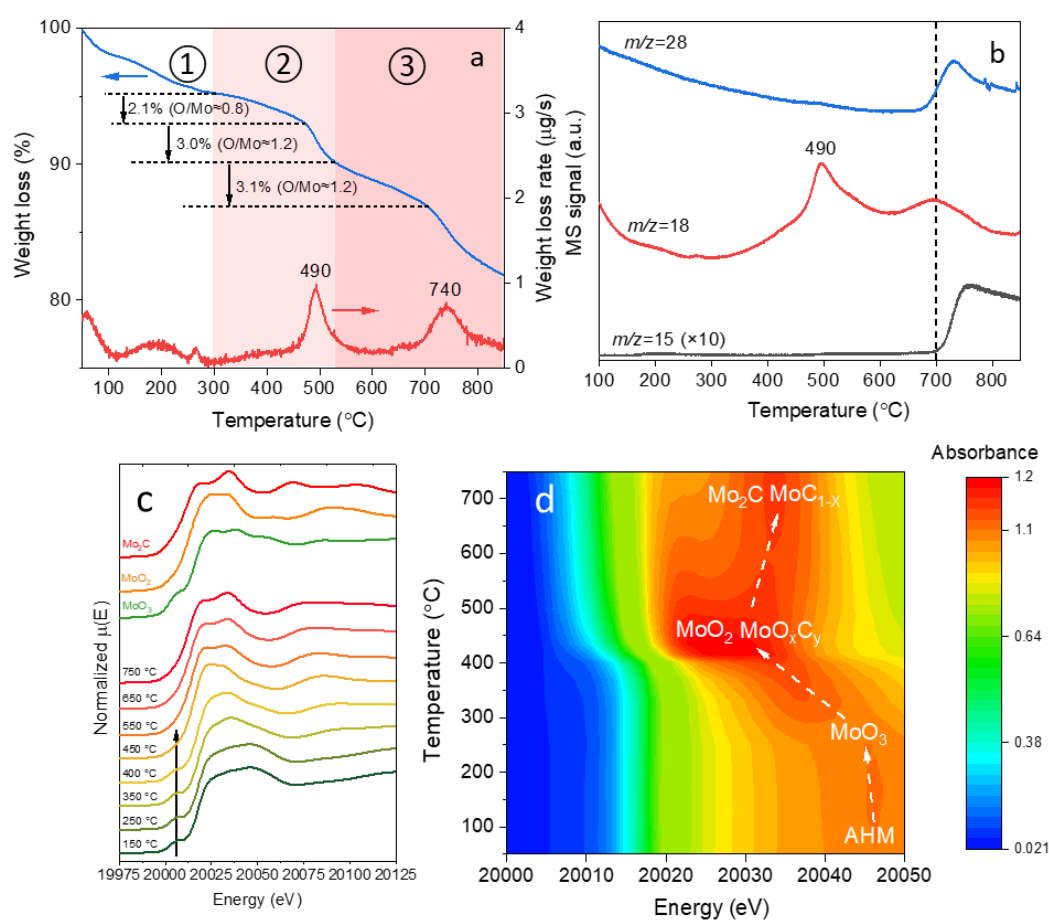

Figure 6.1. Mo/C catalyst precursor carburization process studies. (a) TGA and DTGA profiles and (b) corresponding mass spectra during precursor carburization. (c) In situ XANES spectra and (d) zoom-in of white line region at Mo K-edge during precursor carburization.

In situ XANES (**Figure 6.1c-d**) was further used to trace the evolution of the molybdenum phases during the carbothermal reduction synthesis. **Figure 6.1c** shows the XANES spectra of Mo/C precursor during carburization with increasing temperature together with reference spectra of Mo$_2$C, MoO$_2$ and MoO$_3$. The characteristic pre-edge feature related to the dipole-forbidden 1s → 4d electronic transition and assigned to tetrahedrally coordinated Mo^{VI}

species[42] disappeared, as the temperature increased from 400 °C to 450 °C. We ascribe this observation to the bulk reduction of MoO_3 to MoO_2.[40] The MoO_2-like phase was further reduced and carburized into a Mo_2C-like phase as inferred from the similarity between the final spectrum at 750 °C and the Mo_2C reference spectrum. Based on the TG and XANES results, three major carburization stages are tentatively suggested in **Figure 6.1d**: (i) the AHM precursor decomposition to MoO_3 (< 300 °C), (ii) MoO_3 reduction into a mixture of MoO_2 and MoO_xC_y (300 – 450 °C) followed by (iii) further carburization at higher temperature (> 450 °C) leads to the formation of molybdenum carbide(s). It should be mentioned that both α-MoC_{1-x} and β-Mo_2C phases can be formed from a mixture of MoO_2 and MoO_xC_y[9]. The nature of the formed molybdenum carbide phase(s) cannot be determined conclusively at this stage and will be studied in the following sections.

3.2 Effect of passivation and activation

To examine the effect of passivation-activation procedure on the catalytic performance, we carried out several CO_2 hydrogenation tests with passivated and non-passivated molybdenum carbide catalysts. These catalysts were prepared at 800 °C. The catalytic results (**Figure E.1a**) showed that, without the activation procedure, the passivated catalyst was significantly less active than the non-passivated catalyst. Moreover, even after activating at 550 °C and ambient pressure for 1 h in 10 vol% hydrogen flow (50 mL/min), the resulting catalyst was still much less active than the non-passivated catalyst. Quasi in situ XPS analysis of these catalysts after reaction (**Figure E.1b**) showed that the surface Mo oxidation degree (non-passivated < passivated-activated < passivated) was inversely correlated to the CO_2 conversion (non-passivated > passivated-activated > passivated). This observation clearly points to the superiority of passivation-free approach over the passivation-activation approach for the preparation of molybdenum carbide hydrogenation catalysts. Based on these findings in the present work we will focus on the catalysts prepared by the passivation-free approach.

3.3 Mo/C(T) catalyst characterization

Based on the Mo/C carburization studies and analysis of passivated and non-passivated catalysts, we chose four temperatures (500 °C, 600 °C, 700 °C and 800 °C) to prepare molybdenum (oxy)carbide catalysts with controlled carburization degree without passivation step. We characterized these materials in detail with respect to their structural and surface properties. The as-prepared catalysts were firstly examined by XRD (**Figure 6.2a**). The XRD patterns of the samples carburized at 500 °C and 600 °C can be assigned to MoO_2 phase. The relevant diffraction peaks become broader as the carburization temperature increased, indicating the further reduction/carburization of MoO_2 phase. As the reduction temperature reached 700 °C, diffraction peaks of β-Mo_2C phase appeared while the peaks related to MoO_2 phase disappeared. The β-Mo_2C phase was crystallized further from 700 °C to 800 °C as evidenced by the narrower and more intense XRD peaks observed in the Mo/C(800) sample.

A new diffraction peak at 42.4° was observed in the Mo/C(800) sample, which can be assigned to α-MoC$_{1-x}$ phase.[9] Given the significant broadening of this new peak, we speculate that the α-MoC$_{1-x}$ phase may originate from a highly disordered and/or dispersed molybdenum oxycarbide phase.[9]
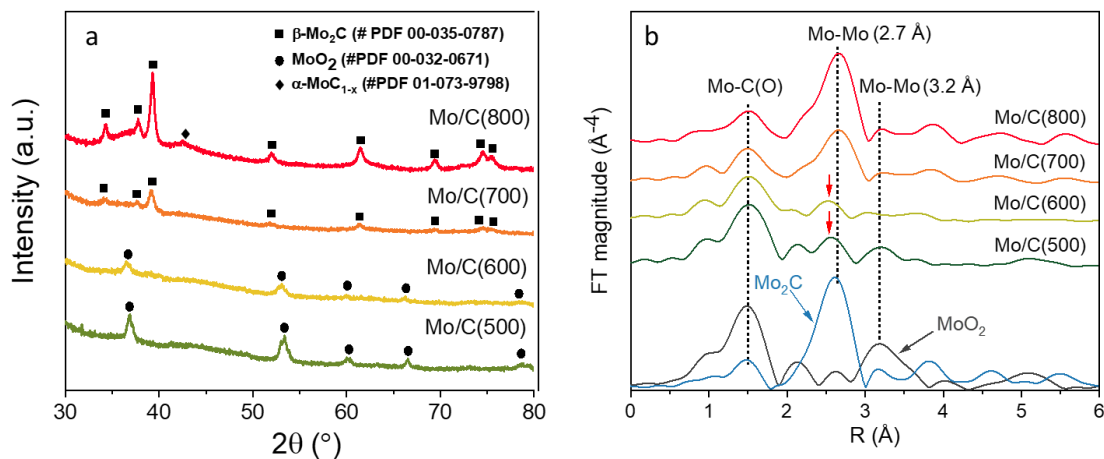

Figure 6.2. (a) XRD patterns and (b) Mo k-edge k^3-weighted R-space plots of as-prepared Mo (oxy)carbide catalysts.

We further studied the (oxy)carbide catalysts by XAS. The data was plotted in R-space with MoO$_2$ and β-Mo$_2$C standards to help data interpretation (**Figure 6.2b**). In line with the XRD results, the MoO$_2$ phase was consumed when the temperature was increased from 500 °C to 600 °C as indicated by the decreasing contribution of the Mo-Mo shell (3.2 Å) from the MoO$_2$ phase. Moreover, the β-Mo$_2$C phase formed at 700 °C and its contribution increased upon further raising the temperature to 800 °C as revealed by the increasing contribution of the Mo-Mo shell (2.7 Å) from the β-Mo$_2$C phase. Additional weak Mo-Mo contributions (marked by red arrows) with a coordination distance of 2.5 Å appeared in the Mo/C(500) and Mo/C(600) samples. Based on the above Mo/C precursor carburization and XRD results, we suggest that this contribution can be related to dispersed molybdenum oxycarbide phase (i.e. MoO$_x$C$_y$).

The XRD and XAS data points to the presence of MoO$_2$ and Mo-carbide species (β-Mo$_2$C and α-MoC$_{1-x}$) in the catalysts, but the presence of MoO$_x$C$_y$ species requires additional characterization. For this purpose, we employed XPS to study the Mo oxidation state and surface composition of the catalysts (**Figure 6.3**). We focused on the Mo 3d and O 1s regions in this study since activated carbon was used as the support and its signal dominates the C 1s region. The Mo 3d spectra were deconvoluted into four doublet contributions (Mo^{5+}, Mo^{4+}, Mo^{3+}, and Mo^{2+}) and the deconvolution results are shown in **Table 6.1**. The Mo^{6+} contribution assigned to MoO$_3$ was negligible in all the samples owing to the passivation-free approach.[43] The Mo^{4+} contribution is assigned to MoO$_2$[13,44] and the Mo^{3+} and Mo^{2+} contributions to Mo-carbides (α-MoC$_{1-x}$ and β-Mo$_2$C).[13,31,45] Significant Mo^{5+} contributions were observed in the Mo/C(500) and Mo/C(600) catalysts, which are assigned to MoO$_x$C$_y$.[41,46] For the O 1s spectra,

the contributions with binding energies of 532.4 eV, 530.9 eV and 530.1 eV are assigned to oxygen from surface groups on carbon support, MoO_xC_y and MoO_2, respectively.[47] The oxygen contributions from MoO_xC_y and MoO_2 species were used to calculate the overall O/Mo atomic ratio in the catalysts (**Table 6.1**). The XPS results showed that significant surface molybdenum carburization occurs upon increasing the temperature from 600 °C to 700 °C as indicated by the shift of the predominant oxidation states from Mo^{5+} and Mo^{4+} to Mo^{3+} and Mo^{2+}, and by the significant decrease of the O/Mo atomic ratio. This observation is consistent with the previous XRD and XAS observations. Importantly, significant amounts of MoO_xC_y species (Mo^{5+}) were observed by XPS which were not detected by XRD. Such difference can be understood since the formed MoO_xC_y surface species from partially reduced MoO_3 are highly disordered and/or dispersed in nature.[41] In line with TG-MS results, molybdenum carburization was not complete even at the highest carburization temperature (800 °C) as indicated by the presence of Mo^{5+} and Mo^{4+} contributions and presence of oxygen on the surface of the Mo/C(800) catalyst. Based on these observations, we conclude that Mo/C(700) and Mo/C(800) samples can be described as carbide surfaces with a certain amount of remaining oxygen atoms.[22]
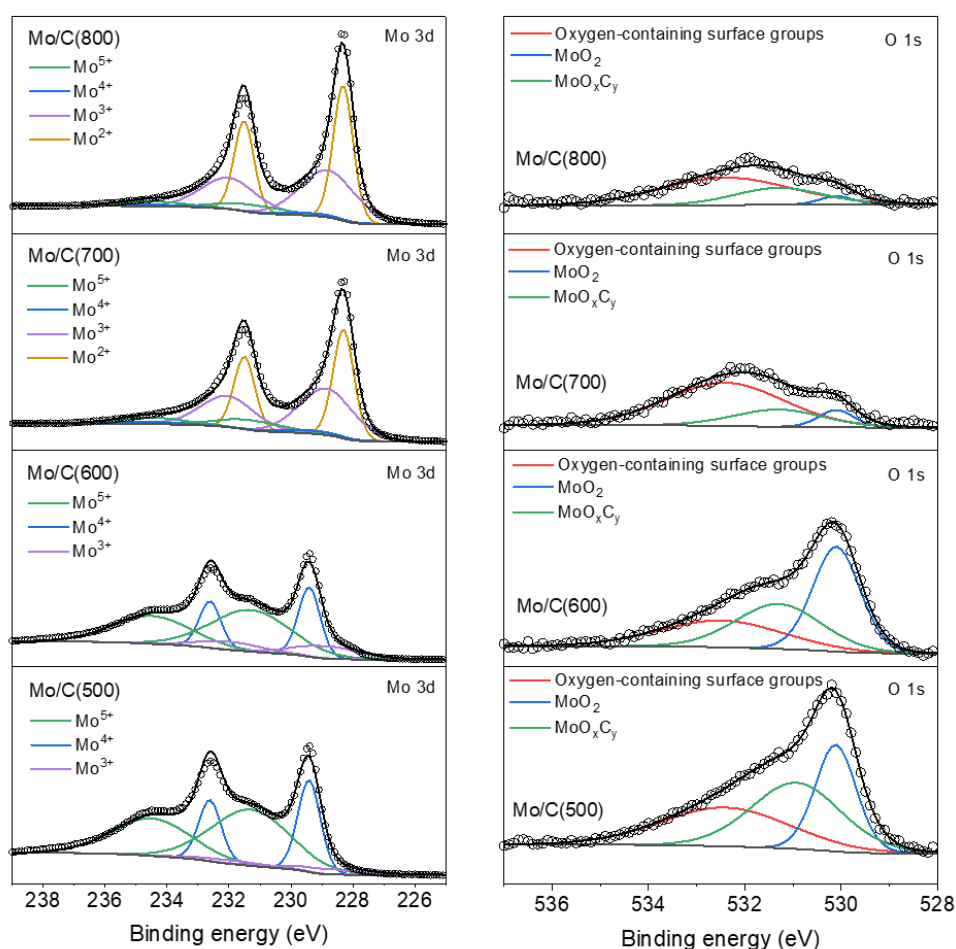

Figure 6.3. Mo 3d and O 1s XP spectra of as-prepared Mo (oxy)carbide catalysts.

Table 6.1. O/Mo atomic ratio and Mo 3d XP spectra analysis of as-prepared Mo (oxy)carbide catalysts.

Catalyst	O/Mo atomic ratio	Mo 3d$_{5/2}$ binding energy (eV)				Composition (mol %)			
		Mo^{5+}	Mo^{4+}	Mo^{3+}	Mo^{2+}	Mo^{5+}	Mo^{4+}	Mo^{3+}	Mo^{2+}
Mo/C(500)	1.43	231.3	229.4	228.9	228.3	64	30	6	0
Mo/C(600)	1.48	231.3	229.4	228.9	228.3	58	21	15	0
Mo/C(700)	0.38	231.3	229.4	228.9	228.3	12	4	44	40
Mo/C(800)	0.22	231.3	229.4	228.8	228.3	9	3	44	45

Table 6.2. Carbidic and oxophilic Mo site density of as-prepared Mo (oxy)carbide catalysts.

Catalyst	Carbidic Mo sites (μmol/g$_{cat}$)	Oxophilic Mo sites (μmol/g$_{cat}$)
Mo/C(500)	0.2	64.0
Mo/C(600)	0.3	62.2
Mo/C(700)	7.2	129.8
Mo/C(800)	11.2	120.8

We further used chemisorption (CO and N$_2$O) to directly probe the surface sites in the catalysts.[48] Control experiments showed that the bare carbon support did not chemisorb CO or N$_2$O. The results in **Table 6.2** show that the Mo/C(500) and Mo/C(600) catalysts contained almost no carbidic Mo sites, while Mo/C(700) and Mo/C(800) catalysts contained considerable amounts of these sites. This observation indicates that significant molybdenum carburization took place between 600 °C and 700 °C. Next, N$_2$O was used as a probe molecule to measure surface oxophilic Mo sites (*i.e.* all oxidizable surface centres) in the catalysts. A representative N$_2$O titration profile is shown in **Figure E.2**. The high surface-sensitivity of this technique was confirmed by a quasi in situ XPS analysis (**Figure E.3**), which showed that no significant oxidation took place after N$_2$O chemisorption. Given that XPS probes top few nm of the surface, the absence of significant oxidation observed in XP spectra implies that only the top atomic layer of the catalysts is probed by N$_2$O. In contrast to CO chemisorption, the N$_2$O titration results show that significant amounts of oxophilic Mo sites were probed by N$_2$O in the Mo/C(500) and Mo/C(600) catalysts. The substantial difference in the Mo sites probed by CO and N$_2$O in the Mo/C(500) or Mo/C(600) suggests that other molybdenum-containing species contribute to the N$_2$O consumption in addition to Mo-carbide species. Reference experiment with MoO$_2$ standards showed that this material was completely inactive for N$_2$O chemisorption. As such, we suggest that N$_2$O molecule also probes the oxophilic Mo sites in the MoO$_x$C$_y$ species (i.e., oxygen vacancies[49]), which can not be probed by CO. The Mo/C(700) and Mo/C(800) also contain significant amounts of oxophilic Mo sites, in line with previous oxygen chemisorption study on molybdenum carbide.[48] It should be mentioned that the difference between the amounts of carbidic and oxophilic Mo sites in the Mo/C(700) and Mo/C(800) is due to the incomplete molybdenum carburization[22] and the relatively high chemisorption temperature (50 ˚C) used in current study.[50] Based on these results, we propose that CO and

N_2O can be used as complementary probe molecules for the quantification of carbidic and oxophilic Mo sites in the (oxy)carbide catalysts.

Using a combination of XRD, XAS, XPS and chemisorption (CO and N_2O), we have demonstrated that molybdenum (oxy)carbide catalysts with controlled carburization degree (i.e. oxygen removal extent) can be prepared by adjusting the carburization temperature. Specifically, the Mo/C(500) and Mo/C(600) catalysts are rich in MoO_xC_y and MoO_2 species and the Mo/C(700) and Mo/C(800) catalysts are rich in Mo-carbide species (α-MoC_{1-x} and β-Mo_2C) with a certain amount of remaining oxygen atoms. In the following sections, therefore, we refer to the Mo/C(500) and Mo/C(600) samples as oxycarbide catalysts and to the Mo/C(700) and Mo/C(800) samples as carbide catalysts.

3.3 Catalytic performance

3.3.1 CO₂ hydrogenation

The CO_2 hydrogenation reaction was evaluated over the as-prepared molybdenum (oxy)carbide catalysts to study the influence on the molybdenum carburization degree (**Figure 6.4a**). Blank catalytic test with carbon support showed that it is inactive for CO_2 conversion. **Figure 6.4a** shows that the catalysts prepared at higher carburization temperature displayed enhanced CO_2 conversion and all the catalysts showed similar product selectivity profiles independent of CO_2 conversion level. CO was the predominant product with a selectivity in the range of 60-75 %. In addition, other products included methane (10-20 %), methanol (10-20 %) and small amounts of ethane and propane (< 2 %). The CO_2 conversion and product distribution as a function of carburization temperature, together with previous characterization results, suggest that Mo-carbide species are responsible for CO_2 hydronation. To gain more insight into the active sites for CO_2 hydrogenation, the CO_2 conversion was plotted against the amount of carbidic Mo (**Figure 6.4b**) and oxophilic Mo sites (**Figure E.6**) from N_2O chemisorption.
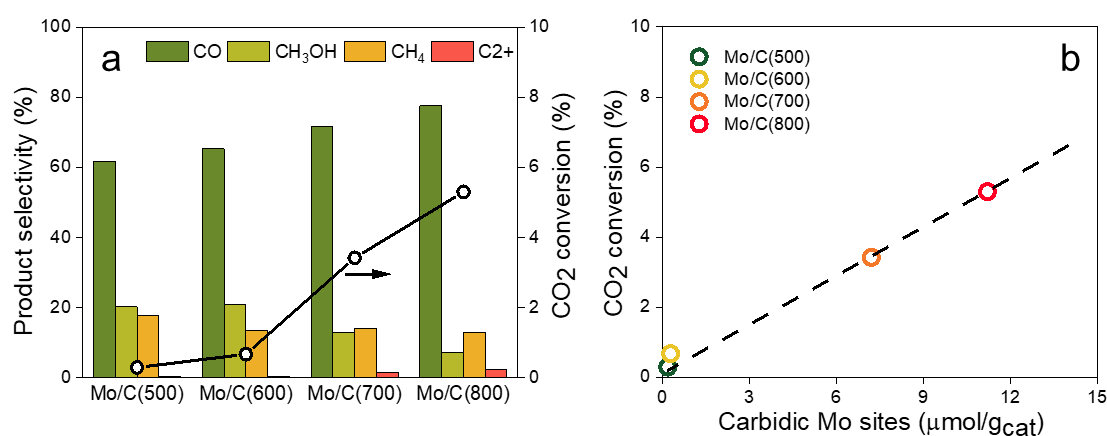

Figure 6.4. (a) CO_2 conversion and product selectivity and (b) correlation between CO_2 conversion and carbidic Mo site density. Reaction conditions: 250 °C, 30 bar and SV=30 L/(g_{cat}*h).

Figure 6.4b shows that CO_2 conversion scales well with the amount of carbidic Mo sites in the catalysts, which underpins the involvement of Mo-carbide species in CO_2 conversion. Such strong correlation, however, between the CO_2 conversion and the amount of oxophilic Mo sites does not exist.

3.3.2 Anisole hydrodeoxygenation (HDO)

Anisole HDO was performed over the as-prepared molybdenum (oxy)carbide catalysts. As similar in above CO_2 hydrogenation, no activity was observed over the bare carbon support. However, the conversion and product distribution in anisole HDO over the as-prepared catalysts show different dependence on the carburization temperature (**Figure 6.5a**) as compared to CO_2 conversion. For example, the conversion difference between the oxycarbide and carbide catalysts is not as significant as in CO_2 hydrogenation. Moreover, different product selectivity profiles were observed between the oxycarbide and carbide catalysts at the end of the test (ca. 1 h) – the selectivity shifted from a mixture of benzene and phenol to predominantly benzene (ca. 93 %) as the carburization temperature increases from 600 °C to 700°C. Moreover, the methyl anisole selectivity over the oxycarbide catalysts was significantly higher than that over the carbide catalysts. It should be mentioned that no significant changes in selectivity were observed during the reaction (ca. 17 – 20 h) as showed in **Figure E.8**. Clearly, active sites other than carbidic Mo sites are available in the oxycarbide catalysts for anisole activation. To gain insights into the active sites for anisole conversion, initial benzene formation rate (TOS = 30 min) was plotted against CO chemisorption data (**Figure 6.5b**). The initial reaction rate was used here as a severe catalyst deactivation occurs at the beginning of the reaction over carbide catalysts (see below). Similar to CO_2 conversion, we found that the initial benzene formation
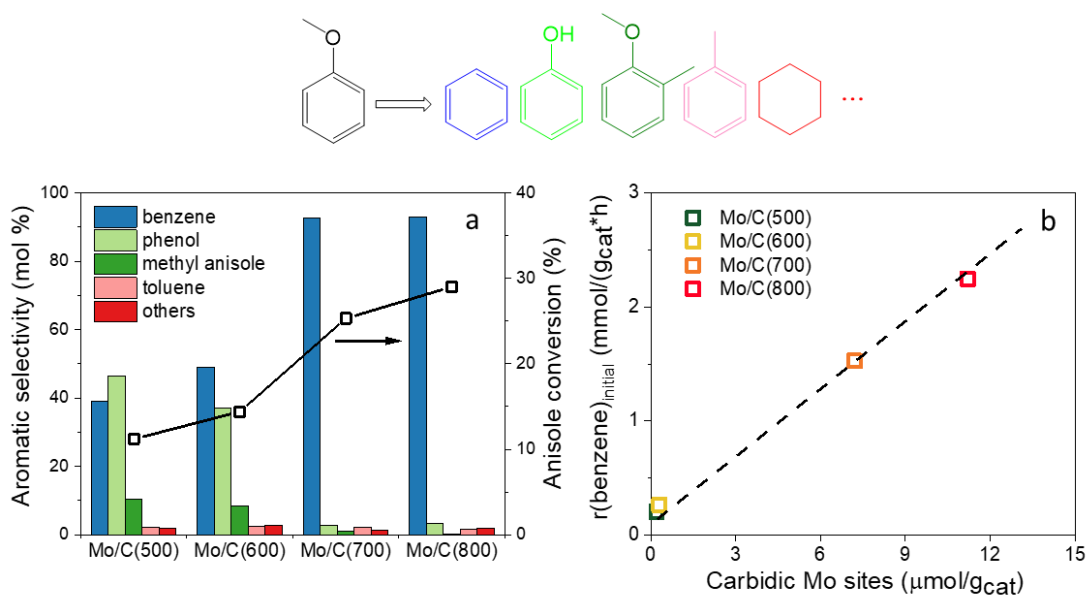

Figure 6.5. (a) Anisole conversion and product selectivity and (b) correlation between initial benzene formation rate and carbidic Mo site density. Reaction conditions: 300 °C and 1 bar.

rate is proportional to the amounts of carbidic Mo sites, pointing to the involvement of these sites in anisole-to-benzene conversion. Regarding anisole-to-phenol conversion, it is likely associated with the oxygen content in the oxycarbide catalysts. This hypothesis is supported by a recent report by Kumar et al.[26] in which the authors showed that oxygen treatment of molybdenum carbide catalysts led to higher phenol selectivity in anisole HDO. In the current study, the phenol production from anisole over the oxycarbide catalysts is likely associated with MoO_xC_y species because MoO_2 was proven to be completely inactive for anisole HDO under similar conditions.[51] Importantly, the presence of such oxycarbide species is explicitly revealed by quasi in situ XPS analysis in this study. Moreover, the oxophilic Mo sites in MoO_xC_y species (e.g. oxygen vacancies[49]), the potential active sites for phenol formation, can be quantified by N_2O chemisorption.
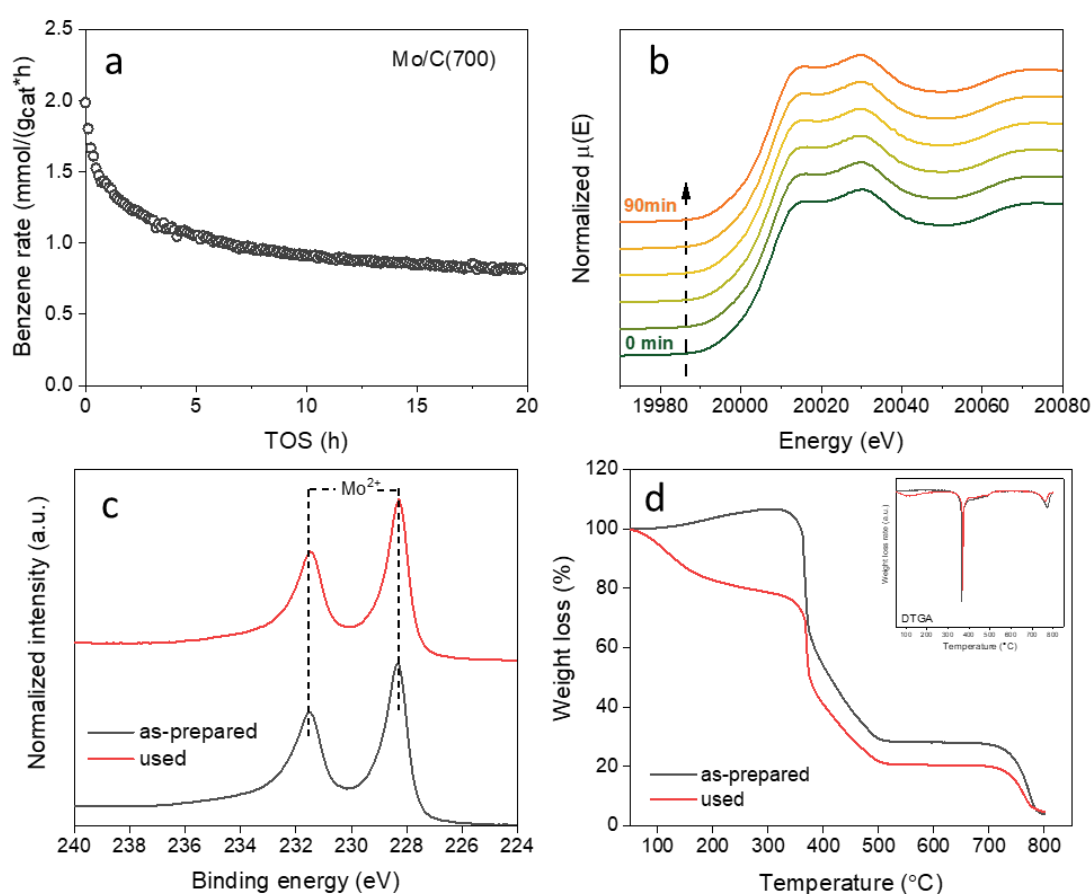

Figure 6.6. (a) Time-on-stream benzene formation rate and (b) in situ XANES spectra at Mo K-edge during anisole HDO (TOS from 0 min to 90 min) over Mo/C(700) catalyst. (c) Quasi in situ XP spectra and (d) TGA and DTGA profiles of Mo/C(700) catalysts before and after anisole HDO.

As molybdenum carbide appears to be a promising catalyst for selective benzene production from anisole, we further investigated its time-on-stream behaviour. **Figure 6.6a** shows that the benzene formation rate decreased significantly at the beginning of the reaction, and then decreased at a slower rate as the reaction continued. Similar catalyst deactivation behaviour

was observed in literature[31] and two main deactivation mechanisms were proposed in literature: carbide oxidation and carbonaceous deposition.[52] To shed light on the deactivation mechanism over the Mo/C(700) catalyst, several (in situ) techniques were used to study the catalyst modification during anisole HDO. In situ XANES spectra (**Figure 6.6b**) revealed that no bulk phase oxidation occurred at the beginning of reaction. Further quasi in situ XPS measurements (**Figure 6.6c**) also showed that no significant surface oxidation took place after anisole HDO reaction, although even more surface-sensitive technique might be necessary to answer this question definitively.[31] On the other hand, carbonaceous deposition after anisole HDO was evidenced by TG analysis of the used catalyst. A significant weight loss occurred in the temperature range of 100 - 300 °C. It should be noted that the initial weight gain in the as-prepared catalyst is due to oxidation of molybdenum carbide in air.[53] The total weight loss until 600 °C was about 8 wt% higher for the used catalyst compared to the as-prepared catalyst. Further calculation indicates that the carbonaceous deposition in the used catalyst after anisole HDO was ~25 wt%. The combined XANES, XPS and TG results suggest that carbonaceous deposition, instead of carbide phase oxidation, is likely the main reason for the quick carbide catalyst deactivation during anisole HDO. To mitigate the deactivation caused by carbonaceous deposition, one might carry out anisole HDO at higher hydrogen pressure and temperature[54] or enhance the hydrogenation ability of molybdenum carbide catalyst such as by increasing phase crystallinity[55] or by adding a second metal function.[56]

3.3.3 Active site(s) of CO_2 and anisole conversion

Although the reactions of CO_2 hydrogenation and anisole HDO both involve CO bond cleavage, our catalytic results show that these two reactions correlate differently to the Mo sites measured by chemisorption. Specifically, the carbidic Mo sites (probed by CO) are associated with CO_2 hydrogenation and anisole-to-benzene conversion, while the oxophilic Mo sites (probed by N_2O) in oxycarbide phase are inactive for CO_2 conversion but associated with anisole-to-phenol conversion. The bond strength of the cleaved C-O bond may explain such difference: C=O bond in CO_2 (BDE: 532.2 kJ/mol) is much stronger than aryl C-O (BDE: 418.8 kJ/mol) and particularly alkyl C-O (BDE: 263.2 kJ/mol) bonds in anisole.[57] In other words, CO_2 activation is more difficult than anisole activation, and it is possible that the oxygen binding energy to oxycarbide surface is not strong enough to dissociate the C=O bond in CO_2 as compared to the carbide surface.[58] Furthermore, the selectivity shift in anisole HDO may be explained by the adsorption geometry anisole adopts over the (oxy)carbide surface. Eng et al. used HREELS to show that benzene interacts with a carbide-modified Mo(110) surface in a planar manner, and such interaction is much weaker on an oxide-modified carbide surface.[59] Based on that, we postulate that anisole may adopt an on-top geometry over the carbide surface and an end-on geometry over the oxycarbide surface. Such difference in adsorption geometry leads to the selective cleavage of aryl C-O or alkyl C-O in anisole.

4. Conclusions

We have demonstrated that the carburization degree of molybdenum (oxy)carbide catalyst can be tuned by varying the carbothermal synthesis temperature. In situ XANES, TGA, XRD, EXAFS, XPS and chemisorption results revealed that the catalyst was transformed from a surface rich in MoO_2 and MoO_xC_y to a surface rich in Mo-carbide (α-MoC_{1-x} and β-Mo_2C) from 600 °C to 700 °C. Catalytic results showed that carbide catalysts were much more active than oxycarbide catalysts for CO_2 conversion, pointing to the relevance of carbidic Mo sites in CO_2 activation. In contrast, oxycarbide and carbide catalysts displayed comparable anisole conversion and different product distribution profile during anisole HDO. The oxophilic Mo sites in MoO_xC_y species promote the anisole-to-phenol conversion, whereas the carbidic Mo sites in Mo-carbide species facilitate the deeper hydrogenolysis of anisole to benzene.

References

1   R. B. Levy and M. Boudart, *Science.*, 1973, **181**, 547–549.

2   S. T. Gyama, *Catal. Today*, 1992, **15**, 179–200.

3   H. H. Hwu and J. G. Chen, *Chem. Rev.*, 2005, **105**, 185–212.

4   G. S. Ranhotra, G. W. Haddix, A. T. Bell and J. A. Reimer, *J. Catal.*, 1987, **108**, 24–39.

5   J. G. Choi, J. R. Brenner and L. T. Thompson, *J. Catal.*, 1995, **154**, 33–40.

6   A. J. Brungs, A. P. E. York and M. L. H. Green, *Catal. Letters*, 1999, **57**, 65–69.

7   J. Patt, D. Moon, C. Phillips and L. Thompson, *Catal. Letters*, 2000, **65**, 193–195.

8   P. M. Patterson, T. K. Das and B. H. Davis, *Appl. Catal. A Gen.*, 2003, **251**, 449–455.

9   W. Xu, P. J. Ramirez, D. Stacchiola and J. A. Rodriguez, *Catal. Letters*, 2014, **144**, 1418–1424.

10   M. D. Porosoff, X. Yang, J. A. Boscoboinik and J. G. Chen, *Angew. Chem. Int. Ed.*, 2014, **53**, 6705–6709.

11   S. F. Viñes, J. A. Rodriguez and C. Sci, *Catal. Sci. Technol.*, 2016, **6**, 6766–6777.

12   F. Christian Kunkel Vines, Francesc Illas, *Energy Environ. Sci*, 2016, **1**, 141–144.

13   J. Gao, Y. Wu, C. Jia, Z. Zhong, F. Gao, Y. Yang and B. Liu, *Catal. Commun.*, 2016, **84**, 147–150.

14   X. Liu, C. Kunkel, P. Ram, D. Piscina and F. Vin, *ACS Catal.*, 2017, **7**, 4323–4335.

15   A. L. Jongerius, R. W. Gosselink, J. Dijkstra, J. H. Bitter, P. C. A. Bruijnincx and B. M. Weckhuysen, *ChemCatChem*, 2013, **5**, 2964–2972.

16   R. Ma, W. Hao, X. Ma, Y. Tian and Y. Li, *Angew. Chem. Int. Ed.*, 2014, **53**, 7310–7315.

17   W. S. Lee, Z. Wang, R. J. Wu and A. Bhan, *J. Catal.*, 2014, **319**, 44–53.

18   W. S. Lee, Z. Wang, W. Zheng, D. G. Vlachos and A. Bhan, *Catal. Sci. Technol.*, 2014, **4**, 2340–2352.

19   X. Ma, R. Ma, W. Hao, M. Chen, F. Yan, K. Cui, Y. Tian and Y. Li, *ACS Catal.*, 2015, **5**, 4803–4813.

20   S. Posada-Perez, F. Vines, P. J. Ramirez, A. B. Vidal, J. A. Rodriguez and F. Illas, *Phys Chem Chem Phys*, 2014, **16**, 14912–14921.

21   Y. Li, Y. Fan, J. He, B. Xu, H. Yang, J. Miao and Y. Chen, *Chem. Eng. J.*, 2004, **99**, 213–218.

22   J.-S. Choi, G. Bugli and G. Djéga-Mariadassou, *J. Catal.*, 2000, **193**, 238–247.

23   C. J. Chen and A. Bhan, *ACS Catal.*, 2017, **7**, 1113–1122.

24   M. Dixit, X. Peng, M. D. Porosoff, H. D. Willauer and G. Mpourmpakis, *Catal. Sci. Technol.*, 2017, **7**, 5521–5529.

25   P. Liu and J. A. Rodriguez, *J. Phys. Chem. B*, 2006, **110**, 19418–19425.

26   A. Kumar and A. Bhan, *Chem. Eng. Sci.*, 2019, **197**, 371–378.

27   A. Mehdad, R. E. Jentoft and F. C. Jentoft, *J. Catal.*, 2017, **347**, 89–101.

28   K.-Y. Wang, Hua-Min Wang, Xiao-Hui, Zhang, Ming-Hui, Du, Xiao-yong, Li, Wei Tao, *Chem*

Mater, 2007, **19**, 1801–1807.

29   K. J. Leary, J. N. Michaels and A. M. Stacy, *J. Catal.*, 1986, **101**, 301–313.

30   D. C. LaMont, A. J. Gilligan, A. R. S. Darujati, A. S. Chellappa and W. J. Thomson, *Appl. Catal. A Gen.*, 2003, **255**, 239–253.

31   K. Murugappan, E. M. Anderson, D. Teschner, T. E. Jones, K. Skorupska and Y. Román-Leshkov, *Nat. Catal.*, 2018, **1**, 960–967.

32   C. Liang, Changhai Ying, Pinliang Li, *Chem Mater*, 2002, **14**, 3148–3151.

33   J. R. Jensen, T. Johannessen and H. Livbjerg, *Appl. Catal. A Gen.*, 2004, **266**, 117–122.

34   N. Kosinov, A. Wijpkema, E. Uslamin, R. Rohling, F. Coumans, B. Mezari, A. Parastaev, A. Poryvaev, M. Fedin, E. Pidko and E. Hensen, *Angew. Chem. Int. Ed.*, 2017, **57**, 1016–1020.

35   B. Ravel and M. Newville, *J. Synchrotron Radiat.*, 2005, **12**, 537–541.

36   S. A. W. Hollak, R. W. Gosselink, D. S. Van Es and J. H. Bitter, *ACS Catal.*, 2013, **3**, 2837–2844.

37   R. Guil-López, E. Nieto, J. A. Botas and J. L. G. Fierro, *J. Solid State Chem.*, 2012, **190**, 285–295.

38   M. L. Frauwallner, F. López-Linares, J. Lara-Romero, C. E. Scott, V. Ali, E. Hernández and P. Pereira-Almao, *Appl. Catal. A Gen.*, 2011, **394**, 62–70.

39   E. Ochoa, D. Torres, R. Moreira, J. L. Pinilla and I. Suelves, *Appl. Catal. B Environ.*, 2018, **239**, 463–474.

40   J. Wienold, R. E. Jentoft and T. Ressler, *Eur. J. Inorg. Chem.*, 2005, **11**, 2124-2133.

41   P. Delporte, F. Meunier, C. Pham-Huu, P. Vennegues, M. J. Ledoux and J. Guille, *Catal. Today*, 1995, **23**, 251–267.

42   N. Kosinov, E. A. Uslamin, L. Meng, A. Parastaev, Y. Liu and E. J. M. Hensen, *Angew. Chem. Int. Ed.*, 2019, **58**, 7068–7072.

43   H. Wang, S. Liu and K. J. Smith, *Energy and Fuels*, 2016, **30**, 6039–6049.

44   J. A. Schaidle, A. C. Lausche and L. T. Thompson, *J. Catal.*, 2010, **272**, 235–245.

45   H. Lin, Z. Shi, S. He, X. Yu, S. Wang, Q. Gao and Y. Tang, *Chem. Sci.*, 2016, **7**, 3399–3405.

46   C. Wan, Y. N. Regmi and B. M. Leonard, *Angew. Chem. Int. Ed.*, 2014, **126**, 6525–6528.

47   J. A. Schaidle, J. Blackburn, C. A. Farberow, C. Nash, K. X. Steirer, J. Clark, D. J. Robichaud and D. A. Ruddy, *ACS Catal.*, 2016, **6**, 1181–1197.

48   T. P. St. Clair, B. Dhandapani and S. T. Oyama, *Catal. Letters*, 1999, **58**, 169–171.

49   T. Prasomsri, T. Nimmanwudipong and Y. Román-Leshkov, *Energy Environ. Sci.*, 2013, **6**, 1732–1738.

50   J. S. Lee, K. H. Lee and J. Y. Lee, *J. Phys. Chem.*, 1992, **96**, 362–366.

51   T. Prasomsri, M. Shetty, K. Murugappan and Y. Román-Leshkov, *Energy Environ. Sci.*, 2014, **7**, 2660–2669.

52   W. S. Lee, A. Kumar, Z. Wang and A. Bhan, *ACS Catal.*, 2015, **5**, 4104–4114.

53   N. Kosinov, E. A. Uslamin, F. J. A. G. Coumans, A. S. G. Wijpkema, R. Y. Rohling and E. J. M. Hensen, *ACS Catal.*, 2018, **8**, 8459–8467.

54   D. C. Elliott, *Energy and Fuels*, 2007, **21**, 1792–1815.

55   D. R. Stellwagen and J. H. Bitter, *Green Chem.*, 2015, **17**, 582–593.

56   Q. Bkour, O. G. Marin-Flores, M. G. Norton and S. Ha, *Appl. Catal. B Environ.*, 2019, **245**, 613–622.

57   Y.-R. Luo, *Comprehensive Handbook of Chemical Bond Energies*, CRC Press, Taylor & Francis Group, 1st edn., 2007.

58   M. D. Porosoff, S. Kattel, W. Li, P. Liu and J. G. Chen, *Chem Commun*, 2015, **51**, 6988–6991.

59   J. Eng, B. E. Bent, B. Frühberger and J. G. Chen, *J. Phys. Chem. B*, 1997, **101**, 4044–4054.
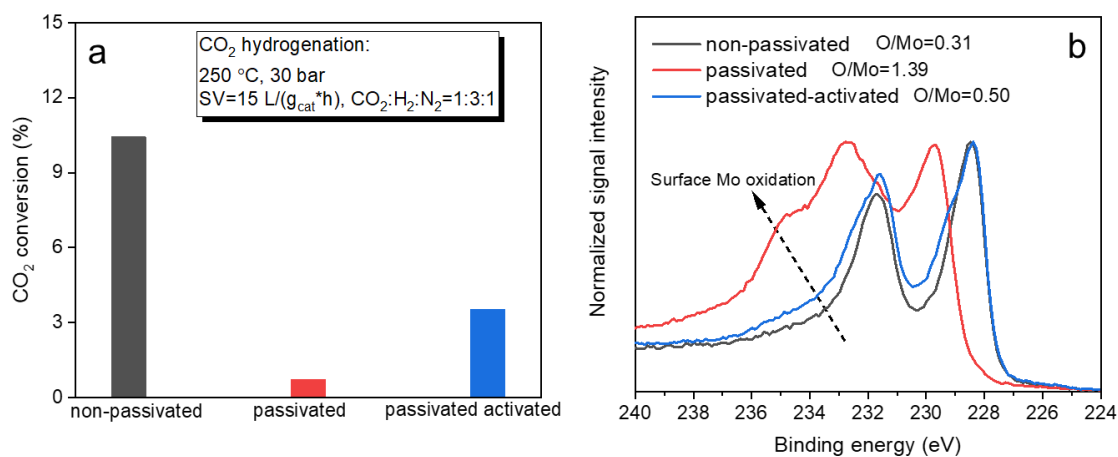
Appendix E

Figure E.1. (a) Conversion of non-passivated, passivated and passivated-activated Mo/C(800) catalysts for CO_2 hydrogenation. (B) Quasi in situ Mo 3d XP spectra of the catalysts after reaction.
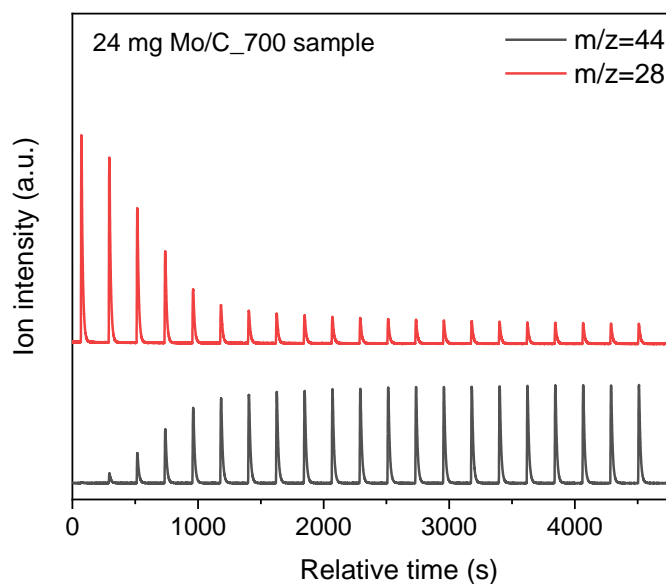

Figure E.2. N_2O pulse titration profiles showing N_2O ($m/z = 44$) consumption and N_2 ($m/z = 28$) production over Mo/C(700). Conditions: 50 °C, 1 mL 2% N_2O pulse into 50 mL/min He flow.
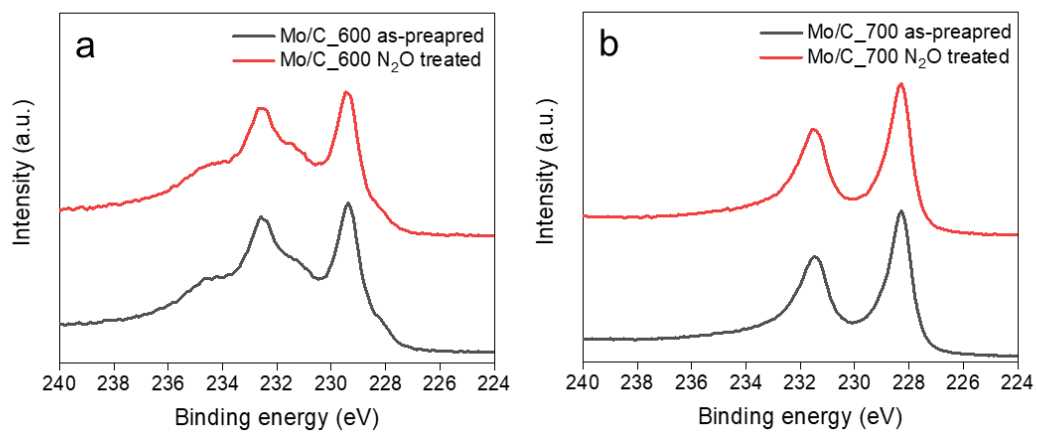
Figure E.3. Quasi in situ XP spectra of as-prepared and N$_2$O-treated (a) Mo/C(600) and (b) Mo/C(700) catalysts.
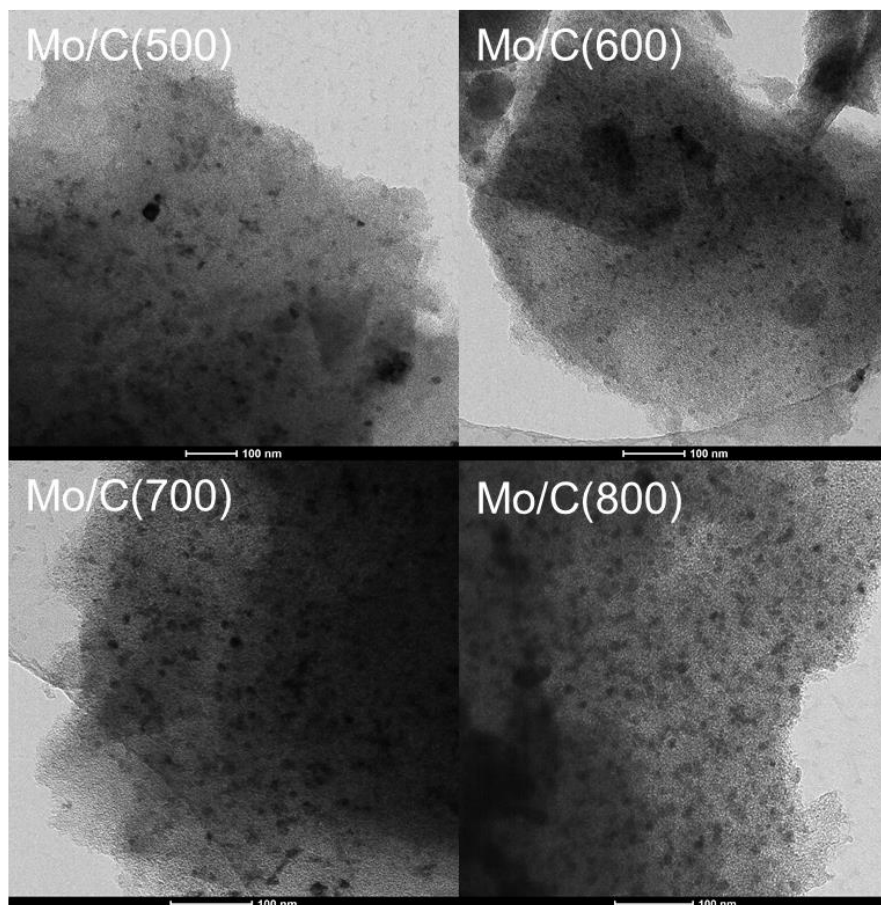

Figure E.4. TEM images of as-prepared molybdenum (oxy)carbide catalysts.
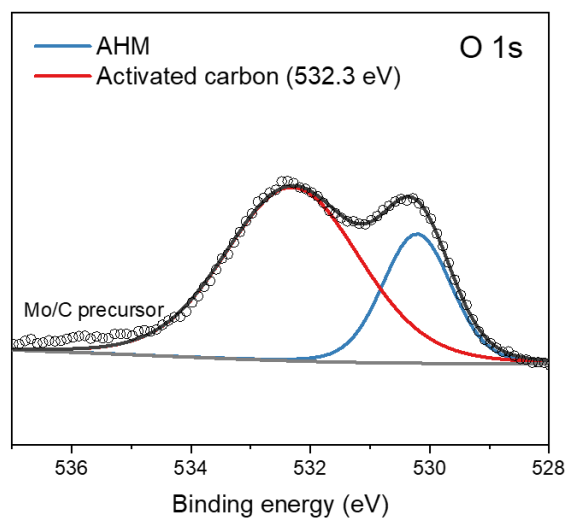
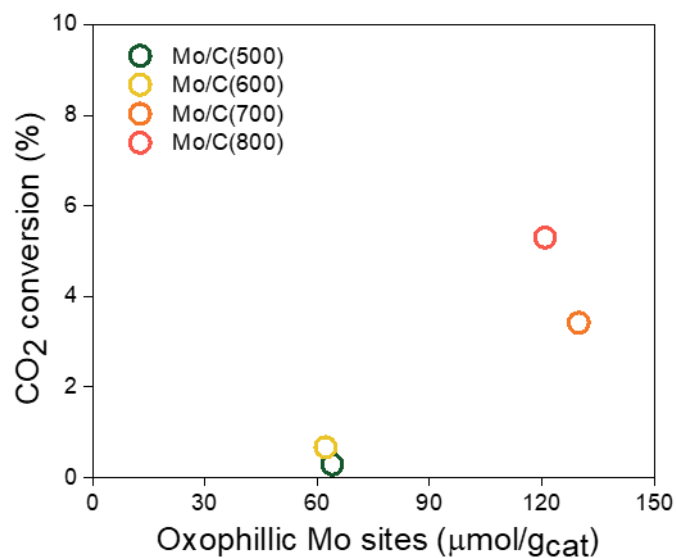**Figure E.5**. Fitted Mo 3d XP spectrum of Mo/C catalyst precursor.

Figure E.6. Correlation between CO_2 conversion and oxophilic Mo site density.

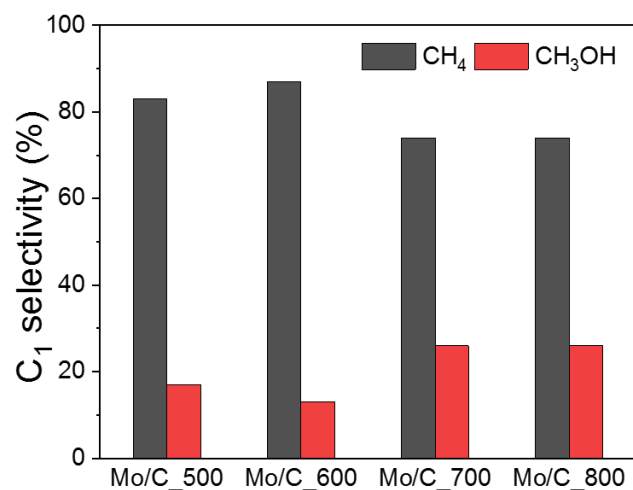**Figure E.7**. C$_1$ products selectivity of as-prepared Mo (oxy)carbide catalysts during anisole HDO.
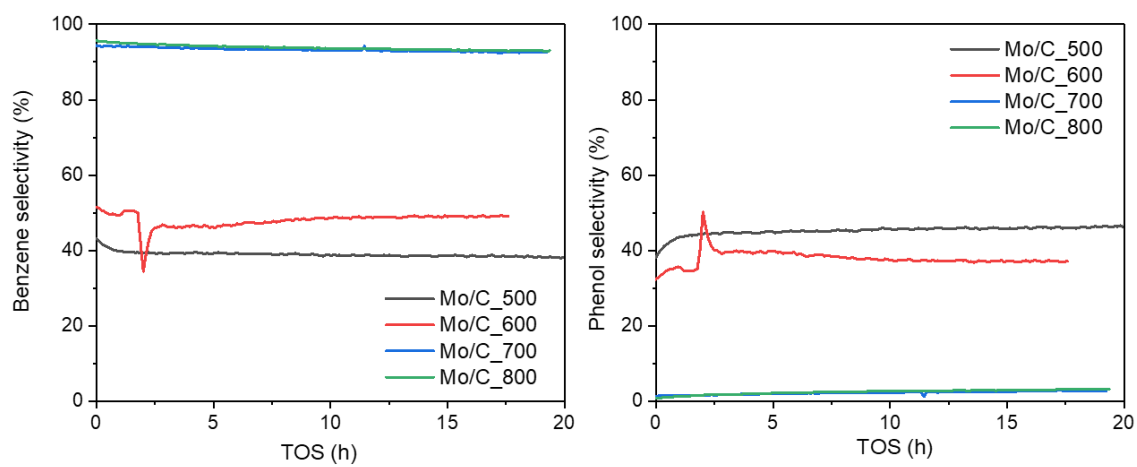

Figure E.8. Time-on-stream (TOS) benzene and phenol selectivity of the Mo (oxy)carbide catalysts.

Summary and Outlook

Methanol synthesis is one of the earliest commercial chemical processes in which catalysts played an essential role. The conversion of synthesis gas to methanol has been practiced for nearly a century since the development of the high-pressure methanol process by BASF in 1923. Due to the depletion of fossil fuels and environmental concerns related to CO_2 emissions, converting CO_2 instead of CO with hydrogen to methanol is considered as an enabling technology for the sustainability transition. Methanol produced from CO_2 with H_2 derived from renewable energy sources is a promising sustainable energy carrier and green chemical intermediate for the manufacture of chemicals that modern society heavily depends on.

Heterogeneous catalysts play a key role in current commercial methanol production. The development of the syngas-to-methanol process has seen the replacement of oxide-based catalysts (e.g., $ZnO-Cr_2O_3$) by more active Cu-ZnO based ones. Although these $Cu-ZnO/Al_2O_3$ catalysts can also convert CO_2 to methanol – in fact it is commonly accepted that CO conversion to methanol involves CO_2 as an intermediate –, hydrogenating feeds with a high CO_2 content suffers from several problems including the production of CO by-product and stability issues due to the low hydrothermal stability of current catalysts. Accordingly, there is a strong need to develop improved Cu-based catalysts or completely novel formulations to efficiently hydrogenate CO_2 to methanol.

The main objective of this thesis was to explore mechanistic aspects of several types of promising catalysts for CO_2 hydrogenation to methanol. **Chapters 2-4** focus on the improvement of Cu-based catalysts by tuning the degree of metal-support interactions using CeO_2 as support. Two new approaches involving alternative systems, i.e., In_2O_3- and MoC_x-based catalysts, were investigated in **Chapters 5 and 6** .

Cu/CeO_2 catalysts have been extensively investigated in **Chapter 2** to understand how Cu-CeO_2 interactions affect CO_2 hydrogenation. A total of 6 Cu/CeO_2 catalysts with different CeO_2 support properties and a reference Cu/SiO_2 catalyst were prepared. To determine the Cu dispersion in the Cu/CeO_2 catalysts, a CO_2-N_2O titration method was developed by which the number of metallic Cu sites and ceria oxygen vacancies can be quantified. The strong $Cu-CeO_2$ interactions lead to an increased Cu dispersion as compared to the use of silica support. A comparison was made in terms of the catalytic performance in CO and CO_2 hydrogenation. For CO hydrogenation, the Cu/CeO_2 catalysts displayed substantially higher CH_3OH synthesis rates than the Cu/SiO_2 catalyst. This indicates that the $Cu-CeO_2$ interface provides active sites for the CO-to-methanol conversion. For CO_2 hydrogenation, comparable methanol synthesis rates were obtained for Cu/CeO_2 and Cu/SiO_2 catalysts, although the Cu/CeO_2 catalysts displayed a higher methanol selectivity. It was also found that the CO_2-to-methanol reaction

on Cu/CeO_2 is structure sensitive as expected for metallic Cu particles (i.e., larger particles give rise to higher activity), implying that $Cu-CeO_2$ interactions do not lead to the promotion in intrinsic CO_2-to-methanol activity. In contrast, the reverse water-gas shift reaction (rWGS) is inhibited on Cu/CeO_2 in comparison to Cu/SiO_2. Mechanistic studies including density functional theory (DFT) calculations and IR spectroscopy were carried out to resolve reaction intermediates and spectator species. The results demonstrated that the rWGS inhibition can be linked to the stabilization of formates species on the Cu surface of Cu/CeO_2 catalysts, blocking active sites for the rWGS reaction.

Intrigued by the different behaviour between CO and CO_2 conversion on Cu/CeO_2, a follow-up study was carried out in **Chapter 3** to elucidate the role of the $Cu-CeO_2$ interface in methanol synthesis. For this purpose, a Cu/CeO_2 catalyst with high Cu dispersion was prepared by a deposition-precipitation method and evaluated for methanol synthesis from a reaction mixture that contained, in addition to H_2, varying amounts of CO and CO_2. In accordance with the previous catalytic results, methanol synthesis from CO proceeds much faster than from CO_2 on Cu/CeO_2. The methanol synthesis rate significantly decreased after adding a small amount of CO_2 to CO/H_2 feed. Isotopic labelling experiments revealed that direct CO-to-CH_3OH conversion is inhibited by CO_2 and CO_2 becomes the main reactant for methanol formation. The mechanism of CO_2 poisoning was studied by in situ IR spectroscopy supplemented by quasi in situ XPS and temperature-programmed hydrogenation (TPH) analysis. The results suggest that the $Cu-CeO_2$ interface, active for the direct CO-to-CH_3OH conversion via a formyl intermediate, is blocked by the carbonate-like species derived from CO_2. The findings in this chapter highlight the important influence of the reactant CO vs. CO_2 on the performance of methanol synthesis catalysts.

The Cu-support interactions were further studied in **Chapter 4**. In this chapter, a series of novel ternary Cu-Zn-Ce oxide catalysts with varying support composition and copper loading were prepared by a one-step flame spray pyrolysis (FSP) method. Detailed characterization demonstrated that (i) the FSP-prepared catalysts displayed similar morphological and textural properties in a broad range of chemical compositions and (ii) Cu interacts more strongly with CeO_2 than with ZnO, leading to a high Cu dispersion in Ce-containing catalysts. For the catalysts with low Cu loadings (~ 5 wt.%), CO_2 hydrogenation results showed that methanol synthesis was significantly promoted by a small amount of ZnO ($Zn/(Ce+Zn) \leq 0.05$) and the ternary Cu-Zn-Ce oxide catalysts displayed higher methanol selectivity in comparison to the binary Cu/ZnO and $Cu/ZnO-CeO_2$ oxide catalysts. A higher methanol selectivity (~10%) was also achieved for a ternary Cu-Zn-Ce oxide catalyst with a high copper loading of ~40 wt.% compared to a commercial Cu-ZnO methanol synthesis catalyst. An exploration of structure sensitivity suggests that the improved methanol selectivity is related to the synergistic Cu-ZnO and $Cu-CeO_2$ interactions: methanol synthesis from CO_2 is promoted on a Zn-modified Cu

surface and the competing rWGS reaction is inhibited by strong $Cu\text{-}CeO_2$ interactions.

In Chapter 5, In_2O_3-based materials prepared by the one-step FSP method were explored for CO_2 hydrogenation to methanol. An initial catalyst screening study led to the finding that CO_2-to-CH_3OH conversion over In_2O_3 is strongly promoted by nickel (Ni). This is surprising, because Ni is usually the preferred catalyst for methanation of CO_2. To elucidate the mechanism of Ni promotion, another series of $NiO\text{-}In_2O_3$ catalysts (screening from In_2O_3 to NiO) with similar morphological and textural properties were prepared by FSP. The catalytic data showed that the methanol synthesis rate first increased with NiO content (from 0 to 6 wt%) and then slowly decreased (from 6 to 100 wt%), pointing to a specific and Ni particle size dependent Ni-In synergy for methanol synthesis from CO_2. Detailed characterization revealed that isolated Ni atoms are substituted in the as-prepared $NiO\text{-}In_2O_3$ catalysts at low Ni loading (≤ 6 wt%). H_2-TPR and quasi in situ analysis (XPS and XAS) of used catalysts showed that the Ni substitution does not only facilitate O_v formation in In_2O_3 but also promotes the intrinsic activity of the formed O_v sites. It was proposed that H_2 activation was enhanced at isolated Ni sites in In_2O_3 surface, which accelerates further hydrogenation steps at adjacent O_v sites through a hydrogen spillover mechanism.

Chapter 6 deals with molybdenum (oxy)carbide $(Mo(O)_xC_y)$ catalysts for CO_2 hydrogenation. A passivation-free carbothermal hydrogen reduction method was utilized to prepare $Mo(O)_xC_y$ catalysts supported on activated carbon. Four different carburization temperatures (500 °C, 600 °C, 700 °C and 800 °C) were selected to investigate the degree of carburization on the hydrogenation performance of the $Mo(O)_xC_y$ catalysts. Quasi in situ characterization (XRD, XAS and XPS) revealed that predominantly molybdenum oxycarbide (500 °C and 600 °C) and molybdenum carbide catalysts (700 °C and 800 °C) were prepared at intermediate and high carburization temperatures. The catalysts were evaluated for their CO_2 hydrogenation performance without passivation and activation steps. It was found that (i) CO_2 conversion increased with carburization temperature and (ii) CO was the main product (60-75 %) over all the $Mo(O)_xC_y$ catalysts in addition to small amounts of methanol (10-20 %) and methane (10-20 %). The surface carbidic Mo sites in the catalysts, an indication of carburization degree, were quantified by CO chemisorption. Further analysis showed that CO_2 conversion was proportional to the amount of Mo carbic sites in the catalysts, pointing to the reactivity of carbidic Mo sites for CO_2 conversion. The findings in this chapter suggest that $Mo(O)_xC_y$ catalysts are more promising for the rWGS reaction than for methanol synthesis.

In **Figure 7.1**, the CO_2-to-methanol performance of the investigated catalysts in this thesis is compared in terms of methanol productivity and selectivity. Clearly, tuning metal-support interactions of Cu-based catalysts is an effective approach to improve the methanol selectivity from CO_2 hydrogenation. Substantially higher methanol selectivity can be achieved on ternary Cu-Zn-Ce oxide catalysts as compared to a commercial Cu-ZnO based methanol synthesis

catalyst. Besides optimization of Cu-based catalysts, the exploration of novel catalyst compositions is another effective approach to arrive at efficient methanol synthesis from CO_2 hydrogenation. For example, Ni-promoted In_2O_3 catalysts displayed promising catalytic performance in CO_2-to-methanol conversion as shown in this thesis.
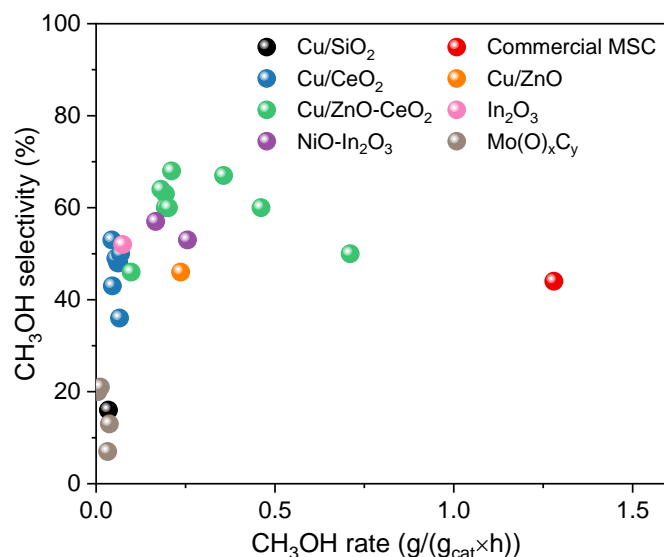

Figure 7.1. A performance comparison of the catalysts studied in this thesis for CO_2 hydrogenation to methanol. Conditions: 250 °C, 30 bar and $H_2/CO_2/N_2$ = 3:1:1 (vol%).

Based on this thesis, several recommendations can be formulated for future research: **(i)** To compete with commercial $Cu/ZnO/Al_2O_3$ catalysts, the active site density of the studied catalyst formulations has to be enhanced to achieve higher methanol productivity. For instance, further optimization of the promising Cu-Zn-Ce oxide system at higher Cu loadings is needed. With respect to the NiO-In_2O_3 system, it is interesting to prepare supported NiO-In_2O_3 catalysts to maximize the utilization of the costly In_2O_3. **(ii)** Based on the potential of NiO-In_2O_3 catalysts in CO_2 hydrogenation to methanol, efforts should be made to resolve the nature of the Ni phase responsible for the Ni-In synergy, e.g., by in situ spectroscopy (IR and XAS) supported by DFT calculations. **(iii)** Catalyst deactivation is another important but less addressed aspect in this work. Evaluation of long-term stability of the most promising catalysts at high CO_2 conversion (*i.e.* high water pressure) is essential for the development of practical CO_2-to-CH_3OH conversion catalysts. **(iv)** Important mechanistic insight can be obtained by CO_2 co-feeding catalytic measurements as shown in **Chapter 3**. It is expected that similar co-feeding approach can also be applied to products (H_2O and CH_3OH), by which the influence of products on methanol synthesis from CO_2 can be studied. **(v) Chapters 4-5** demonstrate that flame spray pyrolysis (FSP) can be used for the synthesis of well-defined heterogeneous catalysts with controlled metal-support interactions. Therefore, it is interesting to extend the utilization of the FSP method to other catalytic reactions where metal-support interactions play an important role, such as CO_2 methanation and three-way catalysis.

Acknowledgements

The four-year PhD journey is definitely an invaluable experience for me – it shapes me both scientifically and personally. I appreciate and I am very grateful that I have the opportunity to do my PhD study at IMC group, which is full of so many amazing people. Without their kind help, it would be impossible for me to reach the finish line of this tortuous PhD journey. Therefore, I would like to give my sincere thanks to all the people who guided me, helped me and motivated me.

My gratitude would first go to my promotor, prof.dr.ir. Emiel Hensen, for offering me the chance to pursue my PhD in the IMC group. I first met you in the master course of Modern Concepts in Catalysis, and it is this course that introduced me to the fascinating catalysis world. It is an interesting coincidence that you started your dean duty when I started my PhD. Looking back, I really appreciate the freedom you gave at the beginning of my project – I grew and learned a lot when almost nothing was working! I am also highly appreciated for your significant efforts to my PhD thesis at the later stage of my PhD. Your critical and rigorous attitude towards science really inspires me a lot to become a better scientific researcher. Thank you very much also for the discussion we had during our regular progress meetings and for providing me the opportunities to present my research in many conferences. I have gained much confidence in presenting and discussing scientific results thanks to these precious experiences. It is also highly appreciated for your interest and open-mindedness for different cultures, which creates a stimulating international atmosphere in the IMC group. Your theoretical and practical knowledge about China is really impressive!

I would also like to express my sincere gratitude to my co-promotor, dr. Nikolay Kosinov, for your daily supervision. Nikolay, I think my PhD project finally started to move to the right direction after your coming back to IMC as assistant professor. Thanks for your extra "push" when I had some doubts about my research. I can imagine the Mo-carbide results cannot be published without your encouragements and synchrotron trips. I also appreciate a lot for your kind personality – you are willing to help with every aspect regarding experiment! Thank you also for being an effective facilitator between Emiel and me while writing manuscripts. Your clear explanations and good suggestions significantly decreased the "energy barrier" of the writing process. Again, thank you for your daily supervision!

I want to give my profound appreciation to my other committee members: prof.dr. A. Urakawa, prof.dr. M. Behrens, prof.dr.ir. J. van der Schaaf, prof.dr.ir. L. Lefferts and prof.dr. F. Gallucci. Thank you very much for evaluating my PhD thesis, providing your precious comments and attending my defence ceremony. I would also thank prof.dr. A.P.H.J. Schenning for chairing my defence ceremony.

I would like to give my acknowledgements to the VICI user committee members – dr. E. Groeneveld, dr. E. Zuidema and prof.dr. E.T.C Vogt. Your constructive evaluation of my work during the regular VICI project meetings is highly appreciated.

My sincere thanks will also go the excellent supporting team of IMC group. Emma, a big thank you for taking care of all the administrative work. I really like your straightforward working style. Thank you as well for organizing Sinterklaas parties, which enabled me to have a bite of authentic Dutch culture. Tiny, many many thanks for your enormous assistance in building my high-pressure and micro-pulse setups. You taught me so many important skills to survive in a catalysis lab. Johan, you are a really nice and friendly person and thank you very much for ordering the components needed for the high-pressure setup. Wish you all the best in your new life. Brahim, thanks for your help with fixing TPR setup and building the micro-pulse setup. I enjoyed a lot our discussions about coming to Netherlands as an expat during the beamtrip at Grenoble. Adelheid, thank you very much for your accurate ICP measurements. I learned much from your many kind reminders regarding lab safety.

Miao and Junke, thank you for accepting to be paranymphs of my defence ceremony. Miao, it is wonderful that we can start and finish our PhD projects at almost the same time. I still remember that Emma often mistook me for you at the beginning of our PhD. Thank you very much for sharing fume hood and GC with me. My PhD is definitely not possible without your sharing! Junke (Boss Wang), it is amazing that we met each other during our master study. I really miss a lot the past time we explored all over the Europe together. Your passion for "ethanol-containing" drink back then is really stunning! You are the most hard-working man I have ever known. It is my honour to also be your paranymph and I believe your defence would be more than awesome!

I am fortunate that I was able to share a big office with so many excellent colleagues. A special "thank you" goes to the fresh doctor – Ouyang. Magically, we shared the office when you started your PhD project although you mainly work in the lignin lab upstairs. Starting from our lignin connection, we quickly became much more than colleagues. Thank you very much for all the scientific discussion, coffee break, hotpot, gym training, squash, basketball, travel and many more. The so much drinking at FORT with you made me a bit more "alcoholic". All the best for your career and life back in China and see you there in the future! Evgeny, you are the most popular officemate ever! I really like your sense of humour. Thanks for your contribution to the Mo-carbide work and all your "useful" Russian words. Aleksei, you have a "unique" taste of music. Thanks for your help with keeping lab consumables in IMC always in stock. Ferdy, I cannot believe that we sit together in the same office again! I like your solid approach towards science. Yanan, thank you for the commercial FSP ceria support and all the scientific discussion. Hao, your rich knowledge in catalysis research is remarkable. Thank you for helping with XAS data analysis. Anna and Lulu, it is nice to chat with you in the office. Good

luck with your future PhD!

I also would like to thank all the colleagues who helped me during my PhD project. A special "thank you" goes to my excellent master student, Diana. You are eager to learn and not afraid of coming up with your own idea. Your initial work on ternary Cu-Zn-Ce oxide catalysts lays a solid foundation for this nice research project. Giulia, thank you for all the help, e.g. teaching me how to synthesize ceria supports hydrothermally, when I just started my PhD in the group. Wilbert, we shared the night shifts during my first beamtrip to Grenoble. Thank you for the chat about football, Malawi, Dutch culture and so on. Arno, thank you very much for "saving" me so many times when I just started my TEM duty in the IMC group. Tobias, Jan and Rim, it is my pleasure to share TEM duty with you, and thank you very much for measuring my samples. Sasha, I am much appreciated for your assistance with my initial TPR experiments. Valery, you know everything about ceria! Thank you for your NAP-XPS measurements and data analysis of my ceria-containing catalysts. Luke, thank you for sharing the night shifts during my second beamtrip to Grenoble and for your help with XRD data analysis. Francesco, it is a great experience to work with you on the Ni-In project. Thank you very much for your massive theoretical calculations! Your kindness and openness make the smooth collaboration possible. JP, thanks for your generous help with Raman setup at the beginning of my PhD. It was an enjoyable experience for me to perform the demonstration experiments during your inorganic chemistry course. Marco, thank you for all the discussion and messages while finalizing our PhD theses. Wish you can find a nice position after your PhD. Jiachun, many thanks for your nice Kratos XPS measurements – they helped a lot for the Cu-CeO$_2$ work. Liang, you came to IMC group to work on similar project as mine. A huge thank you for your help with additional catalytic tests for my catalysts. Take care of the catalytic setup and good luck for your PhD project! Ya-Qiong, your significant DFT calculation contribution to the Cu-CeO$_2$ work is highly appreciated. I believe you will achieve a great success in academia back in China. Longfei, thanks for your initial help with XPS data analysis. Xiaofeng, many thanks for your help with DRIFT measurements. Long, thank you for sharing accommodation during the EuropaCat conference at Aachen. Yue, you are such a happy person! Thank you for all the talks in the lab, which make the experiments during night and weekend much more enjoyable. Xintong, thank you for your "trick" and help with N$_2$ physisorption measurements. Mengyue, much appreciate for your beautiful STEM-EDX images from Delft. My gratitude will also extend to the following former and current IMC members: Ming-Wen, Peng, Wei Chen, Bart H., Marta, Dimitra, Freddy, Geert, Gabriela, Michel, Ivo, Panos, Monica, Mengyan, Shaojie, Yujie, Zhaochun, Dannie, Robert, Nitin, Floriane, Douglas, Jérôme, Aleksei P., Tan, Tim, Bart Z., Robin, Xuefang, Qianqian, Kaituo, Andrey, Lingqian, Chong, Jinxun and Lu Gao. Thank you very much for the help, talk and beer!

Last but definitely not least, I would like to give my deepest gratitude to the people closest to me. 爸爸，妈妈，感谢你们一直以来对我学业的理解和支持。我很幸运你们总是能够尊重我的

Acknowledgements

想法和选择。愿你们以后身体健康，多多享受生活！有些遗憾今年因为疫情你们不能来到荷兰现场参加答辩，今后儿子我一定常回家看看。Jin, it is a once-in-a-lifetime miracle to meet you at IFFR in 2017. I am so fortunate that you are always by my side since then. We have managed together through the distance between Eindhoven, Rotterdam and Amstelveen and other obstacles. Thank you for understanding and sharing my pressure and anxiety during the difficulty time. Thank you for your continuous encouragement, support and love. Thank you for bringing sunshine into my life. Let's explore the future ahead of us together!

October 19, 2020

Jiadong Zhu

List of Publications

Publications within the scope of this thesis

J. Zhu, E.A. Uslamin, N. Kosinov, E.J.M. Hensen, Tuning the Reactivity of Molybdenum (Oxy)carbide Catalysts by the Carburization Degree: CO_2 Reduction and Anisole Hydrodeoxygenation, *Catal. Sci. Technol*. **2020**, 10, 3635-3645.

J. Zhu, Y-Q. Su, J. Chai, V. Muravev, N. Kosinov, E.J.M. Hensen, Mechanism and Nature of Active Sites for Methanol Synthesis from CO/CO_2 on Cu/CeO_2, *ACS Catal*. **2020**, 10, 11532-11544.

J. Zhu, D. Ciolca, L. Liu, N. Kosinov, E.J.M. Hensen, Flame Synthesis of $Cu/ZnO-CeO_2$ catalysts: CeO_2 Promotes CH_3OH Selectivity of Cu/ZnO in CO_2 Hydrogenation, in preparation.

J. Zhu, H. Zhang, L. Liu, N. Kosinov, E.J.M. Hensen, Ni-In Synergy in CO_2 Hydrogenation to Methanol, in preparation.

Publications outside the scope of this thesis

X. Ouyang, X. Huang, **J. Zhu**, M.D. Boot, E.J.M. Hensen, Catalytic Conversion of Lignin in Woody Biomass into Phenolic Monomers in Methanol/Water Mixtures without External Hydrogen, *ACS Sustainable Chem. Eng*. **2019**. 7, 13764-13773.

X. Huang, X. Ouyang, B.M.S. Hendriks, O.M. Morales Gonzalez, **J. Zhu**, T.I. Koranyi, M.D. Boot, E.J.M. Hensen, Selective Production of Mono-aromatics from Lignocellulose over Pd/C Catalyst: the Influence of Acid Co-catalysts, *Faraday Discuss*. **2017**, 202, 141-156.

X. Huang, C. Atay, **J. Zhu**, S. Palstra, T.I. Koranyi, M.D. Boot, E.J.M. Hensen, Catalytic Depolymerization of Lignin and Woody Biomass in Supercritical Ethanol: Influence of Reaction Temperature and Feedstock, *ACS Sustainable Chem. Eng*. **2017**, 5, 10864-10874.

X. Huang, O.M. Morales Gonzalez, **J. Zhu**, T.I. Koranyi, M.D. Boot, E.J.M. Hensen, Reductive fractionation of woody biomass into lignin monomers and cellulose by tandem metal triflate and Pd/C catalysis, *Green Chem*. **2017**, 19, 175-187.

X. Huang, **J. Zhu**, T.I. Koranyi, M.B. Boot, E.J.M. Hensen, Effective Release of Lignin Fragments from Lignocellulose by Lewis Acid Metal Triflates in the Lignin-First Approach, *ChemSusChem*. **2016**, 9,3262–3267.

J.G. Radich, A.L. Krenselewski, **J. Zhu**, P.V. Kamat, Is Graphene a Stable Platform for Photocatalysis? Mineralization of Reduced Graphene Oxide With UV-Irradiated TiO_2 Nanoparticles, *Chem. Mater*. **2014**, 26, 4662−4668.

Conference contributions

J. Zhu, N. Kosinov, E.J.M. Hensen, Cu-Zn-Ce Ternary Catalysts with Improved Methanol Selectivity of CO_2 hydrogenation, ICC XVII, Jun. **2020**, San Diego, USA, (Accepted oral presentation).

J. Zhu, N. Kosinov, E.J.M. Hensen, Cu-Zn-Ce Ternary Catalysts with Improved Methanol Selectivity of CO_2 Hydrogenation, NCCC XXI, Mar. **2020**, Noordwijkerhout, The Netherlands (Poster).

J. Zhu, N. Kosinov, E.J.M. Hensen, Oral, Tuning Catalytic Performance of Molybdenum (Oxy)carbide by Controlling the Carburization Degree, CHAINS **2019**, Dec. 2019, Veldhoven, The Netherlands, (Oral presentation).

J. Zhu, N. Kosinov, E.J.M. Hensen, Poster, Tuning Catalytic Performance of Molybdenum (Oxy)carbide by Controlling the Carburization Degree, EuropaCat 2019, Aug. **2019**, Aachen, Germany, (Poster).

J. Zhu, N. Kosinov, E.J.M. Hensen, Oral, Understanding Methanol Synthesis from CO_2 over Cu/CeO_2, NCCC XX, Mar. **2019**, Noordwijkerhout, The Netherlands, (Oral presentation).

J. Zhu, N. Kosinov, E.J.M. Hensen, Poster, Morphological Effect of Ceria Support on Cu/CeO_2 for CO_2 hydrogenation, NCCC XIX, Mar. **2018**, Noordwijkerhout, The Netherlands, (Poster).

Curriculum Vitae

Jiadong Zhu was born on August 28th, 1991 in Zhejiang, China. He completed his high-school education at Tongxiang Senior High School in 2010 and in the same year started his bachelor education in Chemistry at Fudan University in Shanghai. After obtaining the BSc degree in 2014, he moved to the Netherlands for master education in Chemical Engineering at Eindhoven University of Technology. During his master study, he completed his master thesis entitled *From technical lignin to wood lignin: an evaluation of two approaches for lignin valorization* at the Inorganic Materials & Catalysis (IMC) group of prof.dr.ir. E.J.M. Hensen and did a 5-month internship at SABIC in Geleen. He obtained the MSc degree with the distinction *cum laude* in 2016 and started to pursue his PhD degree afterwards in the IMC group at Eindhoven University of Technology under supervision of prof.dr.ir. E.J.M. Hensen and dr. N. Kosinov. His project focused on the development of novel heterogeneous catalysts for CO_2-to-methanol conversion. The results have been presented at several national and international conferences. The main results of his research are summarized in this thesis.